# Enhancing Rainfall Measurement Using Microwave Links at Three Scales

A thesis

submitted in fulfilment

of the requirements for the degree

of

**Doctor of Philosophy**

at

**The University of Waikato**

by

**SAEID ESMAEIL NIA**


THE UNIVERSITY OF
WAIKATO
*Te Whare Wānanga o Waikato*

2024

# Abstract

The application of microwave signals in telecommunication has advanced in recent decades. Hence the CMLs (Commercial Microwave Links) have been spread all over the lands. Meanwhile, the decrease in power of the signal due to rainfall has raised the idea of measuring rainfall with microwave attenuation. This PhD research delves into the challenges of these techniques and investigates potential solutions to enhance the accuracy of measuring rainfall. The objectives of the study set to three levels of raindrops' impact, signal characteristics, and catchment evaluations.

In the first stage, the cross-sections of different sizes of raindrops are calculated by solving Maxwell's differential equations in COMSOL software. Rainfall is calculated from different Drop Size Distribution (DSD) models. Then, the correlation between the resulting attenuation and rainfall provided different coefficients for the power correlation between rainfall and attenuation. Regarding the variability in DSD with rainfall intensity, alterations in extinction cross-section play a role in establishing a fluid relationship between attenuation and rainfall. This necessitates adjusting constants for the correlation across different rainfall intensities. The results support the idea of having varying coefficients for different rainfall intensities.

At the second level, the signal characteristics were investigated to find a robust method for extracting attenuation from the received power. The study led to defining a reference signal level through signal denoising methods of moving average, Butterworth, and Chebyshev methods. The study showed the superior performance of the moving average in predicting rainfall, especially in 38 GHz links (H and V) indicated by NSE and KGE. Overall, the moving average also resulted in 2%, 16%, and 14% lower RMSE than the conventional method in microwave links 26H, 38H, and 38V, respectively. Butterworth and Chebyshev filters exhibited higher NSE and lower RMSE in 38 GHz links, with competitive accuracy in the 26 GHz link compared to conventional methods. The effect of wet antenna also decreased and even vanished in some cases.

At last, the catchment runoff was used to calibrate the relationship between rainfall and attenuation. In a study in 15 catchments in Melbourne, the suggested method established a relation between attenuation and the quick flow of 15 flow stations. Meanwhile, the coefficients of the rainfall-attenuation formula were calibrated to reach the highest accuracy of runoff prediction. The results indicate a more robust connection between attenuation and quick flow in contrast to conventional rain gauge data. The new suggested method achieved a maximum NSE of 0.78 and KGE of 0.86. Compared to rain gauges, the conventional CML model improved NSE by an average of 197%, while the new model showed an additional 50% enhancement. RMSE optimisation also demonstrated improvement, with a 15% enhancement using the conventional CML model and an additional 4% on average with the new model. Moreover, the revised flow calibration technique reduces the wet antenna effect by an average of 49%.

## Acknowledgements

First and foremost, I extend my heartfelt appreciation to my primary supervisor, Dr. Ali Shokri, for his unwavering support, guidance, and motivation during my doctoral journey. I am equally thankful to my secondary supervisor, Professor Yifan Chen, and former members of the supervisory panel, Associate Professor Earl Bardsley and Professor Ilanko Ilanko, for their invaluable insights and discussions.

I am deeply grateful to my managers and colleagues at Toi Ohomai Institute of Technology, particularly Kate McLaughlin, Rachel Beaton, Reza Enayatollahi, Kierstin Daviau, Josh Haile, Priyank Patel, and Hamish McKenzie, for providing me with the opportunity to join their team and for their unwavering support amidst the challenges of work and study. Without their invaluable assistance, conducting this research would not have been possible.

Special thanks also go to my friends and peers at the University of Waikato, including Saeed Nikghalb, Muhammad Waqas Sarwar, Ali Aghazadegan, and Amir Mohammadi, for their continuous friendship and support.

I am also indebted to my family for their spiritual support throughout this research and in my life in general. My deepest gratitude goes to my wife, Hamideh Karimi, for her boundless love, unwavering support, and belief in me. Her patience and assistance have been indispensable, and I am forever thankful to her.

# Table of Contents

# List of Figures

# List of tables

# Glossary

**Attenuation:** The reduction in the strength of a signal, wave, or beam as it travels through a medium, such as rain in microwave signal propagation. Attenuation is directly related to the amount of rainfall and is used to measure rainfall intensity.

**Butterworth Filter:** A type of signal processing filter designed to have a maximally flat frequency response in the passband. It is commonly used to remove noise from signals without causing ripples in the frequency response.

**Catchment:** An area of land where water collects when it rains, often drained by a river system. Catchments are important in hydrology for understanding how rainfall translates into runoff.

**Chebyshev Filter:** A filter used in signal processing with a sharper roll-off than Butterworth filters. Chebyshev filters come in two types: Type I, which allows for ripples in the passband, and Type II, which avoids passband ripples but allows them in the stopband.

**CML (Commercial Microwave Links):** Refers to microwave links used for telecommunication purposes, often installed on towers or buildings, that are repurposed to measure rainfall by capturing the attenuation of microwave signals due to raindrops.

**COMSOL:** A Multiphysics software used for simulating the behaviour of electromagnetic waves (among other phenomena) by solving Maxwell's equations. It was used in the thesis to calculate cross-sections of raindrops to study microwave attenuation.

**Cross-section (Scattering Cross-section):** A parameter used in wave theory to describe the effective area of an object (e.g., raindrops) that interacts with an incoming wave. The scattering cross-section represents the extent to which a raindrop scatters an electromagnetic wave, such as a microwave.

**DSD (Drop Size Distribution):** A statistical description of the range and number of raindrop sizes in a rain event. The drop size distribution affects the calculation of microwave attenuation, as larger drops cause more attenuation.

**Extinction Efficiency ($Q_{ext}$):** A measure of the effectiveness of a particle (raindrop) in attenuating electromagnetic waves. It is related to the particle's size and the wavelength of the wave. The thesis uses Qext to evaluate the impact of different raindrop sizes on microwave attenuation at various frequencies.

**Extinction Cross-section ($C_{ext}$):** Refers to the total cross-sectional area of a particle (such as a raindrop) that contributes to the attenuation of an electromagnetic wave. It includes both scattering and absorption by the particle.

**Fast Fourier Transform (FFT):** A computational algorithm to transform a signal from the time domain into the frequency domain. FFT is widely used in signal processing to analyse the frequency components of a signal by decomposing it into sine and cosine waves.

**Finite Impulse Response (FIR) Filter:** A type of digital filter used in signal processing, characterized by a finite-duration impulse response. FIR filters are always stable, have linear phase characteristics, and are often used where precise control over frequency response is required.

**Flash Flood:** A sudden and intense flood event caused by heavy rainfall, often over a short period of time. Flash floods are common in urban areas or small catchments with limited capacity for water retention.

**Fourier Transform (FT):** A mathematical transform that represents a function as a sum of periodic components, and transforms a signal into its constituent frequencies. Unlike FFT, which is a computational method, the Fourier Transform is a general mathematical tool.

**Frequency Domain:** A representation of a signal or a function based on frequency rather than time. In this domain, the signal is expressed as a function of frequency, often using Fourier or wavelet transforms.

**Hilbert Vibration Decomposition (HVD):** A decomposition method that calculates the instantaneous frequency and amplitude of a signal by employing the Hilbert transform. It's used to extract the frequency characteristics of non-stationary signals.

**Intrinsic Time-Scale Decomposition (ITD):** A method for time-frequency-energy analysis of signals. It decomposes non-linear signals into proper rotation components to estimate instantaneous frequency and amplitude, while preserving time-localized characteristics.

**Infinite Impulse Response (IIR) Filter:** A type of digital filter that uses feedback and has an infinite-duration impulse response. IIR filters are computationally efficient but can introduce non-linear phase distortions if not properly designed.

**Iterative Filtering:** A signal processing method that decomposes a signal into intrinsic mode functions (IMFs) through repeated filtering, useful in non-linear and non-stationary signal analysis.

**KGE (Kling-Gupta Efficiency):** A performance metric for evaluating hydrological models. It combines correlation, variability, and bias into a single measure, with a value of 1 indicating perfect model performance.

**Local Characteristic Scale Decomposition (LCD):** A signal decomposition method that breaks down complex signals into Intrinsic Scale Components (ISCs) for detailed signal analysis, particularly effective in fault diagnosis.

**Lowpass Filter:** A filter that allows signals with a frequency lower than a selected cut-off frequency to pass through while attenuating higher frequencies. It is commonly used to remove high-frequency noise.

**Moving Average:** A simple filter method that smooths a signal by averaging a set of data points over a specified window of time or frequency, often used to reduce high-frequency noise.

**Noise (in Signal Processing):** Unwanted random variations or disturbances in a signal that interfere with the accurate transmission or interpretation of data. In the context of rainfall measurement, noise can affect the accuracy of microwave signal attenuation measurements.

**NSE (Nash-Sutcliffe Efficiency):** A statistical metric used to assess the predictive accuracy of hydrological models. NSE values range from $-\infty$ to 1, where 1 indicates a perfect match between observed and modelled data, and values below zero indicate poor model performance.

**Proper Rotation Component (PRC):** A component of the ITD method, which represents the highest frequency oscillation on a baseline. It is used to calculate the instantaneous frequency and amplitude of a signal.

**Quick Flow:** The portion of runoff that rapidly enters streams or rivers following rainfall. Quick flow is often generated by intense rainfall or when the ground is saturated, and it plays a key role in flash flood events.

**Rainfall-Runoff Models:** Mathematical models that estimate runoff in a catchment based on rainfall data. These models can be empirical, conceptual, or physical and are used to predict water flow during rainfall events, crucial for flood management and water resources planning.

**Receiver:** A device that detects and captures electromagnetic waves (such as microwaves) after they have travelled through the atmosphere. In microwave link-based rainfall measurement, the receiver detects the attenuated signal after it has passed through raindrops.

**Regression Analysis:** A statistical method used to explore the relationship between variables. In hydrology, it is used to predict runoff from rainfall using linear or non-linear equations. Regression helps in calibrating rainfall-runoff models by correlating different parameters.

**Refractive Index:** A measure of how light or electromagnetic waves are bent when they pass through different mediums, such as raindrops. The refractive index influences how microwaves are attenuated during rain events.

**RMSE (Root Mean Square Error):** A standard statistical measure used to evaluate the accuracy of a model by comparing the observed and predicted values. In the context of rainfall-runoff models, RMSE quantifies the difference between the measured and simulated runoff.

**Runoff:** Water that flows over the surface of the land into rivers and streams after precipitation. It is influenced by factors like rainfall intensity, land use, and soil properties, and is a critical factor in stormwater management.

**SCS Model (Soil Conservation Service):** A widely-used empirical method for predicting runoff from rainfall, based on land use, soil type, and hydrologic conditions. The model estimates runoff using a parameter known as the curve number (CN).

**Signal Attenuation:** The reduction in signal strength as it passes through a medium, like rainfall. In the context of rainfall measurement, signal attenuation is used to estimate rainfall intensity from microwave link data.

**Transmitter:** A device that generates and sends out electromagnetic waves (such as microwaves) for communication or measurement purposes. In rainfall measurement using microwave links, the transmitter emits the signal that is attenuated by raindrops.

**TRMM (Tropical Rainfall Measuring Mission):** A joint satellite mission by NASA and JAXA designed to monitor and study tropical rainfall, which provided valuable data for understanding the global water cycle.

**Water Balance:** A hydrological model that tracks the inflow, outflow, and storage of water in a system, often used to calculate how much rainfall is transformed into runoff.

**Wavelet Transform:** A mathematical technique used in signal processing to decompose a signal into its frequency components at multiple scales. It is particularly useful for analysing non-stationary signals that contain both low and high-frequency components.

# 1. Chapter One – Introduction

## 1.1. Introduction

The effects of rain-induced attenuation on radar systems have been recognised since the World War era (Crane, 1975). Since rainfall affects the propagation of microwave signals, it causes attenuation or scattering signals (Lin and Ishimaru, 1971; Ishimaru and Cheung, 1980b; Mishchenko, Hovenier, and Travis, 2000), which can be measured and used to estimate rainfall intensity (Le-Wei Li *et al.*, 1995).

Microwave links operate at high frequencies and are often installed on towers or buildings to provide high-speed internet access or mobile phone coverage. For the first time in the late 1990s and early 2000s, microwave links were used for rainfall intensity monitoring (Giuli *et al.*, 1991; Giuli, Facheris, and Tanelli, 1999; Holt *et al.*, 2000; Upton *et al.*, 2005). Reviewing the history of studies on electromagnetic waves results a huge number of references have been studied on measuring wave attenuation and parameters in different media and wavelength ranges. A review paper (Nupen., 1955) indicated 267 references relevant to radar meteorology only between 1941 and 1955. Another comprehensive bibliography was provided (Boudreau and Stone, 1965) including 494 theoretical and experimental works in journals and conference papers, reports, and books on wave scattering and attenuation by precipitation particles between 1950 and 1964. Subjects cover research about scattering, attenuation, drop size, rainfall, snowfall, hail, thunderstorms, tornados, radars, and the characteristics and properties of water droplets.

Commercial Microwave Links (CMLs), which are used for wireless communications, are used as rain gauges for the first time in Israel and the Netherlands (Messer, 2006, 2007; Leijnse, Uijlenhoet and Stricker, 2007b). Recent studies have shown promises as a new method for estimating rainfall (Messer, 2006, 2007; Goldshtein, Messer and Zinevich, 2009; Overeem, Leijnse and Uijlenhoet, 2011, 2013, 2016d; David, Alpert and Messer, 2013; Messer and Sendik, 2015; Alpert, Messer and David, 2016; Pudashine *et al.*, 2021).

Microwave links are becoming increasingly prevalent in urban and suburban areas, providing the potential for rainfall measurements (Leijnse, Uijlenhoet and Stricker, 2007b, 2007a, 2008a; Overeem, Buishand and Holleman, 2008; Goldshtein, Messer and Zinevich, 2009; Overeem, Holleman and Buishand, 2009; Zinevich, Messer and Alpert, 2009; Hazenberg, Leijnse and Uijlenhoet, 2011; León, Hernández-Serrano and Soriano, 2011; Overeem, Leijnse and Uijlenhoet, 2011, 2013, 2016b; Abdulrahman *et al.*, 2012; Fenicia *et al.*, 2012; van de Beek *et al.*, 2012; Chwala *et al.*, 2012; Bianchi, Rieckermann and Berne, 2013; Liberman *et al.*, 2014; Trömel *et al.*, 2014; Kantor and Bito, 2015; Martin Fencl *et al.*, 2015b; Brauer *et al.*, 2016; D'Amico, Manzoni and Solazzi, 2016; Fencl *et al.*, 2017, 2020; Rios Gaona *et al.*, 2017, 2018; Shrestha and Choi, 2017; van Leth *et al.*, 2017; De Vos *et al.*, 2017; Eshel *et al.*, 2017; Song *et al.*, 2019b; Graf *et al.*, 2020; Overeem *et al.*, 2021; David *et al.*, 2021; Blettner *et al.*, 2022; Nebuloni *et al.*, 2022; Pastorek *et al.*, 2022; Wolff *et al.*, 2022; Zheng *et al.*, 2022; Janco, Ostrometzky and Messer, 2023; Liu *et al.*, 2023; Daher, Al Sakka and Chaaban, 2023).

This technology offers a cost-effective alternative to traditional rain gauge networks, which can be expensive to install and maintain, particularly in remote or inaccessible areas (Zinevich, Alpert and Messer, 2008; Gosset *et al.*, 2015). The links can provide a higher temporal and spatial resolution, ground-level non-point data which is less sensitive to wind.

### 1.1.1. Measuring rainfall with microwave signals

The idea of using microwave signals for measuring rainfall comes from the development of radars and the effect of rainfall and other hydrometeors on the attenuation of the power of microwaves (Le-Wei Li *et al.*, 1995). During the development of radio, television, and other terrestrial wave

propagation systems in the early to mid-20th century, the effects of hydrometeors were studied extensively.

Calculating rainfall is conducted using a relationship between attenuation and rainfall (Olsen, Rogers and Hodge, 1978; ITU-R, 2005):

$$\gamma_R = kR^{\alpha} \qquad \text{Equation 1-1}$$

where $\gamma_R$ is the specific attenuation (dB/km), $R$ is the rainfall rate (mm/hr), and $k$ and $\alpha$ are constants that are determined as functions of frequency.

In reverse, the relationship between attenuation $A$ and $R$ could be defined as:

$$R = aA^{b} \qquad \text{Equation 1-2}$$

where $A$ is attenuation and $a$ and $b$ are constants.

### 1.1.2. Advantages of CML as rain gauges

**Low costs of development:** Due to the established placement of transmitter and receiver antennas for Commercial Microwave Links (CMLs) in both urban and rural areas to ensure comprehensive mobile access coverage, the infrastructure required for implementing such a measurement system is relatively economical (Zinevich, Alpert and Messer, 2008; Gosset et al., 2015). Despite ongoing developments in underground fibre optic cable networks, the high costs associated with such infrastructures mean that CMLs will likely remain in use worldwide for several decades (Overeem, Leijnse and Uijlenhoet, 2016b).

In contrast to conventional radar setups that involve substantial financial investments running into millions of dollars, the implementation of CMLs is a cost-effective alternative. Regular mobile networks continuously record attenuation data for each link to ensure a stable, undisturbed, and sufficiently robust connection for cell phones (Zinevich, Alpert and Messer, 2008; David, Alpert and Messer, 2009). Essentially, all that is required is a data-gathering and analysing system, typically comprising software or computer codes. This cost-effective approach makes CMLs an attractive option compared to radar setups, which involve significant expenses in the deployment and maintenance of widespread gauges.

**High spatial distribution:** The advancement of cell phone technology has led to comprehensive coverage of both urban and rural areas by mobile networks. Figure 1-1 illustrates the extensive network of microwave links in Israel, the Netherlands, and New Zealand. Notably, the Netherlands boasts over 3300 microwave links, surpassing the 325 manual rain gauges and 32 automatic rain gauges in the region (Overeem, Leijnse and Uijlenhoet, 2016d).

In New Zealand, the estimated number of microwave links exceeds 26,000 (Hansen, 2011a) , significantly outnumbering the 600 climate stations with records of rainfall more than once a day, as reported by the National Institute of Water and Atmospheric Research(National Institute of Water and Atmospheric (NIWA)). This widespread deployment of Cellular Microwave Links (CMLs) offers a higher resolution compared to satellite-based alternatives.

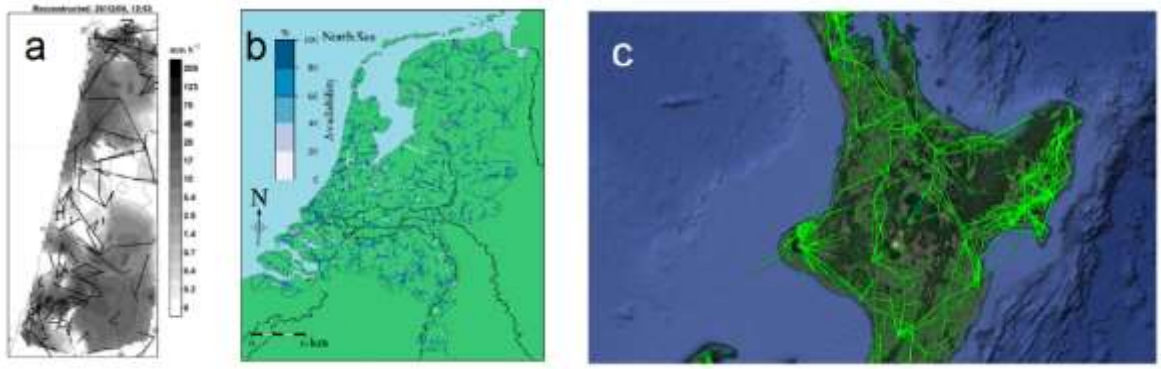


*Figure 1-1- Microwave links of CMLs in different countries. (a): Israel, Black lines (Gazit and Messer, 2018), (b): the Netherlands, Blue to white lines (de Vos et al., 2019), and (c) New Zealand's north island, Green lines (Hansen, 2011b)*

**High temporal resolution:** Commercial microwave links typically capture attenuation data at intervals as short as 15 minutes (Messer, Zinevich and Alpert, 2012; Messer and Sendik, 2015; Eshel et al., 2017; Ostrometzky et al., 2017). Moreover, other microwave links have the flexibility to be set at even higher recording frequencies, potentially as low as one second. While it is conceivable to adjust commercial links to a lower recording frequency, such adjustments might be contingent upon corporate interests or financial considerations.

In contrast, the majority of rain gauges typically record data only once a day, with a few situated in climate stations offering 3-hourly data recording. Given that urban catchments respond more rapidly to precipitation changes compared to rural and undeveloped areas, the ability to collect more frequent data enhances the simulation accuracy of urban catchments using CMLs (Martin Fencl *et al.*, 2015a).

**Non-point data:** In contrast to rain gauges, CMLs provide measurements across a volume of air and rainfall area, offering a more comprehensive understanding of spatial variations than traditional point sources of records (Trömel et al., 2014; van Leth et al., 2019).

**Ground-level measurement:** Unlike radar systems that measure rainfall at higher altitudes, CMLs capture rainfall data just a few tens of meters above the ground (Wang et al., 2012; D'Amico, Manzoni and Solazzi, 2016).

**Less sensitive to wind:** When a CML network records high-frequency data, the information tends to converge toward the actual rainfall rate, thereby mitigating the influence of wind (Messer, 2007).

### 1.1.3. Errors and inaccuracies in measuring rainfall

In addition to the complexity of rainfall measurement methods, traditional approaches are susceptible to errors in monitoring rainfall. These errors can be categorized based on their sources.

**Reading Errors:** Errors may arise during the process of reading data from the gauge. This type of error is more common in manual gauges and is seldom encountered in automated logging gauges due to the reduced likelihood of human error. Various methods exist to rectify such errors in the data.

**Errors of instrument:** At times, rain gauges may deviate from standard conditions, often requiring maintenance or repairs over time. Instrumental errors can also arise when various types of gauges are employed across different weather stations. Changes in gauge types can impact the continuity of long-term rainfall data series (Kidd and Huffman, 2011a).

**Errors of method:** Certain systematic errors are inherent in specific types of rain gauges. Some of these errors are linked to the environmental conditions surrounding the gauge, while others are intrinsic to the gauge type itself. Repetitive factors have been extensively documented in the

literature (Rodda, 1971; Sevruk, 1982; B Sevruk and Klemm, 1989; Strangeways, 2004, 2007, 2010; Molini, Lanza and La Barbera, 2005; Kidd and Huffman, 2011; Ochoa-Rodriguez *et al.*, 2019). The most significant ones have been succinctly outlined in the WMO report (Nespor, 2013):

a) Deviation of precipitation due to wind
b) Wetting of the inner parts of the gauge
c) Evaporation of water from the container
d) Splashing in or out of raindrops

Wind can impact all types of catching gauges, including simple buckets, tipping buckets, weighing, and capacitance gauges, as well as non-catching gauges like disdrometers. Previous studies suggest errors ranging from 5 to 40% inaccuracy in measuring rainfall under windy conditions (Groisman and Legates, 1994; Sevruk, 1996). In a single storm, this error may escalate to 75% (Neff, 1977).

Other weather conditions, such as wetting and evaporation, can also contribute to monitoring errors. For instance, wetting is reported to potentially increase monitoring errors by up to 10% (Rodda, 1967, 1971; Green, 1970; Sevruk, 1973, 1982, 1996; Goodison, 1978; Groisman and Legates, 1994; Chvíla, Sevruk and Ondrás, 2005).

Additional errors arise from the location and spatial factors of measurements. Measurement methods fall into three types: point, 2D, and 3D measuring systems. Satellites record 2D horizontal images, CMLs measure in a 3D volume, and all other gauges are assumed as point gauges. Point gauges are unable to capture the spatial variability of rainfall, affecting the accuracy of modelling, especially in small catchments like urban areas (Ochoa-Rodriguez et al., 2019). For instance, due to the rapid response of urban catchments to rainfall events, it is recommended to provide a resolution of 1 km and 1-5 minutes for urban drainage modelling (Ochoa-Rodriguez et al., 2015; Ochoa-Rodriguez et al., 2019).

Despite the importance of getting access to sufficient spatial data on precipitation, there are not adequate rain gauges currently operating around the globe. The number of gauges is estimated at 150,000 worldwide (B. Sevruk and Klemm, 1989). However, data from all stations are not available at hourly or daily intervals. Rainfall data is collected from 8,000 to 12,000 first-class stations through the World Meteorological Organization (WMO) Global Telecommunication System (GTS), providing 3-hourly and daily data (WMO, 2011).

For daily records, there are more options available. A total of 180 institutes contribute to the Global Precipitation Climatology Project (GPCP), providing daily scale measurements at 85,000 locations (Kidd et al., 2017). However, the total equivalent area of the orifice area of all rain gauges, in comparison with the total land and ocean surface, is only 3,026 $m^2$ from 123,014 gauges, representing a mere $5.93 \times 10^{-10}$% of Earth's surface (Kidd et al., 2017). Even when considering a 5 $km^2$ area of influence for a gauge, this proportion does not exceed 1% of the Earth's surface.

In addition to common errors and challenges encountered in all types of rainfall monitoring, each method has specific errors stemming from its underlying mechanism and technology.

**Tipping bucket gauges:** The movement of mechanical parts in tipping bucket gauges introduces errors in rainfall monitoring. Previous research indicates an underestimation of rainfall by this type of gauge (Luyckx and Berlamont, 2001; Upton and Rahimi, 2003; Molini, Lanza and La Barbera, 2005). This error is attributed to water loss during the process of changing buckets under continuous intensive rainfall. Tipping buckets with the highest accuracy may not measure steps smaller than 0.1 mm, and their calibration can change over time (Strangeways, 2004). Consequently, while residual uncertainty typically complies with WMO specifications, there can be considerable errors at certain flow rates (Lanza and Stagi, 2006). Additionally, a delay in recording rainfall of up to 30 minutes has been reported due to the time required for melting snow filled in the buckets (Savina et al., 2011).

**Radars:** While radars offer superior spatial resolution of rainfall and coverage of distant areas, certain inaccuracies are inherent in the method. The primary error arises during the conversion of radar reflectivity to rainfall. Since the drop size distribution of rain varies not only from location to location but also over time, unchanging constants can introduce errors (Lee and Zawadzki, 2005; Krajewski, Villarini and Smith, 2010; Ochoa-Rodriguez et al., 2019).

Furthermore, different types of precipitation, such as drizzle or melting snow, can alter reflectivity, necessitating adjustments to the constants in the formula (Krajewski et al., 2006; Strangeways, 2007).

The beam angle limitation prevents measurements at lower heights in the distance, representing only the rainfall amount higher than the ground surface. Occasionally, the topography of the land obstructs the beam, resulting in missed data, as illustrated in Figure 2 during the rainfall event in Dunedin, New Zealand, on June 3rd and 4th, 2015 (Murray, 2015).

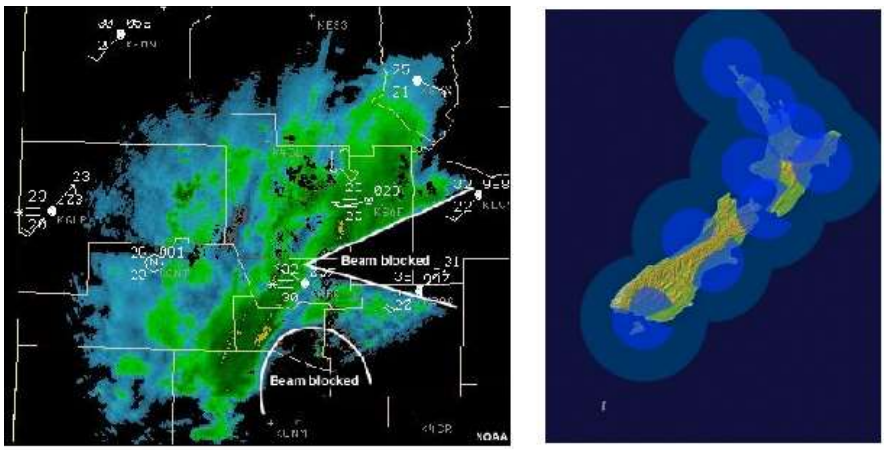


*Figure 1-2- A typical blocking in radar beam in Dunedin, New Zealand (a)(Weather Radar Fundamentals), coverage of radars in New Zealand (b)(the incomplete circles indicate blockage (Murray, 2015)*

Methods exist to correct radar estimations, such as utilising dual frequencies and detecting rain types (Delrieu et al., 1999; INOUE et al., 2009; Rossi et al., 2017). Adjusting the constants of Equation 1-1 is feasible through calibration, using gauge data. However, due to the high spatial variation of rainfall, a considerable number of gauges are required (Strangeways, 2007).

Although not technically an error, one of the drawbacks associated with radar technology is its considerable expense. For example, the installation of a new radar in Otago, New Zealand, carries a significant price tag of $2.8 million. (Edwards, 2019).

**Satellites:** Depending on the type of sensors, whether Visual (VIS) frequency or Infrared (IR), certain errors may arise. In VIS, the image is available only during the daytime, and the relationship between cloud brightness and precipitation under clouds is relatively poor (Kidd and Huffman, 2011a). On the other hand, in IR systems, the relationship between cloud top temperature and rainfall is indirect and varies with the time of rainfall (Pellarin *et al.*, 2008; Kidd and Huffman, 2011a). Additionally, the high speed of satellites does not allow for adequate coverage of rainfall, and the low resolution of images may miss small rain events (Strangeways, 2007).

Correction methods are crucial for satellite measurements. Similar to other methods and akin to radars, the initial step involves using gauge data for calibration. Adjusting and improving the algorithm for deriving rainfall from satellite images is another common approach to aligning data with gauge records. Some innovative approaches also suggest using satellite soil temperature

measurements to calculate or modify rainfall amounts (Zhao, Su and Zhao, 2006; Pellarin et al., 2008, 2009; Brocca et al., 2014).

### 1.1.4. Current challenges of the CML method

The principles of the CML methods are also similar to weather radars. In CML methods, a decrease in wave power is utilised, correlating with the number of raindrops in the detected volume of air. The primary distinction between CML and radar lies in the spatial arrangement of transmitters and receivers. In CML, waves pass through raindrops before being captured by the receiver, whereas in radar, the transmitter and receiver share the same location, with the antenna capturing the returning echo of incident waves. Some challenges associated with the CML method include:

- *Wet antenna*

Raindrops cause wave attenuation not only in the space between the transmitter and receiver but also on the antennae. A wet antenna constitutes a significant source of error in the CML method (Kharadly and Ross, 2001; Leijnse *et al.*, 2010; M Fencl *et al.*, 2015; Fencl *et al.*, 2019; Valtr, Fencl and Bares, 2019) and may result in up to a 40% overestimation (Overeem, Leijnse and Uijlenhoet, 2016d). The additional attenuation from a wet antenna can be considered a portion of the total attenuation (Kim and Kwon, 2018):

$$\mathrm{A_{tot}} = \mathrm{A_{clear}} + \mathrm{A_r} + \mathrm{A_{wa}} \qquad \text{Equation 1-3}$$

where $A_{tot}$ is the total attenuation, $A_{clear}$ is clear sky attenuation, $A_r$ is rainfall attenuation, and $A_{wa}$ is a wet antenna attenuation.

The wet antenna error is typically corrected by employing techniques to distinguish between wet and dry periods when it is not raining. Various methods and studies have demonstrated successful results in correcting rainfall measurements (Overeem, Buishand and Holleman, 2008)

- *Variation in Drop Size Distribution (DSD)*

Similar to radars, variations in Drop Size Distribution (DSD) at temporal and spatial scales result in fluctuations when converting attenuation to rainfall. Therefore, as each location has its own unique DSD, Equation 1-2 needs to be calibrated with local constants. Improved adoption has been observed by adjusting Equation 1-2 based on local DSD data (Leijnse *et al.*, 2010; Song *et al.*, 2019a). In addition to adopting local DSD, another technique to minimise the effect of DSD is using dual-frequency links. The difference between the attenuation of the two frequencies exhibits a better correlation with rainfall (Rincon and Lang, 2002; Rahimi et al., 2003). It is also possible to use dual-polarization links to achieve better results (Ruf et al., 1996) compared to using a single microwave link.

- *Low frequencies*

The use of CMLs or any microwave link setup for measuring rainfall is typically limited to higher frequencies, primarily exceeding 12 GHz (Ruf *et al.*, 1996; Rahimi *et al.*, 2003; Upton *et al.*, 2005; Leijnse, Uijlenhoet and Stricker, 2008b; van Leth *et al.*, 2017, 2018). Some sources propose frequencies higher than 5 GHz (Kesavan et al., 2014) for the effective utilisation of CMLs in measuring rainfall, with the International Telecommunication Union recommendation P-838.3 (ITU-R, 2005) (ITU-R P838-3, 2005) indicating that the attenuation for frequencies below 6 GHz is negligible, rendering the attenuation data useless for deriving rainfall amounts.

The underlying reason lies in the scattering properties of raindrops at low frequencies, where the attenuation is very low in the presence of water drops (Ishimaru and Cheung, 1980a, 1980b; Ishimaru *et al.*, 1982). Consequently, telecommunication companies opt for lower frequency links in regions with higher rainfall, such as south eastern Asia (Abdulrahman *et al.*, 2012) as higher frequencies are more affected by higher rainfall attenuation.

Only a few studies have identified an acceptable range for attenuation to be used in attenuation-rainfall rate relationships. For instance, in Ecuador, a 5.52 GHz microwave link with an 18 km length measured an attenuation of about 6 dB (Ramos et al., 2017). It is recommended that the microwave link must be longer than 15 km, with the quantization step finer than 0.02 dB (Ramos et al., 2015).

The primary motivation for investigating the application of lower frequencies is their significant representation among existing operational microwave links. A nationwide inspection was conducted using data on all registered radio links in New Zealand as of 5 December 2022, to examine the distribution of frequency ranges—specifically comparing those below and above 10 GHz. The findings are presented in Figure 1-3 , showing that radio frequency (RF) links between 1 and 10 GHz make up 18% of all links, which is 64% more than the number of links operating above 10 GHz.

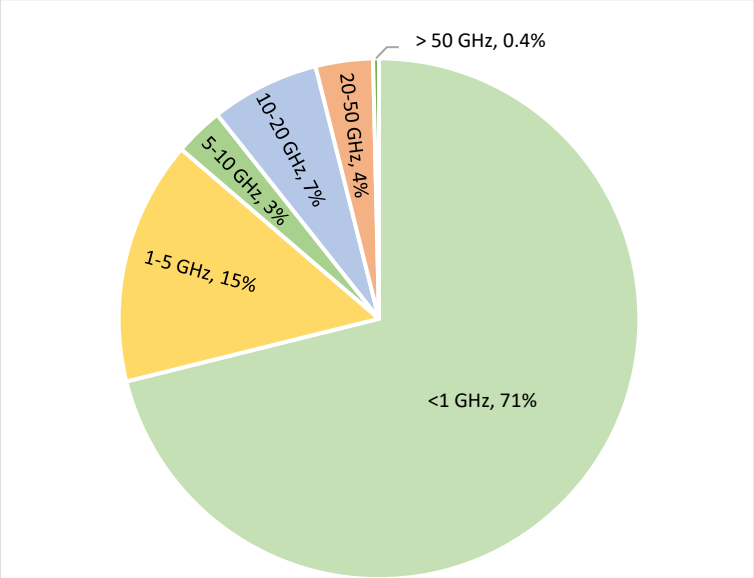


*Figure 1-3- The ratio of different frequencies among 99485 RF links registered in New Zealand https://www.rsm.govt.nz/assets/Uploads/documents/prism/prism.zip*

These links serve various purposes, including telecommunications, mobile networks, and internal communications. Mobile service providers, in particular, commonly use higher frequencies in the 20–40 GHz range for cell tower communication. To further investigate the use of lower frequencies within mobile services, an additional analysis focused on Vodafone's registered microwave links in New Zealand.

Figure 1-4 illustrates that 41% of Vodafone's links operate in the 1–10 GHz range, compared to 25% above 10 GHz (Radio Spectrum Management (RSM)). These results highlight the potential value of leveraging low-frequency microwave links, which are 64% more available than higher-frequency ones, for enhancing rainfall measurement applications.

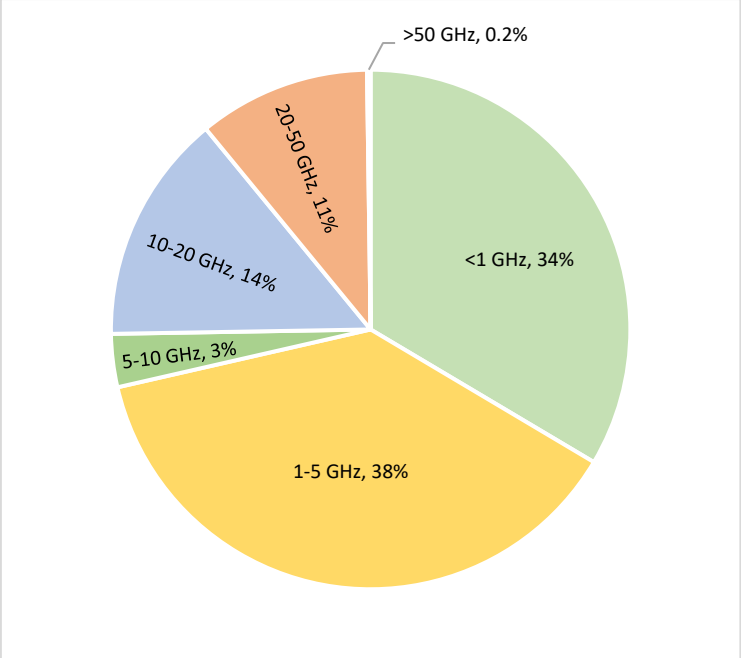


*Figure 1-4- The ratio of different frequencies among 7986 microwave links registered for Vodafone in New Zealand (Radio Spectrum Management (RSM))*

On the other hand, the 3G and 4G generation of cell phones are going to be replaced by the new generation of 5G. Hence, the links in frequencies of 900, 1800, 2100, and 2400 MHz are going to be redundant. However, the frequency that is proposed for 5G by Office of the Minister of Broadcasting, Communications and Digital Media to allocated to the 5G network is 3500 MHz (3.5 GHz, with a 390 MHz spectrum range between 3.41 GHz and 3.8 GHz) (2019a, 2019b). Therefore, the share of under 5 GHz links will be kept at a high rate.

- *Defining the reference power level*

Attenuation is the difference between the source power and the received power. When the received power drops because of rainfall effects, this attenuation can be used for rainfall measurement. However, there are other sources of attenuation other than the rainfall. They include atmospheric gases and water vapour (ITU-R, 2016) fog (David, Alpert and Messer, 2013; David *et al.*, 2015), interference in line of sight, diffraction, tropospheric scatter, surface ducting, elevated reflection and refraction (Recommendation ITU-R P.452-17, 2021). Buildings, trees, knife-edge diffraction, rounded hilltops, surface diffraction, and other types of interference in scattering also cause signal loss (John Price, 1993).

Conventional methods assume that the same variations in the base signal level, during a rainy time and the preceding dry time (Huang *et al.*, 2023). In addition, the conventional methods need wet-dry classification before baseline calculations. This may lead to overestimating or underestimating rainfall.

- *Accuracy of rainfall measurement*

The accurate determination of the actual precipitation on Earth poses a significant challenge. Contrasting the localised measurements of traditional rain gauges with the linear path measurements of microwave links amplifies this challenge, questioning the true extent of water collected in a catchment (Mory *et al.*, 2024). Additionally, any calibration of rainfall calculation methods requires a comparison with reliable rainfall records. Ground-level rain intensity information is still crucial for remote sensing methods, serving as the standard reference in rainfall calibration for meteorological satellite and radar applications (Choi *et al.*, 2023).

### 1.1.5. The significance of advancing the CML method

Considering the numerous advantages of CMLs, the development of this method enhances rainfall measurement, leading to improved hydrological models, simulations, and prediction models for catchment and weather. The high spatial and temporal resolution of data allows models to provide more accurate and realistic estimations of water cycle quantities. Additionally, long microwave links enable access to remote areas, while shorter links offer higher resolution in urban settings.

The availability of high-resolution rainfall records strengthens forecasting models, particularly in small areas and just before impending hazards, such as floods and high-intensity rainfall events (Davis *et al.*, 2022). This granular data allows forecasters to better understand and predict rainfall dynamics, especially in small catchment areas vulnerable to flash floods (Younis, Anquetin and Thielen, 2008). Additionally, the ability to capture rainfall variations at second-scale intervals enhances the precision of flood prediction models, enabling timely warnings and effective mitigation strategies (Charlton-Perez, Cloke and Ghelli, 2015). By coupling high-resolution rainfall data with advanced forecasting models, such as those utilizing ensemble techniques, forecasters can improve the accuracy and lead time of flood predictions, thereby enhancing disaster preparedness and response efforts (Cattoën, McMillan and Moore, 2016).

Moreover, the infrastructure for the CML system is already established and operational. The next logical step involves engaging telecommunication companies in collaborative weather forecasting projects and data sharing. In contrast to million-dollar radar systems that often struggle to provide adequate coverage, the cost of sharing CML data remains highly reasonable.

Recent research trends indicate a growing interest in the utilisation of the CML method, despite current challenges and inaccuracies. For example, a startup company (ClimaCell) has been predicting urban rainfall using a mobile network since 2016. They are also developing a short-term forecast system by leveraging extensive data sources from the Internet of Things (IoT), drones, airplanes, cellular signals, satellite communications signals, and cameras, along with traditional data sources. ClimaCell's products prove valuable for assessing flood risks, wildfire threats, and road conditions (ClimaCell).

## 1.2. Research objectives

Summarising the advantages and disadvantages of CML rainfall measurement techniques, along with their challenges and potential improvements, bring some ideas for investigating the possibility of enhancing the methods and techniques. These ideas provide a foundation for establishing research goals and objectives to enhance accuracy.

Considering the characteristics of microwave signal scattering, drop size distribution, rainfall intensity, and runoff production, adjustments are contemplated at three levels: raindrop scale, signal power scale, and catchment scale. Grouped under these three themes, a number of research questions have been identified to address these potentials.

Therefore, the overall objective of this study is to refine the formulas and improve the implementation of CML methods in rainfall and runoff estimation. Within this framework, the study proposes and addresses a set of guiding research questions in each of the three scales.

### 1.2.1. Raindrop scale

**Questions:**

(A) Looking at the number of microwave links in frequencies lower than 10GHz, could they be applicable in CML rainfall measurement?
(B) How significant is the signal attenuation at frequencies below 10 GHz, and how do these compare with the conventional higher-frequency ranges?

(C) The conventional methods suggest a specific relationship for each location, according to different DSD models and rainfall characteristics. Are these factors the only variables affecting the relationship?
(D) Does the attenuation–rainfall relationship vary with rainfall intensity within the same location?

**Rationale:**

Questions (A) and (B) investigates the restrictions in using frequencies below 10 GHz. The main reason to limit the application of such frequencies is the negligible attenuation rate at this range. However, if attenuation patterns at these frequencies can be quantified effectively—especially under varying rainfall intensities—then a broader set of existing infrastructure can be used for rainfall estimation.

Questions (C) and (D) challenge the current assumption that the coefficients in the power-law relationship (Equation 1-2) are fixed for each location. While DSD has been considered in past models, rainfall intensity as a dynamic influencing factor has not been deeply examined. This study explores whether the coefficients should be treated as variable parameters rather than constants.

**Potential Contribution:**

- Improved theoretical understanding of attenuation behaviour under different conditions.
- Development of adaptive or dynamic models for rainfall estimation.
- Potential to utilize lower-frequency CMLs, increasing coverage in under-monitored regions.

### 1.2.2. Signal power scale

**Questions:**

(E) Can mathematical signal denoising techniques improve the detection of rainfall events by removing unrelated fluctuations in received signal strength?
(F) Are denoising filters capable of handling wet–dry classification and mitigating the wet antenna effect, which are traditionally addressed using auxiliary rainfall data?

**Rationale:**

The received signal in a CML is inherently noisy, influenced by both long-term and short-term fluctuations due to technical and environmental conditions. By treating this as a signal processing problem, this study investigates whether filters such as Moving Average, Butterworth, and Chebyshev can extract the underlying attenuation caused solely by rainfall.

If successful, this approach could reduce dependency on external rain gauge data for wet–dry classification and baseline definition.

**Advantages:**

- Development of a more autonomous CML-based rainfall estimation method.
- Reduction in the need for co-located meteorological instruments.
- Improved accuracy and adaptability in signal interpretation.

### 1.2.3. Catchment scale

**Questions:**

(G) Can attenuation data from CMLs predict catchment runoff more accurately than conventional methods based on rain gauge measurements?

(H) Does the attenuation–runoff relationship offer stronger correlations than the traditional two-step approach of attenuation-to-rainfall followed by rainfall-to-runoff?

**Rationale:**

Rain gauges measure rainfall at a single point, whereas CMLs provide path-averaged values, potentially offering better spatial representation across a catchment. This study investigates whether attenuation data alone—when calibrated with flow measurements—can serve as a proxy for estimating runoff, eliminating the intermediate step of rainfall estimation which introduces additional uncertainty.

**Potential Contribution:**

- A novel attenuation–runoff modelling framework.
- Improved runoff prediction, particularly in small or urban catchments.
- Potential applications in areas lacking dense rain gauge networks.

## 1.3. Thesis structure

Research questions outlined in Research objectives are addressed from chapter 2 to chapter 4 by integrating under-review and published peer-reviewed publications in accordance with the University of Waikato guidelines.

Chapter two addresses the study in raindrop scale exploring the answers to questions (A) and (B). At the scale of raindrops, the study investigates the characteristics of raindrops and microwave signals to identify aspects that are underdeveloped and could enhance the accuracy of the rainfall-attenuation relationship. Microwave cross-sections are examined across different frequencies, particularly those below 10 GHz, to identify attenuation variations in this range. Different range of frequency and rainfall intensity are employed to Subsequently refine Equation 1-2 for various conditions.

Chapter three includes the investigations of denoising methods to extract the rainfall attenuation from CML signal to answer questions (C) and (D). At this scale, the analysis focuses on the characteristics of microwave received power to determine the optimal estimation of attenuation. This study examines shortcomings in existing methods and suggests new approaches and alternative methods to improve the accuracy and precision of attenuation measurement. Various mathematical and electromagnetic engineering solutions are explored as potential alternatives to conventional approaches. Through investigation and application, certain methods are identified as having superior structures suited to the characteristics of rainfall events, and they are subsequently tested using real data.

Chapter 4 studies the catchment scale studies to answer questions (E), (F), (G) and (H). In this chapter the rainfall-runoff models are enhanced by the application of CML methods. A better correlation is practiced replacing the existing relationships by new coefficients. A new calibration approach is employed to adjust the accuracy of predicting runoff. Therefore, as an adjustment in models, a direct attenuation-runoff relation is investigated to be replaced instead of the traditional rainfall-runoff methods.

Finally, chapter 5 concludes by presenting analyses of the research contributions, significant findings, potential future research avenues considering limitations, and possible applications of the knowledge gained on CML rainfall measurement methods.

## 1.4. Outcomes of the study

Two papers have been extracted from this study and are under review in academic journals. A third paper is being prepared and will be submitted in future. They are:

- Enhancing runoff prediction by exploring attenuation-runoff as an alternative to conventional rainfall-runoff models, under review in Journal of Hydrology.
- Rainfall intensity effects on the rainfall-attenuation correlation, submitted in Journal of Quantitative Spectroscopy and Radiative Transfer.
- Employing denoising filters for determining the base power of the microwave links to enhance CML rainfall measurement techniques, under revision by authors.

The studies have been presented in conferences as well, as:

- Development of an agent-based model for monitoring rainfall between two telecommunication antennae, NZHS 2019, Rotorua
- Enhancing runoff prediction: exploring attenuation-runoff as an alternative to rainfall-runoff models, AGC-NZHS 2023, Auckland
- Employing denoising methods for defining base power of microwave link for enhancing rainfall estimation, AGC-NZHS 2023, Auckland

# 2. Chapter Two – Raindrop scale

## 2.1. Introduction

Radio waves have been used for telecommunication for more than a century (Saakian, 2011). However, the primary focus on atmospheric effects, particularly rainfall, on microwave propagation, was raised after World War II (Louis J. Ippolito, 1986; Whiton *et al.*, 1998; Saakian, 2011). Weather meteors such as raindrops, snow folks, and water vapour can boost the loss of the power of electromagnetic (EM) waves (Ippolito, 1989). Therefore, the intensity of precipitation directly impacts the attenuation of the EM waves. Calculating EM wave attenuation requires some information on the characteristics of rainfall intensity along the wave path (John Price, 1993).

A probability factor is often used to show how long a microwave link may be interrupted by rainfall during a year. For example, the International Telecommunication Union (ITU) recommends a rainfall intensity equal to $R_{0.01}$ for designing microwave links (ITU-R P.837-6, 2012), where $R_{0.01}$ is the annual rainfall rate with a probability of exceedance of 0.01% of the average annual time (ITU-R, 2012). Therefore, in any location, the power and frequency of a microwave link should be calculated considering the rainfall rate ($R_{0.01}$), in which the attenuation causes interruption, not more than 0.01% of a year (Pablo Angueira, 2012). As a result, knowing the highest attenuation is vital for maintaining a stable connection.

A simple power correlation between rainfall intensity and attenuation is often used to measure the attenuation of EM waves in a rain event (Equation 1-1). on the other hand, the reverse correlation (Equation 1-2) can also be implemented to estimate the rainfall intensity using the attenuation from microwave links.

For the first time in the late 1990s and early 2000s, microwave links were used for rainfall intensity monitoring (Giuli *et al.*, 1991; Giuli, Facheris, and Tanelli, 1999; Holt *et al.*, 2000; Upton *et al.*, 2005). In addition, cell phone antenna towers with frequencies above 18 GHz are used as rain gauges in Israel and the Netherlands (Messer, 2006, 2007; Leijnse, Uijlenhoet, and Stricker, 2007).

However, the attenuation in the frequencies from 1 to 3 GHz, which are commonly used between cell phones and Base Transceiver Station (BTS), is reported to be too low for rainfall monitoring (Ishimaru and Cheung, 1980a, 1980b; Ishimaru *et al.*, 1982). There are also recommendations by other studies to use particular frequencies. According to (Kesavan et al., 2014), (ITU-R P838-3, 2005), and (Lin, 1973), frequencies above 5, 6, and 10 GHz, respectively, are more suitable for measuring rainfall intensity and volume.

A few studies showed a detectable range for attenuation to be used in attenuation-rainfall rate relationships (Ramos et al., 2017). However, the microwave link is recommended to be longer than 15 km and the quantisation step finer than 0.02 dB (Ramos et al., 2015).

Another difference between the higher and the lower frequencies has been detected as more errors in some frequencies. Early studies indicate a decrease in frequency from 34.8 GHz to 9.4 GHz, resulting in an increase in the average errors of estimating rainfall, from 9% to 21% in regression coefficients (Atlas and Ulbrich, 1977). In addition, some more recent studies suggest that the frequencies above 30GHz correlate better with ground rainfall monitoring than the lower frequencies (Leijnse, Uijlenhoet and Sstricker, 2008; Leijnse, Uijlenhoet, and Berne, 2010).

Studying the physics of scattering and attenuation of EM waves in confronting raindrops may reveal the limitations and unfold the potential of using lower frequencies in rainfall monitoring. James Clerk Maxwell was the first to formulate EM waves' fundamentals in the 19$^{th}$ century (Serway and John W. Jewett, 2005). Later, Waterman (Waterman, 1965) solved Maxwell's equations for scattering light by non-spherical particles and introduced the "T-matrix" approach (Mishchenko, Travis and Mackowski,

1996). Finally, Mishchenko et al. (1996) show that the T-matric method turns to the Mie scattering theory for spherical particles.

The total attenuation of EM waves passing through a rainfall event is dependent on drop size distributions (DSD) (Atlas and Ulbrich, 1977; Oguchi, 1981; Medeiros Filho, Cole and Sarma, 1986; Jiang, Sano and Sekine, 1997). DSD describes the statistical characteristics of the size of raindrops (Best, 1950; Jameson and Kostinski, 2001), which determine the average number of each size of raindrops during the rainfall event. Exponential, gamma or log-normal distributions are the most common forms of DSD in practice (Bringi *et al.*, 2003). Among a few DSD models, which are generally proven and used in different studies, Marshall and Palmer's (1948) model is widely applied. A three-parameter gamma distribution by Ulbrich (1983) is also suggested to describe the variation of raindrops. DSD curves show that the number of larger drops increases in heavier rainfalls (Sekhon and Srivastava, 1971; Jameson and Jameson, 1991; Harikumar, 2009; Lam, Din, and Jong, 2015; Serio, Carollo, and Ferro, 2019).

On the other hand, the power decrease in the wave also depends on the size of the drop. Finally, the determinative factor in wave attenuation is the interaction rate between the target and the radiation, which could be described with a scattering cross-section ($C$) (Kotlarchyk, 1999). The scattered and absorbed waves describe the scattering and absorption cross-sections.

Therefore, in a rainfall event, a combination of DSD and the scattering/absorption cross-section of water drops in the air is implemented to predict rainfall attenuation (Oguchi, 1960; Ulbrich and Atlas, 1984). The total attenuation between two antennas summarises all drops' effects on the wave by their corresponding cross-section (Atlas and Ulbrich, 1977; Oguchi, 1981). At the same time, a scattering/absorption cross-section that dimensionally represents an area should not be considered an actual geometric cross-sectional area but an effective area proportional to the probability of interaction between the radiation and target (Kotlarchyk, 1999).

Regarding the application of EM waves in telecommunication, previous studies calculated cross-sections for droplets in frequencies above 10 GHz. For example, studies have been carried out for a range of 10 to 100 GHz (Lin and Ishimaru, 1971), or some specific frequencies like 10, 30, and 120 GHz in one study (Ishimaru and Cheung, 1980b) and 30, 60, and 120 GHz in another study (Ishimaru and Cheung, 1980a). A single 34.8 GHz frequency (Okamura and Oguchi, 2010) is also getting more attention due to a higher application for communication purposes. However, the frequencies lower than recommendations for rainfall measurements (Kesavan *et al.*, 2014), ITU-R P838-3, 2005, Lin, 1973)(lower than 10GHz), are largely ignored in the literature in this regard. Limited studies focused on frequency ranges as low as 0.6 GHz (Lin and Chen, 2001) and 1 GHz (Amarjit and R P S Gangwar, 2008). However, they focused on specific frequencies, not the entire range.

Therefore, because $\alpha$ and $k$ In Equation 1-1 are dependent on the variation of $\gamma_R$ (attenuation) and $R$ (rainfall intensity), any improvement in these variables would improve the rainfall estimation. Looking for a better $\alpha$ and $k$, this study tried to analyse the variation of scattering cross-sections to detect the variation of attenuation of microwaves below 10 GHz frequency. Considering the selected range is the most commonly used frequency band in cell phone telecommunication networks, including 3G, 4G, and 5G generations (Office of the Minister of Broadcasting, 2019a, 2019b), this paper explores the unfulfilled potential and limitation of using a lower frequency range from 1 to 10 GHz for rainfall monitoring.

### 2.1.1. Goals

The goal of this study is to analyse the raindrops and microwave signals and their interaction in different frequencies to distinguish among the attenuation-rainfall relationship in each frequency and rainfall intensity.

It is expected to find more precise correlations between rainfall and attenuation by exploring the details of scattering microwave when passing through the raindrops. The final aim of this chapter is

adjusting the rainfall-attenuation power law (Equation 1-2) to the range of frequencies and drop size distribution which is different in locations and the rainfall intensities.

## 2.2. Methods and Results

### 2.2.1. Scattering approximations

The quantity and magnitude of the effects of particles on microwaves could be delivered to calculations using scattering cross-sections of particles. The scattering theories are developed to solve Maxwell's equation for waves passing a media including particles. The early studies introduced Mie and Rayleigh scattering (approximations) for electromagnetic wave propagation through the particles within a space (Rayleigh, 1881, 1899; Mie, 1908). The main difference between the Mie and Rayleigh approximations is the relative size of the particle and wavelength. Rayleigh scattering region applies when the particle with the radius $a$ and refractive index $n$ is electrically small $(2\pi a/\lambda \ll 1)$ (Barclay, 2003). Mie scattering is applicable for particles with a reasonably big enough size to be independent of the wavelength (Hecht, 2002), with a diameter equal to or larger than the wavelength.

For applying scattering theories in the study of microwaves in rainfall, some characteristics of raindrops, including raindrop size, shape, and velocity, need to be involved. The size of raindrops is limited as the air resistance does not allow them to extend. Studies on raindrops' characteristics show droplets larger than 6 mm are unstable due to the drag force at the bottom of the raindrop and split when they expand beyond 6 mm (Marshall and Palmer, 1948; Gunn and Kinzer, 1949; Pruppacher and Beard, 1970; Beard, 1976, 1977). Smaller drops in the range of 0.2 to 0.5 mm in diameter are assumed to drizzle (Strangeways, 2007). Therefore, the diameters of raindrops range from 0.5 to 6 mm for this study.

On the other hand, the actual shape of raindrops is not spherical or teardrop shape and changes when their diameter extends (McDonald, 1954). Small drops are more sphere-shaped than large drops with a flattened base (Jones, 1959; Barclay, 2003). Some of the shape models of raindrops are suggested by Beard and Chuang (1987), Pruppacher and Beard (1970), and Pruppacher and Pitter (1971). Four models of raindrops are shown in Figure 2-1 explaining models for a 5 mm diameter droplet (Beard and Chuang, 1987; Beard, Bringi and Thurai, 2010).

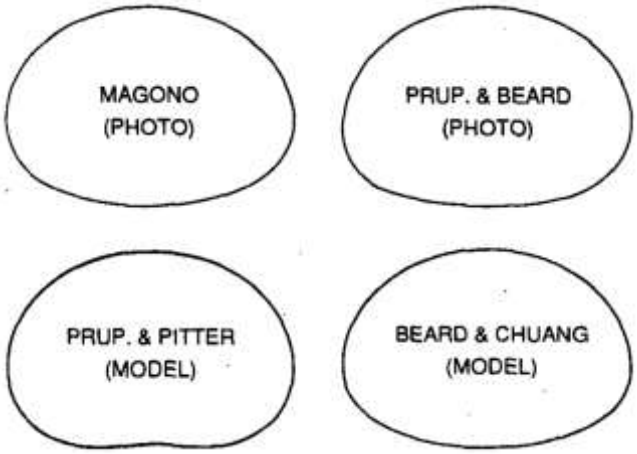


*Figure 2-1- Comparison of drop shape in different models for a 5 mm diameter drop (Beard and Chuang, 1987; Beard, Bringi and Thurai, 2010)*

Defining the exact size and shape of raindrops improves the approximation of the attenuation. The scattering cross-section thus more depends on the relative size of the particle to the wavelength and angle of radiation. Therefore, The scattering cross-section is related to the volume of the target (Bohren and Huffman, 1983).

Utilising Equation 7-19 to Equation 7-25, finally, the total attenuation could be found from (Amarjit and R P S Gangwar, 2008):

$$A = 4.343 \times 10^3 \int \sigma_t(a).N(a)da \qquad \text{Equation 2-1}$$

where $\sigma_t$ is the total (extinction) cross-section and $N$ is the number density of drops, $a$ is the equivalent radius of raindrops, and $da$ is the drop diameter interval.

For this study, the MiePlot (MiePlot) and COMSOL (COMSOL Multiphysics Reference Manual, 1998) are used to calculate the scattering and absorption cross-sections of raindrops in a range of microwave frequencies. The calculations help to study the specific effect of each drop size on a particular wave frequency. Raindrops are assumed to be spherical as a simplification assumption. This assumption also allows comparing the results of this study with previous investigations.

Extinction cross-section and efficiency are calculated for the frequencies between 1 and 10 GHz and two relatively higher frequencies of 20 GHz and 30 GHz. Droplets' diameters vary between 1 mm and 10 mm. Thus, the range is wider than the diameter of raindrops to give a better perspective of the changing trend when choosing lower frequencies.

For the first step, extinction efficiency ($Q_{ext}$) was calculated to detect the effects of individual drops confronting waves. Figure 2-2 shows changes in extinction efficiency ($Q_{ext}$) in this range of diameter against different frequencies.

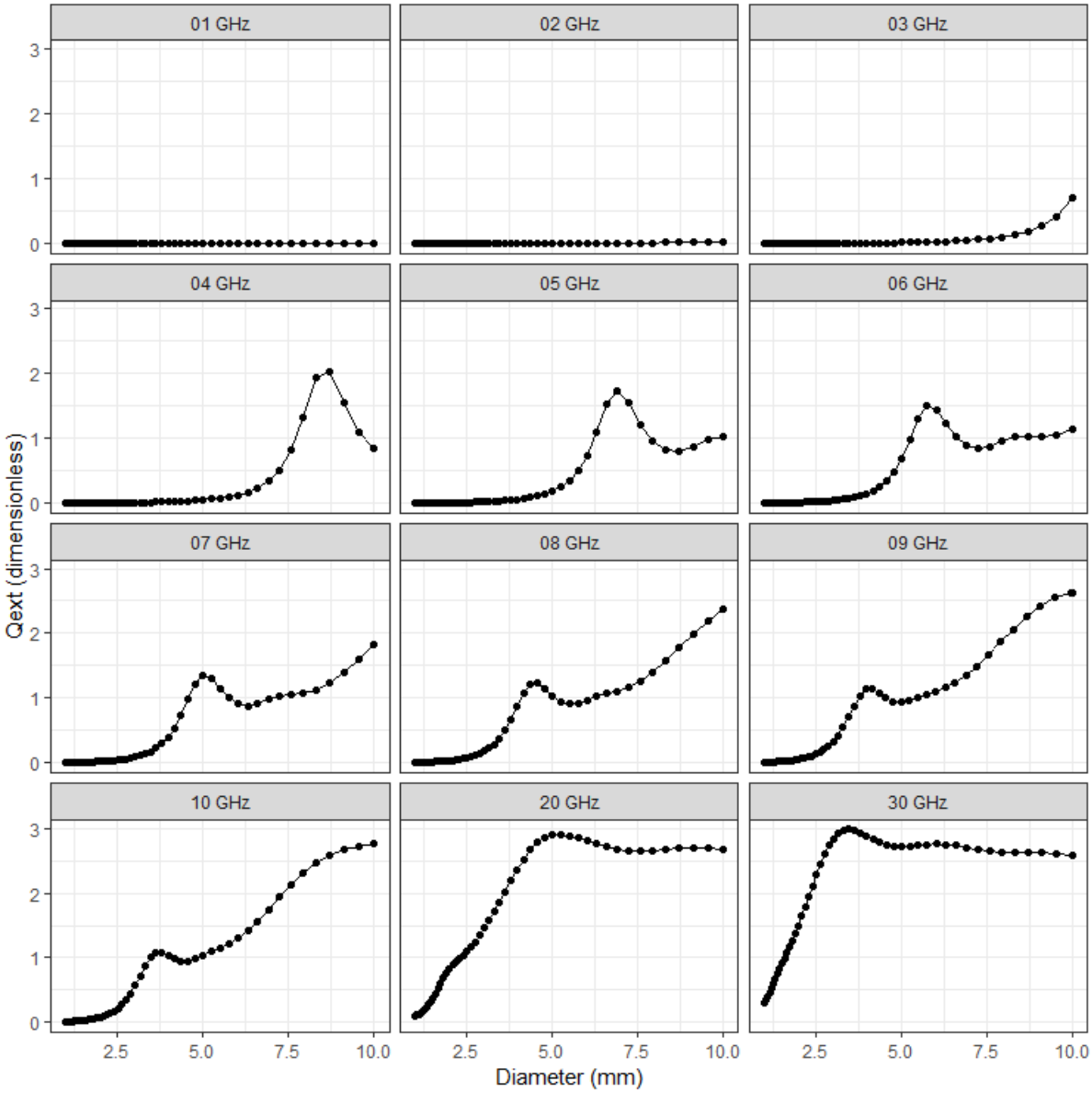


*Figure 2-2- Extinction efficiency of different diameters of water drops in frequencies 1 to 10 GHz, 20 GHz, and 30 GHz using MiePlot.*

In frequencies 1 to 3 GHz, $Q_{ext}$ is relatively low, and droplets in the size of raindrops do not significantly affect the wave. However, in frequencies above 4 GHz, $Q_{ext}$ increases gradually by increasing the frequency. Also, a contradiction could be observed in the form of a particular peak that appears at 4 GHz in around 8 mm drops and slides towards 3.5 mm diameter drops at 10 GHz. The peak flattens at 20 GHz and 30 GHz.

### 2.2.2. The effects of the complex refractive index

The refractive index is related to the change in velocity of electromagnetic waves in a medium regarding a vacuum (Liou, 2002). The refractive indices of meteors are composed of a real and an imaginary part. The real part of the refractive index refers to the scattering wave, while the imaginary part is related to the absorption by the material (Bohren and Huffman, 1998; Liou, 2002; Fu, 2015). The refractive index also varies by changing frequency (Stamnes, Thomas and Stamnes, 2017).

The wave propagation is simulated with only the real part of the refractive index to see what happens when the microwave hits the drop. This simulation, therefore, distinguishes some special

effects of wave number on scattering patterns inside and around a droplet. As a result, when the ratio of wavelength to the drop diameter varies, some unique patterns of wave propagation appear in the electric field of the mediums of air and the particle.

In these simulations, the absorption part in wave propagation is set aside by assuming the imaginary part of the refractive index in MiePlot is equal to zero. Then, calculations are applied for the same frequencies in Figure 2-2. The results are presented in Figure 2-3 as the (R) curve for only the real part of the refractive index and beside the (R&I) curve for calculations using a refractive index including the real and the imaginary parts together.

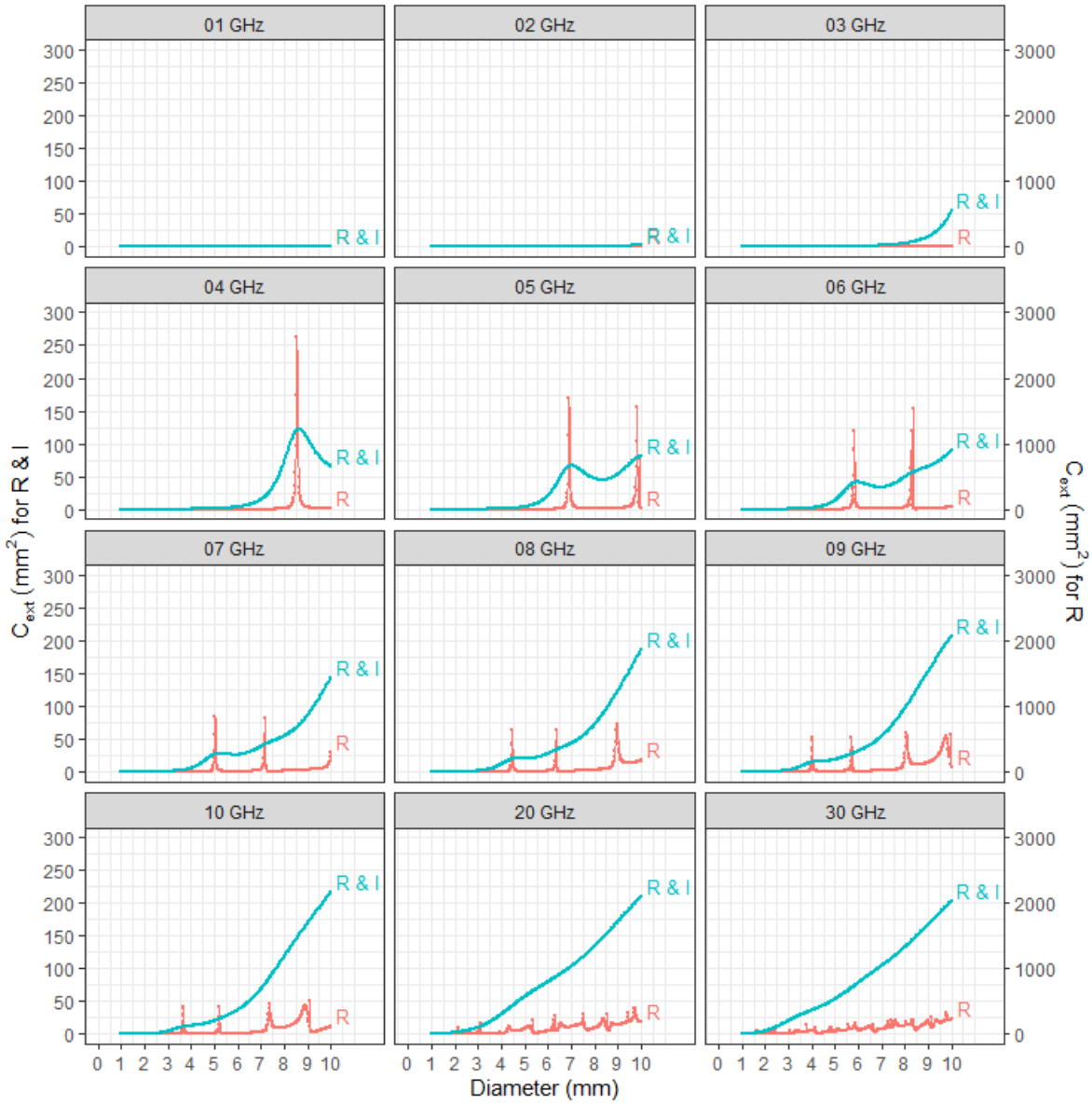


*Figure 2-3- Extinction cross-sections calculated, (R&I): with the real and the imaginary part, (R): with the real part and zero imaginary part (using MiePlot)*

$Q_{ext}$ only shows the proportion of scattered waves to the irradiance. Thus, considering Equation 2-1, $C_{ext}$ would be more applicable to analyse the effects of drops on the amount of power and replaced in calculations and graphs. MiePlot is used directly for calculating $C_{ext}$ and the results are presented in Figure 2-2 (R&I curve). In comparison with $Q_{ext}$ curves, peaks disappear at 8 GHz and above. Therefore, the attenuation of the wave which is directly the result of $C_{ext}$ shows peaks only in the frequency range of 4 to 7 GHz.

Figure 2-3 illustrates that the smooth peaks in frequencies of 4 to 8 GHz in the (R&I) curve turn to sharp peaks in the (R) curve, which is scattering without absorption. For example, in the 5 GHz and (R&I) line, a drop diameter of 7.18 mm shows a peak $C_{ext}$ of 65.1 mm$^2$. In the (R) graph, this smooth peak appears in a sharp peak of 1680 mm$^2$ in a 6.89 mm diameter drop.

The peak base is also narrower for the drop diameter range, and peaks happen in fewer drop diameters. The higher amount of $C_{ext}$ peaks in the R graph appear in other frequencies, although the high rates fall to 839 mm$^2$ at 7 GHz and 505 mm$^2$ at 10 GHz. The peaks at 20 and 30 GHz are around 200 to 400 mm$^2$. However, they appear more frequently in more drops in the range of diameter of raindrops.

While the imaginary part of the refractive index is omitted in simulating waves, the sharp peaks in scattering cross-sections generate some unique situations in wave scattering, refraction, and reflection. Visualising the simulation of wave equations can display the patterns of the electric field and hence the wave propagation inside and around the drops.

### 2.2.3. Numerical solution of Maxwell equations

In another attempt to show the scattering patterns of electromagnetic waves confronting raindrops of different sizes, the Maxwell equations are solved using COMSOL Multiphysics, a comprehensive simulation software environment for a wide range of applications (COMSOL Multiphysics Reference Manual, 1998). COMSOL simulations can illustrate the wave pattern inside and around a drop. Unlike the scattering-approximations approach, directly solving the Maxwell equations calculates electric and magnetic fields for space points in time steps and describes the spreading of the electromagnetic wave (Seybold, 2005). Therefore, the electromagnetic field change inside and around the droplets could be observed instead of a black-box simulation.

### 2.2.4. Cross-section calculations in COMSOL

Simulations of drops and electromagnetic waves are carried out using the radio frequency module and the frequency domain. In the first step, the imaginary part of the complex refractive index is set to zero for the electric field displacement model to solve the wave equation. Then, the three-dimensional simulation is set up with a water drop in a spherical space surrounded by a perfectly matched layer (García-Etxarri *et al.*, 2011; Laurell and Hillborg, 2018). Figure 2-4 shows the simulation setup and mesh in COMSOL. The drop, surroundings and technical details followed the method used by Garcia-Etxarri (2011).

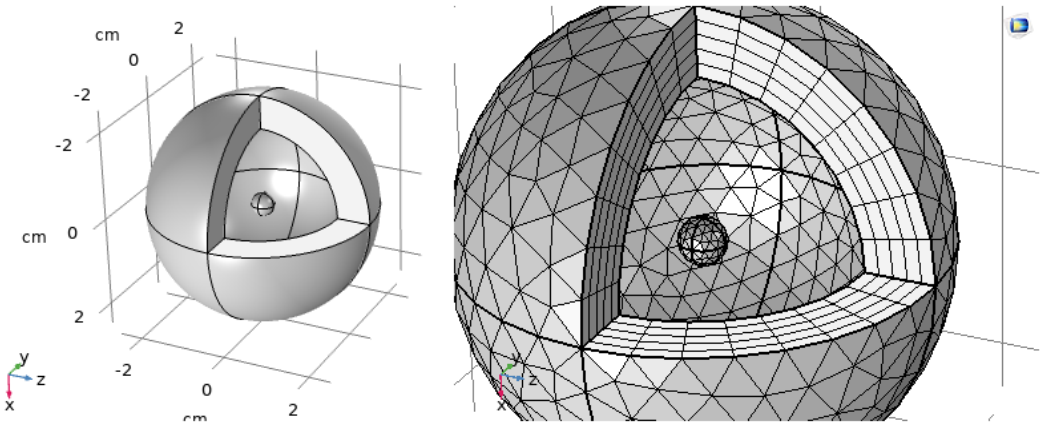


*Figure 2-4- The sphere inside as a water drop and the sphere around for a perfectly matched layer in COMSOL (left)- simulation mesh (right)*

The mathematical relations calculate scattering and absorption cross-sections through the power of the wave and the diameter of the drops. The absorption cross-section ($C_{abs}$) indicates the amount of the absorbed incident wave and is defined as:

$$C_{abs} = \frac{1}{I_0}\int_{\mathbb{v}} d^3xQ \qquad \text{Equation 2-2}$$

where the integral is calculated over the droplet volume and $Q$ is the power loss density in the particle. $d$ is drop diameter and $I_0$ is the incident energy. The scattering cross-section ($C_{sca}$) describes the amount of the wave, scattered away on the droplet and is defined as:

$$C_{sca} = \frac{1}{I_0}\int_{\mathbb{s}} d^2x\bar{n} \cdot \overline{S_{sca}} \qquad \text{Equation 2-3}$$

where $\bar{n}$ is the vector pointing outwards, normal to the droplet and $\overline{S_{sca}}$ is the Pointing vector. The extinction cross-section determines the lost wave and is given by the sum of the absorption and scattering cross-section:

$$C_{ext} = C_{abs} + C_{sca} \qquad \text{Equation 2-4}$$

The results of COMSOL and MiePlot were compared in different conditions. The extinction cross-sections are calculated in COMSOL for droplets by assuming a zero imaginary part for the complex refractive index. The extinction cross-sections of the two methods are drawn on a logarithmic scale in Figure 2-5.

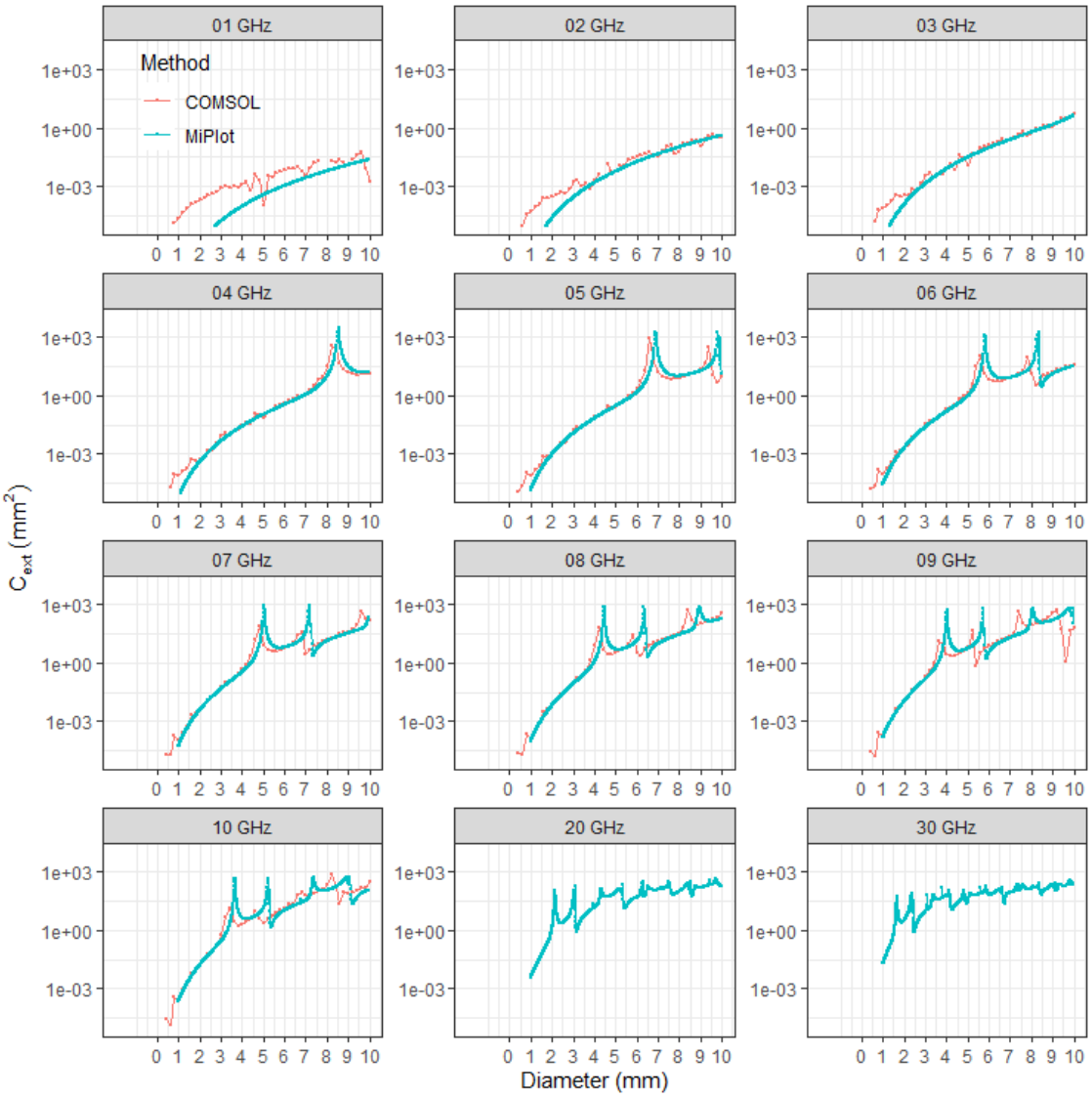


*Figure 2-5- Extinction cross-sections without imaginary part, calculated with COMSOL and MiePlot*

In general, Figure 2-3 shows that COMSOL findings are similar to the Mie approximation of cross-sections by MiePlot. However, some minor differences between the methods are recognisable, especially in frequencies between 1 to 4 GHz. The magnitude of the fluctuation is not considerable. However, variations are mostly because of the size of the mesh and the discrete nature of simulations in the finite element method while Mieplot uses an analytical method. The same explanation can describe the differences between methods in the size of drops when a peak appears. The mesh size is defined considering twelve degrees of freedom regarding the wavelength to maintain the minimum requirements for variations in final results. Such a number eventuates in less than 1% deviation from the wave approximations (Koppenhoefer, 2013).

The logarithmic scale is selected to emphasise the general trends in the graphs and a gradual increase in cross-sections. COMSOL simulations for 20 and 30 GHz were needed using a supercomputer which was not necessary at the time, as the results would be similar to the cross-sections from MiePlot.

Further steps in analysing the propagation of microwaves among droplets simulate the dynamic behaviour of microwaves confronting a droplet. The same setup in COMSOL with a time-dependant

radiofrequency module is used to display how the drop size affects the wave when the wave enters and exits a droplet.

### 2.2.5. Illustration of peak electric fields in COMSOL

Simulating the electric field around a raindrop provides insights into the impact of various raindrop diameters on wave propagation. Therefore, raindrop diameters ranging from 0.2 mm to 10 mm are considered to simulate the electric field and estimate scattering cross-section curves as depicted in Figure 2-2.

The electric field simulation in COMSOL mirrors the trends observed in the extinction efficiency calculated by MiePlot in Figure 2-2 and extinction cross-sections in Figure 2-3. Notably, the electric field within the drops exhibits an increase at specific diameters, aligning with peaks in the extinction cross-section and efficiency.

The simulations were conducted assuming a zero imaginary part of the refractive index. This assumption enhances the visualization of wave refraction and reflection inside the drop, making variations in the behaviour of different drop sizes more apparent at each wave frequency. Although non-zero imaginary refractive index simulations exhibit similar differences among drop sizes, the electric field is not as intense as in simulations with a zero refractive index.

Figure 2-6 presents a 2D section of 3D simulations illustrating the electric field in spherical drops of various diameters. For each frequency, drops displaying a peak in cross-section are compared with smaller and larger drops. For instance, in the first row, at a frequency of 5 GHz, the maximum electric field is observed in a droplet with a diameter of 6.9 mm, aligning with the first peak at 6.9 mm in Figure 2-3 for the 5 GHz frequency. Similarly, at 7 GHz, the maximum electric field occurs in droplets with diameters around 5.0 and 7.2 mm, validating the cross-section simulations in Figure 2-3.

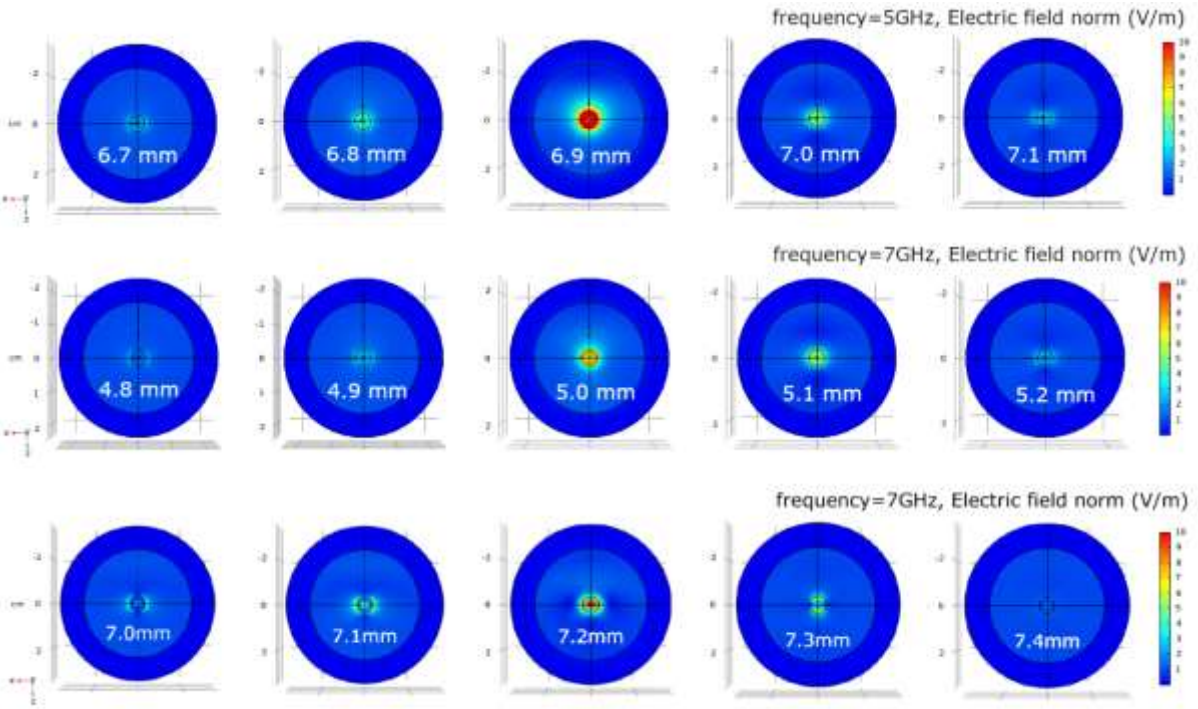


*Figure 2-6- The electric field simulation inside and around the drops, from top to bottom, one peak in 5 GHz frequency, appears in 6.9 mm diameter, and two peaks in 7 GHz frequency appear in 5.0 and 7.2 mm diameters.*

The same peaks are evident whit a non-zero refractive index. However, their peaks on the curve of R and I in Figure 2-3 and the extinction efficiency in Figure 2-2 are flatter, and for example, at 7 GHz, the drop with a diameter of 7.2 mm does not exhibit a significant difference from adjacent drop sizes.

### 2.2.6. Time domain simulations in COMSOL

A Fast Fourier Transform (FFT) is incorporated into the frequency domain to analyse the variation in the electric field, while a Perfectly Matched Layer (PML) is devised in the time domain to simulate the electrical field across time steps. The simulation, spanning a picosecond timeframe, is iterated over a range of drop diameters from 1 mm to 10 mm.

Specifically, a picosecond-timeframe simulation is conducted for a 5 mm droplet to illustrate the changes in the electric field when the droplet interacts with a 7 GHz electromagnetic wave. Figure 2-7 presents the simulation results, with each timestep showcasing how the wave penetrates the droplet and the varying degrees of reflection and refraction on the inner and outer walls of the droplet.

In Figure 2-7 the deep red colour inside the drop in timesteps 45 to 55 ps, signifies the concentrated electric field attributed to the repetitive reflection of the wave on the inner walls before it exits the droplet.

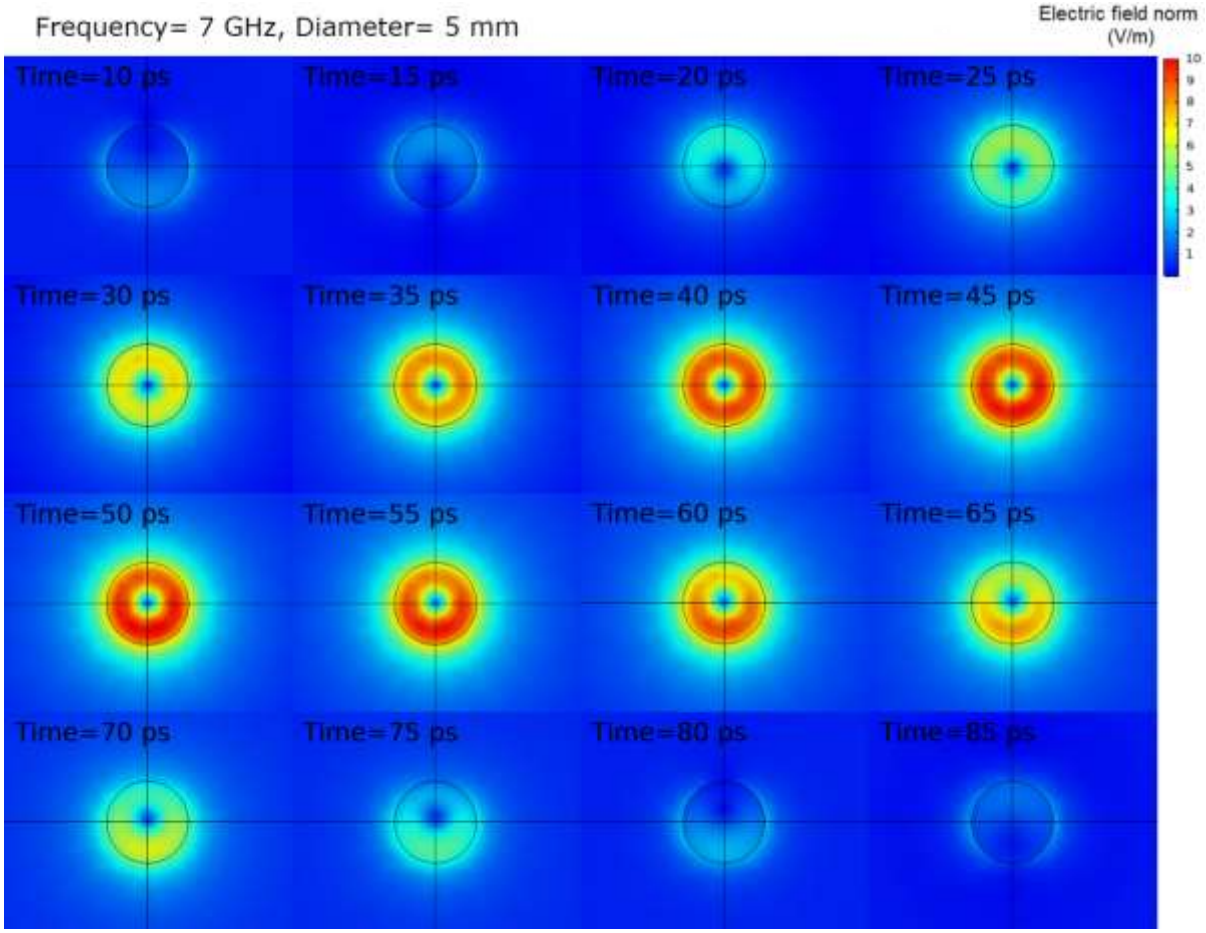


*Figure 2-7- Electric field inside and around a 5 mm diameter droplet in time steps 10 to 85 picoseconds with a 7 GHz wave. (Imaginary part of refractive index = 0)*

### 2.2.7. Scattering in real shape of raindrops

The same phenomena manifest in raindrops with a flattened base shape. When real raindrop shapes encounter microwave signals, they induce scattering, absorption, refraction, and diffraction. Notably, the peak increase in the electric field inside a raindrop with a flattened base occurs at a different diameter compared to spherical drops.

Figure 2-8 illustrates the changes in electric field inside and around a flattened base raindrop based on the (Beard and Chuang, 1987) model when exposed to a 5 GHz electromagnetic wave. The simulation spans nine timeframes, from 0 to 80 picoseconds. As depicted, the electric field inside the drop is less pronounced than the electric field in a spherical drop, as shown in Figure 2-6.

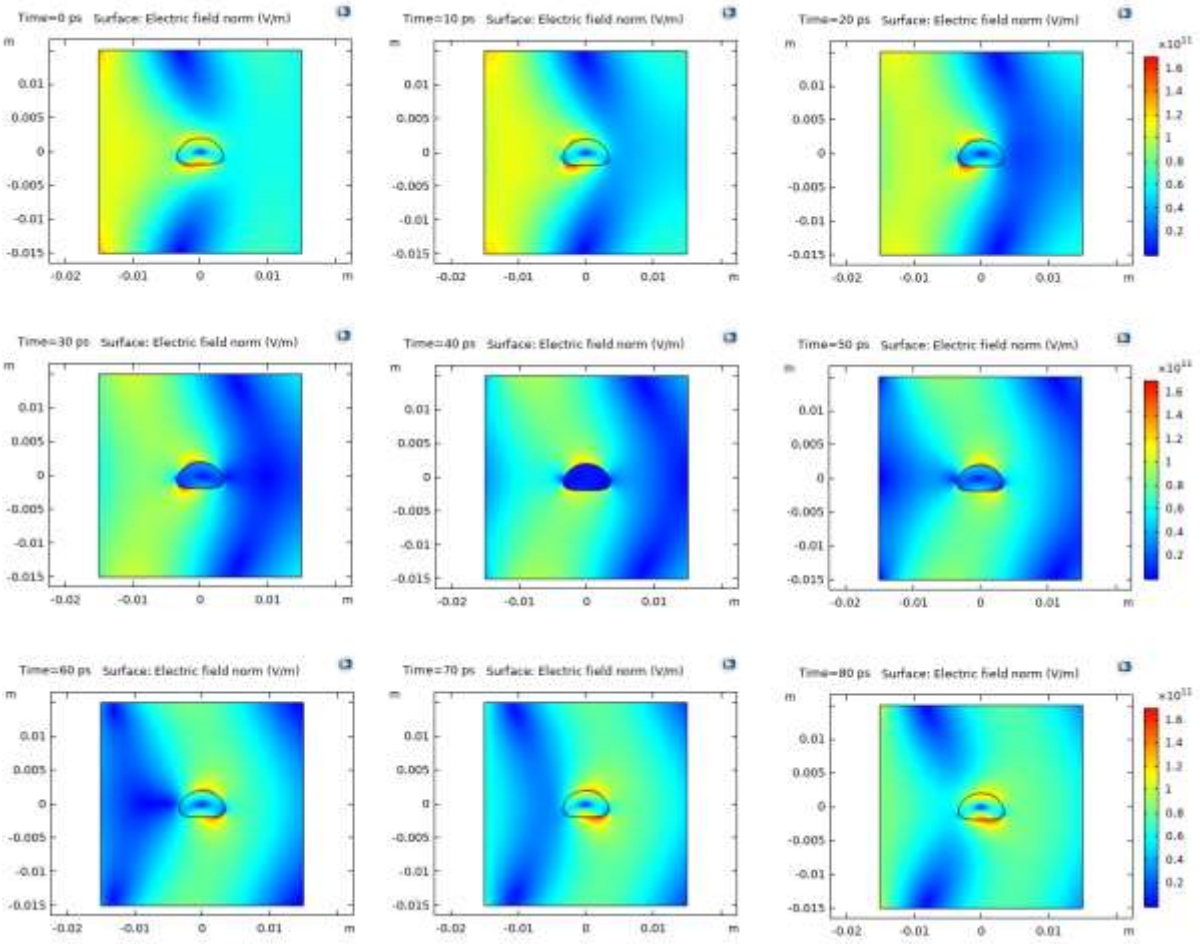


*Figure 2-8- Electric field inside and around a 6.9 mm flatten base raindrop (Beard and Chuang, 1987) confronting a 5 GHz wave.*

### 2.2.8. Analysing the Impact of Cross-Sectional Variations on Rainfall Computations

The results indicate that microwave signals at various frequencies exhibit distinct behaviours when traversing through raindrops. This discrepancy arises from the varied responses of each raindrop size to the signal mixing with the different raindrop size distribution in different rainfall intensities. Consequently, regarding the cross-section analysis and extinction calculations across different frequencies, it is anticipated observing diverse correlations between attenuation and rainfall.

According to various hypothetical drop size distributions (DSD) it is possible to analyse the total attenuation resulting from any rainfall intensity. The combination of DSD from rainfall intensity and

cross-section values for each frequency and drop size, results in the total attenuation for the rainfall intensity.

The amount of rainfall is the sum of all drops falls on a surface at one moment:

$$R = \sum_{D_{min}}^{D_{max}} v(D_i)N(D_i)V(D_i) \qquad \text{Equation 2-5}$$

Where $R$ is rainfall rate, $D$ is the diameter of the raindrop, $v(D_i)$ is raindrop velocity, $N(D_i)$ is drops size distribution (or number of each size of drops), and $v(D_i)$ is the volume of the raindrop.

On the other hand, attenuation can be calculated from the extinction efficiency as (Ishii *et al.*, 2016):

$$A = 4.343 \int_0^{\infty} N(D)Q_t(D, \lambda, m)dD \qquad \text{Equation 2-6}$$

where $Q_t$ is the extinction efficiency which depends on, diameter ($D$), frequency ($\lambda$), and the complex reflection coefficient of raindrops ($m$).

Now, comparing Equation 2-5 and Equation 2-6 with the power law (Equation 1-2) of rainfall-attenuation results in different constants of the Equation 1-2 for each frequency. The different powers are calculated by International Telecommunication Union recommendations P-838.3 (ITU-R, 2005). The constants are suggested for horizontal and vertical polarised signals in rainfall-attenuation relationship in Equation 1-1 ($\gamma_R = kR^{\alpha}$). The constants are $k_H$ and $\alpha_H$ for Horizontal polarisation and $k_V$ and $\alpha_V$ for vertical polarisation.

Figure 2-9 and Figure 2-10 show the $k$ and $\alpha$ variations for frequency range of 1 to 30 GHz, generated from ITU-R P-838.3 (ITU-R, 2005).

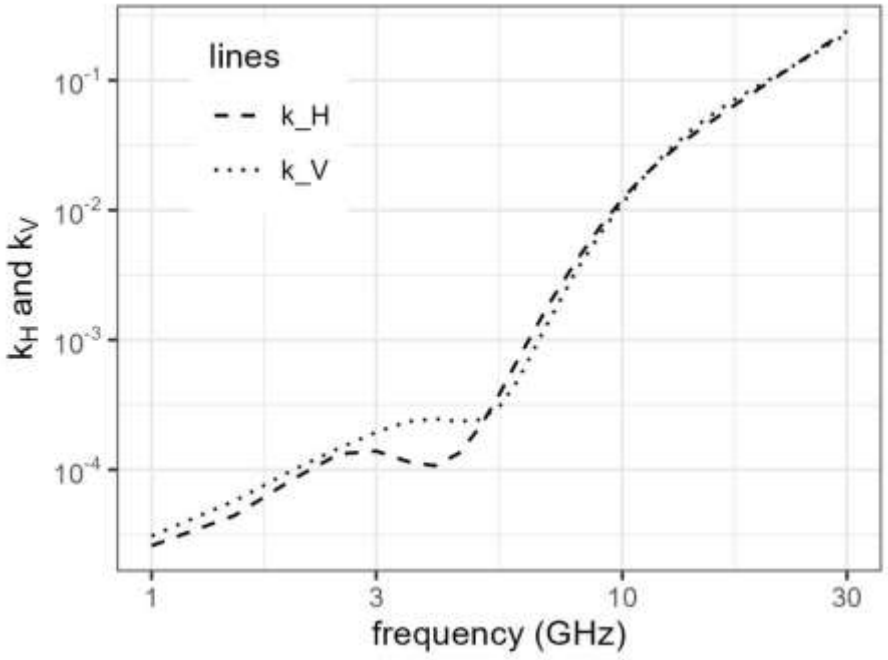


*Figure 2-9- k coefficient in Equation 1-1 for horizontal and vertical polarisations. (regenerated from (ITU-R, 2005))*

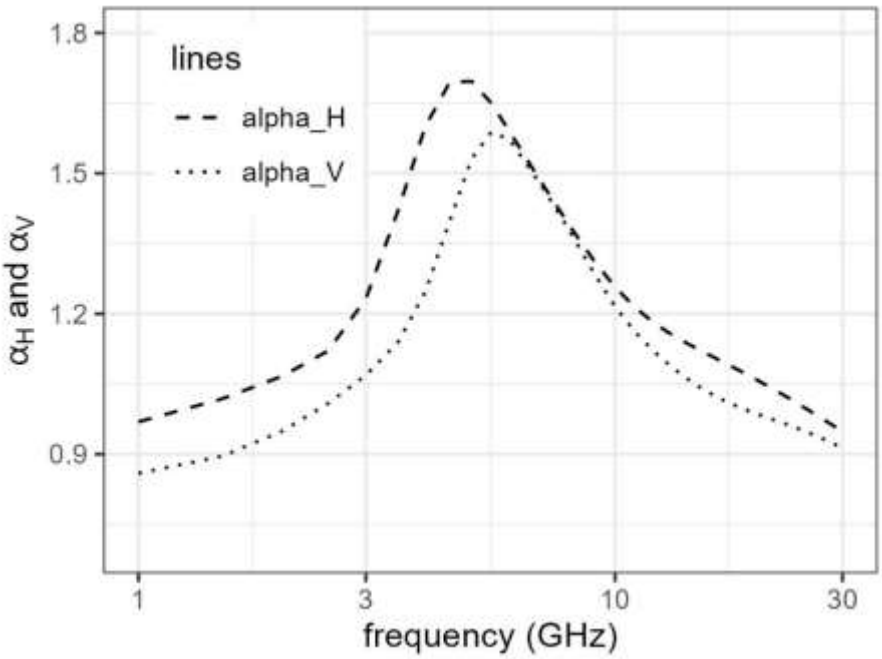


*Figure 2-10- Alpha coefficient in Equation 1-1 for horizontal and vertical polarisations. (regenerated from (ITU-R, 2005))*

Combination of Equation 2-5 and Equation 2-6 and the power law results:

$$R = a\left(4.343\int_0^\infty N(D)Q_t(D,\lambda,m)dD\right)^b \qquad \text{Equation 2-7}$$

where $a$ and $b$ are constants of Equation 1-2.

Analysing alterations in the correlation between rainfall and attenuation requires the definition of $N(D)$. Various rainfall intensities yield different $N(D)$ values. Subsequently, utilising the outcomes of extinction cross-sections and efficiency, attenuation can be computed using Equation 2-6. Following a power correlation between Equation 2-6 and Equation 2-7 the constants $a$ and $b$ can be derived. It is important to note that these coefficients are dependent upon the intensity of rainfall.

Analysis needs to define a model for drop size distribution. There are different drop size distribution models suggested to calculate $N(D)$. Marshall and Palmer distribution (Marshall and Palmer, 1948) was derived through the fitting of empirical data obtained in Ottawa, Canada, in 1946. However, the alignment between this distribution and the experimental dataset was unsatisfactory, particularly for drops with a diameter less than 1 mm. Better distribution are suggested for the raindrop size distribution based on gamma distribution (Ulbrich and Atlas, 1984) and Weibull distribution (Sekine and Lind, 1982).

The Marshall-Palmer and Sekine-Lind models are chosen to generate $N(D)$. Subsequently, attenuation is computed using Equation 2-6, considering the rainfall intensity derived from Equation 2-7. A sequence of $N(D)$ values is calculated to investigate the influence of variations in rainfall intensity. The analysis covers a range of rainfall intensities from 1 to 200 mm/hr. Through determining a series of attenuation and rainfall values, a power correlation is established to ascertain the constants.

Figure 2-11 displays the outcomes of $b$ calculations derived from the rainfall-attenuation correlation, resolved for various rainfall intensities using a Marshall-Palmer drop size distribution (DSD). Figure 2-12 is the same calculations using a Sekine-Lind distribution. The dotted and dashed lines in these graphs represent ITU P-383.3 recommendations for $b_H$ and $b_V$ in vertical and horizontal

polarisations. $b_H$ and $b_V$ are calculated by substituting $\alpha_H$ and $\alpha_V$ from Equation 1-1 into the Equation 1-2.

Ten blue lines depict the variations in $b$ for rainfall intensities ranging from 100 to 1000 mm/hr solved for each DSD with spherical raindrops for a range of ± 10 mm/hr. Therefore, the 100 mm/hr curve is related to calculating DSD for rainfall intensities between 90 and 110 mm/hr while the 1000 mm/hr curve is for calculating DSD from 990 to 1010 mm/hr.

Rainfall intensities exceeding 300 mm/hr represent events of very low frequency but are included to complete the spectrum and offer insights into the power variation and how rainfall intensity influences the rainfall-attenuation correlation.

The calculations are performed with spherical drops for simplicity and efficiency in solving, providing an approximation within the range of real-shaped drops and for both horizontal and vertical polarized signals. Real-shaped drops would require a more intricate method for extinction cross-section calculations, such as the T-matrix method.

As depicted in the graphs, the drop size distribution significantly impacts the $b$ values. In Figure 2-11, $b$ values fall within the ITU recommendation range for rainfall intensities between 100 and 400 mm/hr at frequencies higher than 10 GHz and even for higher intensities in the range of 1 to 4 GHz. However, $b$ values surpass the ITU recommendations at frequencies higher than 5 GHz.

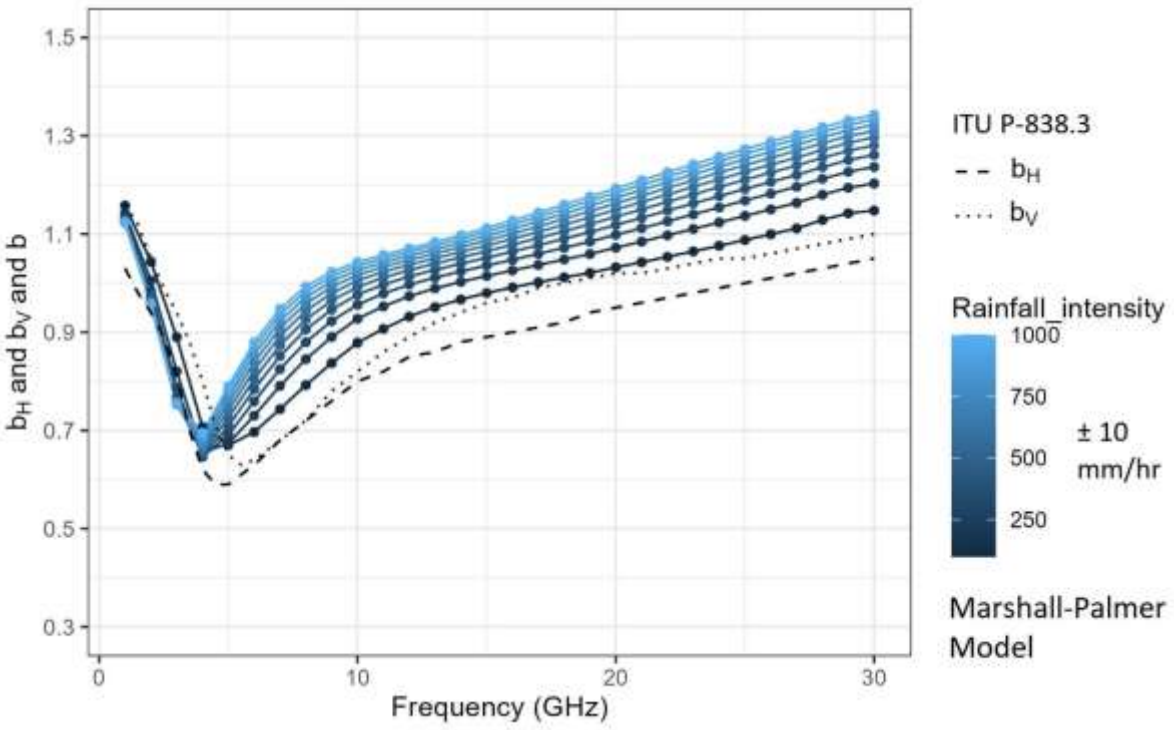


*Figure 2-11- $b_H$ and $b_V$ derived from ITU P-838.3 recommendation and b for attenuation-rainfall power law with spherical rain drops and Marshall-Palmer drop size distribution.*

In Figure 2-12 with Sekine-Lind model, the $b$ values are consistently lower than the ITU recommendations in rainfall intensities lower than 300 mm/hr. By increasing the rainfall intensity, the $b$ values exceed ITU recommendation.

The least variation in $b$ occurs in the frequency below 4 GHz where the cross-section values are low and in a flat range for all drop sizes. The variation of $b$ in different rainfall intensities decreases while frequency increases. However, the variation extends for frequencies over 10 GHz. In both distributions, $b$ decreases with increasing rainfall intensities at frequencies below 5 GHz, while at higher frequencies, $b$ increases with rising rainfall intensities.

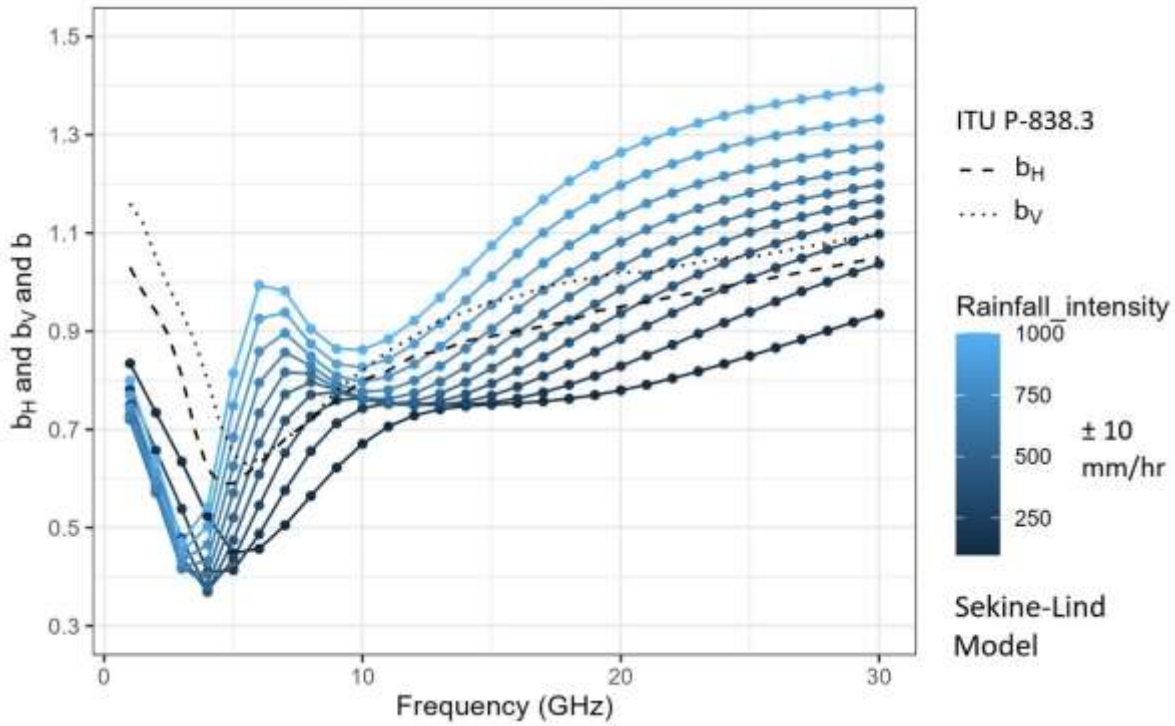


*Figure 2-12- $b_H$ and $b_V$ for ITU P-383.3 recommendation and b for attenuation-rainfall power law (Equation 1-2) with spherical rai drops and Sekine-Lind drop size distribution.*

The other coefficients are $\alpha_H$ and $\alpha_V$ in Equation 1-1 which is correlated with $a_H$ and $a_V$ in Equation 1-2 which are simply reverse of each other. Figure 2-13 and Figure 2-14 present the coefficients $\alpha_H$ and $\alpha_V$ in Equation 1-1 as recommended by ITU (ITU-R, 2005) and as calculated for different rainfall intensities from Equation 1-1, Equation 2-5 and Equation 2-6 for different DSD models.

Figure 2-13 uses Marshall-Palmer model for DSD. The variation of $\alpha$ for spherical drops is between 0.1 to 0.2. $\alpha$ increases by increasing rainfall intensity at frequencies less than 5 GHz while decreases at higher frequencies.

In Figure 2-14 the same calculations are conducted using Sekine-Lind model. the variation in $\alpha$ is greater here. Like Marshall-Palmer model, the variation trends are different below and above 5 GHz. However, the range of changes in Sekine-Lind model is considerably greater and does not accord with the ITU recommendations.

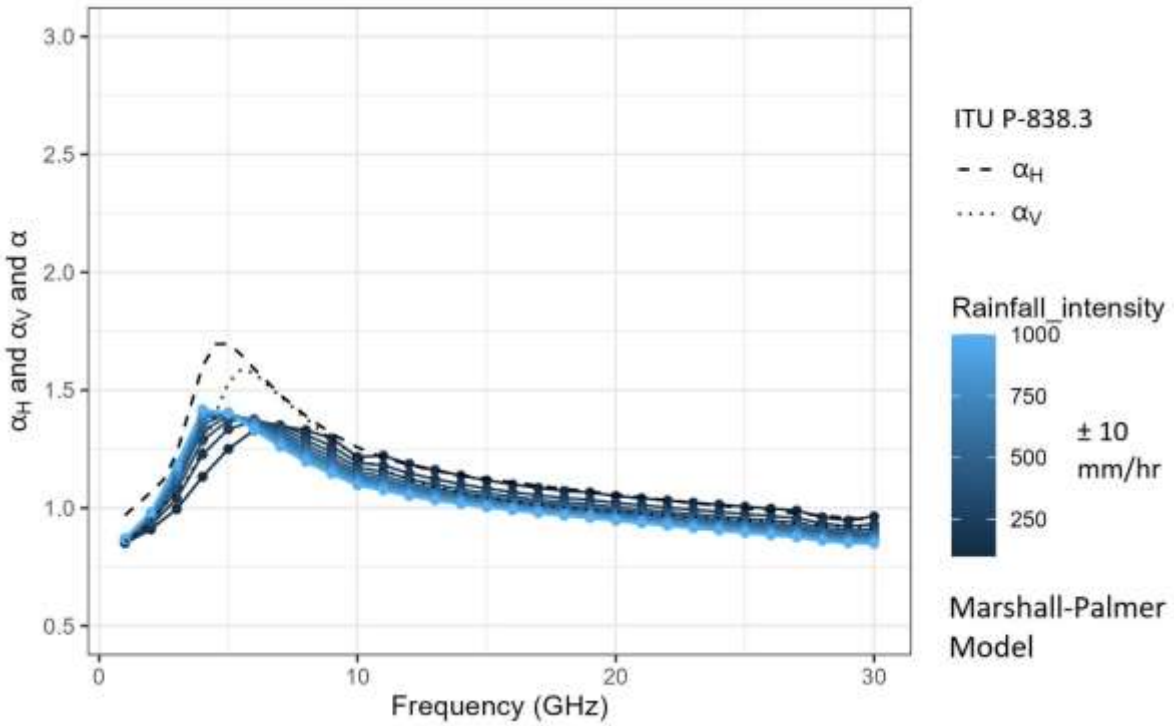


*Figure 2-13- The coefficient α in power law for different rainfall intensities and frequencies with a Marshall-Palmer DSD model.*

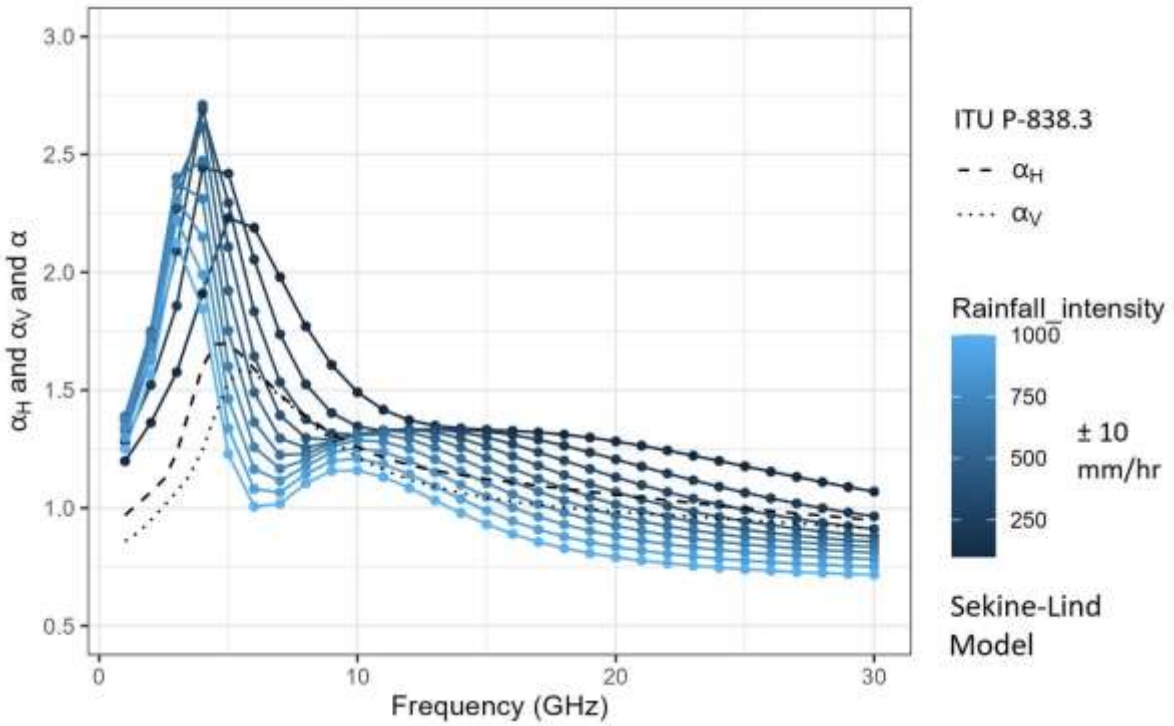


*Figure 2-14- The coefficient α in power law (Equation 1-2) for different rainfall intensities and frequencies with a Sekine-Lind DSD model.*

Considering the variation of $N(D)$ with rainfall intensities, Equation 2-7 is proposed to be adjusted, considering $a$ and $b$ changing with rainfall intensity:

$$R = 4.343 \cdot a_i \left( \int_0^\infty N_i(D) Q_{t_i}(D, \lambda, m) dD \right)^{b_i}$$ Equation 2-8

Where $a_i$ and $b_i$ are supposed to be different for each rainfall intensity.

This equation can be transformed into the well-known rainfall-attenuation formula with varying coefficients:

$$R = a_i A^{b_i}$$ Equation 2-9

## 2.3. Discussion

### 2.3.1. Differences in extinction cross-section

The results of the study illustrate and emphasise the behaviour differences between the extinction cross-sections of droplets in frequencies less and more than 10 GHz. Simulation of electric field and calculating extinction cross-sections of drops using Mie scattering theory and Maxwell equations showed similar results in illustrating the behaviour of microwave signals in different frequencies.

The feature of the droplets that shows some significant impact on some particular drop sizes in lower frequencies affects the total attenuation. Simulating microwaves with different refractive indices may illustrate some unique patterns of reflexing waves inside a droplet and magnify their impact. Considering a complex refractive index with or without the imaginary part assisted the simulations in pointing out those sizes of drops. The real part of the complex refractive index refers to the scattering wave, while the imaginary part is related to the absorption by the material (Bohren and Huffman, 1998; Fu, 2015).

Therefore, utilising both the real and the imaginary parts produces total power loss. However, ignoring the imaginary part produces patterns of scattering waves inside and around the particle, which can distinguish the reflection of the wave inside some particular diameters of droplets. Therefore, the real part of the refractive index shows how repetitive reflecting happens inside a droplet before the wave exits the drop. In this condition, the path of the wavefront can be followed.

Findings of the study showed some distinctive peaks in extinction cross-sections in frequencies lower than 10 GHz. Peaks were amplified by simulating with a zero imaginary part of the refractive index. The peaks appeared in the range of the diameter of raindrops in frequencies 6-9 GHz. These peaks were not presented in higher frequencies (20 and 30 GHz), or they are much flatter.

As can be seen in Figure 2-2 and Figure 2-3, the lower value of scattering cross-sections in frequencies of 1 to 4 GHz could be a real obstacle to using these frequencies in rainfall measurement. In comparison, although scattering cross-sections in frequencies of 4 to 10 GHz are still relatively lower than 20-30 GHz, the appearance of some peak values in the larger drops can significantly increase the attenuation in heavy rainfall events. Therefore, long microwave links covering more raindrops can show some measurable attenuation values.

### 2.3.2. The effects of DSD

The value of cross-sections alone is not able to describe the attenuation-rainfall relationship. The total attenuation is a result of multiplying cross-sections by the number of raindrops in rainfall events ($N(a)$ in Equation 2-1), which is represented as DSD.

The effect of DSD on the attenuation-rainfall relationship is that when rainfall intensity increases, larger drops appear, and the total attenuation increases. This is in addition to an increase in the total number of raindrops. Meanwhile, in higher frequencies, the cross-sections increase gradually, and the appearance of larger drops affects the total attenuation gradually and ascendingly. However, for lower frequencies, the total attenuation may decrease when a high rainfall intensity contains droplets with a larger size than the peak range. Decreasing attenuation, while the rainfall intensity is

increasing, results in a lower rate of increase for attenuation in comparison with the rainfall. Then, the attenuation-rainfall trendline needs to be corrected after reaching a particular rainfall intensity.

### 2.3.3. Varying rainfall-attenuation relationship with changing rainfall intensities

The results of analytical correlation between attenuation and rainfall using different DSD models show that the coefficients of the rainfall-attenuation power law (Equation 1-2) are not constant. They change in different rainfall intensities. Therefore, it is needed to use different coefficients for a lower or higher rainfall intensity to achieve a better rainfall-attenuation correlation.

Calculations on such a varying coefficient is not straightforward. At first, the constants $a$ and $b$ vary with frequency as ITU recommends and the results prove. On the other hand, given that $N(D_i)$ relies on rainfall intensity and both $a$ and $b$ are contingent on rainfall intensity, the parameters are interconnected in a circular manner. Attenuation is influenced by $a$ and $b$, and these coefficients, in turn, hinge on rainfall intensity. However, it's noteworthy that rainfall intensity itself remains undefined and necessitates the definition of $a$ and $b$. Consequently, employing specific methods such as iteration may prove instrumental in solving the equation.

### 2.3.4. Low rate of attenuation at lower frequencies

It is possible to calculate the rainfall and attenuation mathematically or measure them along with a microwave link and between two antennas. However, the most critical barrier in measuring rainfall would be the less total power attenuation in lower frequencies that is not always detectable.

Studies show the effects of DSD on total attenuation (Åsen and Gibbins, 2002). The flatter $C_{ext}$ curve provides fewer variations in total attenuation when DSD changes. Also, using ITU recommendations (ITU-R, 2005) for a and b constants of the attenuation-rainfall relation can produce significant errors when the local DSD data is not applied (Berne and Uijlenhoet, 2007; Leijnse *et al.*, 2010; Song *et al.*, 2019a).

# 3. Chapter three – Signal power scale

## 3.1. Introduction

The decrease in the power of a microwave signal is known as attenuation. Therefore, attenuation happens when the received signal level drops below the base level of the signal power. There are three sources of attenuation. Rainfall attenuation, wet antenna attenuation and other phenomena attenuation (Ostrometzky and Messer, 2018). However, the base level of a microwave link is not constant and varies over time. The initial observations revealed variations in microwave power, not only between different seasons but also between day and night (Berger, 2003).

There are different reasons for instability in the received power level other than the rainfall. They include Oxygen, Nitrogen, water vapour and other gasses in the atmosphere (ITU-R, 2016). Other types of humidity, such as fog, also cause attenuation (David, Alpert and Messer, 2013; David *et al.*, 2015). In addition to hydrometeors, other sources of attenuation include interference in line of sight, diffraction, tropospheric scatter, surface ducting, elevated reflection and refraction (Recommendation ITU-R P.452-17, 2021). Buildings, trees, knife edge diffraction, rounded hilltops, surface diffraction, diffraction over a sea, and ground reflection also cause the signal loss (John Price, 1993).

On the other hand, impedance mismatch also causes missing a portion of power in microwave transmission which is not related to obstacles (Zenteno, Isaksson and Handel, 2015; Wang and Cao, 2019). Scintillation and multipath are the other reasons for a decline in power (Ho *et al.*, 2004).

Among all these factors, rain attenuation becomes notable above 5 GHz and in higher frequencies it can be a substantial factor (Seybold, 2005). Therefore, in order to measure the rainfall attenuation, a reference power level needs to be established for each CML under rain-free conditions. This reference or base level includes all other fluctuations in power and excludes the decline in power due to rainfall. Rain attenuation is the difference between this base level and the received power during the rainfall event (Nebuloni *et al.*, 2020).

This base level forms the basis for calculating rainfall rates during precipitation events. Meanwhile, various forms of interference and noise distort the reference power level, and subsequently, affect the accuracy of rainfall measurements.

## 3.2. Need for a better base power method

The conventional methods employed for determining the base level of received power exhibit varying degrees of accuracy. Their initial inaccuracy stems from the assumption made before calculations. Typically, conventional methods assume that the variations in the base signal level during a rainy period are similar to the preceding dry period (Huang *et al.*, 2023). However, maintaining a constant base level proves impractical during wet periods (Huang *et al.*, 2023).

Additional drawbacks of conventional methods become evident when considering the necessity of wet-dry classification before baseline calculations. All conventional methods require dry period classification to disregard spurious attenuation, which leads to an overestimation of rainfall. Enhancing the base power to drop appropriately during dry periods and minimise attenuation may mitigate the reliance on wet-dry classification.

Address these challenges, this chapter delves into the process of establishing a base power level for the received microwave signals. This study investigates the deficiencies and limitations of the current methods, proposing some new approaches and the incorporation of alternative methods to enhance the accuracy and precision of attenuation measurement concerning magnitude and time intervals.

A broad range of methods investigated as potential alternatives to conventional approaches. They are mathematical solutions rooted in algebra, calculus, trigonometry, and electromagnetic engineering. By investigating the methods and their applications, some of them found to have a better structure regarding the characteristics of rainfall events and tested through the real data.

## 3.3. Goal of the study

Ultimately, this chapter aims to contribute to the development of more robust and accurate attenuation monitoring techniques to define the base (reference) power level of the microwave signal, that reduce the inaccuracies related to the microwave power level.

## 3.4. Selected Methods

A comprehensive review on different denoising methods is carried out and presented in Appendix B. according to the investigations and Summarising the advantages and disadvantages of various methods, as well as analysing the characteristics and variations in microwave signal behaviour during both dry and wet periods, led to the selection of three methods for evaluation in comparison to the conventional method using the median of dry periods. Considering the fluctuations in amplitude and frequency of both long-term and short-term variations in signal power and recognising the limitations of FFT, Wavelet transformations, and other decomposition methods, these were excluded from the selection.

The first chosen method is the moving average, a technique that effectively smooths minor oscillations caused by noise and filters out abrupt changes such as rainfall attenuation. The accuracy of defining the baseline with this filter depends on the size of the averaging window.

The second filter is the Butterworth filter, functioning as a lowpass filter. This method suppresses high-frequency noises while allowing low-frequency daily patterns to pass through the filter. Rainfall attenuation, having a frequency higher than daily changes, is effectively trapped and prevented from passing through the filter.

The third selected filter is the Chebyshev filter, also a lowpass filter that eliminates noises. The Chebyshev filter has a sharper cutoff compared to the Butterworth filter, but it introduces ripples in passband frequencies.

Only two IIR filters are chosen for examination, with a focus on analysing filter parameters such as cutoff frequency, ripple, and sampling frequency. The emphasis is placed on understanding which characteristic of the lowpass filter is more effective. This analysis aids in choosing the right filter with preferred parameters.

These three filters contribute to exploring mathematical solutions for base power calculations, particularly when the base power level is not dependent on whether the period is wet or dry. The calculations in these methods are solely dependent on the power level in the vicinity of the time step.

## 3.5. Material

### 3.5.1. Microwave links

Three microwave links used in this study which previously were used in an extensive study in Netherlands (van Leth *et al.*, 2018). The data from these three microwave links are available and provided by the researchers (Overeem, Leijnse and Uijlenhoet, 2016c).

The experimental setup is primarily composed of three microwave links positioned along the same trajectory connecting two Wageningen university buildings located on opposite sides of the college town of Wageningen (van Leth *et al.*, 2018). This path spans approximately 2.2 kilometres and predominantly traverses urban terrain (see Figure 1a). All transmitting antennas are affixed to a mast,

which is positioned about 2 meters high and approximately 1.5 meters from the mast's base (refer to Figure 1b). This mast is situated on top of a seven-story building, which rests on a slightly elevated area at the southern extremity of Wageningen, with coordinates at 51.968657° N and 5.68273° E. On the other end of the link, the receiving antennas are also mounted on an identical mast, but on the roof of an eight-story building located at the northern end of Wageningen, with coordinates at 51.985230° N and 5.664312° E. The height above ground level is 27 meters on the transmitting end and 40 meters on the receiving end, and the total height above sea level is 62 meters at the transmitting end and 51 meters at the receiving end (van Leth *et al.*, 2018). The intervening terrain between these endpoints mainly consists of terraced housing, a sports field, and other structures of three stories or less. When considering the height of the antenna placements relative to the intervening landscape, there are no permanent obstructions that significantly impact the signal path.

The experiment was conducted from August 22, 2014, to January 8, 2016 (van Leth *et al.*, 2018). However, it's worth noting that not all instruments were operational for the entire duration of this period. Furthermore, between August 7 and August 25, 2015, all transmitters were shut down due to a power outage. Table 3-1 lists the name of microwave links, their frequency and polarisation and the length of the data availability.

*Table 3-1- Microwave links, their frequency, polarisation, and data periods*

| Link name | Frequency | Polarisation | Start date | End date | Total records (20 per second) | Period (seconds) | Period (days) |
|---|---|---|---|---|---|---|---|
| RAL 26H | 26 | H | 10/11/2014 | 3/01/2016 | 724,627,520 | 36,231,376 | 419.345 |
| RAL 38H | 38 | H | 20/08/2014 | 4/01/2016 | 867,456,000 | 43,372,800 | 502.000 |
| RAL 38V | 38 | V | 20/08/2014 | 4/01/2016 | 867,456,000 | 43,372,800 | 502.000 |

The links are made-to-order by Rutherford Appleton Laboratories (RAL) (UK). The first operates at 26.00 GHz and horizontally polarised. It encompasses both linear and logarithmic detectors. The other two RAL links functions at 38.00 GHz, one horizontally and the other vertically polarised (van Leth *et al.*, 2018). The microwave links are named 26H, 28H, and 38V hereafter.

The frequency of the records of signal level is 20Hz means there are 20 records every second(van Leth *et al.*, 2018). The power data accumulated for every 30 seconds to agree with the disdrometer rainfall records.

### 3.5.2. Disdrometers

OTT Parsivel laser disdrometers have been used to measure rainfall along the link path (van Leth *et al.*, 2018). These devices offer the capability not only to measure precipitation intensity but also to assess the size and velocity distributions of precipitation particles passing through in 30-second intervals. Given the limited coverage area of these instruments, they may not provide a fully representative ground truth for the aggregated path measurements.

Five disdrometers at four different locations positioned along the link path to mitigate the limited coverage area of these instruments taking into consideration the urban terrain constraints (van Leth *et al.*, 2018).

At the receiving end of the link path, two disdrometers are placed in close proximity and arranged orthogonally to assess the disdrometers' accuracy. All these disdrometers are installed on flat or gently sloping rooftops within Wageningen. They include an integrated preprocessing unit that samples raw laser amplitude signals, converts them into hydrometeor counts using an algorithm developed by OTT (details private) (van Leth *et al.*, 2018). These counts are then aggregated at 30-second intervals. One of the disdrometers at the receiver end has been operational since the start of

the experiment and is linked to the same data logger as the link detectors. The other four disdrometers have been active for a shorter duration, and each is connected to a UMTS modem, enabling real-time transmission of disdrometer data to a remote server. Table 3-2 presents a summary of disdrometers names, start and end time of recording data and total length of the records.

*Table 3-2- Information of disdrometers, names and operating period*

| Number | Disdrometer name | Number of records (every 30 seconds) | Period length (days) | Start date | Start time | End date | End time |
|---|---|---|---|---|---|---|---|
| 1 | Biotechnion | 866,454 | 300.852 | 9/03/2015 | 14:08 | 4/01/2016 | 10:34 |
| 2 | Bongerd | 880,862 | 305.855 | 11/03/2015 | 13:19 | 11/01/2016 | 9:50 |
| 3 | Forum 1 | 1,445,760 | 502.000 | 20/08/2014 | 0:00 | 3/01/2016 | 23:59 |
| 4 | Forum 2 | 866,373 | 300.824 | 9/03/2015 | 15:22 | 4/01/2016 | 11:08 |
| 5 | NVWA | 884,035 | 306.957 | 10/03/2015 | 14:08 | 11/01/2016 | 13:05 |

### 3.5.3. Study period

According to the length of the available data from microwave links and disdrometers, the study period starts from 00:00:00, on 2015/03/10 to 23:59:30 on 2016/01/03. The length of this period is 300 days and ensures a coverage of signal power data by the disdrometers rainfall measurements.

### 3.5.4. Computer program

A series of independent and dependent computer codes developed for all calculations from reading data to apply the conventional and new suggested methods and producing rainfall depth. The codes include the process of:

- Reading the disdrometers' data, organise, trim, and prepare them for calculations.
- Reading the microwave links' records, organise, trim, and prepare them for calculations.
- Wet-dry classification
- Reference signal level calculations
- Rainfall calculations
- Output graphs preparation

The algorithm of the reference signal level for the conventional method and rainfall calculations is developed based on RAINLINK (Overeem, Leijnse and Uijlenhoet, 2016a) open source code, written in R, developed for calculating the rainfall, with CML data in Netherlands (Overeem, Leijnse and Uijlenhoet, 2016b). RAINLINK is available for free from GitHub (Overeem, Leijnse and Uijlenhoet, 2016a).

However, RAINLINK is developed for rainfall retrieval from a number of CMLs in an area. Hence, the code consists of a nearby link approach for wet-dry classification and a section for connecting to online map resources, computing the spherical model, and kriging interpolation of rainfall results plus a section for plotting the rainfall maps.

Therefore, since there was only one link path (the three CMLs transmitters and receivers are at the same location) and because of using a different wet-dry classification method, a completely new code in R is developed from the scratch to adopt the experimental setup, disdrometers, and the purposes of this study. The new code also allowed to develop the procedure for the new suggested methods.

## 3.6. Method

### 3.6.1. Conventional method

The median reference level deriving method followed for the conventional method (Overeem, Leijnse and Uijlenhoet, 2016b). This method has been a popular reference level detection in recent CML studies (Huang *et al.*, 2023). In this method, the reference power is calculated using the median of the signal level in the last 24 hours dry period and corrected with wet-dry classification.

The algorithm follows the main steps as:

1. Power unit change, At the first step, the power unit changed from milliwatt to decibel by the relations found in the original experiment in Netherland (van Leth *et al.*, 2018):

$$Power(dBm) = c_1 + c_2 \cdot Voltage(V) \qquad \text{Equation 3-1}$$

where $c_1$ and $c_2$ are constants of the equation derived from the calibration of power and voltage of the links conducted by the manufacturer before the start of the experiment (van Leth *et al.*, 2018). The constants are as Table 3-3.

*Table 3-3- The constants of the calibration of power and voltage in microwave links (van Leth* et al.*, 2018).*

| Microwave link | $c_1$ | $c_2$ | $r^2$ |
|---|---|---|---|
| RAL 38 GHz (vertical) | -99.755 | 20.595 | 0.999 |
| RAL 38 GHz (horizontal) | -99.871 | 20.596 | 0.999 |
| RAL 26 GHz (horizontal) | -99.871 | 20.596 | 0.999 |

2. Wet-dry classification, using the weighted average of rain depth over all five disdrometers. Unlike RAINLINK which uses nearby link approach (Overeem, Leijnse and Uijlenhoet, 2016b) to classify the period as wet or dry, in this study, only one link path (all three links are at the same start and end points) is used for analysis and comparing to the measured rainfall. Therefore, a path-aggregated rainfall depth (van Leth *et al.*, 2018) from disdrometer data used for wet-dry classification, independent of the microwave signal.
3. Reference signal level calculations, using the median of the power of the signal in all dry times in the last 24 hour (Overeem, Leijnse and Uijlenhoet, 2016b).
   The power of the signal here, is the average of the minimum and the maximum of the received signal level:

$$\bar{P} = \frac{P_{min} + P_{max}}{2} \qquad \text{Equation 3-2}$$

   Where, $\bar{P}$ is the average signal level and $P_{min}$ and $P_{max}$ are the minimum and maximum received power respectively.
   The reference signal level ($P_{ref}$) is determined by finding the median of $\bar{P}$ across all dry time intervals when there is at least a total 2.5 hours of dry time steps in the last 24 hours. If the count of dry time intervals within the past 24 hours is less than 2.5 hours, then Pref, and consequently the rainfall intensity, cannot be calculated and considered as not available 2.5 and 24 h are suggested by the RAINLINK studies (Overeem, Leijnse and Uijlenhoet, 2016b) and can be modified.
   Minimum and maximum received power correction, using the suggested method to consider the rainfall and reference level (Overeem, Leijnse and Uijlenhoet, 2016b).
   In case the reference level does not match with the expected minimum and maximum signal level and the wet and dry periods, a further step is required to correct the minimum and

maximum signal level according to the wet-dry period and reference level. As suggested in RAINLINK approach:

$$P_{min}^{C} = \begin{cases} P_{min} \; if \; wet \; AND \; P_{min} < P_{ref} \\ P_{ref} \qquad otherwise \end{cases} \quad \text{Equation 3-3}$$

$$P_{max}^{C} = \begin{cases} P_{max} \; if \; P_{min}^{C} < P_{ref} \; AND \; P_{max} < P_{ref} \\ P_{ref} \qquad otherwise \end{cases} \quad \text{Equation 3-4}$$

where $P_{min}^{C}$ and $P_{max}^{C}$ are the corrected minimum and maximum signal level (in $mV$) and $P_{ref}$ is the reference level (in $mV$), derived from the median of dry periods.

4. Minimum and maximum Attenuation is calculated from the difference between the reference power and maximum and minimum corrected powers (Overeem, Leijnse and Uijlenhoet, 2016b):

$$A_{min} = P_{ref} - P_{max}^{C} \quad \text{Equation 3-5}$$

$$A_{max} = P_{ref} - P_{min}^{C} \quad \text{Equation 3-6}$$

where $A_{min}$ and $A_{max}$ are the minimum and maximum attenuation (in $dB$).

5. Minimum and maximum Heaviside function is calculated from minimum and maximum attenuation and the wet antenna effects (Overeem, Leijnse and Uijlenhoet, 2016b). The Heaviside function ensure that no negative rainfall is produced, and it is defined as:

$$H(A_{min} - A_a) = \begin{cases} 0 & if \; (A_{min} - A_a) < 0 \\ 1 & if (A_{min} - A_a) \geq 0 \end{cases} \quad \text{Equation 3-7}$$

$$H(A_{max} - A_a) = \begin{cases} 0 & if \; (A_{max} - A_a) < 0 \\ 1 & if (A_{max} - A_a) \geq 0 \end{cases} \quad \text{Equation 3-8}$$

Where $H$ is the Heaviside function.

6. Minimum and maximum rainfalls for each time step are calculated by the means of minimum and maximum attenuation and minimum and maximum Heaviside function (Overeem, Leijnse and Uijlenhoet, 2016b):

$$R_{min} = a\left(\frac{A_{min} - A_a}{L} H(A_{min} - A_a)\right)^{b} \quad \text{Equation 3-9}$$

$$R_{max} = a\left(\frac{A_{max} - A_a}{L} H(A_{max} - A_a)\right)^{b} \quad \text{Equation 3-10}$$

where $R_{min}$ and $R_{max}$ are the minimum and maximum rainfall (in $mm$) calculated by the means of minimum and maximum received signal level and $L$ is the length of the microwave link (in $km$).

7. Total rainfall for each time step is calculated from a relation between minimum and maximum rainfall, calculated in the previous time step:

$$R = \alpha R_{max} + (1 - \alpha) R_{min} \quad \text{Equation 3-11}$$

Alpha selected as 0.33, according to the recommendations (Overeem, Leijnse and Uijlenhoet, 2016b).

### 3.6.2. Moving Average

As a novel approach, the moving average of the signal power calculated as the reference power level. This study suggests using a rolling average centred around the power value at each time step, averaging periods both ahead and behind. While this method may not provide an immediate rainfall calculation, it offers several advantages that may compensate for any latency in response.

The difference of the suggested method with the previous studies which used the moving average method for the reference signal level (Zinevich, Messer and Alpert, 2010a) is that the previous studies used a variable averaging window before and after a rainfall event, extending for 2 to 27 hours. In the suggested method, the averaging window is stable and get the average of a longer period including both wet and dry periods.

The approach follows the same steps as the median method to calculate the rainfall rate. The only change is how to calculate the reference power level. The reference signal level calculated from a moving average over a period, centred at the time step.

A 6-hour window selected for reference level retrieval to be compared with the other methods of $P_{ref}$ calculations. Other time windows, ranging from 1 hour to 24 hours, also investigated individually to be compared to the conventional method.

### 3.6.3. Butterworth Filter

Butterworth Filter is used for calculating the reference signal level as a new approach to other conventional methods.

Butterworth filter needs filter order and cutoff frequency parameters to be set. The package signal (Ligges *et al.*, 2021) is used to apply the Butterworth filter to the microwave signal. A piece of code is written to analyse the data, generate the filtered signal and produce the output graphs.

The main code line for Butterworth filter is simply:

```
# Design the Butterworth filter
filter_coefs <- butter(order, normalized_cutoff, type = "low")
```

where `order` is the order of the filter and `normalized_cutoff` is the cutoff frequency after normalisation of frequencies to zero to one. A higher order of the Butterworth filter results in a sharper cut in passband frequency.

The `type` is set to `low` to use a low-pass filter to allow the low frequency pulses pass the filter. The low frequency part of the signal is associated to the basic trends in received signal level while the high frequency part of the signal is related to the noise.

After setting the coefficients, filter command can calculate the filtered signal as:

```
# Apply the filter to the signal
filtered_signal <- filter(filter_coefs, signal)
```

where the `filtered_signal` is the produced reference level with Butterworth filter using the prefixed filter coefficients: `filter_coefs` and the original received power: `signal`.

### 3.6.4. Chebyshev Filter

The other new method of filtering to produce the reference power level in this study is Chebyshev filter.

```
# Design the Chebyshev filter
filter_coefs <- cheby1(order, Aa_C, normalized_cutoff, type = "low")
```

where `order`, `normalized_cutoff`, and `type`, are the same as Butterworth filter and `Aa_C`, is the passband ripple (in dB).

In this study the passband ripple is sat to the wet antenna effect. Therefore, the wet antenna effect in Chebyshev filtering method, `Aa_C`, is calculated in a loop to achieve the lowest RMSE for the final rainfall prediction. This is in addition to $A_{a_C}$ factor used through the rainfall calculations like the other methods.

Once the coefficients are defined, the signal can be filtered as:

```
# Apply the filter to the signal
filtered_signal <- filter(filter_coefs, signal)
```

where `filtered_signal` is the resulted signal after filtering which represent the reference received power.

A value of 0.2 dB is used for the ripple in pass band frequency. This value obtained by testing a range of ripples and finding the minimum RMSE for the results. The filter order for Butterworth and Chebyshev methods selected as 9 to achieve the sharpest cutoff frequency. The cutoff frequency was 10 Hz and sampling frequency 1000.

## 3.7. Results

The results of this chapter of the study are presented in two parts. The first part is the results of the rainfall calculations with different reference level method, for each of the microwave links. The second part is a more comprehensive analysis on the moving average method with different time steps, for finding the reference signal level.

For each of the microwave links, four different methods have been used for determining the reference signal level with a varying wet antenna effect. Reference power methods include the conventional method (or median), moving average, Butterworth, and Chebyshev filters.

The best wet antenna effect selected by minimising RMSE of the simulation compared to the measured rainfall. The results are presented for 26H, 38H, and 38V microwave links.

### 3.7.1. Optimising wet antenna effect ($A_a$)

A range of $A_a$ values, ranging from -1 to 4 dB selected to calculate the rainfall intensity for each microwave link. The minimum RMSE of the simulated rainfall is selected as the optimal $A_a$ values for the conventional method and three suggested filters.

The outcomes of minimizing RMSE between simulated rainfall and measured rainfall are displayed through three graphs for each microwave link. Figure 3-1 displays the results of simulation in microwave link 26H. The graph depicts R-squared, NSE, and RMSE results of comparing simulated rainfall using different methods of reference level derivation with measured rainfall from disdrometers. Each method's curve shows variations in statistical factors across a range of wet antenna effects ($A_a$), ranging from -1.0 to +4.0.

The graphs illustrate that RMSE and NSE vary with changing $A_a$. The optimal $A_a$ for each of the four methods is denoted by a vertical dashed line, along with the method name achieving the minimum RMSE. While this optimum $A_a$ is the same for achieving the maximum NSE, the maximum R-squared is attained with a different $A_a$ value. Since the simulation's goal is to minimize RMSE, the final $A_a$ values for each method are found to be 0.0 dB for Chebyshev filter, 0.2 dB for Moving Average, 0.5 dB for Butterworth, and 1.3 dB for the conventional median method.

In this study, negative values between -1 and 0 dB also checked for accuracy of the models and showing the trends of variations in accuracy of the model for $A_a$ values close to 0 dB. However, a negative $A_a$ means adding extra attenuation to the signal, resulting in overestimated rainfall intensity, especially during zero rainfall periods. A negative $A_a$ introduces some rainfall intensity during periods classified as dry in wet-dry classification.

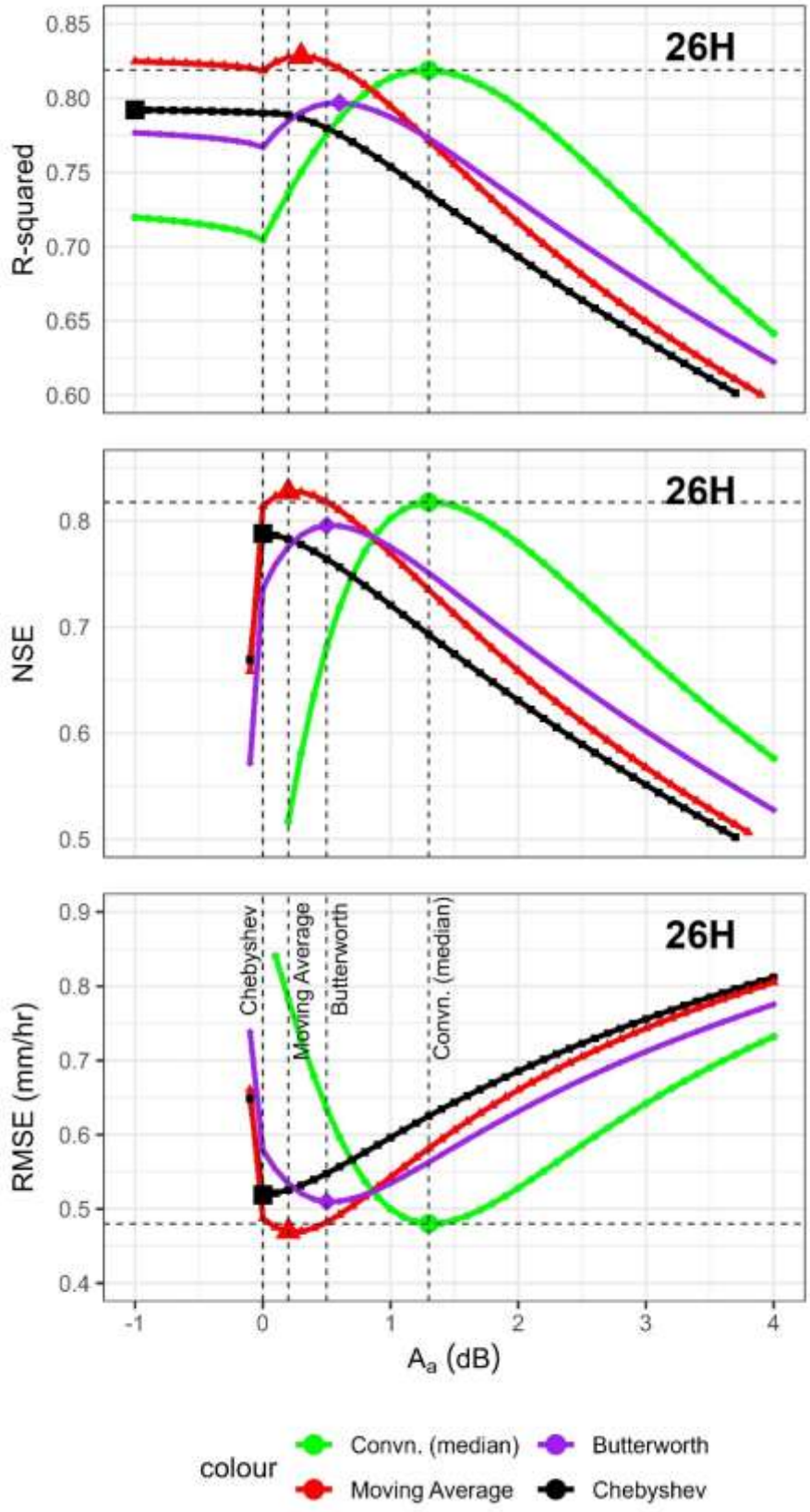


*Figure 3-1- RMSE, NSE, and R-squared of simulated rainfall with different methods of reference power level for Aa value, ranging from -1 to 4 dB for microwave link 26H.*

The same procedure used for analysis of the microwave link 38H. Each method of calculating the reference power used a range of wet antenna effect ($A_a$) between -1 and 4 dB. Then the variation of statistical factors, including RMSE, NSE, and R-squared, is provided in a graph to compare the methods and finding the optimal $A_a$ value to minimise RMSE.

In microwave link 38H, all suggested methods resulted in a lower RMSE and higher NSE and R-squared value using the optimal $A_a$. Figure 3-2 shows the optimum $A_a$ values for each method with a point on the method's curve. The optimum value for $A_a$ is selected according to the minimum RMSE of the simulation. The optimisation results are a wet antenna effect of 2.6 dB for conventional method (median), 0. 40 dB for Butterworth filter, and 0.0 dB for Chebyshev and moving average methods.

In this microwave link, the conventional median method is sensitive to lower $A_a$ values. Therefore, using a $A_a$ value, 1 dB less than the optimal value, NSE drops to below 0.70 from a maximum of 0.75. On the other hand, using $A_a$ value 1.2 dB greater than the optimal value in moving average and Butterworth filters still provides an NSE greater than 0.75, which is the maximum of the conventional method.

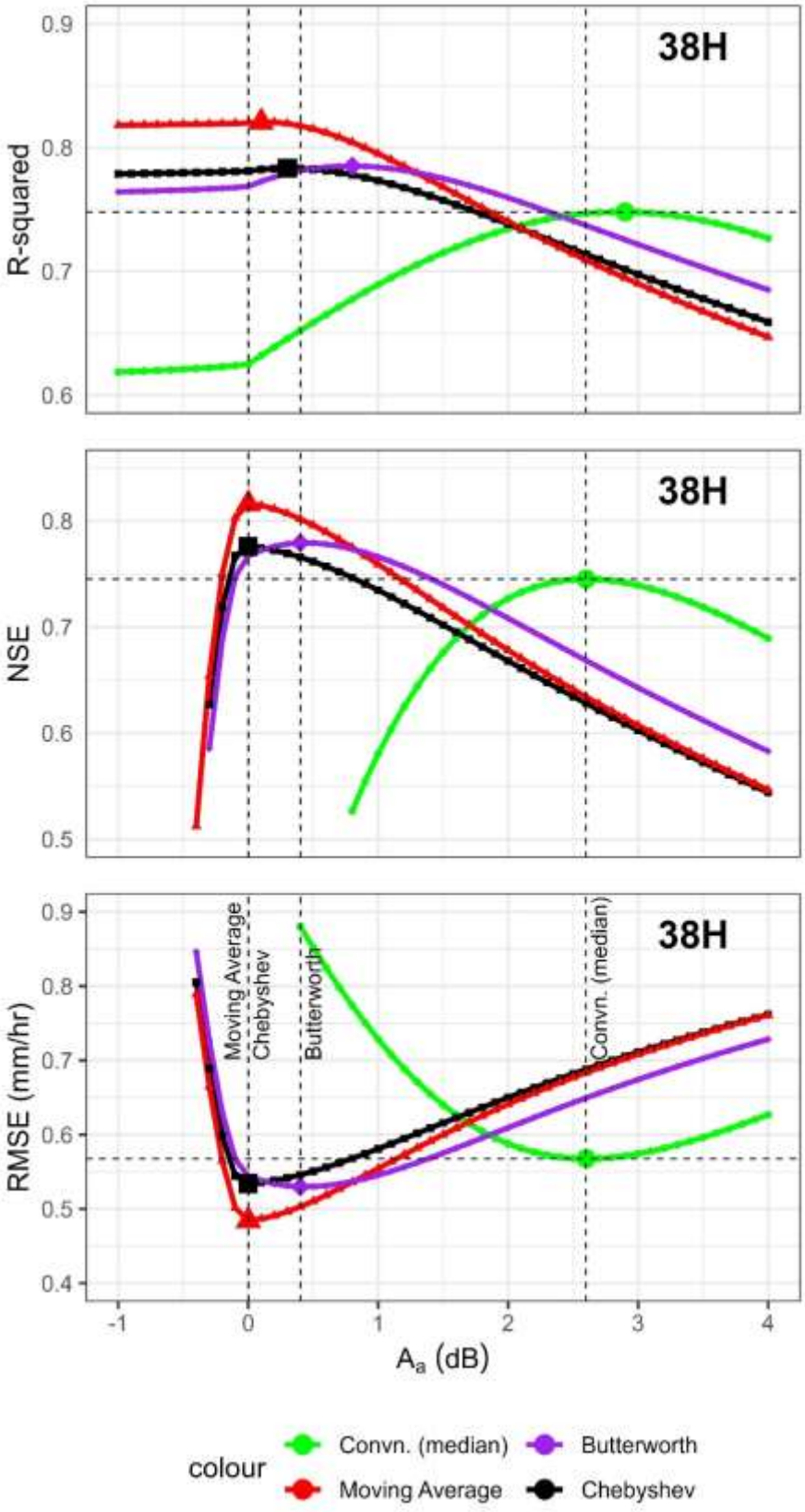


*Figure 3-2- RMSE, NSE, and R-squared of simulated rainfall with different methods of reference power level for Aa value, ranging from -1 to 4 dB for microwave link 38H.*

The calculations repeated for microwave link 38V. The same as link 38H, the suggested filters for calculating reference power level achieved a lower RMSE and a higher NSE and R-squared.

Figure 3-3 is the presentation of the accuracy and fitness of the suggested methods compared to the conventional method. The minimum RMSE in the conventional method achieved at $A_a$=2.4 dB. However, the Butterworth filter resulted in a lower RMSE at $A_a$= 0.5 dB. Moving average and Chebyshev filters could reach at the lowest RMSE with zero $A_a$. In this microwave link, moving average filter provided the lowest RMSE among the methods.

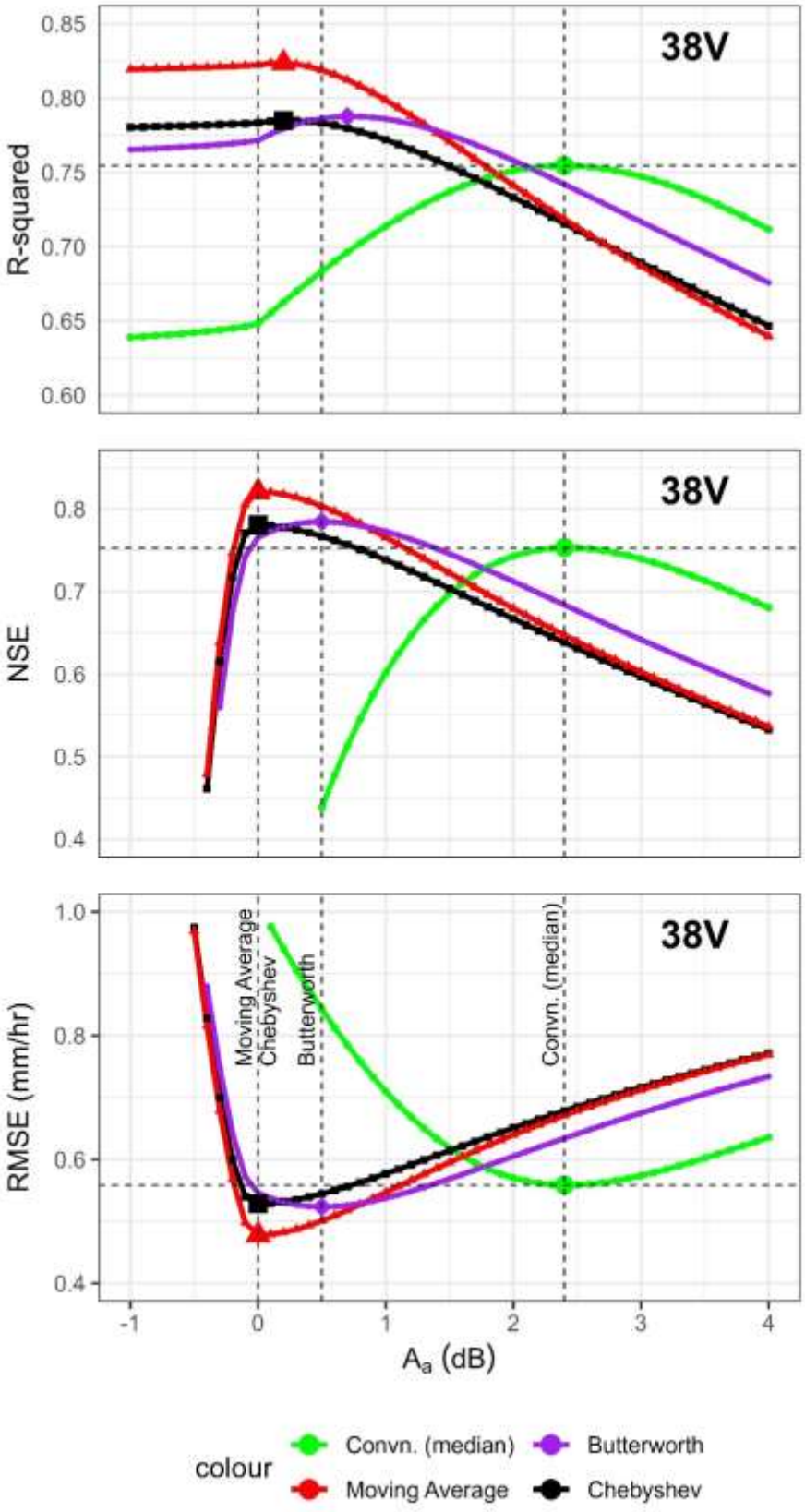


*Figure 3-3- RMSE, NSE, and R-squared of simulated rainfall with different methods of reference power level for Aa value, ranging from -1 to 4 dB for microwave link 26H.*

### 3.7.2. Reference power level fluctuations

At the previous stage, the optimal $A_a$ value, which minimizes the RMSE of the model simulation, is determined by assessing 300 days of data. This value ensures the highest accuracy in simulating the model over this period. However, the accuracy of each reference power modelling method varies daily and in distinct periods. Certain periods throughout the entire data collection duration have been compared to provide an understanding of the differences in power reference levels among various methods and periods.

Once $A_a$ value is optimised, rainfall intensity is calculated using this value for the whole length of the data period. Calculations are conducted in 30 second time steps, equal to the disdrometers records and the accumulated microwave link records, transferring 20 records per second to a 30-second value.

While the overall RMSE and NSE of the model are within acceptable limits, the reference power exhibits notable fluctuations in shorter time frames. Figure 3-4 shows rainfall, the received signal power, and the calculated reference level in four distinct periods for 26H microwave link. The reference level derived through conventional, moving average, Butterworth, and Chebyshev filters are presented for these periods. As the picture depicts the conventional median method demonstrates minimal fluctuations during these time intervals. In contrast, Butterworth and Chebyshev filters exhibit more pronounced oscillations. The moving average method, as seen in Figure 3-4 (a) and (b), provides a smoother slope, while for shorter durations of 43 and 55 minutes in Figure 3-4 (a) and (d), moving average results in a horizontal line.

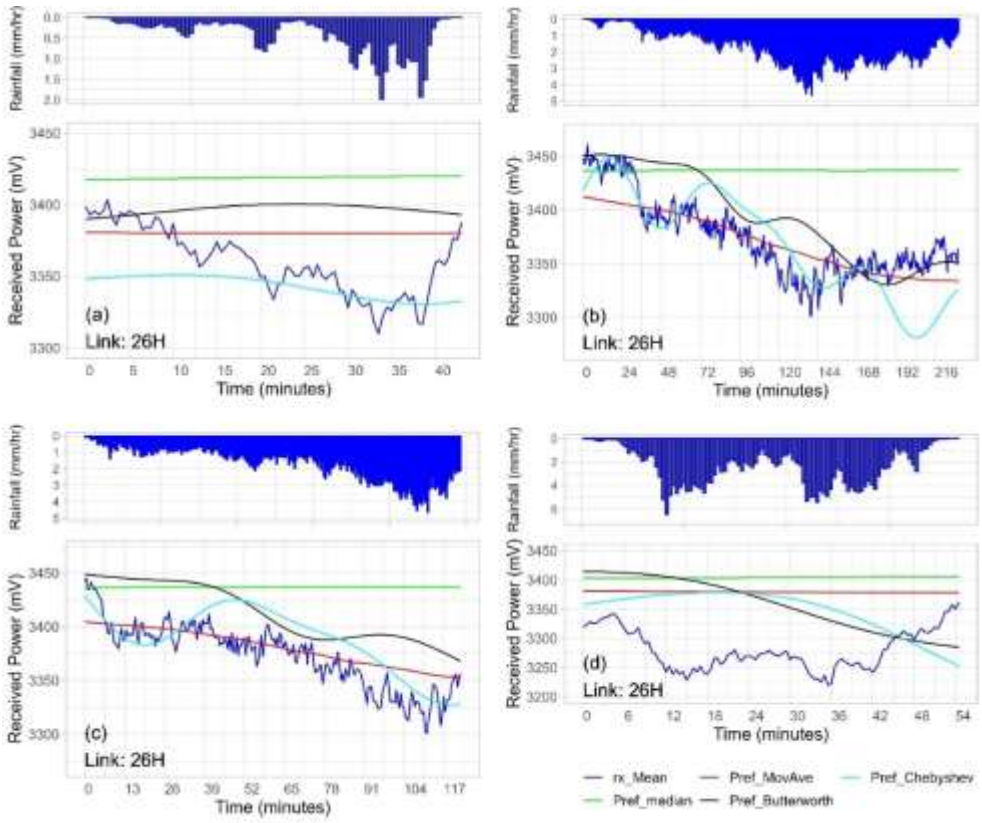


*Figure 3-4- Rainfall, received signal power, and four methods of reference power calculation for different periods in microwave link 26H (rx_Mean=received signal level)*

Figure 3-5 illustrates the signal level of the same microwave link, 26H, alongside the corresponding rainfall and the results of four reference level calculation methods over a span of 120 hours. This figure illustrates the varying oscillations in reference power for the suggested methods compared to the conventional technique. The conventional median method exhibits minimal fluctuation in the reference level, while the moving average line closely aligns with the received signal. Despite the highly oscillating line produced by the Chebyshev filter, the total RMSE and NSE of the simulation remain competitive compared to the other methods.

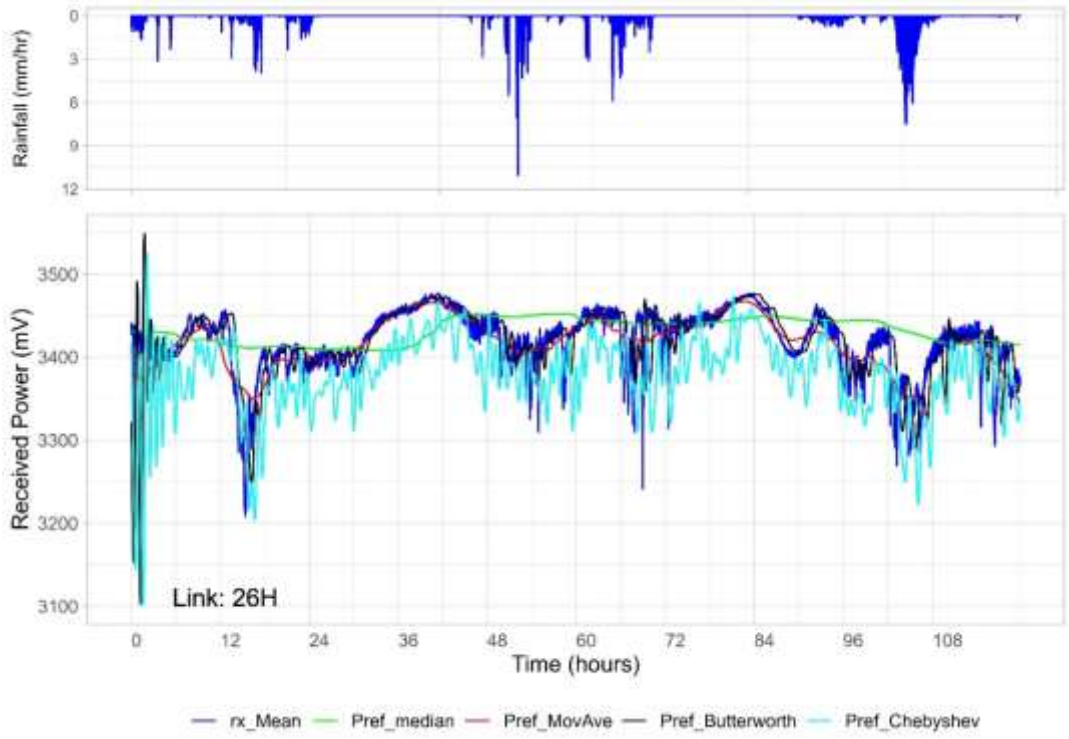


*Figure 3-5- Rainfall, received signal level and four methods of reference power derivation methods for 120 hours or signal records in microwave link 26H.*

The same trends could be seen in the other microwave links. After optimising $A_a$ values, the optimal values are used for calculating rainfall intensity for the whole 300 days of available and for each of four methods of reference power. After calculating rainfall for 300 days, the reference power, received signal and the measured and calculated rainfall intensities are investigated in different time length and steps to evaluate the accuracy of the model for shorter periods.

Similar to the microwave link 26H, the reference power displays significant differences in fluctuations among the four methods in shorter time frames. Figure 3-6 depicts rainfall and the received signal power in microwave link 38H, along with four methods of reference power derivation in four distinct periods. Figure 3-7 illustrates the same variables over a longer period of 5 days. A comparison of these two graphs indicates that the conventional median method yields a more stable and less variable reference level, while the Chebyshev method exhibits the highest fluctuations.

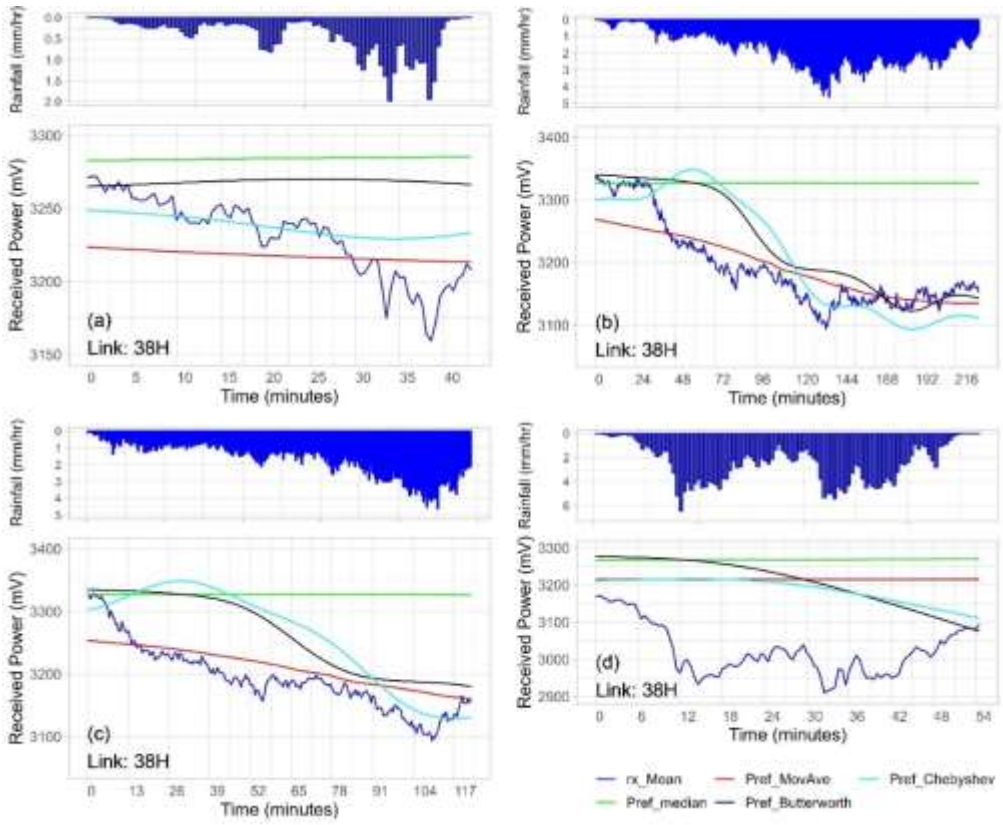


*Figure 3-6- Rainfall, received signal power, and four methods of reference power calculation in different periods in microwave link 38H (rx_Mean=received signal level)*

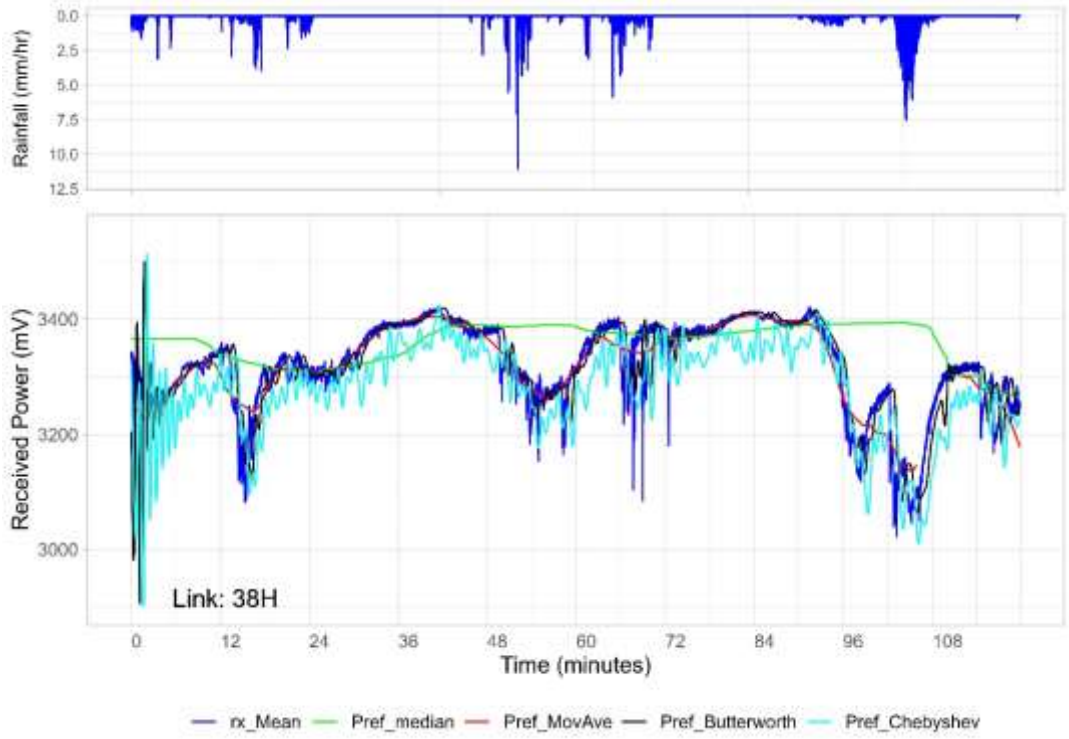


*Figure 3-7- Rainfall, received signal power, and four methods of reference power calculation in 120 hours in microwave link 38H (rx_Mean=received signal level)*

Finally, the fluctuations of the received signal level and the reference power level calculated with four methods in microwave link 38V is presented in Figure 3-8 and Figure 3-9. Similar to the other links, conventional median reference level remains more stable, and the Chebyshev filter fluctuates more compared to the other methods.

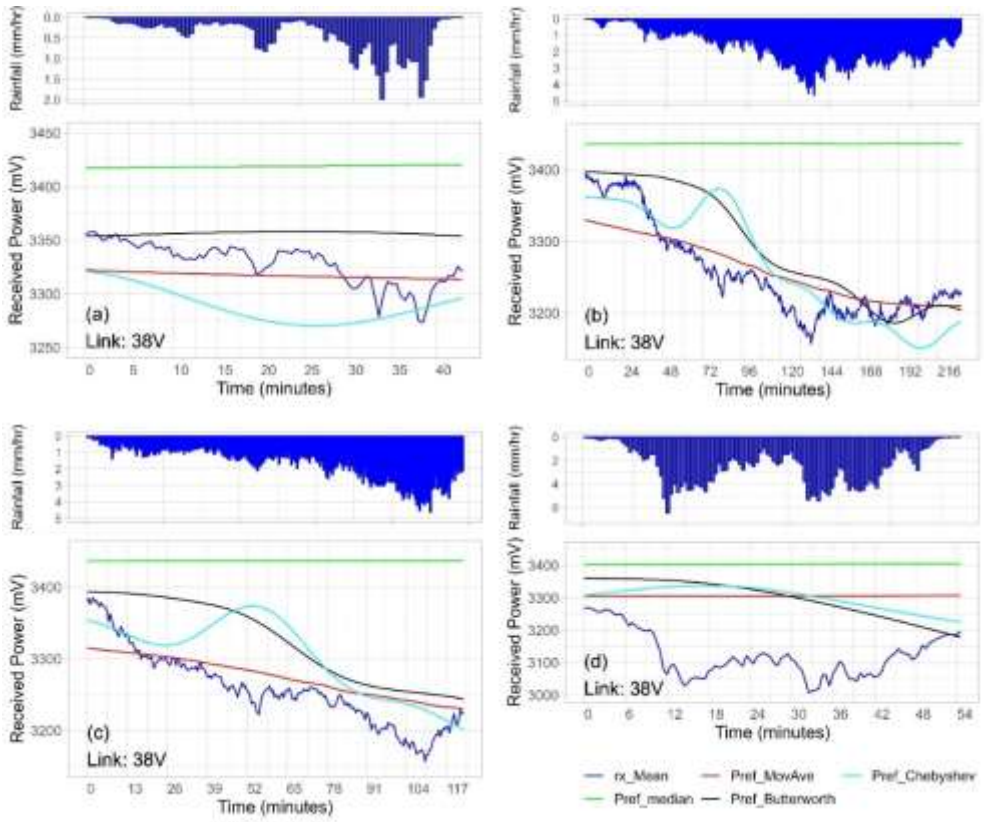


*Figure 3-8- Rainfall, received signal power, and four methods of reference power calculation in different periods in microwave link 38V (rx_Mean=received signal level)*

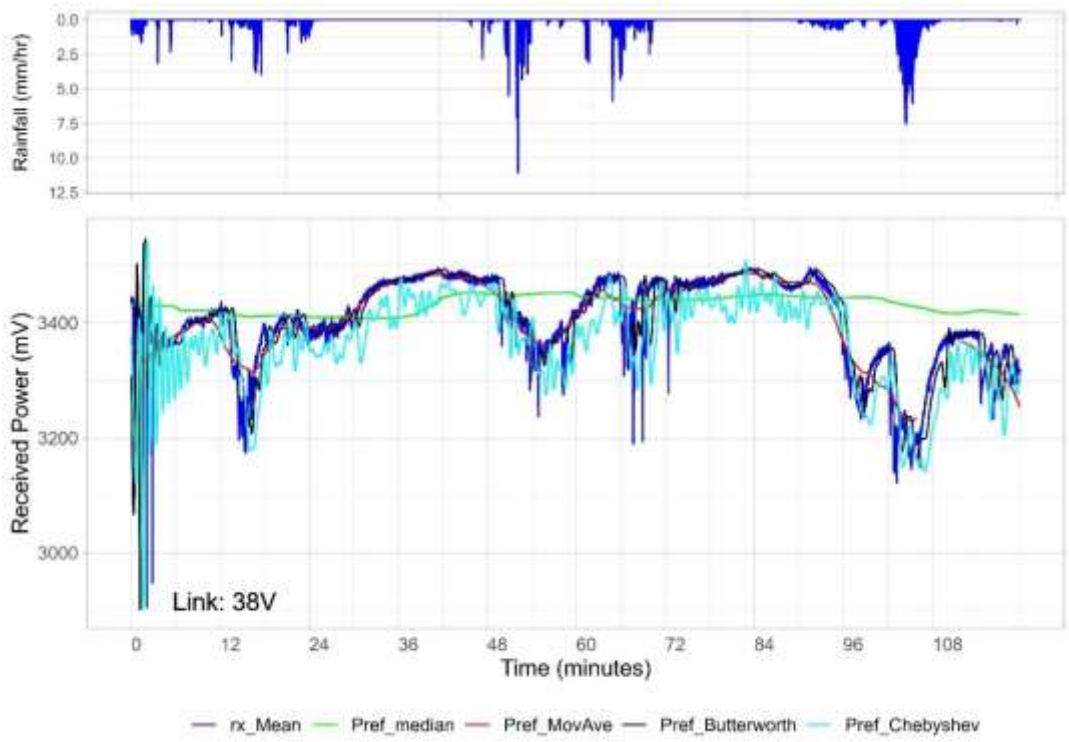


*Figure 3-9- Rainfall, received signal power, and four methods of reference power calculation in 120 hours in microwave link 38V (rx_Mean=received signal level)*

### 3.7.3. Cumulative rainfall

The other approach to evaluate the quality of the prediction using each method is comparing the total cumulative rainfall at the end of the simulation. The cumulative values are computed using the optimal $A_a$ values determined in the previous step.

A cumulative rainfall depth for the entire period of 300 days is calculated for three microwave links. The results show that all the methods, including the conventional method and the suggested filters, underestimate the total rainfall depth. In all microwave links the moving average provided the best estimation for 300 days rainfall depth.

Figure 3-10 shows the cumulative rainfall for the total period of simulation in microwave link 26H. As this graph illustrates, the moving average method results in the closest approximation of the total rainfall depth in link 26H. The total rainfall depth for 300 days of simulation is calculated the same with Butterworth filter and the conventional method while the Chebyshev results stays lower at the end of the period.

The total rainfall depth at the end of the period of 300 days analysis is 804.2 mm measured by disdrometers. The conventional method, moving average, Butterworth, and Chebyshev methods, resulted in a cumulative rainfall depth equal to 629.3 mm, 741.3 mm, 629.6 mm, and 550.3 mm respectively.

Figure 3-11 illustrates the cumulative rainfall calculated from four methods of reference level in microwave link 38H, compared to the measured rainfall with disdrometers. In this link, the conventional method results in the lowest and the most underestimated cumulative rainfall depth during 97% of the simulation period. Total rainfall depth by conventional method, reaches to a total depth of 569.0 mm at the end of the period, close to 568.7 mm by Chebyshev filter. Butterworth and moving average filters result in 628.6 mm and 682.8 mm respectively, compared to a total 804.2 mm measured by disdrometers.

Figure 3-12 presents cumulative rainfall in microwave link 38V using four different reference level compared to the measured values. Similarly, in this link, the moving average method results in the closest total rainfall to the measured values. The same as link 38H, the conventional method yields the lowest values and the most underestimated cumulative rainfall over the entire 300 days of simulation.

The conventional method, moving average, Butterworth, and Chebyshev methods, resulted in a cumulative rainfall depth equal to 574.1 mm, 706.5 mm, 604.6 mm, and 577.7 mm respectively.

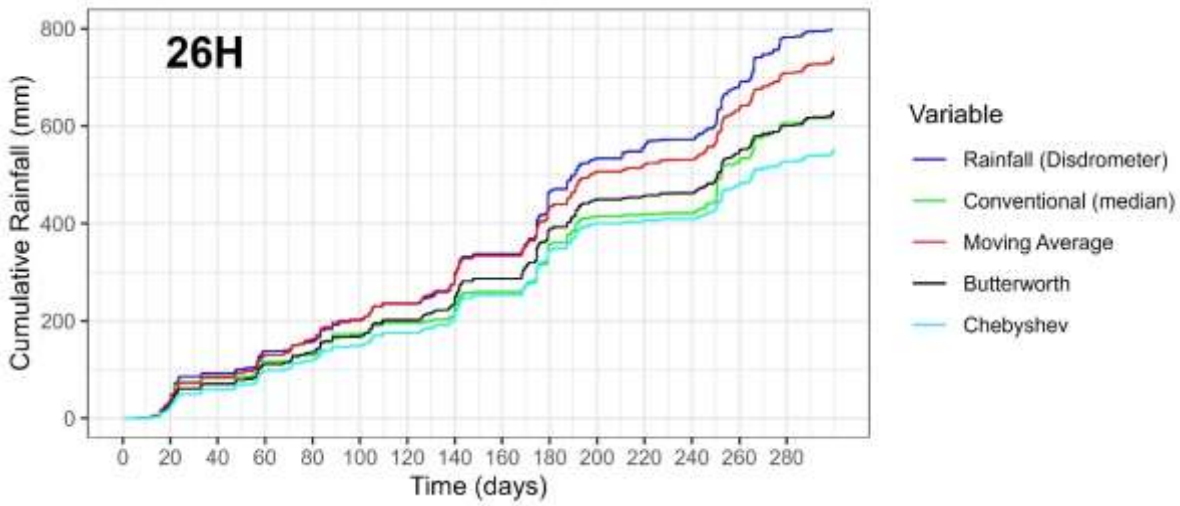


*Figure 3-10- Cumulative rainfall in 300 days for measured rainfall with disdrometers and 4 methods of reference power level calculations with optimal $A_a$ values for the microwave link 26H.*

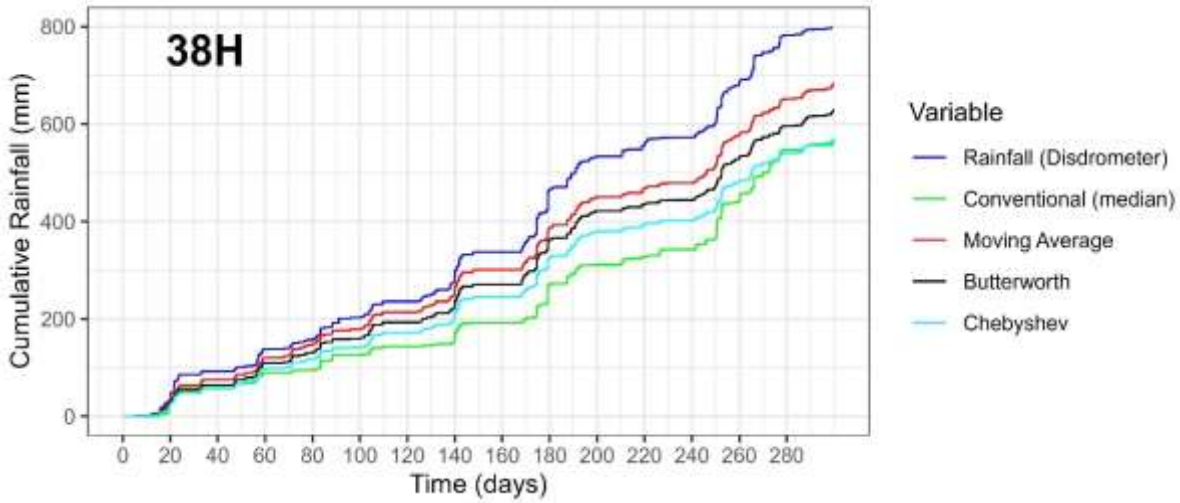


*Figure 3-11- Cumulative rainfall in 300 days for measured rainfall with disdrometers and 4 methods of reference power level calculations with optimal $A_a$ values for the microwave link 38H.*

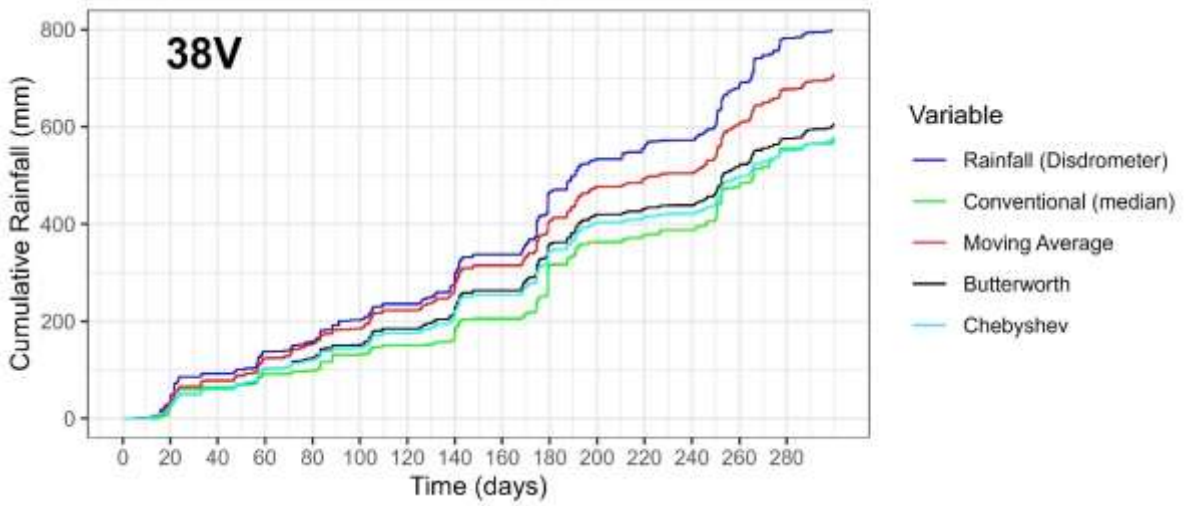


*Figure 3-12- Cumulative rainfall in 300 days for measured rainfall with disdrometers and 4 methods of reference power level calculations with optimal $A_a$ values for the microwave link 38V.*

### 3.7.4. Cumulative rainfall in short periods

Some short periods were selected to compare the accuracy of simulation of the instance rainfall intensity across different methods with their cumulative rainfall depths. Different methods in different links show different accuracy levels.

Figure 3-13, Figure 3-14, and Figure 3-15 show the variation of rainfall intensity, simulated with four methods and compared to the measured rainfall in microwave links 26H, 38H, and 38V respectively in a 43 minutes time period. Since the links have the same location and link path and they are compared to the same disdrometers, the accuracy of models could be compared. While the total cumulative rainfall for the whole 300 days of simulation is underestimated in all links and all models, the results are different in short term. In microwave link 26H, as Figure 3-13 shows, the conventional method results in a high overestimated value of total rainfall. Butterworth and moving average methods also result in a higher total rainfall depth while the Chebyshev underestimate the rainfall in this period.

Utilizing the power levels in two other links, 38H and 38V, yields the lowest total rainfall value, approaching zero, when employing the conventional method. Figure 3-14 and Figure 3-15 show that in these two links and in this period, the Butterworth filter results in a more accurate total rainfall depth, close to the measured values.

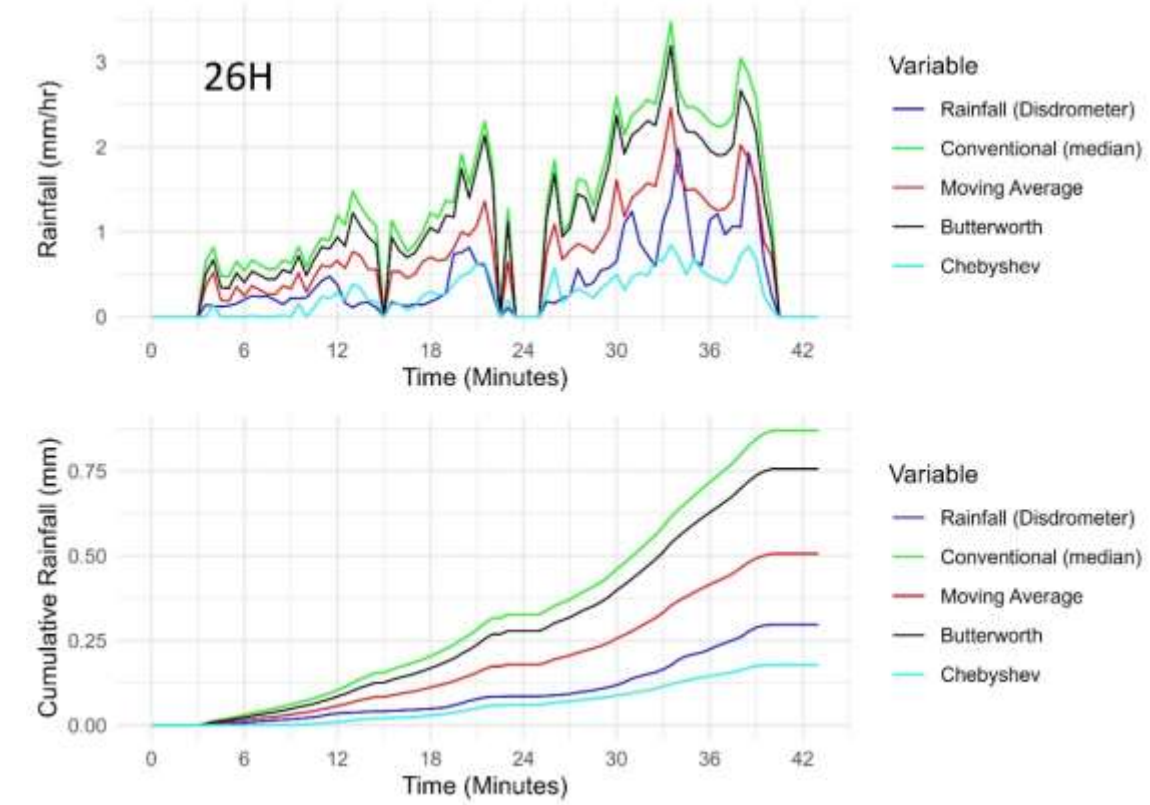


*Figure 3-13- Measured and the instant rainfall intensity and the cumulative rainfall depth calculated with different methods of reference power level for the microwave link 26H in a 43-minute period.*

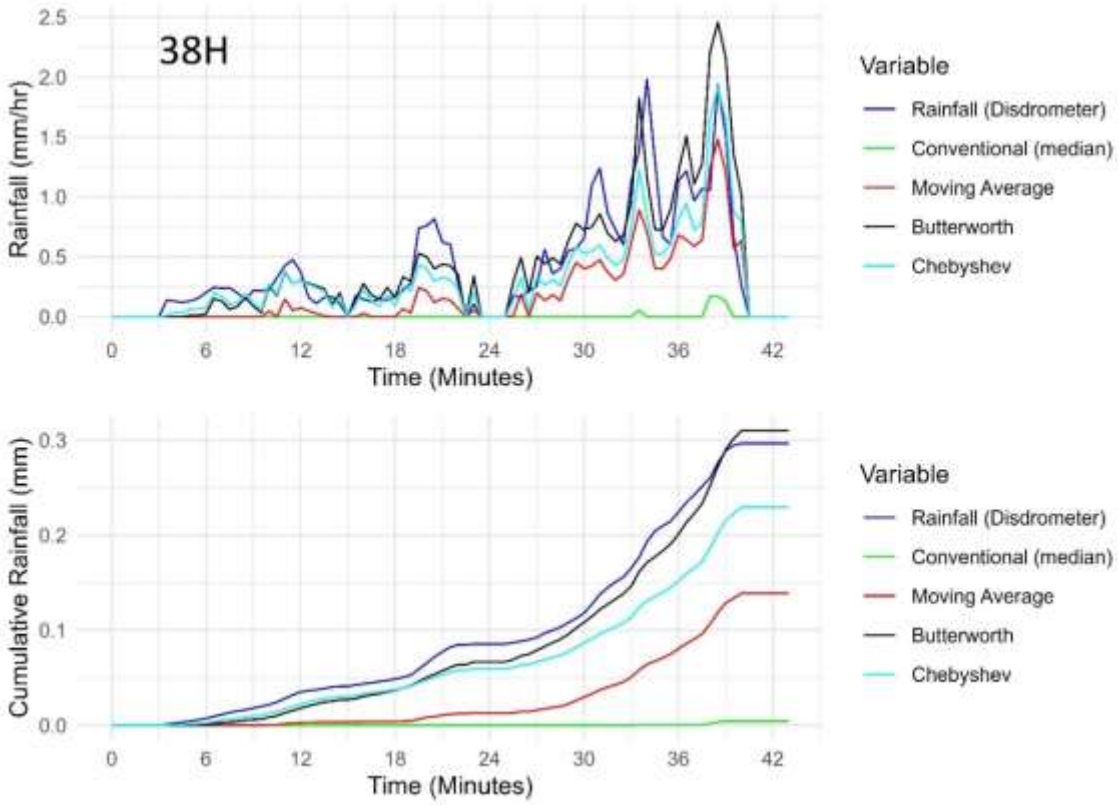


*Figure 3-14- Measured and the instant rainfall intensity and the cumulative rainfall depth calculated with different methods of reference power level for the microwave link 38H in a 43-minute period.*

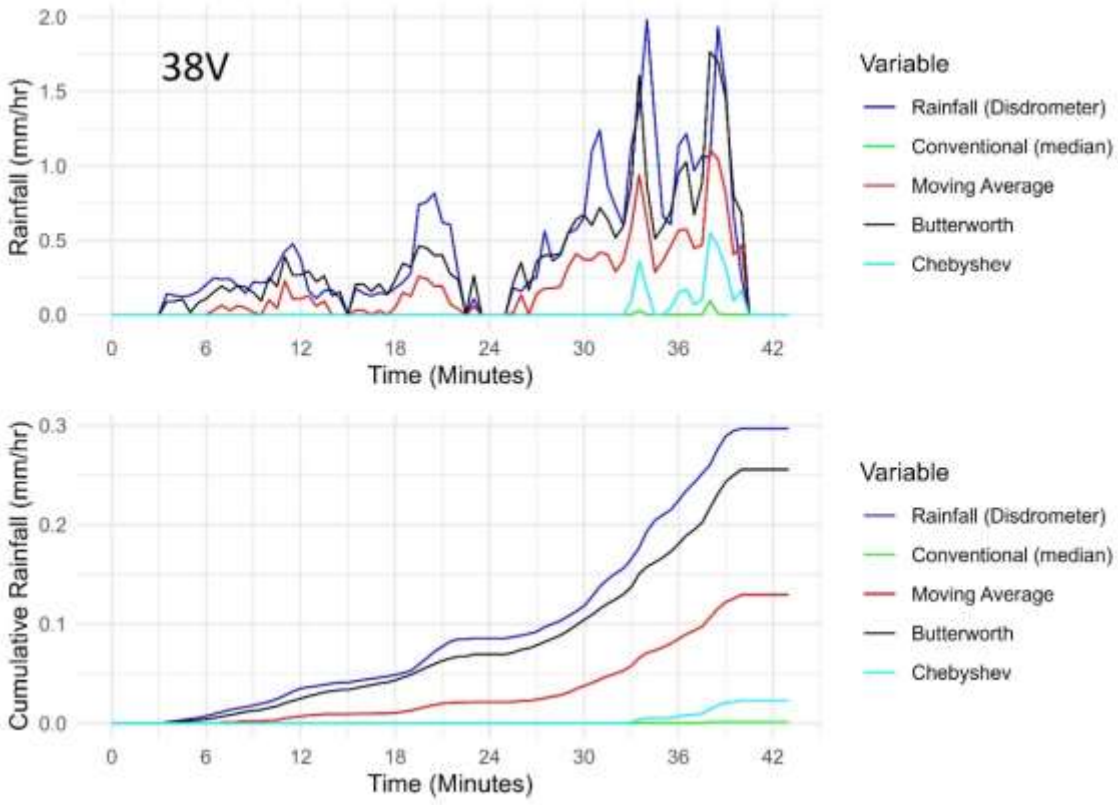


*Figure 3-15- Measured and the instant rainfall intensity and the cumulative rainfall depth calculated with different methods of reference power level for the microwave link 38V in a 43-minute period.*

In certain periods, alternative methods demonstrate different performance compared to the conventional method. In another period of the length 133 minutes, reference level methods are compared. Figure 3-16, Figure 3-17, and Figure 3-18 are the illustration of the instant rainfall intensity and the cumulative rainfall depth, calculated with four methods of reference level compared to the disdrometers, in microwave links 26H, 38H, and 38V respectively. Figure 3-16 shows that the conventional method in link 26H yields rainfall depth higher that measured. In this link, the suggested methods remain close to the measured total rainfall until the minute 84. After this time, they drop below the measured values.

In Figure 3-17 and microwave link 38H, moving average and Butterworth filters produce the same total rainfall depth as disdrometers after 60 minutes. The moving average closely aligns with the measured value until 90 minutes, while the Butterworth filter decreases. As illustrated in both Figure 3-17 and Figure 3-18 show, the moving average is the preferred method during this time period for links 38H and 38V.

It's important to note that trends in cumulative rainfall may not accurately reflect instant rainfall intensity, as instant values can surpass or fall below the measured value at any given moment. Therefore, depending on the start time of evaluation and the collection of rainfall depth, the accuracy of total rainfall prediction varies among the methods and links.

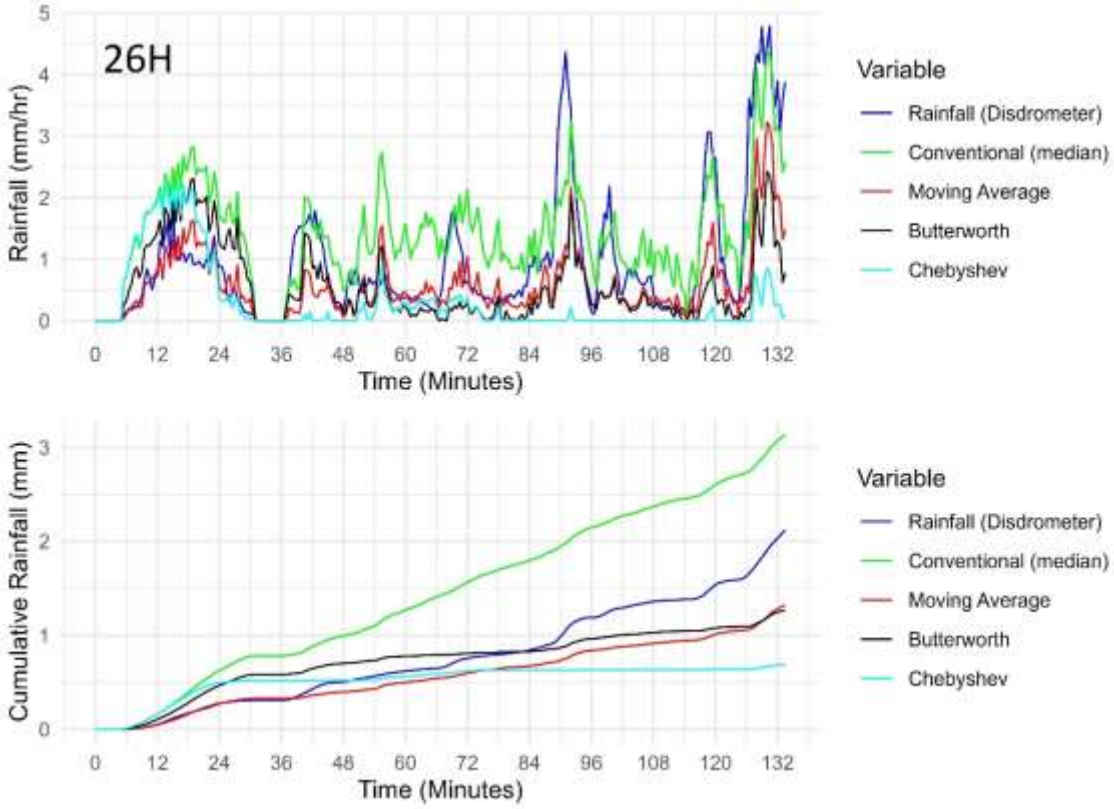


*Figure 3-16- Measured and the instant rainfall intensity and the cumulative rainfall depth calculated with different methods of reference power level for the microwave link 26H in a 133-minute period.*

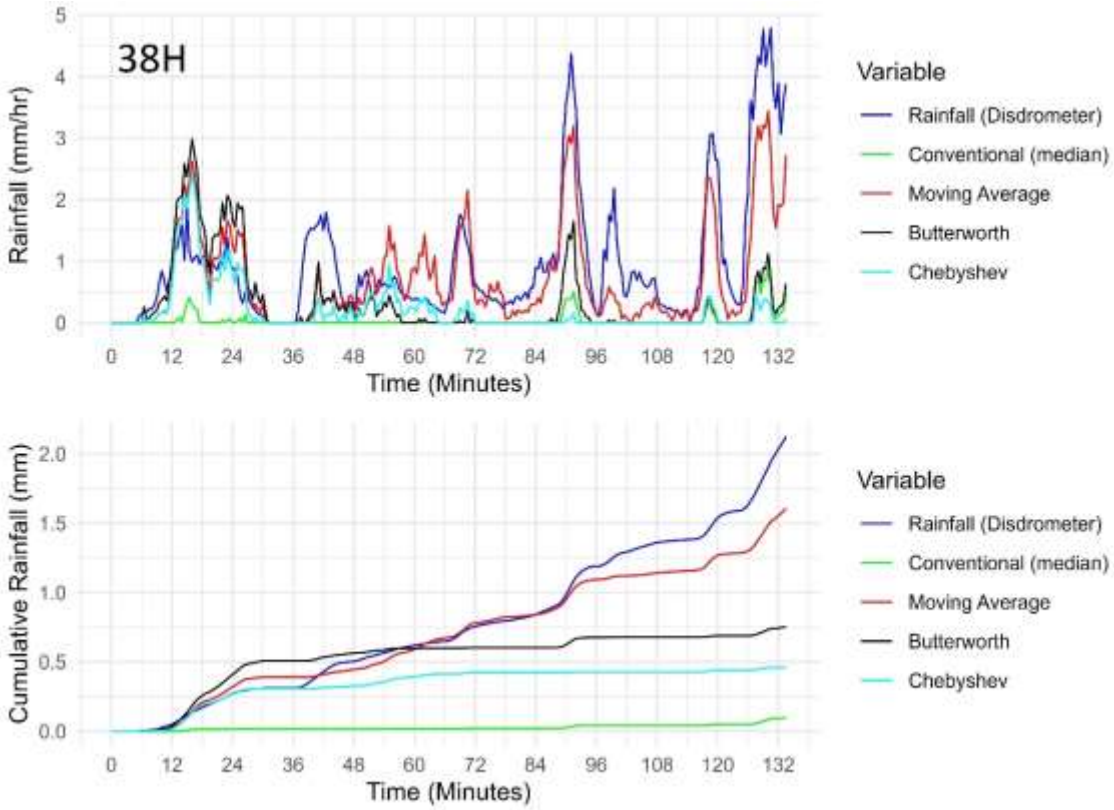


*Figure 3-17- Measured and the instant rainfall intensity and the cumulative rainfall depth calculated with different methods of reference power level for the microwave link 38H in a 133-minute period.*

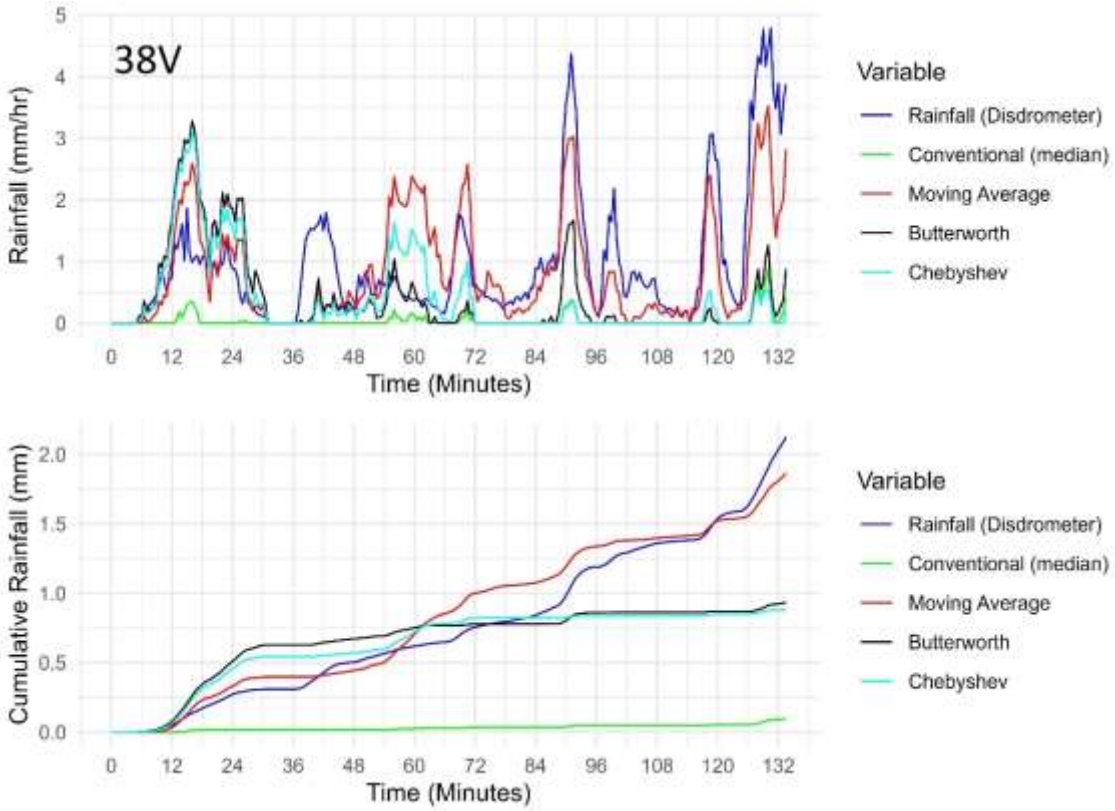


*Figure 3-18- Measured and the instant rainfall intensity and the cumulative rainfall depth calculated with different methods of reference power level for the microwave link 38V in a 133-minute period.*

### 3.7.5. Analysis of periods of 10 days

The comparison between time periods needs a consistent method with specific duration of rainfall or a specific condition, for example start and end of a rainfall event. On the other hand, the calculation methods in this study lack a rainfall event detection approach. Therefore, fixed periods utilised for consistent.

A 10-day analysis conducted for assessing different methods in shorter periods. Figure 3-19 is illustration of the comparison of RMSE among various methods over 10-day periods comparing simulated rainfall with measured rainfall from disdrometers. Although the higher rainfall intensities produce higher RMSE in simulation, this pattern is not uniform across time.

Figure 3-20 depicts a similar comparison across NSE values, shows fluctuations across different times and methods. NSE varies between less than 5 percent and up to 90 percent in a single method for different times of the year.

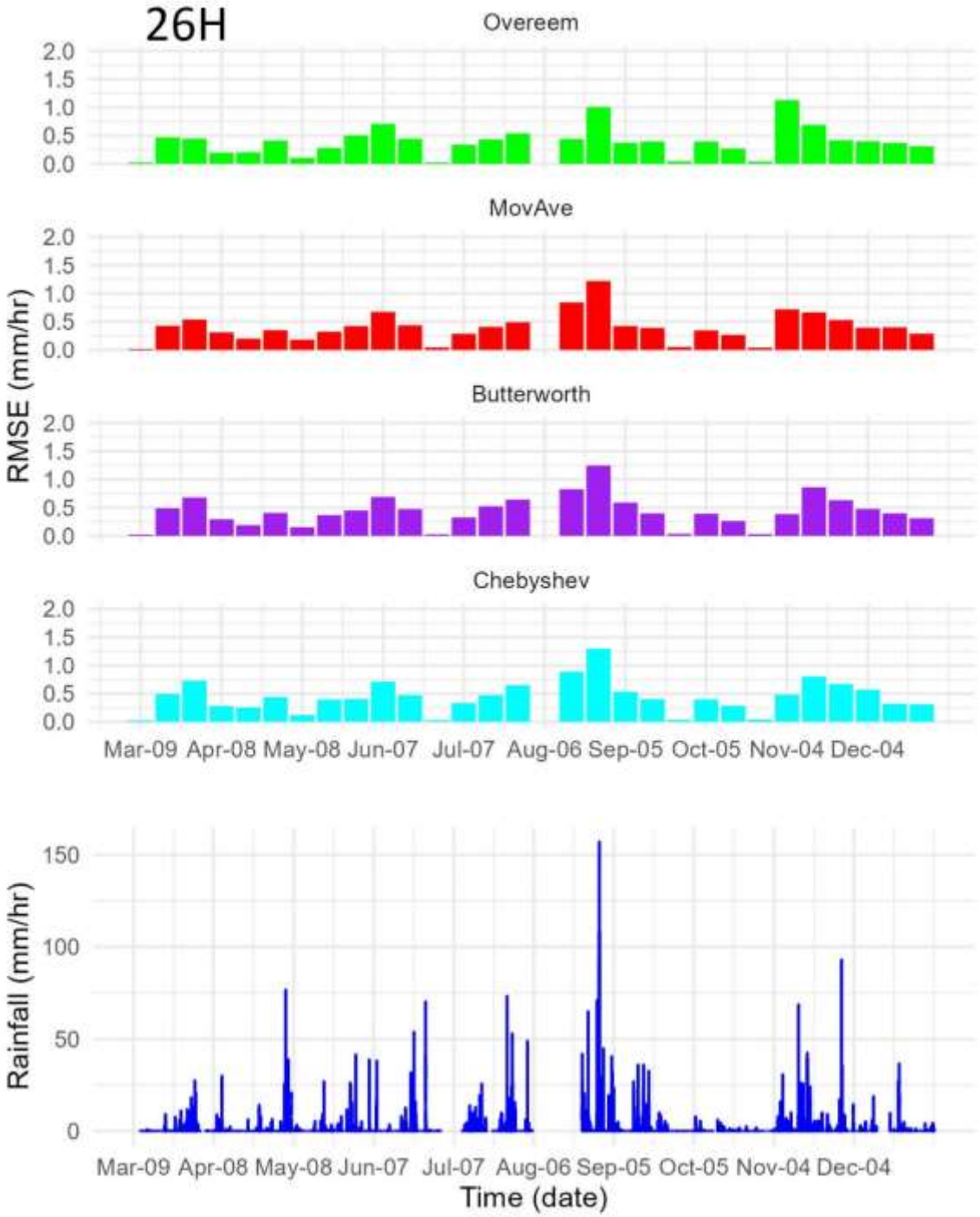


*Figure 3-19- Comparison of RMSE for various methods of reference power calculation in 10-day periods- microwave link 26H.*

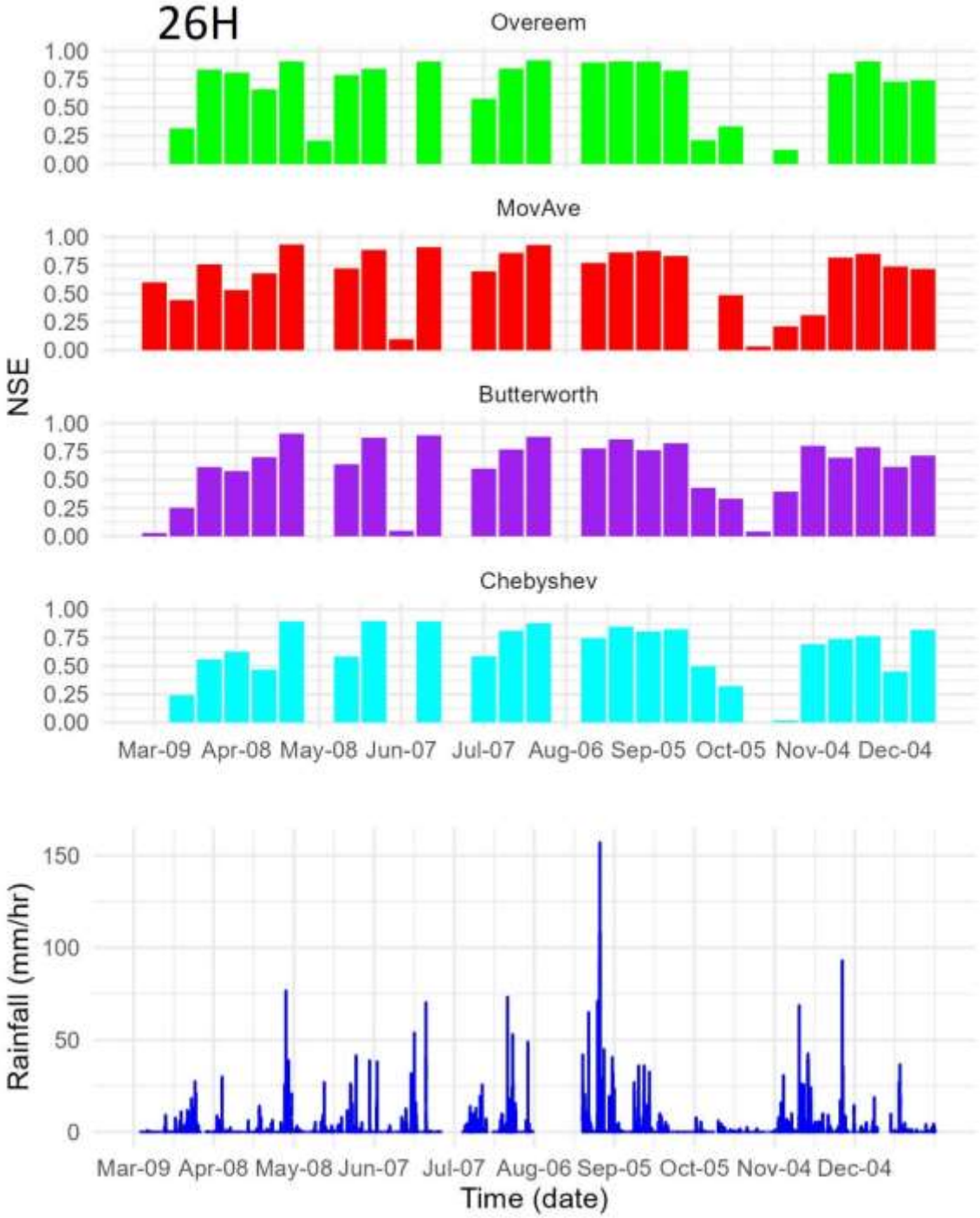


*Figure 3-20- Comparison of NSE for various methods of reference power calculation in 10-day periods- microwave link 26H.*

These graphs highlight that the precision of all methods fluctuates over time. Due to varying amounts of rainfall, different environmental conditions, and different days of the year, the models' ability to simulate rainfall exhibits variations. Given the absence of event detection methods, a shorter time span for calculation can unveil the accuracy of the models in briefer periods and address the question of how well they predict rainfall events.

The same analysis conducted for links 38H and 38V. Figure 3-21, Figure 3-22, Figure 3-23, and Figure 3-24 are the results of RMSE and NSE of 10-days analysis of the simulated rainfall intensity with the suggested methods, the conventional method, compared to the measured rainfall in microwave links

38H and 38V. As the graphs show, the accuracy of the models, either the conventional or the suggested reference levels are highly varying during time and in each period, a different model results in a better simulation.

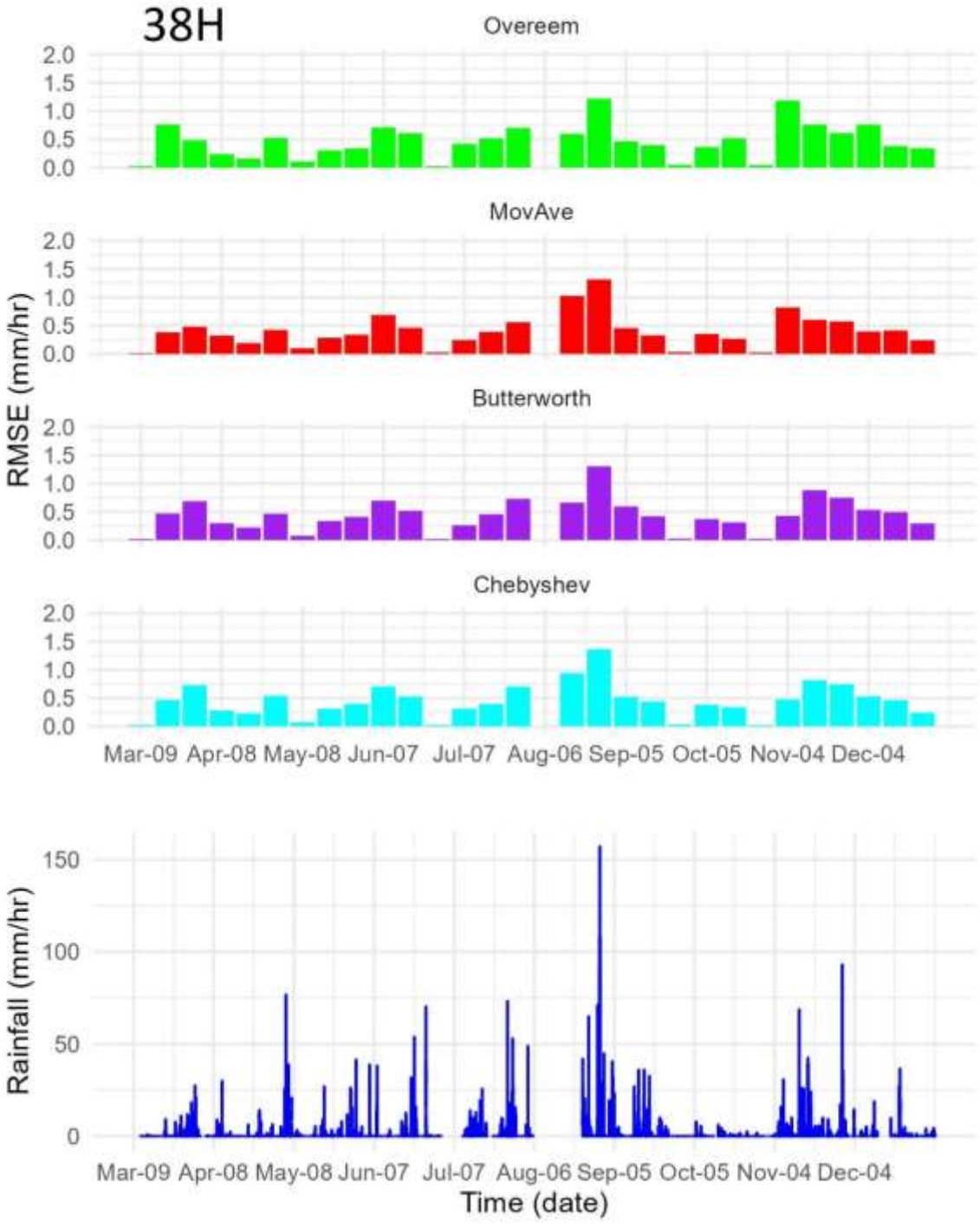


*Figure 3-21- Comparison of RMSE for various methods of reference power calculation in 10-day periods- microwave link 38H.*

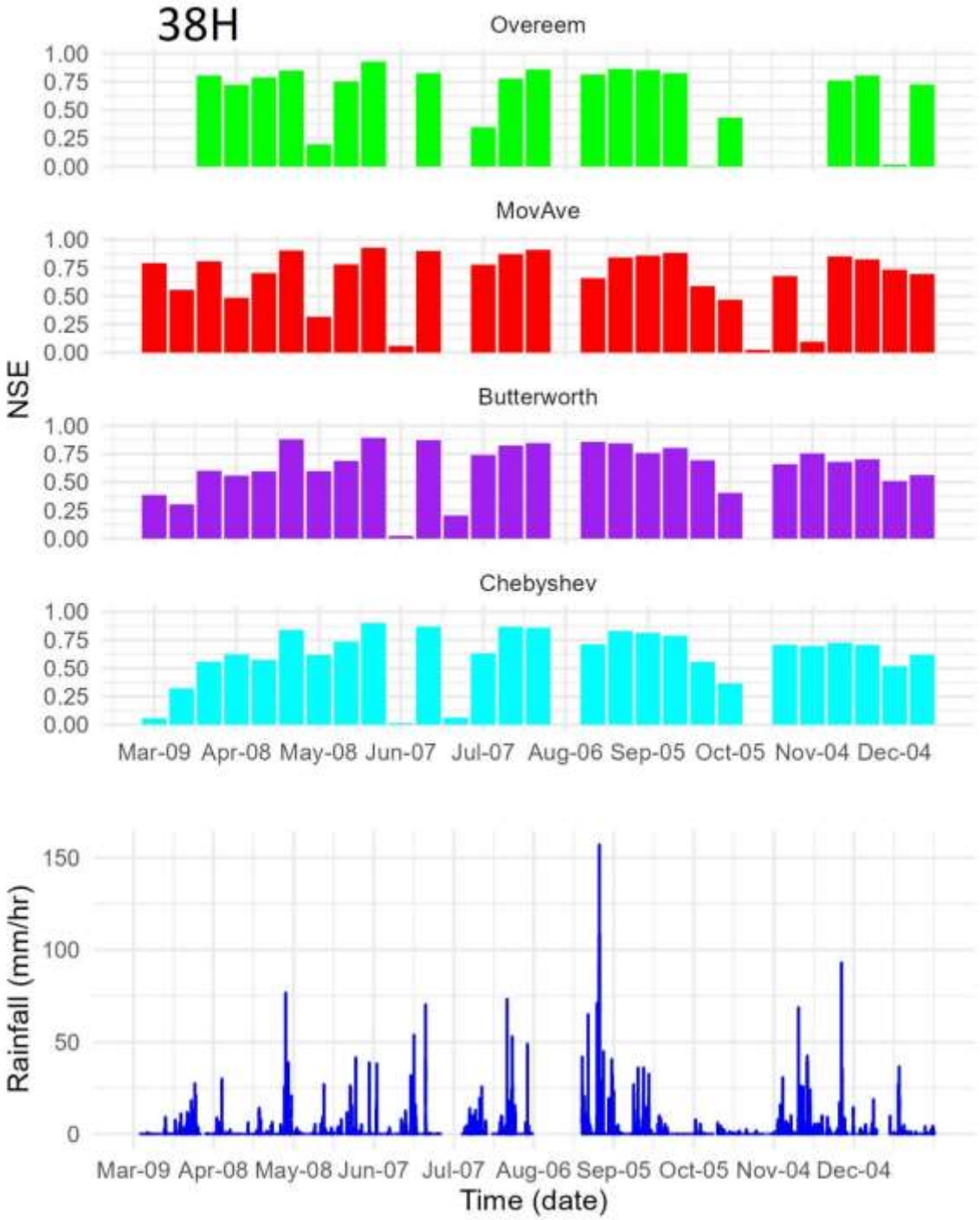


*Figure 3-22- Comparison of NSE for various methods of reference power calculation in 10-day periods- microwave link 38H.*

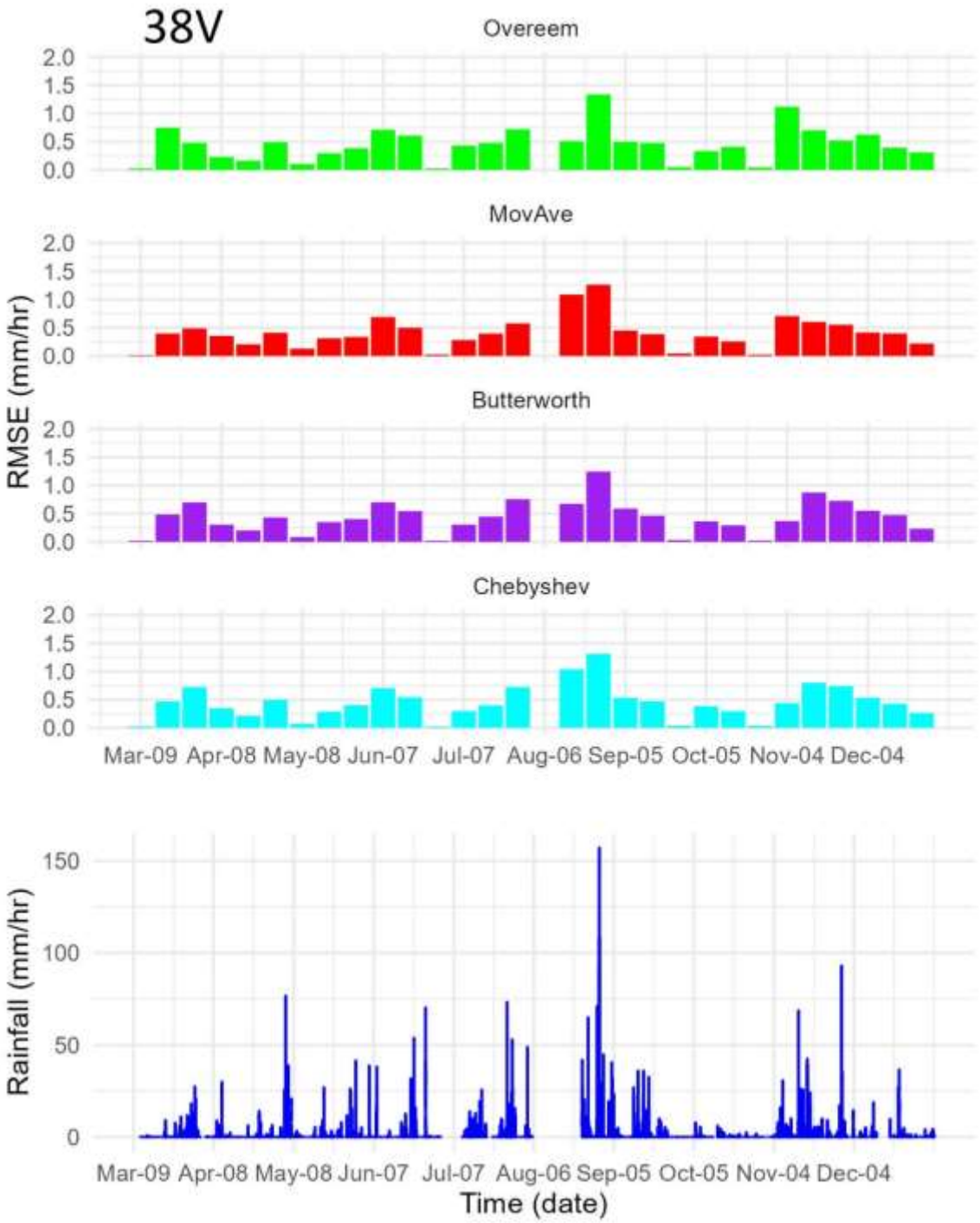


*Figure 3-23- Comparison of RMSE for various methods of reference power calculation in 10-day periods- microwave link 38V.*

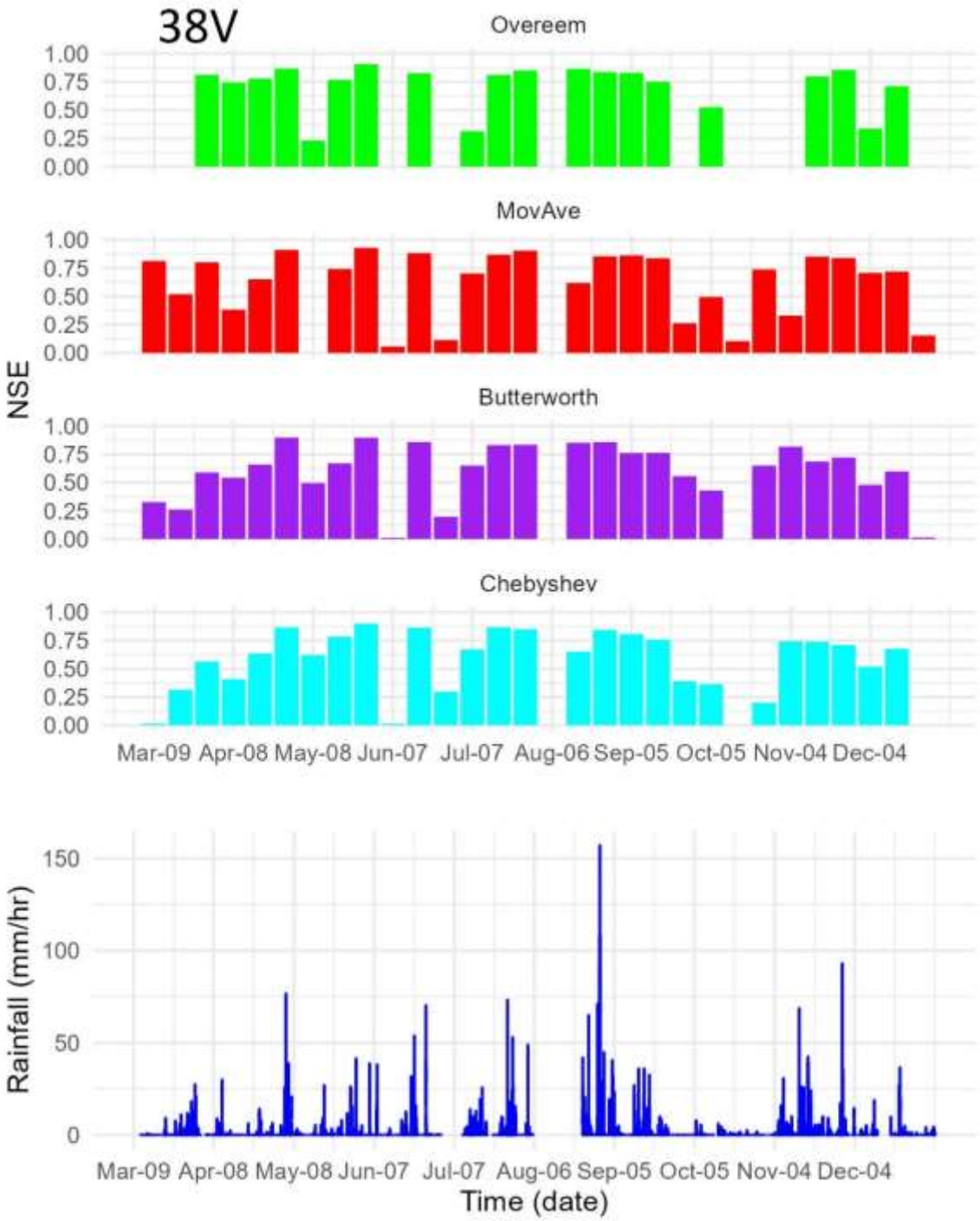


*Figure 3-24- Comparison of NSE for various methods of reference power calculation in 10-day periods- microwave link 38V.*

### 3.7.6. Short periods analysis

A thorough analysis is conducted for periods of 1, 3, and 12 hours, as well as 1, 2, 3, 5, 10, and 30 days. This aims to compare the performance of the conventional method and three suggested techniques in even shorter periods, with an attempt to scale down to rainfall events. A violin graph is employed to illustrate the quantity of the higher fitted periods and the variations of each statistical factor across different periods for each method of reference level calculation.

Figure 3-25, Figure 3-26, and Figure 3-27 illustrate the variations in NSE, R-squared, and RMSE when simulating rainfall using four methods of reference signal level over different period lengths ranging

from 1 hour to 30 days in microwave links 26H, 38H, and 38V respectively. All the calculations of each method are conducted using the optimum $A_a$ values, obtained in the previous section. Then, the length of the sample adjusted to 1 hour to 30 days and the fitness of this length of observed and simulated rainfall was calculated.

In these figures, the slender shapes in these periods indicate variability in results, with NSE, RMSE, and R-squared values fluctuating between highs and lows in various 1 or 3-hour selected intervals. Consequently, they indicate that the outliers in periods of 1 and 3 hours outnumber the values closer to the median. In these graphs, a broader shape signifies more results at that level of fitness. Hence, different times of the year exhibit consistently high or low values of the statistical factor. With an increase in the evaluation period length, the number of outlier results diminishes, exposing greater consistency in either high or low NSE, R-squared, and RMSE values.

In Figure 3-25 the conventional method shows considerable number of low NSE values in the range of 12 hours to 5 days. At the same analysis period, NSE values of the simulation with moving average stand higher and closer to 1.0. The extension of the plots for R-squared values of conventional, Butterworth and Chebyshev methods are considerably wider than moving average method.

As the comparison period extends to 30 days, the low NSE and R-squared outliers decrease and the shapes width increase. While the fitness of the methods increases in longer periods, their consistency of results and distribution of NSE and RMSE values along the time is different and the highest value is not a representer of the whole simulation time.

Figure 3-26 and Figure 3-27 are the same analysis for microwave links 38H and 38V respectively. The short periods of one and three hours are presented as narrow lines which are the same as link 26H and indicate the low consistency in results and highly varied NSE and RMSE values. As the length of the samples increase, the number of high NSE and low RMSE values increase. In these two microwave links with frequency of 38 GHz, the moving average method results in considerably more number of high NSE and R-squared values especially in periods longer than 2 days. The other methods remain with more outliers in results, even in longer periods.

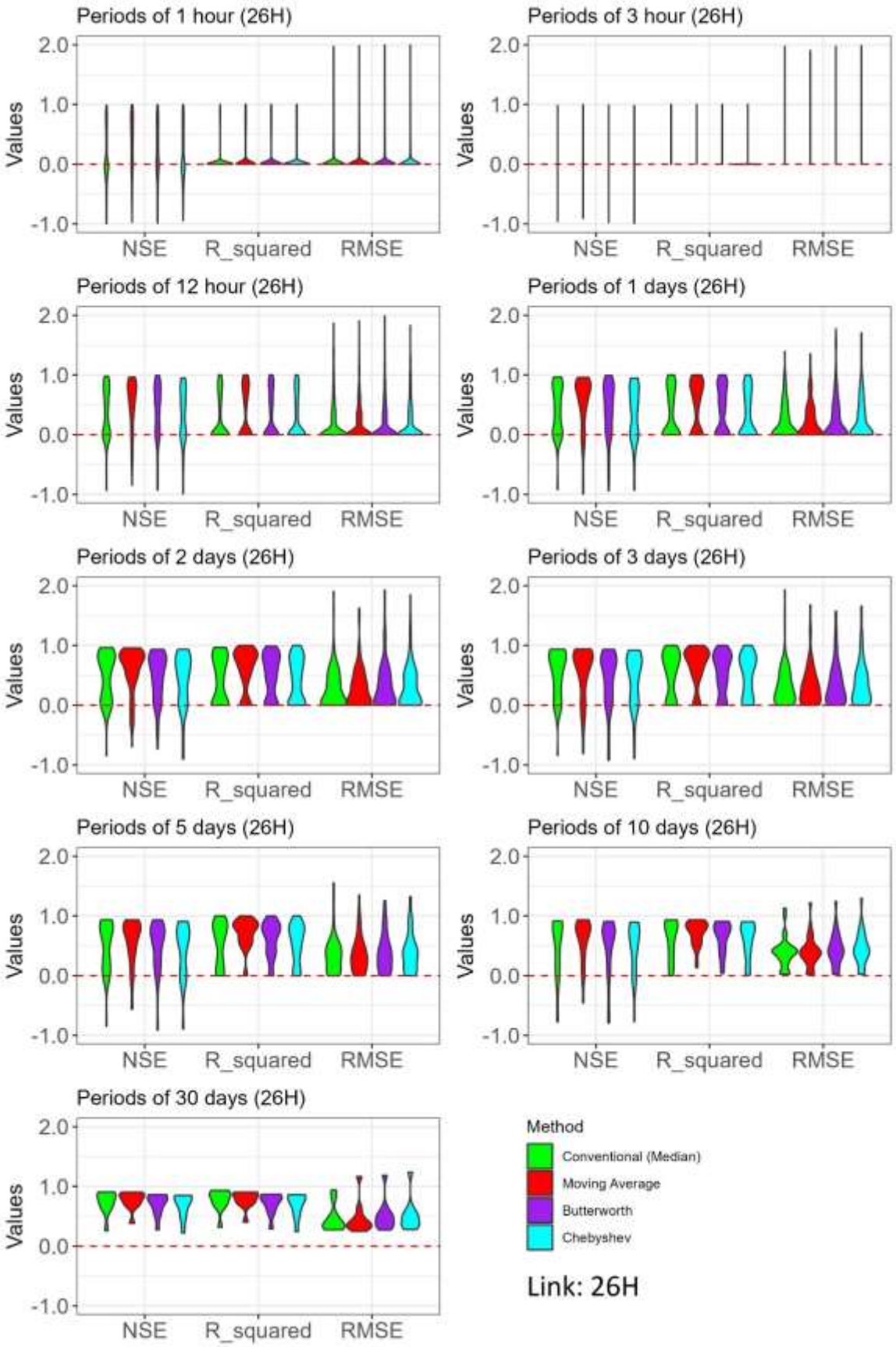


*Figure 3-25- Violin plots of variations in NSE, R-squared, and RMSE for simulated rainfall using four methods of reference signal level in different period lengths. (microwave link: 26H)*

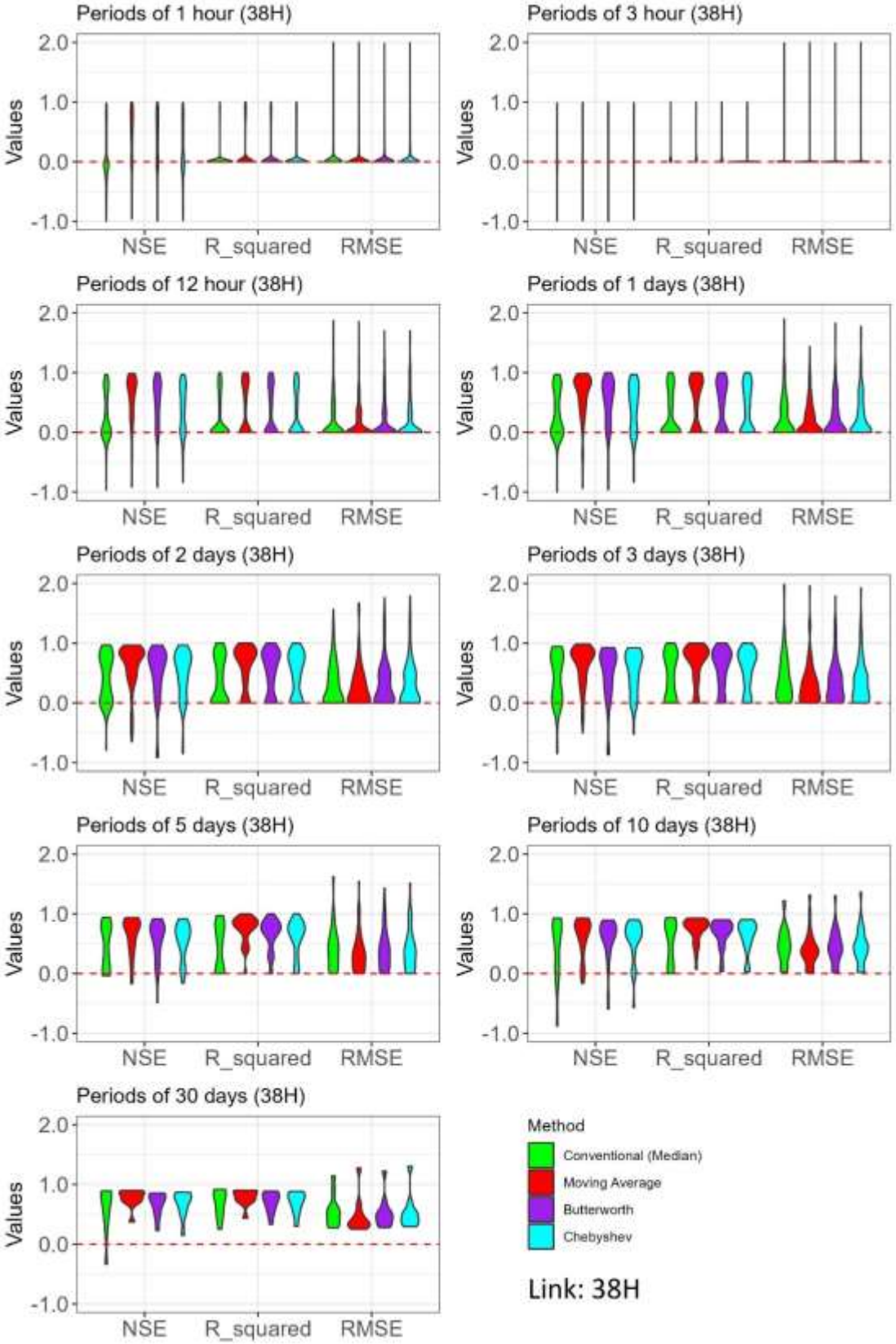


*Figure 3-26- Violin plots of variations in NSE, R-squared, and RMSE for simulated rainfall using four methods of reference signal level in different period lengths. (microwave link: 38H)*

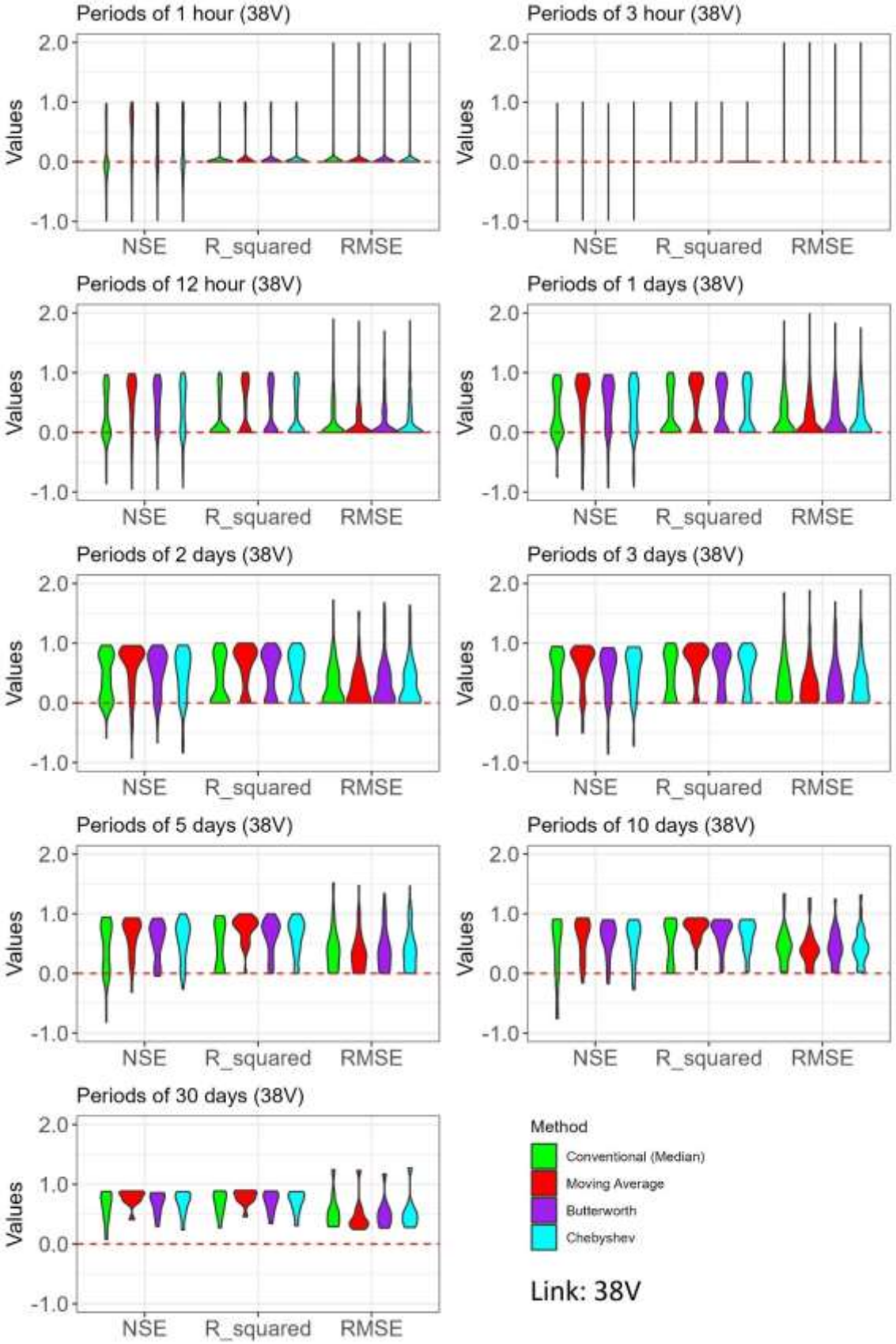


*Figure 3-27- Violin plots of variations in NSE, R-squared, and RMSE for simulated rainfall using four methods of reference signal level in different period lengths. (microwave link: 38V)*

### 3.7.7. Moving average analysis

As evident from the previous sections, the moving average filter emerges as the superior choice for simulating rainfall using CML data. It consistently yields the highest NSE and R-squared values and the lowest RMSE compared to both the suggested methods and the conventional method for calculating the reference power level. For the purpose of this study, a six-hour moving average was chosen for simulation, determined as the optimal interval after analysing various time steps.

The analysis of the moving average time window spanned periods ranging from one to 24 hours, with the window rolling around the central time step. Consequently, the six-hour moving average represents the average power from three hours before to three hours after the time step.

Calculations for deriving the reference level using the moving average filter for rainfall simulation were conducted for averaging windows ranging from 1 hour to 12 hours, step 1 hour and time steps 15, 18, and 24 hours. These calculations were applied to three microwave links: 26H, 38H, and 38V.

The results revealed minimal variations in maximum NSE across different time steps, with values closely clustered. The simulation outcomes are presented in Table 3-4 for each microwave link. The results are the RMSE and the NSE variation in simulating rainfall by calculating the reference power level using the moving average method with time steps ranging from 1 to 24 hours.

As the Table 3-4 shows, the variation of fitness and accuracy of rainfall simulation is not changing widely with different moving average time steps. The minimum RMSE and the maximum NSE achieves with 5-hours moving average window in link 38V, while a range of time steps from 5 to 7 hours provide the minimum RMSE and maximum NSE in link 38H. Microwave link 26H needs a 15 hours time step to result the optimum NSE-RMSE values.

*Table 3-4- NSE and RMSE of simulating rainfall with moving average method in different time steps and for three microwave links*

| Moving Average time step (hour) | 38V | | | 26H | | | 38H | | |
|---|---|---|---|---|---|---|---|---|---|
| | NSE | RMSE | Aa | NSE | RMSE | Aa | NSE | RMSE | Aa |
| 1 | 0.6270 | 0.6900 | 0.4 | 0.6680 | 0.6510 | 0.4 | 0.6230 | 0.6930 | 0.4 |
| 2 | 0.7670 | 0.5450 | 0.0 | 0.8000 | 0.5210 | 0.0 | 0.7570 | 0.5560 | 0.0 |
| 3 | 0.8020 | 0.5020 | 0.0 | 0.8120 | 0.4900 | 0.0 | 0.7930 | 0.5130 | 0.0 |
| 4 | 0.8200 | 0.4790 | 0.0 | 0.8220 | 0.4760 | 0.1 | 0.8120 | 0.4900 | 0.0 |
| 5 | **0.8220** | **0.4760** | **0.0** | 0.8270 | 0.4700 | 0.2 | **0.8160** | **0.4840** | **0.0** |
| 6 | 0.8210 | 0.4780 | 0.0 | 0.8270 | 0.4700 | 0.2 | **0.8160** | **0.4840** | **0.0** |
| 7 | 0.8210 | 0.4780 | 0.1 | 0.8300 | 0.4670 | 0.3 | **0.8160** | **0.4840** | **0.0** |
| 8 | 0.8210 | 0.4790 | 0.2 | 0.8310 | 0.4650 | 0.3 | 0.8160 | 0.4850 | 0.1 |
| 9 | 0.8200 | 0.4800 | 0.3 | 0.8320 | 0.4630 | 0.4 | 0.8160 | 0.4850 | 0.2 |
| 10 | 0.8200 | 0.4800 | 0.3 | 0.8340 | 0.4610 | 0.4 | 0.8160 | 0.4850 | 0.3 |
| 11 | 0.8200 | 0.4810 | 0.4 | 0.8350 | 0.4600 | 0.4 | 0.8160 | 0.4850 | 0.3 |
| 12 | 0.8180 | 0.4820 | 0.5 | 0.8350 | 0.4600 | 0.5 | 0.8150 | 0.4860 | 0.4 |
| 15 | 0.8160 | 0.4870 | 0.6 | **0.8360** | **0.4590** | **0.5** | 0.8130 | 0.4900 | 0.5 |
| 18 | 0.8120 | 0.4920 | 0.8 | 0.8330 | 0.4630 | 0.6 | 0.8090 | 0.4950 | 0.7 |
| 24 | 0.8080 | 0.4980 | 1.0 | 0.8320 | 0.4660 | 0.7 | 0.8050 | 0.5020 | 0.9 |

It is worth noting that the subsequent maximum values for NSE with the next optimum time step differ by only 0.005 in each of the microwave links. This value for RMSE is 0.006 mm/day. Therefore, the time step does not significantly impact the results over the entire 300 days of the study duration. This slight variation in NSE is observable in Figure 3-28 depicting NSE values for rainfall simulation using the moving average method for each time step from 1 to 24 hours.

As evident from the graphs for each microwave link, NSE changes more with alterations in $A_a$ than with changes in the time step. Therefore, goodness of fit in simulation is more sensitive to calibrating $A_a$. Except for time steps of 1 to 4 hours, the maximum NSE values consistently remain at a high range above 0.80. However, for each simulation, NSE drops to 0.75 and lower when selecting a 1 dB greater value for $A_a$.

Considering the results from the moving average simulation across different time steps, as presented in Table 3-4 and Figure 3-28, a 6-hour time step has been selected for the moving average method for calculating the reference power level. This time step ensures achieving the maximum NSE and the minimum RMSE with the lowest possible $A_a$ value while minimising the lag time in calculations. Considering the window of moving average, spanning 3 hours before and 3 hours after the time step, there will be 3 hours delay in calculations. It proves to be the optimal time step for microwave links 38H and 38V. Although the maximum NSE and the minimum RMSE are achieved with a 15-hour time step in link 26H, a 6-hour time step still provides a high NSE, even surpassing the conventional method. Additionally, it requires a lower $A_a$ value, specifically 0.2 dB compared to 0.5 dB for the 15-hour time step.

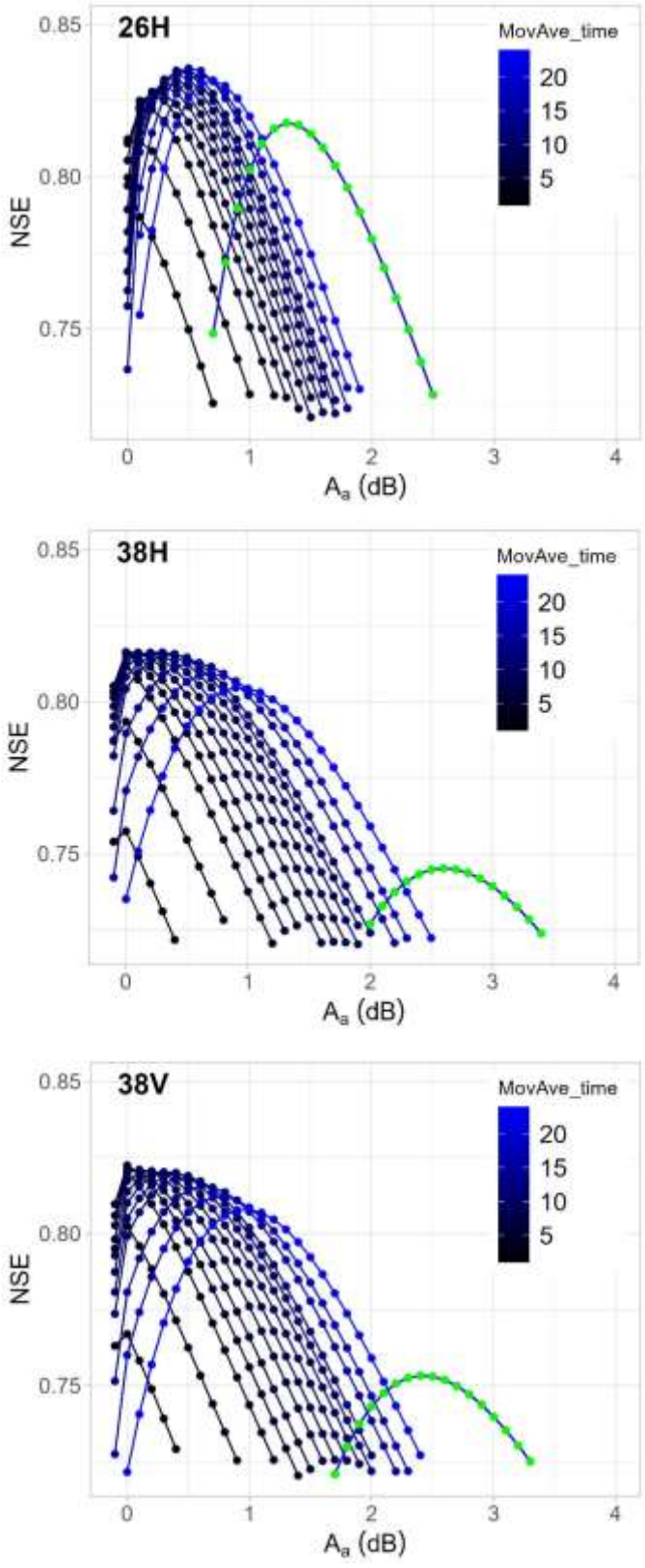


*Figure 3-28- NSE of simulating rainfall with moving average with different time steps (1 to 24 hours) compared to the conventional method of reference level calculation (green dots), for three microwave links.*

## 3.8. Discussion

The comparison of different methods for calculating reference power levels in microwave links and their impact on rainfall simulation yields valuable insights. The study focused on three suggested methods —moving average, Butterworth, and Chebyshev filters— compared to the conventional method (median). The analysis was conducted across three microwave links: 26H, 38H, and 38V.

The outcomes of this section of the study affirm the viability of the proposed reference power calculation methods when contrasted with the median method, a conventional approach commonly employed in CML rainfall retrieval methodologies.

The optimal choice among the investigated methods is the moving average with a 6-hour time step, proving effective in accurately calculating both rainfall intensity and depth throughout the 300-day simulation period. Cumulative rainfall simulated using the moving average closely aligns with the measured values obtained from disdrometers. Notably, the performance of Butterworth and Chebyshev filters in simulating 300 days of rainfall depth closely resembled that of the conventional method but deviated from the measured rainfall values.

For the hourly calculations, Table 3-5 collects the lowest RMSE and the corresponding NSE and R-squared values of the conventional and the suggested methods for three microwave links. This table is ranked by the lowest RMSE, shows the accuracy and capability and the privilege of the suggested methods in microwave links 38H and 38V. The suggested methods in this links provide a lower RMSE and higher NSE and R-squared while need a lower to zero wet antenna correction as well. In microwave link 26H also the moving average method performed better than the other methods. However, the performance of Butterworth and Chebyshev filters was not better than the conventional method.

*Table 3-5- the summary of minimising RMSE for four methods of calculating the reference power level in three microwave links, ranked by the lowest RMSE.*

| Microwave link | Reference level method | $A_a(dB)$ | $RMSE$ $(mm/hr)$ | $NSE$ | $R^2$ |
|---|---|---|---|---|---|
| 26H | Moving average | 0.2 | 0.47 | 0.83 | 0.83 |
| | Conventional (median) | 1.3 | 0.48 | 0.82 | 0.82 |
| | Butterworth | 0.5 | 0.51 | 0.80 | 0.80 |
| | Chebyshev | 0.0 | 0.52 | 0.79 | 0.79 |
| 38H | Moving average | 0.0 | 0.48 | 0.82 | 0.82 |
| | Chebyshev | 0.0 | 0.53 | 0.78 | 0.78 |
| | Butterworth | 0.4 | 0.53 | 0.78 | 0.78 |
| | Conventional (median) | 2.6 | 0.57 | 0.75 | 0.75 |
| 38V | Moving average | 0.0 | 0.48 | 0.82 | 0.82 |
| | Butterworth | 0.5 | 0.52 | 0.79 | 0.79 |
| | Chebyshev | 0.0 | 0.53 | 0.79 | 0.79 |
| | Conventional (median) | 2.4 | 0.56 | 0.75 | 0.75 |

Across three microwave links, the moving average method consistently outperforms other methods, including the conventional approach. In link 26H, the moving average method achieves the lowest RMSE (0.47 mm/hr) and the highest NSE (0.83), outshining the conventional method in both metrics.

Links 38H and 38V also demonstrates the superiority of the moving average method with the lowest RMSE (0.48 mm/hr) and a high NSE (0.82).

The conventional method, represented by the median, lags behind in terms of NSE and RMSE in links 38H and 38V. In link 26H, the conventional method results in a higher RMSE (0.48 mm/hr) and lower NSE (0.82) compared to the moving average method.

It is important to note that NSE and RMSE values across different methods remain closely comparable, signifying their compatibility as viable options in CML rainfall retrieval techniques. On the other hand, a notable achievement in this study is the substantially lower $A_a$ values for the suggested methods compared to the conventional method. Specifically, the Chebyshev method consistently requires a zero $A_a$ value across all links, while moving average requires zero for links 38H and 38V, and only 0.2 dB in link 26H. The Butterworth filter, meanwhile, necessitates an $A_a$ value ranging from 0.4 to 0.5 dB across different links.

This accomplishment in mitigating the wet antenna effect is noteworthy and captures attention in CML rainfall methodologies. Utilizing a method that doesn't require $A_a$ reduces the number of parameters that need calibration. The calibration of any factor necessitates data and model evaluation, a critical aspect, especially in the absence of reliable long-term data. In remote areas with no rain gauge for rainfall calibration, this poses a challenge. In such data-deficient locations, studies often resort to recommendations on parameters like $A_a$ or constants in the power law of rainfall attenuation.

Overall, moving average resulted in 2%, 16% and 14% lower RMSE than the conventional method in microwave links 26H, 38H and 38V. RMSE of simulation with Butterworth and Chebyshev was 6% to 8% higher in link 26H, however, 7% lower in link 38H and 5% to 7% lower in link 38V. Moving average in link 26H performed 1% better than the conventional method regarding to NSE, while Butterworth and Chebyshev were not better and resulted in 2% and 4% lower NSE in simulating total 300 days. These two filters performed better in links 38H and 38V as the NSE of the application of Butterworth and Chebyshev was 4% in link 38H and 5% in link 38V higher than the conventional method.

Short-term validation of the methods reveals the varying sensitivity of each model for simulating rainfall events across different times and periods. Notably, rainfall events as short as one to three hours did not yield significant and valid results for simulation. NSE, R-squared, and RMSE of the simulations indicated remarkably low fitness during these short durations. The number of periods with satisfactory fitness in rainfall simulation increased with longer comparison periods. Better NSE and R-squared, along with lower RMSE, were more evident in validations of two days or longer.

In Figure 3-25, Figure 3-26, and Figure 3-27 the wider and shorter violin shapes for the moving average graph signify its superiority compared to other suggested filters and the conventional method.

The lower NSE and R-squared and the higher RMSE of the simulation of the suggested models in shorter time spans indicate the suitable scale of the models. As the results show, even the conventional model is not a good fit for short duration rainfall prediction. Therefore, these CML rainfall calculations may be more useful for long term prediction and total depth instead of instance rainfall intensity.

This study demonstrated that straightforward mathematical filters exhibit comparable precision to complex methods reliant on hydrological parameters, like wet-dry classification. Microwave signals exhibit discernible patterns during days and seasons that can be isolated from other influencing factors such as rainfall or additional sources of noise. These predictable patterns can be mathematically extracted from the carrier wave to establish the power's baseline. Consequently, the calculations are not exclusively dependent on the physics of the problem but can be derived from other inherent characteristics of the concept.

One defect in conventional median method is the need for dry periods in the last 24 hours which produces many not available values in results. On the other hand, the suggested methods work and produce reference level all the time and the performance of them prove that using the wet periods power level has the least negative impact on the results.

The results of the microwave link 26H (26GHz, horizontally polarised) were different from two 38 GHz links. The conventional method in link 26H resulted better NSE and lower RMSE compared to Butterworth and Chebyshev and the moving average results were slightly better, not as much as what it showed in 38GHz links. The difference here first indicates that the methods should be evaluated for other microwave frequencies and the other locations, climates, rainfall models, elevations, and urban/rural catchments as well. By investigating the reasons of difference, the methods could be properly and more accurately selected and calibrated.

One of the possible reasons for a different result in 26H link could be related to the peak attenuation of 26 GHz microwave signals due to water vapour in atmosphere.

# 4. Chapter Four – Catchment scale

## 4.1. Introduction

Rainfall flows in natural streams and rivers in natural catchments. A part of rainfall goes into the ground by infiltration and some portion to the atmosphere through evaporation and transpiration. The major part remains will run over the ground surface. The runoff in a catchment is a matter of interest when it interacts with the humanmade structures and population habitat.

The volume of rainfall draws attention while designing urban drainage systems. Stormwater in cities is under control by channels and pipes which are designed according to the runoff peak discharge. The probability of occurrence of a runoff event with a specific flow rate depends on the rainfall intensity and duration. Therefore, rainfall measurement and forecasting are the keys to calculating and designing the stormwater system.

Primary stormwater systems use short-term return periods, as low as 5 to 10 years (Auckland Council, 2022; Christchurch City Council, 2022). While the peak flows happen more frequently, they are also sensitive to climate change. Most areas worldwide have shown a significant increase in rainfall intensities (Alexander *et al.*, 2006; Donat *et al.*, 2016) and heavy precipitation occurs more often due to global warming (Min *et al.*, 2011; Westra, Alexander and Zwiers, 2013).

All the reports and research about climate change and increasing precipitation intensities alarm cities to be prepared for managing excess runoff. Major cities have particular policies and management plans to cope with the changes and extreme precipitation events (Axelsson *et al.*, 2021). On the other hand, preparation is also considered as adjusting the design flow for water structures in cities. The key to regulating the flow is providing a more accurate updated rainfall-runoff model or having a better estimation of how much rainfall becomes runoff.

### 4.1.1. Estimating runoff

Calculating, estimating, and predicting runoff in a catchment is generally a result of rainfall-runoff models. While the main factor seems to be rainfall depth or intensity, extracting runoff from rainfall is not a straightforward transformation. The whole process is complicated by temporal and spatial variations and is extremely non-linear (Rajurkar, Kothyari and Chaube, 2004). The more parameters are added to the models, the more complicated the model will be. Precise estimates of parameters and calibration will be challenges for an accurate runoff prediction. Below, the common approaches are discussed and compared to the alternative simple correlation to achieve the goal.

### 4.1.2. Rainfall-runoff models

Changes in rainfall across the catchment are not the only challenge here because rainfall alone is unable to fully uncover this complexity (Frezghi and Smithers, 2008). Other factors that impact this process include, but are not limited to, the catchment area, main streamflow length, and catchment slope, shape and storage (Philip B Bedient, Huber and Vieux, 2013).

Rainfall-runoff models vary in the number of parameters they use. Empirical models use a minimal number of parameters, while Conceptual models utilize simplified water storage equations and Physical models employ numerous parameters and real hydrologic response equations (Sitterson *et al.*, 2018). Despite their simplicity, simpler models have drawn attention due to their ease of use, but they may not accurately reflect non-linear variations in the rainfall-runoff transformation (Rajurkar, Kothyari and Chaube, 2004).

There was also development of dynamic solutions for monthly rainfall-runoff models by adding catchment parameters (Hamel *et al.*, 2017). Other methods tried to increase the accuracy of models by adding other parameters like evapotranspiration, temperature, and humidity (Xu and Vandewiele,

1995) or using water balance equations and potential evapotranspiration (Abulohom, Shah and Ghumman, 2001).

Modèle du Génie Rural (Perrin, Michel and Andréassian, 2003) (the Rural Genius model in British (Martínez-Sifuentes *et al.*, 2023)) has been developed by the French Research Institute for Agricultural and Environmental Engineering for annual (GR1A), monthly (GR2M) and daily (GR4J) data time steps (Martínez-Sifuentes *et al.*, 2023). These models have been used in different research and have showed satisfying results in large catchments, as big as hundreds of $km^2$ (Mouelhi *et al.*, 2006; Dezetter *et al.*, 2008; Rwasoka *et al.*, 2014; Belarbi *et al.*, 2016; Ouhamdouch *et al.*, 2020; Ditthakit *et al.*, 2021)

Data-driven approaches also conducted to predict runoff (Abrahart, See and Solomatine, 2008; Elshorbagy *et al.*, 2010). Research using Gaussian process regression were successful in finding a reasonable correlation between runoff and precipitation and other catchment parameters (Sun, Wang and Xu, 2014).

The most important parameters to utilise in models are soil infiltration rate and soil moisture which cause a part of the process to occur underground (Latron and Gallart, 2008). These catchment characteristics help to calculate the time of concentration and find the total volume of runoff. Therefore, topography, soil, and vegetation control the process of dividing rainfall into overland flow and underground flow (Rossi, Whipple and Vivoni, 2016).

Land use or coverage of the catchment is also an important parameter here which needs to be estimated as precisely as possible. It is usually calibrated by the measured rainfall and runoff in the catchment. However, any error, underestimating or overestimating the surface coefficient causes a big change to the runoff estimations. For instance, in SCS model, a 10-15% lower or higher curve number, results in 50% less or more discharge (Boughton, 1989). Aridity, which affects the soil moisture and rainfall rate, also increase nonlinearity of rainfall-runoff correlation (Rossi, Whipple and Vivoni, 2016).

### 4.1.3. Rainfall-Runoff correlations (Annually, Monthly, Daily)

There are some barriers to having a simple regression between rainfall and runoff in daily or hourly intervals. As discussed, non-uniform distribution of rainfall and variable soil and surface conditions cause different values for runoff even for the same rainfall intensity observed in a gauge (Şen and Altunkaynak, 2004). As generating runoff is influenced by these factors (Tromp-Van Meerveld and McDonnell, 2006; Weiler and McDonnell, 2007; Latron and Gallart, 2008; Norbiato *et al.*, 2009; Zehe *et al.*, 2010; Zhao *et al.*, 2014; Bao *et al.*, 2017), uncertainty and changes during the year prevent reaching a stable correlation over time.

Previous Researches show that Runoff variability is typically heavier-tailed than rainfall variability and is a reflection of the nonlinear transformation from rainfall to runoff that is imprinted into probability distributions (Rossi, Whipple and Vivoni, 2016).

While more information is needed for modelling hourly or daily runoff from rainfall, on the other hand, there is an acceptable correlation between monthly rainfall and monthly runoff. An estimation of monthly runoff can provide the long-term water yield in a catchment. The cumulative water flow in a river is an indicator of drought and water resource tension (Saft *et al.*, 2015, 2016; Xiao *et al.*, 2018; Zhang *et al.*, 2018) or simply could be used for flood control, water storage, consumption and management purposes (Miao *et al.*, 2020). On a yearly scale, rainfall-runoff relationship indicates the annual runoff coefficient to analyse moisture balance and water yield in a catchment (Hrachowitz *et al.*, 2013; Zhang *et al.*, 2018).

Monthly rainfall-runoff relationships have been investigated in linear and non-linear models (Mimikou, Rao and Asce, 1983; Miao *et al.*, 2020). Artificial Neural Network has also been used for

modelling runoff based on rainfall data in daily (Hsu, Gupta and Sorooshian, 1995; Tokar and Johnson, 1999; Rajurkar, Kothyari and Chaube, 2009) and monthly scales (Anmala *et al.*, 2000).

### 4.1.4. Challenges of modelling rainfall-runoff in a catchment

- *Complicated urban drainage models*

The constituents and factors involved in the design of urban drainage systems encompass elements that impact visual appeal and natural solutions (Melbourne Water, 2021). The process involves multiple interconnected processes, including hydrologic processes, hydraulic processes, and water quality processes, which must be accurately represented in the model to ensure its reliability.

Urban drainage modelling involves the use of computer models to simulate the flow of stormwater through urban drainage systems, including pipes, channels, and other drainage structures. Hence, it is complex and requires a detailed understanding of the local catchment characteristics, including the topography, land use, and soil properties (Melbourne Water, 2021). This information is not always readily available and may require extensive research on the catchment. Eventually, Models need calibrating using field data to ensure that the simulation results are accurate and reliable.

The intricacy of the interrelationships among hydrological and hydraulic parameters within a catchment has resulted in the widespread adoption of empirical models that employ a minimal number of parameters in the modelling process.

- *Challenges with Catchment parameters*

Considering the right number of factors which affects the process of runoff generation is challenging. In large and heterogeneous catchments, a model that incorporates numerous input variables and parameters and is more complex leads to higher-quality simulations (Flores *et al.*, 2021). However, this is just the tip of the iceberg. A big problem appears when models need enough data across the catchment. the vast spatial and temporal variations in watershed features make it even more complex (Tokar and Johnson, 1999). The variability of the factors and measuring and collecting all the information of every corner of the land is not actually possible.

This is not just the size of the catchment that leads to high variability of the parameters. Even in small catchments, parameterizing the variability of soil-water relationships is crucial in achieving accurate simulations, as even small variations can impact the prevalence of different hydrological processes and alter outputs (Flores *et al.*, 2021). Therefore, model selection comes to the importance according to data availability and resolution (Kumari *et al.*, 2021).

- *Challenges with rainfall measurements*

In large catchments the location of rain gauges has a significant effects on rainfall-runoff modelling as a single rain gauge may fail in capturing a rainfall event which is representative for the whole catchment (Vaze *et al.*, 2011). Many studies conducted in extensive catchment show the importance of spatial variability of the rainfall as a factor in hydrological process of transforming rainfall to runoff (Obled, Wendling and Beven, 1994). The numerical experiments show that variation of rainfall in time and space significantly change the timing and peak discharge of runoff (Dawdy and Bergmann, 1969; Beven and Hornberger, 1982; Corradini and Singh, 1985; Krajewski *et al.*, 1991; Obled, Wendling and Beven, 1994).

Small catchments like urban catchments are the same where the time of concentration is shorter than vast natural catchments (Blanchet, Brunelle and Guillon, 1992; Obled, Wendling and Beven, 1994; Bruni *et al.*, 2015). In urban catchments, the larger portion of rainfall flows overland, therefore, spatial variation in rainfall records greatly impacts on the results in comparison with natural basins, where infiltration and soil type and land use make a balance among inputs (Obled, Wendling and Beven, 1994; Bruni *et al.*, 2015).

Radars, as new methods of measuring rainfall, also are affected by the accuracy of the rainfall records. In this technique, as studies show (Bruni *et al.*, 2015; Peleg *et al.*, 2018) the resolution and model scale come to be considered important. The basin data grid size and rainfall data resolution are the factors to play a role in the model response (Ogden and Julien, 1994). This is important since downscaling and upscaling is needed to prepare data for models and radar data is modified and adjusted by rain gauges. The resolution difference is considerably high, roughly a surface as big as 20 $cm^2$ for rain gauge and 1 km by 1 km for radar (Gires *et al.*, 2014)

- *Calibration*

Accessing to reliable and sufficient data for calibration is another challenge in finding the "close" to real runoff estimations. The majority of river basins globally lack sufficient gauging or have inadequate gauging (Sivapalan *et al.*, 2003; M. Hunger and P. Doll, 2008; Durga Rao, Shravya and Dadhwal, 2020). Therefore, data is not available all the time and everywhere. It is also reported that the number of flow gauges has dropped around the world and the stream flows are being monitored annually decreased by 75% (Sneeuw *et al.*, 2014). The lower control on rivers and streams is a result of the less monitoring stations available. The data show a decrease from around 8000 to near 2000 stations since before 1970 to around 2010 (Sneeuw *et al.*, 2014).

### 4.1.5. New horizons

Recent advances in technology have opened up new horizons in hydrological and hydraulic modelling of catchments. With advancements in satellite technology, it has become possible to collect high-quality data over large areas and at high spatial and temporal resolutions. This data can be used to develop more accurate and reliable models for predicting runoff and flood events in catchments.

For instance, during disappearing the gauges, satellites have been used for monitoring rivers (Koblinsky *et al.*, 1993). Satellite data enhances hydrology through diverse means, ranging from basic improvement of basin knowledge (ungauged) to precise augmentation of existing data for specific purposes (gauged) (Gleason and Durand, 2020). Early studies used remote sensing data to estimate river discharge, and later studies used a combination of satellite and ground-based data (Gleason and Durand, 2020).

The main use of satellites for river flow measuring includes the use of data from the TOPEX/Poseidon satellite mission in the 1990s (Chen *et al.*, 1998; Kouraev *et al.*, 2004), and the use of the Gravity Recovery and Climate Experiment (GRACE) satellite mission in the 2000s (Tapley *et al.*, 2004; Rowlands *et al.*, 2005).

Advantages of using satellite data include its ability to cover large areas and remote locations, while weak points include difficulties in accounting for variability in catchment characteristics and changing climate conditions. (Gleason and Durand, 2020).

The other key application of satellite technology in hydrological modelling is measuring soil moisture (Prashant K. Srivastava, 2016), which can provide valuable data for predicting runoff and flooding. Integrating this data with other hydrological and hydraulic parameters can lead to the development of more accurate models, making it a subject of significant attention. To collect soil moisture data from satellites, various products, datasets, and programs have been developed (Peng *et al.*, 2021). The Nimbus-7 satellite collected initial data in 1978 (Owe *et al.*, 1999; Peng *et al.*, 2021). Other institutions also started collecting data and producing soil moisture products. The Soil Moisture Active Passive (SMAP) mission (*SMAP, Soil Moisture Active Passive*, no date) is a satellite-based mission developed by NASA's Jet Propulsion Laboratory (JPL) to provide global measurements of soil moisture and its freeze-thaw state using both active and passive microwave sensors (Entekhabi *et al.*, 2010).

The main challenges in measuring soil moisture using satellites include the high spatial variability of soil moisture, the complexity of the emission processes, the lack of validation data sets, and the

heterogeneity of the land surface (Peng *et al.*, 2021). Additionally, traditional methodologies that attempted to relate remotely sensed data to observed or modelled soil moisture were highly empirical and failed to account for the properties that affect the microwave emission processes (Peng *et al.*, 2021).

Along with developing new and novel methods for measuring flow in rivers, the same development achieved in measuring rainfall. For instance, satellites are being used for climatological studies and monitoring rainfall since 1970s (Kidd, 2001) and developed with different methods, techniques and programs in 1980s (Atlas and Thiele, 1981; Levizzani, Vincenzo and Bauer, Peter and Turk, 2007; Kidd and Huffman, 2011b). Satellite-based rainfall estimates can provide valuable information on the spatial and temporal distribution of rainfall in a catchment, which is critical for modelling runoff. Various satellite-based precipitation products have been developed in recent years, such as the Tropical Rainfall Measuring Mission (TRMM) (*TRMM Comes to an End after 17 Years | NASA Global Precipitation Measurement Mission*, no date; *TRMM: Tropical Rainfall Measuring Mission | Climate Data Guide*, no date) which replaced with the Global Precipitation Measurement (GPM) mission (Hou *et al.*, 2014; Huffman, 2022; *GPM, NASA Global Precipitation Measurement Mission*, 2023). These products use various techniques, such as passive and active microwave sensors and infrared sensors (Kidd *et al.*, 2003), to estimate precipitation over large areas.

The use of big data and machine learning has also been gaining popularity in hydrological and hydraulic modelling. These techniques can be used to process and analyse large amounts of data, which can lead to more precise and reliable models. By training machine learning models on historical data, it is possible to predict future hydrological and hydraulic events with greater accuracy.

Another emerging technology is the use of commercial microwave links for measuring rainfall. These links are typically used for telecommunications, but they can also be used to measure the attenuation of microwave signals caused by rainfall (Messer, Zinevich and Alpert, 2006; Messer, 2007; Leijnse, Uijlenhoet and Berne, 2010b; Overeem, Leijnse and Uijlenhoet, 2011). This allows for real-time measurement of rainfall at high spatial and temporal resolutions, which can be very useful for hydrological and hydraulic modelling.

Overall, these new technologies are providing researchers and practitioners with more tools to accurately model catchments and predict hydrological and hydraulic events. With the continued development of these technologies, it is likely that we will see even more accurate and reliable models in the future.

The main advantages and disadvantages of using satellites for measuring rainfall and utilizing models can be summarized as follows: (Frezghi and Smithers, 2008; Kucera *et al.*, 2013; Hou *et al.*, 2014; Trenberth and Asrar, 2014):

Advantages:

- Satellite-based rainfall estimates provide global coverage, including remote and inaccessible regions.
- They can provide continuous data, which is useful for monitoring and predicting rainfall patterns.
- Satellites can provide data in real-time, which can be used for flood forecasting and early warning systems.
- They are relatively cost-effective compared to traditional methods such as rain gauges.

Disadvantages:

- Satellite estimates can have errors, especially in areas with complex terrain, high variability, or low rainfall rates.

- The accuracy of satellite estimates may vary depending on the type of rainfall, such as convective or stratiform. They may not capture certain types of precipitation, such as light rainfall or snow, as effectively as ground-based instruments.
- The spatial and temporal resolution of satellite estimates may not be high enough for certain applications, such as hydrological modelling in small catchments.
- satellite-based rainfall data can be affected by atmospheric conditions, such as cloud cover and water vapor, which can cause further inaccuracies.
- Calibrating and validating satellite estimates can be difficult. The results should be verified against other independent and reliable records, such as ground-based measurements. However, such records may not be available in some regions.

While radars have been used for decades, microwave links are the other tools to measure the intensity of rainfall.

### 4.1.6. Commercial Microwave Links as rain gauges

Rainfall-induced attenuation affecting microwave signals in radar systems has been recognized since World War II (Crane, 1975). This phenomenon causes attenuation or scattering of microwave signals, influencing their propagation (Lin and Ishimaru, 1971; Ishimaru and Cheung, 1980b; Mishchenko, Hovenier and Travis, 2000), which can be measured and used to estimate rainfall intensity (Le-Wei Li *et al.*, 1995).

Commercial Microwave Links (CMLs) are increasingly used for wireless communications and have shown promise in estimating rainfall intensity. This innovative approach has been successfully applied in various studies across different regions.(Leijnse, Uijlenhoet and Stricker, 2007a, 2007b, 2008a; Overeem, Buishand and Holleman, 2008; Zinevich, Messer and Alpert, 2009; van de Beek *et al.*, 2012; Fenicia *et al.*, 2012; Overeem *et al.*, 2013; Liberman *et al.*, 2014; Martin Fencl *et al.*, 2015b; Brauer *et al.*, 2016; Overeem, Leijnse and Uijlenhoet, 2016b; De Vos *et al.*, 2017; Ostrometzky *et al.*, 2017; van Leth *et al.*, 2017; Fencl *et al.*, 2017, 2020; Rios Gaona *et al.*, 2018; Song *et al.*, 2019a; Graf *et al.*, 2020).

Microwave links are prevalent in urban and suburban areas, providing an opportunity for rainfall measurements. The technology offers a cost-effective alternative to traditional rain gauge networks, particularly in remote or inaccessible areas. (Zinevich, Alpert and Messer, 2008; Gosset *et al.*, 2015). CMLs provide higher temporal and spatial resolution, offering non-point data at ground level that is less sensitive to wind conditions.

The application of CMLs as rain gauges is a fast and cost-effective method, making it suitable for early flood warning systems (Eshel *et al.*, 2017; Lian *et al.*, 2022).

### 4.1.7. The application of rainfall measurement in flood warning systems

Early flood warning systems are used to detect and alert communities of imminent flooding, allowing them to take necessary precautions and minimize damage. There are several types of early flood warning systems, including:

a) Hydrological based systems: These systems use data from rainfall and river level sensors, as well as weather forecasts, to monitor potential flooding (Adriana Maria Erazo Chica, 2017). They are particularly useful in areas with reliable and continuous monitoring of water levels.
b) Meteorological based systems: These systems use weather forecasts, satellite imagery, and radar data to predict areas at risk of flooding. They are particularly useful in areas with a high frequency of flash floods caused by intense rainfall (Henao Salgado and Zambrano Nájera, 2022).
c) Remote sensing based systems: These systems use satellite data and aerial imagery to monitor changes in land cover and water levels, which can indicate potential flooding. (Wania *et al.*, 2021)

d) Community-based systems: These systems rely on the observations and reports of local communities, which can provide valuable information on ground conditions and potential flooding (Pradhan *et al.*, 2016).
e) Hybrid systems: These systems combine multiple types of flood warning systems to provide a comprehensive approach to flood prediction and warning (Li and Willems, 2020; Wannachai *et al.*, 2022).

The choice of the most appropriate flood warning system for a particular location depends on several factors, including the nature of the floods, the available infrastructure and technology, and the needs and capacity of the local community. However, all the above-mentioned systems rely on the rainfall measurement and its accuracy.

On the other hand, hydrological networks in river basins are insufficiently covered and lack backup equipment (Perera *et al.*, 2019) and nearly half of the participants reported that their forecasting models are not sophisticated or precise enough to generate dependable predictions (Perera *et al.*, 2019).

Therefore, the unpredictability and uncertainty of rainfall and urban drainage processes make nowcasting and forecasting challenging due to rainfall's spatiotemporal heterogeneity, complex system operation, and nonlinear response of urban catchments. Flood probability nowcasting relies on ensemble rainfall nowcasts in urban inundation models, but there is a need for probabilistic methods to consider uncertainties in the urban system and inundation models. (Li and Willems, 2020)

## 4.2. Goals

This paper aimed to explore the correlation between microwave attenuation and flash floods in urban catchments to explore a more direct relationship between the attenuation and runoff in a catchment.

Due to the challenges in accurately measuring rainfall in terms of spatiotemporal distribution, the goal is to find a solution that is less reliant on rainfall measurement accuracy. This could involve a new method or hybrid model that incorporates additional tools or parameters to improve flood forecasting and nowcasting methods.

## 4.3. Proposed method

The process of conventional and suggested runoff calculations begins with collecting the data from rain gauges, microwave links, and flow stations. The methods involve transferring the attenuation of microwave link to rainfall rate, and then transferring rainfall to runoff.

Figure 4-1 illustrates the conceptual framework of the methodology implemented in this study, highlighting its differentiation from conventional flow estimation methods. In conventional approaches, the attenuation-rainfall power law is typically employed to compute CML-based rainfall by seeking the optimal correlation between measured gauge rainfall and calculated rainfall through CMLs. Consequently, these methods optimise the functions and coefficients of the attenuation-rainfall relationship to align the calculated rainfall with gauge-recorded rainfall. Subsequently, the product of this correlation is integrated into rainfall-runoff models to estimate flow.

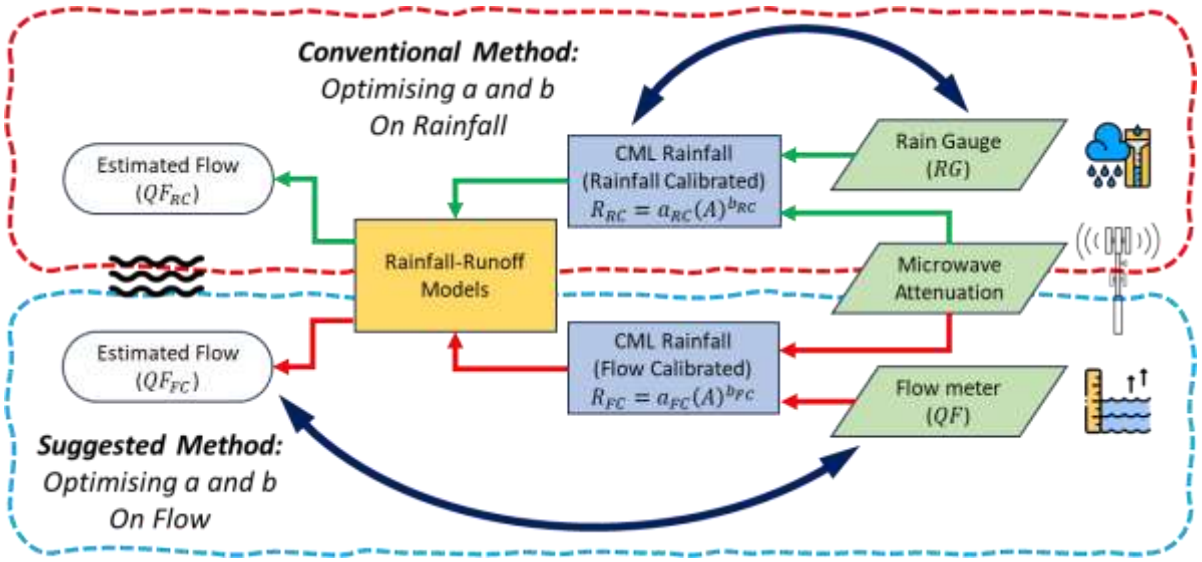


*Figure 4-1- The schematic of the research goals and process, conventional CML approaches (up), and proposed approach (down)*

In contrast, the novel approach optimises the coefficients of the power law to maximise the alignment of the correlation between attenuation and flow. This optimisation introduces the Flow Calibrated CML Rainfall ($R_{FC}$) with coefficient calibrated to flow ($a_{FC}$, $A_{a_{FC}}$, and $b_{FC}$). Consequently, this new method bypasses the rain gauge, obtaining the catchment's total water yield from the attenuation measurements to avoid the corresponding errors in estimating rainfall depth.

## 4.4. Materials

The area of study is located at the east of Melbourne, where Yarra is the major river flowing from east to west. Spanning 242 kilometres, the Yarra river supplies 70 percent of drinking water in Melbourne (Melbourne Water, 2022b). The catchment with an area of 4110 km$^2$, originates from the southern slopes of the Great Dividing Range and runs through the Yarra Valley and metropolitan Melbourne before reaching Port Phillip Bay. The forested upstream catchment area plays a crucial role as a primary source of urban water supply for the region (*National Water Account*, 2015).

Bunyip river catchment, 4078 km$^2$, is situated to the south and east of Port Phillip Bay, covering the southeastern suburbs of Melbourne and the Mornington Peninsula. It ranges from the eastern highlands in the north to Western Port Bay in the south. As it is described by the Australia Bureau of Meteorology (*National Water Account*, 2015), Yallock, Toomuc, Cardinia, and Dandenong creeks, as well as the Lang Lang, Tarago, and Bunyip rivers, are all part of the catchment. The length of Dandenong Creek is about 53 kilometres flows from Dandenong Range to Port Philip Bay and its catchment covers 881.61 km$^2$, is one of the sub-catchments of the Bunyip river basin and encompasses a part of the basins examined in this study (*National Water Account*, 2015).

The study catchments are sub-catchments of the Yarra and Bunyip catchments. The sub-catchment areas vary in size, ranging from 2.2 km² to 232.6 km², as illustrated in Figure 4-2.

The flow patterns of the rivers reflect the local rainfall trends, which remain relatively stable throughout the year but experience a slight increase during the winter and early spring months spring (*National Water Account*, 2015).

The rain gauges are either at the outlet or in the vicinity of the outlet. The location of 15 flow stations and 12 rain gauges within the study area are shown in Figure 4-2. The data of rain gauges and flow meters are available from Melbourne Water via:
https://www.melbournewater.com.au/water-and-environment/water-management/rainfall-and-

river-levels#/ (Melbourne Water, 2023). Automatic rain gauges record the amount and time of rainfall and transmit them every hour (Melbourne Water, 2022a).

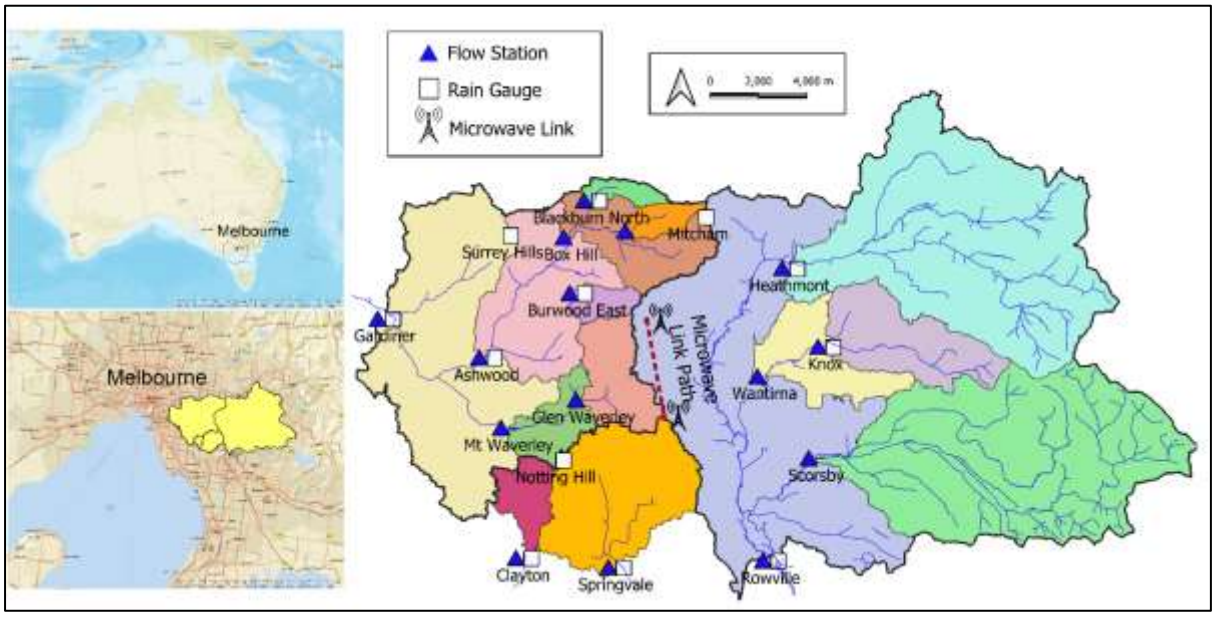


*Figure 4-2- Catchments in the study area and the location of flow stations, rain gauges and microwave link*

The data on power attenuation in a microwave link were obtained from a rainfall retrieval study in Melbourne (Pudashine *et al.*, 2020). The microwave link was a 22.715 GHz and 3.79 Km pathway between transmitters and receivers located in the Rowville catchment. The maximum, minimum, and average received powers are stored every 15 minutes in this link. Calculations were conducted with a uniform data interval of one hour to ensure synchronisation between microwave links, flow, and rain data within Equation 1-2. However, for the rainfall-runoff model, a longer time step is used to account for lag time and time of concentration in the catchments. Opting for a daily interval proves to be sufficiently extensive to capture rainfall variations at the catchment outlet. Thus, all calculations have been aggregated on a daily basis for a meaningful comparison of model results.

## 4.5. Methodology

### 4.5.1. Quick flow separation

In this study, quick flow was used to establish a correlation with rainfall and attenuation, instead of the total flow in streams. By separating the base flow from the total flow, the method focuses on the direct impact of rainfall on stream flow, excluding the groundwater impact.

The base flow was extracted using Eckhardt's two-parameter recursive digital filter method (Eckhardt, 2005) as a simple model with the minimum number of parameters. The coefficients of this filter are calculated in R, using the FlowScreen package (*CRAN - Package FlowScreen*, 2019). As an example, the base flows and the extracted quick flows in the Ashwood catchment are illustrated in Figure 4-3 for four different periods.

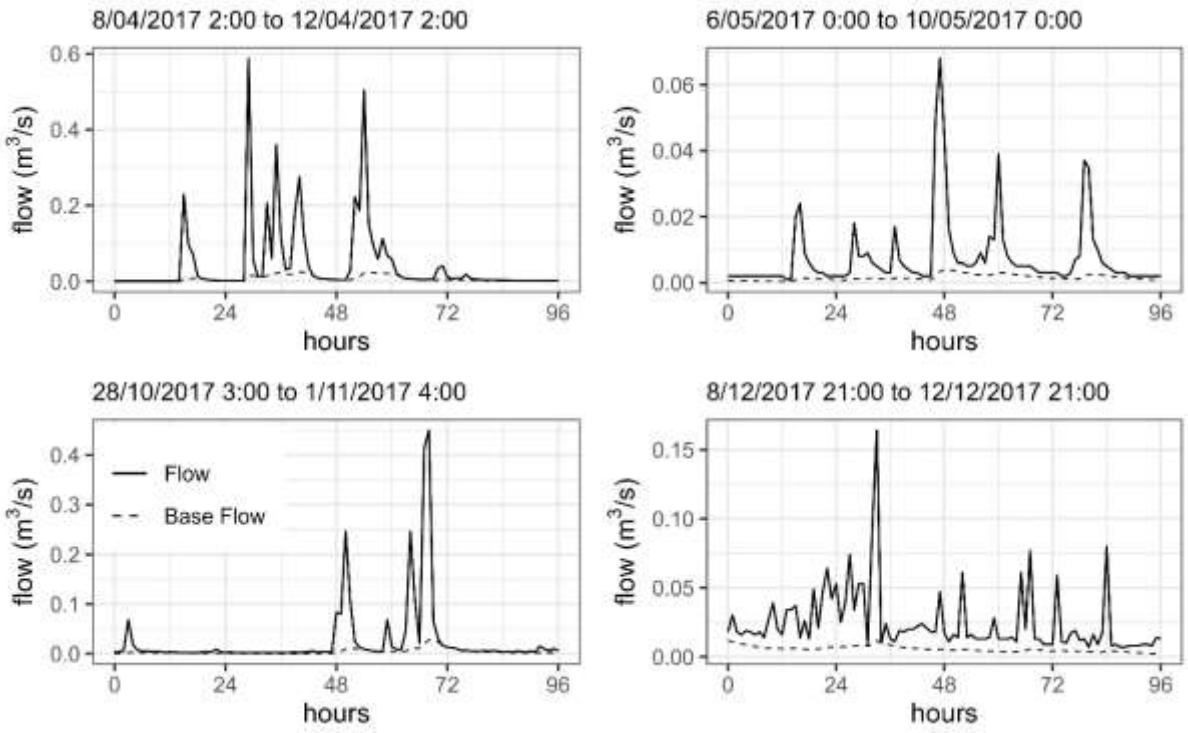


*Figure 4-3- Base flow extraction at four different periods in the Ashwood catchment*

### 4.5.2. Attenuation and rainfall calculations

The attenuation ($A$) represents how much the power of a microwave signal decreases during rainfall events. However, the received power is not stable and fluctuates even in dry weather. Therefore, it is required to establish a reference level for the received signal. The difference between this reference level and the received signal at any time is the attenuation.

An investigated commonly employed approach to establish a reference signal level ($P_{ref}$) is utilising the received signal level during dry periods within the previous 24 hours, typically using the median value (Overeem, Leijnse and Uijlenhoet, 2011, 2016d; van Leth *et al.*, 2017). The utilisation of a low-pass filter in CML-rainfall calculations is another approach to extract the base power in microwave signals, as a constant baseline may not reflect the actual conditions realistically (Fenicia *et al.*, 2012). Consequently, a 6-hour moving average filter is used for the received signal level to define the reference power of the microwave signal which studied in the previous chapter. This moving average spanned a duration of 3 hours prior to and 3 hours following the specific time step.

On the other hand, raindrops on the surface of the antenna have been identified as a significant source of error in rainfall measurement, leading to an overestimation of rainfall during dry periods (Kharadly and Ross, 2001; Minda and Nakamura, 2005; Leijnse, Uijlenhoet and Stricker, 2007b). Several mathematical-statistical methods have been developed to mitigate the impact of wet antenna effects (Leijnse, Uijlenhoet and Stricker, 2008c; Zinevich, Messer and Alpert, 2010b). These methods require additional information on characteristics such as raindrop properties, antenna specifications, frequency, and calibration of specific parameters.

One of the suggested methods used in this study is correcting the attenuation by optimising the microwave link and obtaining a fixed correction parameter to deduct from the base attenuation (Overeem, Leijnse and Uijlenhoet, 2016d):

$$R = a(A - A_a)^b \qquad \text{Equation 4-1}$$

where $A_a$ is the wet antenna correction factor.

Even after applying the reference power level and wet antenna effect, there are still some dry periods in which attenuation shows rainfall rates. This is attributed to the imperfect validation of $P_{ref}$ and $A_a$. Therefore, by wet-dry classification of the periods, all the attenuation values in dry periods are considered zero rainfall.

Wet-dry classification is a useful auxiliary technique that incorporates data from rain gauges or other microwave links to determine whether a decrease in power is caused by precipitation or persists due to the wet antenna effects even after rainfall has ceased. Several methods have been investigated to detect wet-dry periods using CMLs directly. For example, one approach involves employing long short-term memory units (Habi and Messer, 2018) for classification, achieving an accuracy rate of up to 90%. Another method is utilising the nearby link approach (Overeem, Leijnse and Uijlenhoet, 2016d), which necessitates the comparison of multiple surrounding CMLs. Utilising the existing infrastructure, such as rain radars and gauges is another approach to wet-dry classification (Upton *et al.*, 2005; Overeem, Leijnse and Uijlenhoet, 2011).

In this study, the attenuation data consists of power level records from a single microwave link. Consequently, rain gauge data are used to classify the time steps as wet or dry. This classification method enables the maximum utilisation of the existing operational instruments and allows for subsequent accuracy adjustments by incorporating other tools, such as CMLs.

### 4.5.3. Performance evaluation

Root Mean Square Error ($RMSE$) is used in the optimisation process and minimises the errors of the simulating models. (Moriasi *et al.*, 2007):

$$RMSE = \sqrt{\frac{\sum(s_i - o_i)^2}{n}} \qquad \text{Equation 4-2}$$

where $o_i$ and $s_i$ are observed and simulated records and $n$ is the number of records.

The other statistical indicators were utilised to evaluate the accuracy of the prediction models. The first indicator is Nash-Sutcliffe efficiency ($NSE$) (Nash and Sutcliffe, 1970), which is widely used to evaluate the hydrological models' performances (Knoben, Freer and Woods, 2019; Schwemmle, Demand and Weiler, 2021; Duc and Sawada, 2023):

$$NSE = 1 - \frac{\sum(o_i - s_i)^2}{\sum(o_i - \mu_o)^2} \qquad \text{Equation 4-3}$$

where $\mu_o$ is the observed mean.

A more commonly used indicator in recent times is the Kling-Gupta Efficiency (Gupta *et al.*, 2009):

$$KGE = 1 - \sqrt{(r-1)^2 + (a-1)^2 + (b-1)^2} \qquad \text{Equation 4-4}$$

where $r$ shows the linear correlation coefficient linking the simulated and observed records. $a$ represents the relative variability, denoting the ratio of the standard deviation of simulated flows to that of observed flows. Additionally, $b$ signifies the ratio of the mean of simulated flows to the mean of observed flows. While NSE primarily assesses the matching of observed and simulated hydrographs, KGE incorporates additional dimensions such as the correlation coefficient and variability of the observed and simulated data. This inclusion offers a more holistic understanding of model performance by considering not only the timing and magnitude of simulated flows but also their variability and pattern.

### 4.5.4. Stablishing an attenuation-rainfall-quickflow model

In this study two methods were used to stablish a relation between attenuation, rainfall and quickflow. The first procedure is using a linear relationship each two parameters without including the other impacting factors. The next process is using a rainfall-runoff model which includes a few parameters, more than just rainfall.

### 4.5.5. Investigating linear relationships between Parameters

In this section the process of investigation of the proposed model will be described versus the conventional method. These two procedures will use a linear relationship between each of two factors of attenuation-rainfall-runoff. The linear regressions utilised as the rainfall was found to be the most important factor in the rainfall-runoff process (Dunkerley, 2012; Guan et al., 2016; Ran et al., 2019; Xue and Gavin, 2008) This addresses the key question: which factor holds a greater impact on runoff, CML attenuation, or rainfall recorded by rain gauges.

The difference between the two method is the calibration of coefficients. In the conventional method, the coefficients of the power law, Equation 4-1, is calibrated with rain gauges while in the proposed method they are calibrated with flow stations.

Before describing these two models, another relationship is explored to evaluate the quality of predicting runoff with using only one parameter of rainfall which is measured by rain gauges.

- *Relationship between Rainfall and Qickflow*

A benchmark was initially established by performing linear regressions between the measured rainfall ($RG$) and measured quick flow ($QF$). Figure 4-4 (a) shows this relationship in the Ashwood catchment, as a sample, which creates a linear equation as:

$$QF_{RG} = c(RG) + d \qquad \text{Equation 4-5}$$

where $RG$ is the rainfall depth, measured by rain gauge and $QF_{RG}$ is the quick flow calculated from the linear regression and $c$ and $d$ are constants.

Then we used this formula to predict quick flow ($QF$). The accuracy of this prediction is measured using RMSE, NSE, and KGE which compare the measured quick flow ($QF$) and the simulated quick flow ($QF_{RG}$). Figure 4-4(b) shows the similarity of simulated quick flow ($QF_{RG}$) and the measured quick flow ($QF$).

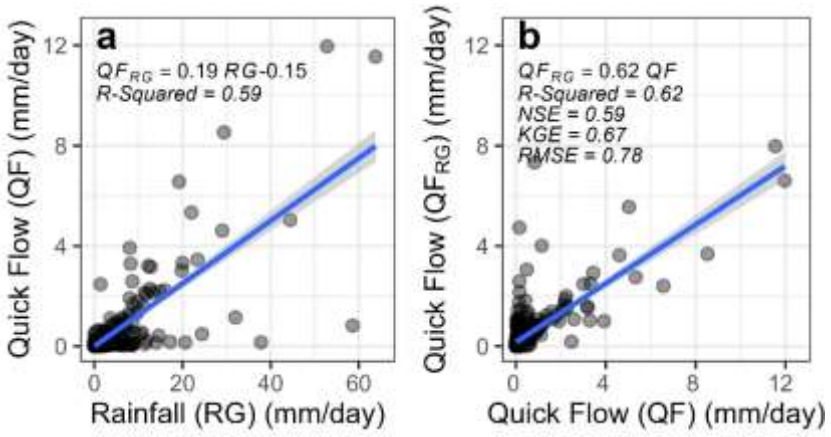


*Figure 4-4- Regressions and statistical factors for the measured values for flow (QF) and rain gauge (RG) in the Ashwood catchment (a) and quality of the regression between the calculated quickflow ($QF_{RG}$) and the measure quickflow (QF) (b)*

The next two methods (conventional and proposed CML methods), will use the same steps as described above, however, they will have one initial step of calculating ranfall from attenuation.

- *Conventional Attenuation-Rainfall-Quickflow Relationship*

In this method, rainfall is calculated from attenuation by using Equation 4-1. Similar to the existing methods of calculating rainfall from CML attenuation, the values for the coefficients of this formula were obtained by calibrating the equation to the measured rainfall from rain gauges.

The processes in this method are as below:

i. Calculating rainfall from attenuation with:

$$R_{RC} = a_{RC}\left(A - A_{a_{RC}}\right)^{b_{RC}} \qquad \text{Equation 4-6}$$

Where $a_{RC}$, $b_{RC}$ and $A_{a_{RC}}$ are the constants of Equation 4-1, calibrated by rainfall and $R_{RC}$ is the rainfall depth from CML method when it is calibrated with measured rainfall in rain gauges.

Figure 4-5 (a) shows the quality of this calibration by comparing the simulated rainfall ($R_{RC}$) and measured rainfall ($RG$) in Ashwood rain gauge.

ii. Stablishing a linear regression between the calculated rainfall ($R_{RC}$) and the measured quickflow ($QF$) (Figure 4-5 (b)).

$$QF_{RC} = e(R_{RC}) + f \qquad \text{Equation 4-7}$$

where $QF_{RC}$ is the quick flow calculated from CML, when the rainfall estimation is calibrated to rain gauge depth. $e$ and $f$ are constants of the linear equation.

iii. Calculate quickflow ($QF_{RC}$) from this linear equation.
iv. Control the quality of calculated quickflow ($QF_{RC}$) by comparing it to the measured quickflow ($QF$) (Figure 4-5 (c)).

The coefficients of the Equation 4-6 in the first step are selected to minimise RMSE in estimating quickflow in the last step.

Comparing Figure 4-5 (b) with Figure 4-4(a) reveals that the measured quick flow has a stronger relationship with CML rainfall than rain gauges, improving the R-squared from 0.59 to 0.78. Significant improvements in quick flow prediction in the Ashwood catchment are also evident in Figure 4-5 (c) compared to Figure 4-4 (b). These figures reveal that with a linear relationship between rainfall and quickflow, CML rainfall was more successful in predicting quickflow compared to using rain gauges data. Comparing two methods, NSE increased from 0.59 to 0.78, KGE from 0.67 to 0.84, and RMSE decreased from 0.78 to 0.56 mm/day, showcasing the benefits of the conventional CML method.

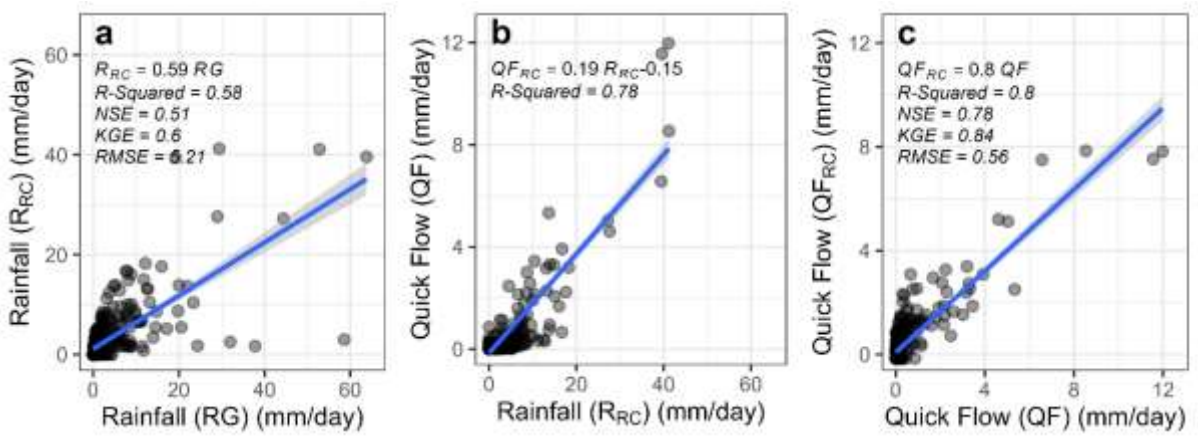


*Figure 4-5- Correlations and statistical factors for the conventional CML method in Ashwood catchment flow and rain gauge*

- *Suggested Attenuation-Rainfall-Quickflow Relationship*

The new suggested novel approach retains the core relationships and correlations from conventional methods. However, a significant change is how to calibrate CML rainfall depth, now using measured quick flow rates instead of rain gauge measurements.

This innovative approach guarantees a direct and robust correlation between attenuation and quick flow. Since the absolute magnitude of the calculated rainfall is no longer the primary focus, the constants within the power law equations gain flexibility, allowing them to deviate from rain gauge measurements.

Addressing the raw attenuation of the signal power necessitates adjustments for reference power and accounting for wet-dry periods. Consequently, employing the same formula to apply these corrections in the new method, transforms attenuation measurements into a new estimate of rainfall depth. This recalibrated rainfall depth becomes a critical component in the series of correlations and regressions that ultimately link attenuation to quick flow. It is important to note that the calculated rainfall values generated by this new method will differ from both rain gauge measurements and conventional CML rainfall estimates.

In addition, the novel procedure does not involve a sequential series of equations and regressions; instead, it solves them simultaneously to minimize the RMSE of the quick flow simulation.

Therefore, the process in the suggested method is as below with a graphical presentation as per Figure 4-6 which shows the relationships and formulas for a sample flow and rain gauge at Ashwood catchment:

i. Calculating rainfall from attenuation with:

$$R_{FC} = a_{FC}\left(A - A_{a_{FC}}\right)^{b_{FC}} \qquad \text{Equation 4-8}$$

where $a_{FC}$, $b_{FC}$ and $A_{a_{FC}}$ are the constants of Equation 4-1, calibrated by quick flow and $R_{FC}$ is the rainfall depth from CML method when it is calibrated with quick flow.

Quality of this estimation is shown in Figure 4-6 (a).

ii. Stablishing a linear regression between the calculated rainfall ($R_{FC}$) and the measured quickflow ($QF$) (Figure 4-6 (b)).

$$QF_{FC} = g(R_{FC}) + h \qquad \text{Equation 4-9}$$

where $QF_{FC}$ is flow calibrated quick flow, which means the quick flow calculated from the CML method when the CML rainfall is calibrated with quick flow. $g$ and $h$ are constants of the linear equation.

iii. Calculate quickflow from this linear equation.
iv. Control the quality of calculated quickflow ($QF_{FC}$) by comparing it to the measured quickflow ($QF$) (Figure 4-6 (c)).

The coefficients of the Equation 4-8 in the first step are selected to minimise RMSE in estimating quickflow in the last step.

Figure 4-6 (a) is the relation between measured rainfall and CML rainfall with the new flow calibration method in the Ashwood catchment. As the equation and R-squared value show, the correlation is weaker than Figure 4-5 (a) when CML rainfall was calibrated by rainfall. However, Figure 4-6 (b) and (c) show slightly stronger correlations between the new CML rainfall and measured quick flow, as well as between the new CML quick flow and the measured quick flow in the new method.

Using the flow meter and rain gauge in the Ashwood catchment, R-squared of the linear regression between the new flow calibrated CML rainfall ($R_{FC}$) and the measured quick flow ($QF$) is 0.84 compared to 0.78 for the conventional rain calibrated CML rainfall ($R_{RC}$) and the measured quick

flow ($QF$). In addition, the RMSE of the quick flow simulation achieved 0.48 mm/day in the new method, compared to 0.56 mm/day in the conventional method and 0.78 mm/day when simulating by rain gauge linear regression.

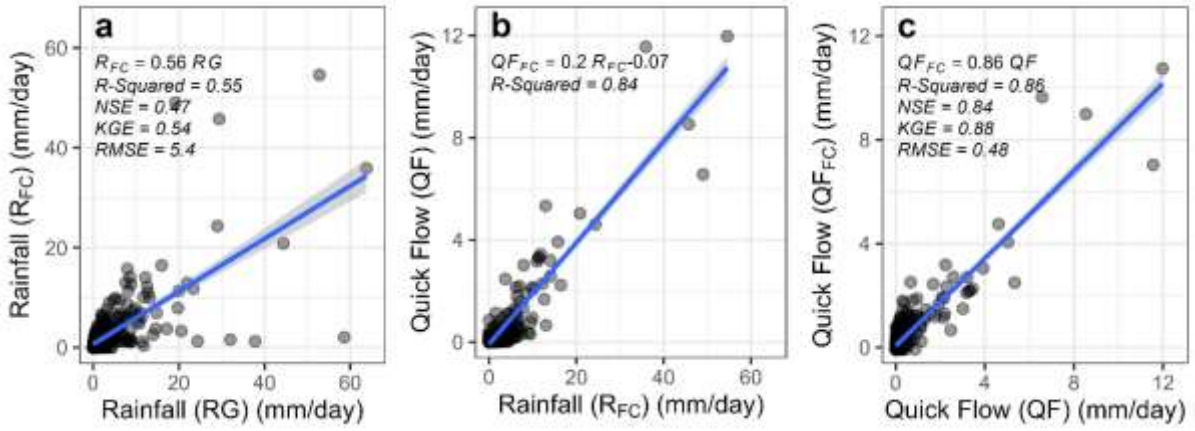


*Figure 4-6- Correlations and statistical factors for the new suggested CML method in the Ashwood catchment flow and rain gauge*

### 4.5.6. Rainfall-runoff model simulations

A simple linear relationship between rainfall and runoff may not adequately capture the complexity of natural hydrological processes. To evaluate the performance of the proposed method using a more robust and physically-based approach, a rainfall-runoff model is employed. This model estimates quickflow not only from rainfall inputs but also incorporates additional parameters that reflect catchment characteristics and conditions.

In this section, rainfall estimates derived from both the conventional and the proposed CML-based methods are used as inputs to the rainfall-runoff model. The resulting quickflow simulations are then compared to assess which rainfall estimation method provides more accurate predictions within the modelling framework. The results of the model then compared to the linear estimations.

In this study, Modèle du Génie Rural (Perrin, Michel and Andréassian, 2003) (the Rural Genius model in British (Martínez-Sifuentes et al., 2023)) is used to estimate quickflow. This model was developed by the French Research Institute for Agricultural and Environmental Engineering for annual (GR1A), monthly (GR2M) and daily (GR4J) data time steps (Martínez-Sifuentes et al., 2023). These are aggregated models suitable for diverse time intervals, spanning from hourly to yearly. It is necessary to calibrate their conceptual parameters based on observed streamflow data (Coron *et al.*, 2017). These models were used in different research and showed satisfying results in large catchments, as big as hundreds of km$^2$ (Mouelhi *et al.*, 2006; Dezetter *et al.*, 2008; Rwasoka *et al.*, 2014; Belarbi *et al.*, 2016; Sezen, Bezak and Šraj, 2018; Ouhamdouch *et al.*, 2020; Ditthakit *et al.*, 2021; Yahiaoui *et al.*, 2022)

GR4J (Perrin, Michel and Andréassian, 2003) is a minimum parameter lumped empirical model (Edijatno and Michel, 1989; Edijatno, 1991; Edijatno *et al.*, 1999) which selected to simulate daily quick flow from two methods of conventional and suggested calibration of CML rainfall models.

GR4J uses the daily data of rainfall, precipitation, and flow. Despite its simplicity, the model demonstrated valuable performance on a dataset comprising 140 French catchments, vastly outperforming a linear model with 16 parameters (Edijatno *et al.*, 1999). Additionally, it has been compared with other hydrological models in different countries, consistently yielding favourable results (Perrin, Michel and Andréassian, 2003; Andréassian *et al.*, 2009).

airGR package (*CRAN - Package airGR*, no date) in R is used for simulating the rainfall-runoff model. This package was developed in INRAE (France) (*airGR: the INRAE GR Hydrological Models in a R Package*, 2023). According to the daily data, the model ran for GR4J function mode. In this study, 15 days were selected for warmup time, 6 months for calibration and 6 months for simulation. A sample output of the model for the rain gauge and flow meter in the Ashwood catchment is presented in Figure 4-7. The output graphs include the time series of rainfall, observed and simulated discharge, monthly rolling average of them, a cumulative probability graph of observed and simulated discharge and their scatterplot in log scale.

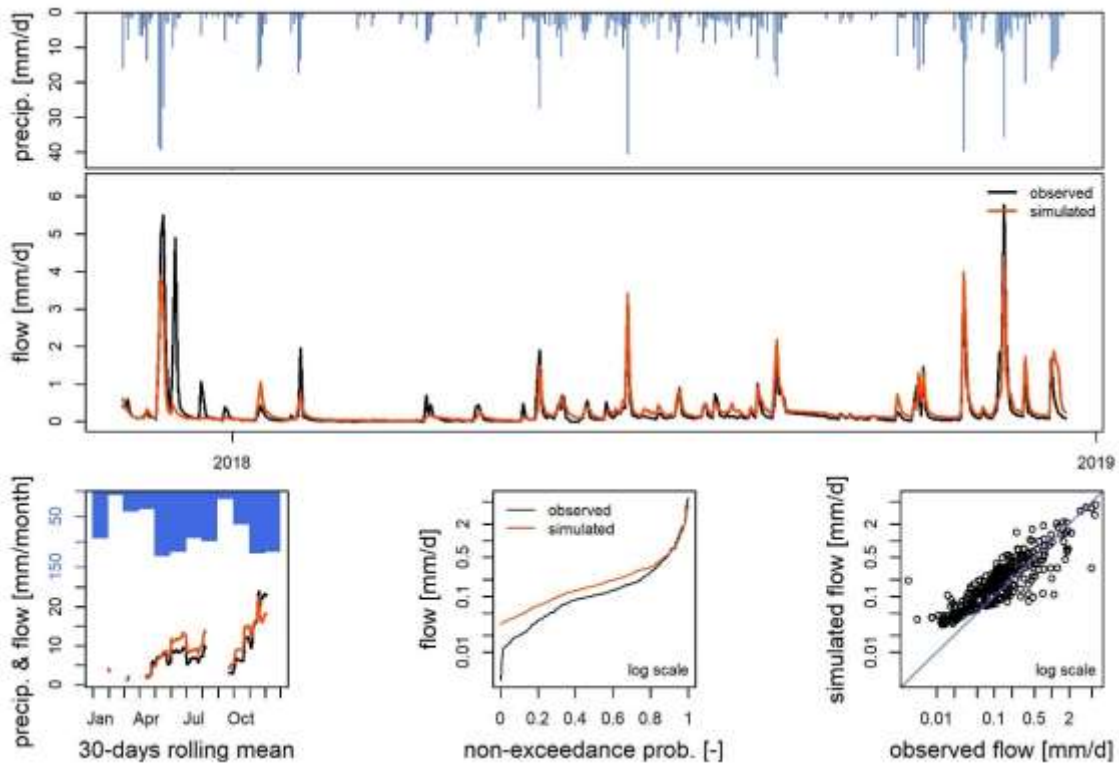


*Figure 4-7- Sample output of the GR4J model for the rain gauge and flow meter in the Ashwood catchment*

## 4.6. Results

### 4.6.1. Enhancement in regressions

All three described procedures were carried out for all 180 possible pairs of rainfall-quick flow. The rainfall-runoff pairs were investigated across 15 small catchments using 12 rain gauges and their locations are presented in Figure 4-2. Each flow-rainfall pair was individually evaluated to assess the impact of station locations and the spatial variation of rainfall. This analysis allowed for a detailed examination of the specific characteristics and influences at each location, providing valuable insights into the spatial dynamics of rainfall patterns and their corresponding effects on the flow.

The analysis of linear regressions reveals a strong correlation between rainfall-calibrated CML quick flow ($QF_{RC}$) and the measured quick flow ($QF$), with R-squared values reaching up to 0.81. Model performance, as indicated by NSE value, is also favourable, with values up to 0.81. Notably, the application and optimisation of the new model of flow calibration further improved these metrics, resulting in an NSE value of 0.87 by calculating flow-calibrated CML quick flow ($QF_{FC}$).

Figure 4-8 provides an overview of the NSE and KGE findings for the regression analysis of all stations. The flow stations are sorted by the NSE and KGE values of CML quick flow, calibrated by flow. Figure 4-8 (a) illustrates NSE values for predicting quick flow by correlating to rain depth from

rain gauges, represented by the white boxes, mostly hovering around 0.50. Utilising conventional CML rainfall significantly enhances NSE, as indicated by the green boxes. NSE increased by 4% on average reaching a maximum of 39% increase in one of the sub-catchments. Further improvement in NSE is achieved by optimising the constants of Equation 4-8 with the quick flow, resulting in the new suggested method of calibration. This optimisation leads to increased NSE for most of the flow-rain gauge pairs, presented with the blue boxes in Figure 4-8 (a), denoting the highest NSE values. The average NSE rose by an additional 6% on average and 23% in one of the catchments when using the new method, compared to the conventional CML model.

The same improvement observed in KGE values for the new method is presented in Figure 4-8 (b). KGE values increased by 8% on average and up to 24%, reaching a maximum equal to 0.63 in the new suggested method when compared to the conventional method.

The NSE and KGE values and the strength of the correlation in the conventional method are lower than the new suggested method in all 15 flow stations. However, CML rainfalls, neither the conventional nor the new method, were not a better predictor than rain gauge data in Blackburn, and Rowville catchments.

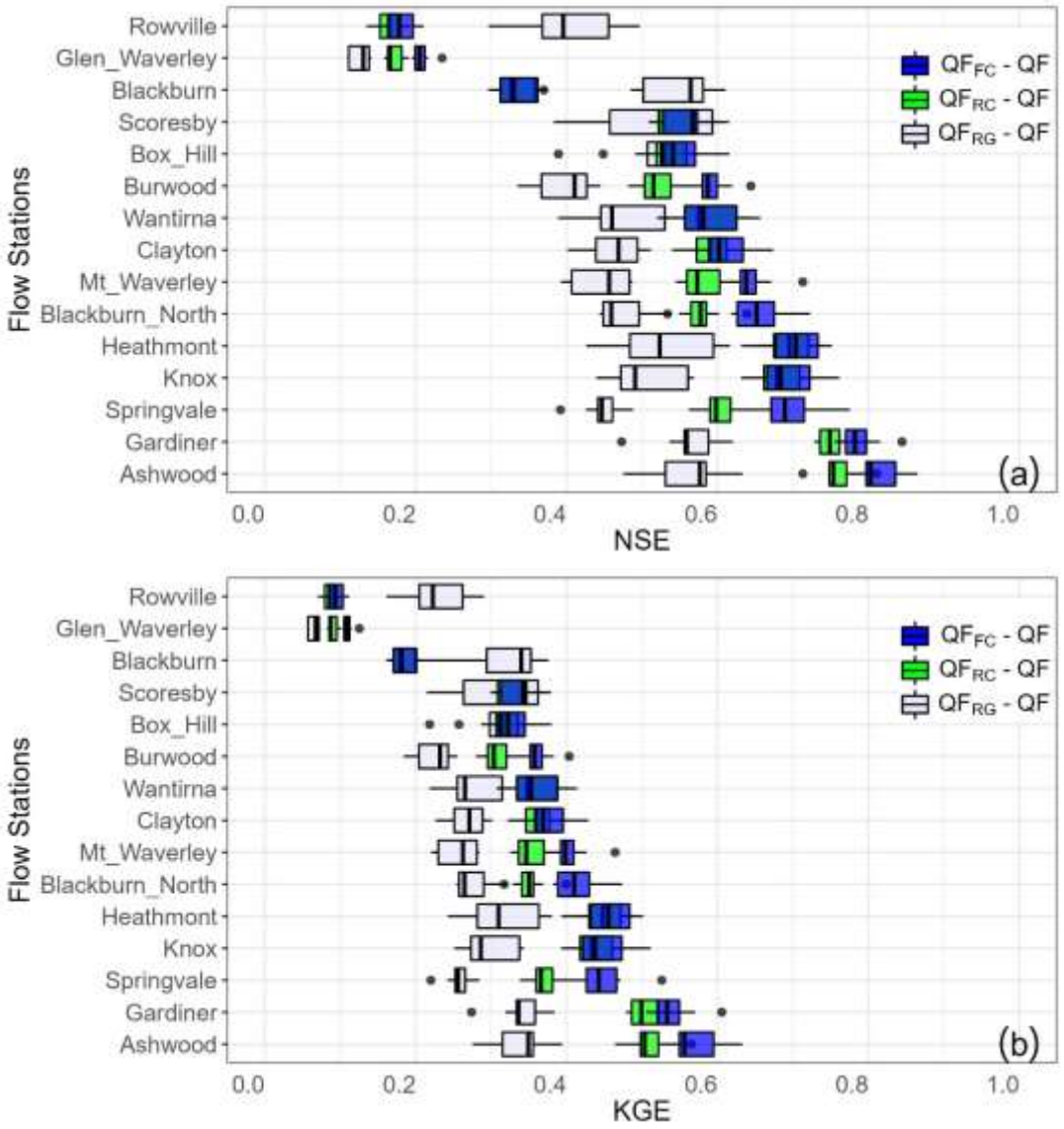


*Figure 4-8- (a) NSE and (b) KGE variations for quick flow estimation by regression in 15 flow stations when paired with each of 12 rain gauges.*

The other comparison is the R-squared values of the two models. The scatterplot in Figure 4-9 compares R-squared values of the CML quick flow, calibrated by flow ($QF_{FC}$), and the quick flow, predicted by the rain gauge ($QF_{RG}$). As the 1:1 line indicates, the R-squared of the CML model is higher than the simple rain gauge model. Each of the flow meters at the outlet of the catchments is presented with a different ellipse colour while each of them is paired with 12 rain gauges which are presented with points inside the ellipses. The points above the 1:1 line indicate a stronger relationship between the flow-calibrated CML quick flow and the measured quick flow with a higher R-squared value. Two areas for Blackburn and Rowville catchments under the 1:1 line indicate the unsatisfactory performance of the conventional CML model in these catchments. The limited and focused spread of the ellipses for each catchment reveals that the quality of the model performance is more related to the flow meter than the rain gauge location.

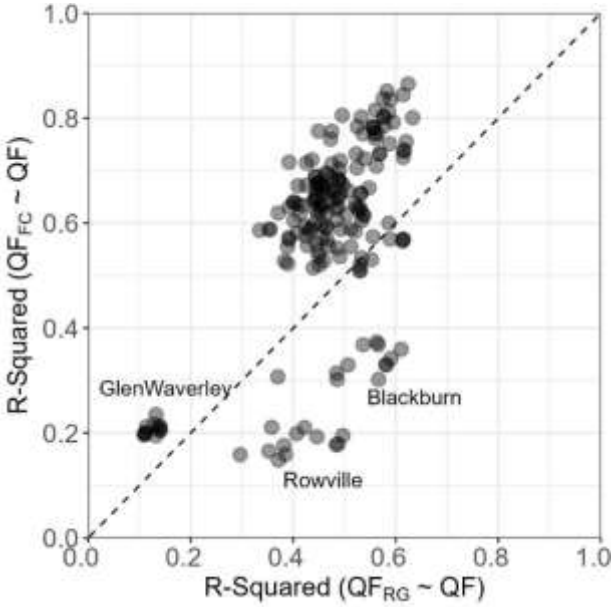


*Figure 4-9- Comparing R-squared using flow calibration approach versus using rain gauge data in 180 pairs of flow-rain gauges.*

The linear regression between attenuation and rainfall and the other regression between rainfall and runoff can be used to predict runoff. This is not a complete rainfall-runoff as it does not consider the nonlinearity of runoff prediction. However, these linear relationships can give a perspective of effectiveness of using attenuation as the main factor of calibration in a catchment. Figure 4-10 is a sample period of rainfall and flow prediction in Ashwood catchment and rain gauge.

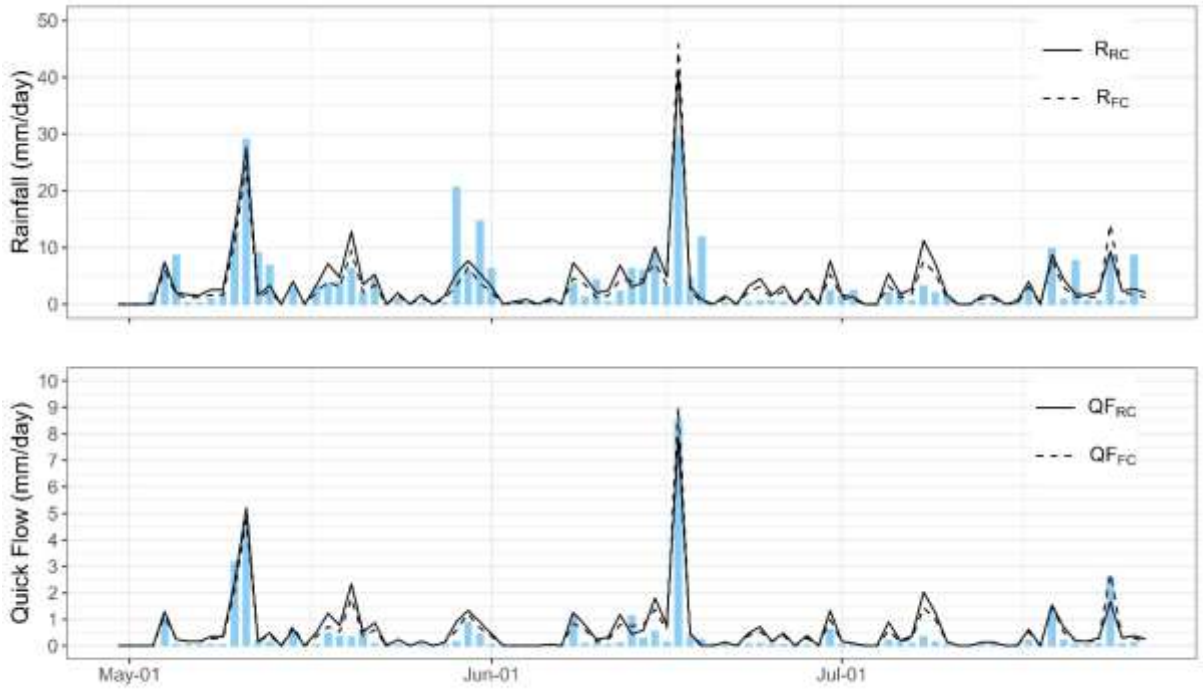


*Figure 4-10- Simulated rainfall and quick flow from linear regresions. sample period from Ashwood catchment and rain gauge.*

### 4.6.2. Enhancement in rainfall-runoff model

All 180 possible pairs of rain gauge-flow meters are used for modelling the quick flow from rainfall data. Therefore, the quick flow data from flow meters applied with three different sources of rainfall estimation: rain gauge measurements ($RG$), rainfall calibrated CML ($R_{RC}$), and flow calibrated CML ($R_{FC}$).

Comparable to the regression outcomes, the performance of the rainfall-runoff model is notably enhanced when relying on CML rainfall estimations and even more favourable results are achieved when the new suggested procedure is applied for calibrating CML rainfall using flow data.

NSE and KGE of the simulation for three methods of rainfall estimation are depicted in Figure 4-11 (a) and b. Consistent with the regression analysis, the Ashwood and Gardiner catchments exhibit the highest NSE values. Likewise, Rowville and Glen Waverley yield the lowest NSE factor. A maximum NSE value of 0.78 and KGE value of 0.86 were achieved in the new suggested method.

The variation of NSE in rain gauge-flow meter pairs was significantly high. The conventional CML model improved the NSE of simulation by 197% on average (green boxes versus white boxes in Figure 4-11 (a)). The new model showed an extra 50% enhancement which means a 25% improvement compared to the conventional model.

The KGE showed an average of 21% enhancement when the conventional CML model was used instead of rain gauges. Compared to the conventional model, simulating runoff improved by a further 4% when the new method was applied. A maximum of 34% higher KGE was achieved in one of the rain gauge-flow meter pairs.

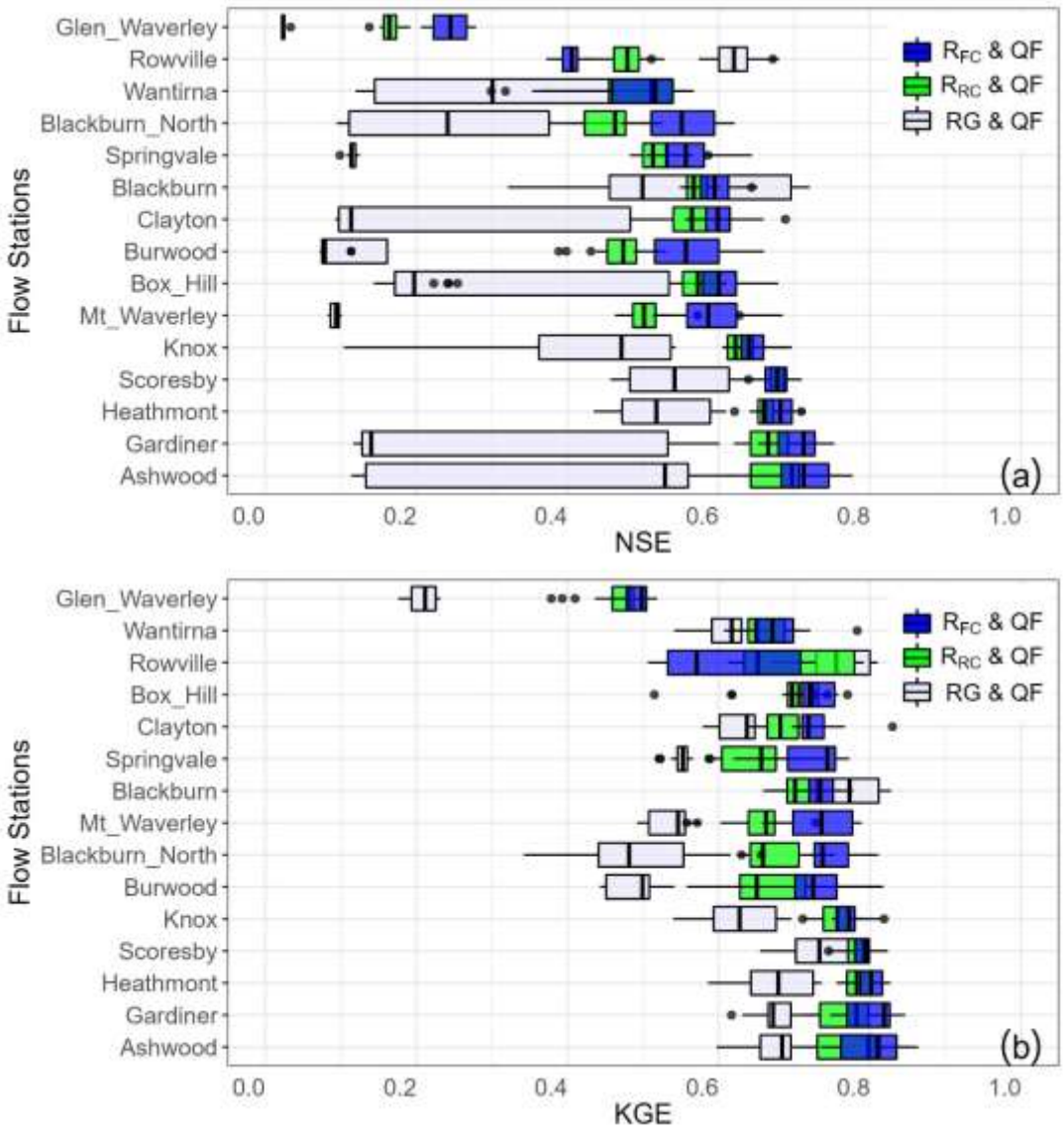


*Figure 4-11- (a) NSE and (b) KGE for rainfall-runoff models in 15 flow stations, when paired with each of 12 rain gauges.*

RMSE is the parameter used for optimisation which reflects the simulation's achieved through the utilisation of flow data for calibration. Figure 4-12 illustrates the variation of RMSE in modelling flow in each of the catchments with different approaches. The lowest RMSE was observed in the Scoresby catchment and the highest RMSE in Blackburn flow station. Utilising CML rainfall generally results in a narrower range of variation in both NSE and RMSE when different rain gauges are used for dry-wet periods and calibration. The average improvement in RMSE was 15% by applying the conventional CML model. The new proposed model adjusted RMSE values by an extra 4% on average, achieving 28% lower RMSE in one of the pairs.

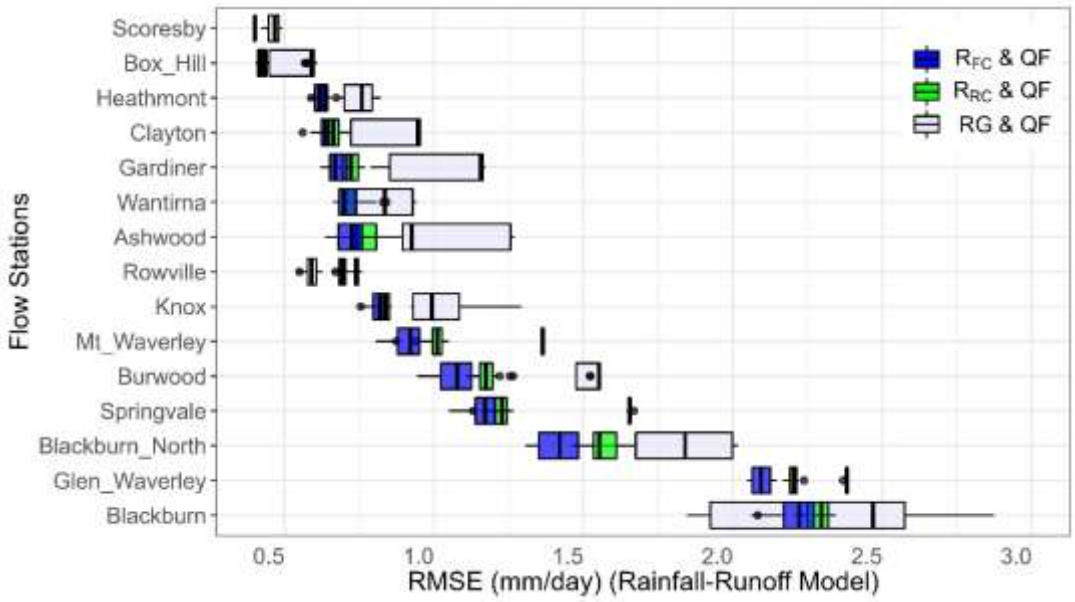


*Figure 4-12- RMSE for rainfall-runoff models in 15 flow stations, ranging for 12 rain gauges, comparing three methods of rainfall inputs.*

Both Figure 4-11 and Figure 4-12 illustrate the higher sensitivity of the rainfall-runoff model to changing the rain gauge for model input. Meanwhile, the flow-calibrated model is less sensitive, and all 12 rain gauges selected for wet-dry classification, provide a uniform pattern for CML-derived rainfall across all the catchments.

### 4.6.3. Wet antenna effect

An interesting finding in this study was the effect of optimising attenuation with quick flow on the wet antenna coefficient. The coefficient of the wet antenna was smaller when attenuation-quick flow relationships were calibrated by flow ($A_{a_{FC}}$) compared to when optimised by using rain gauge ($A_a$) in conventional method. As depicted in Figure 4-13, $A_a$ ranged from 1.5 to 2.0 dBm when Equation 4-1 was optimised using rain gauges. However, $A_{a_{FC}}$ exhibited a significant decrease in each pair of stations, as low as 0.7 dBm in some stations. $A_{a_{FC}}$ in all catchments, found to be 49% less than $A_a$ on average. In Figure 4-13 each data point above the 1:1 line indicates a reduction in the wet antenna effect for each validation data. The only flow station with no decrease in $A_{a_{FC}}$ is Rowville (with a higher range of $A_{a_{FC}}$, excluded from the graph) which showed an increase in all rain gauge pairs.

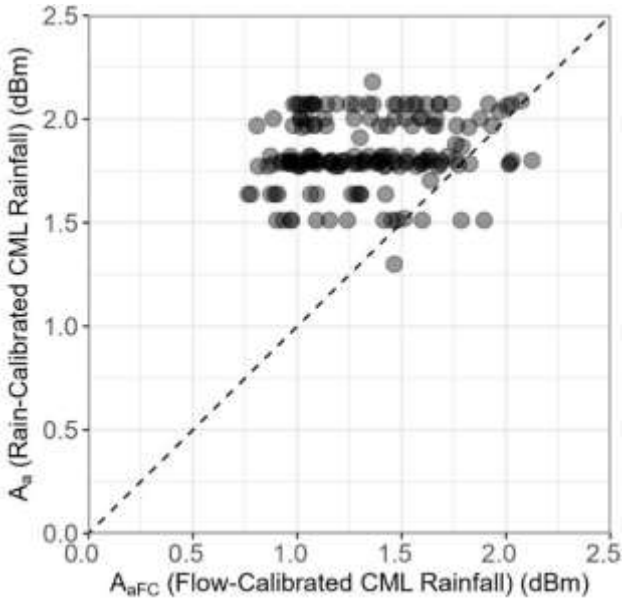


*Figure 4-13- Comparing $A_{a_{FC}}$ using flow calibration versus $A_a$ using rain calibration for CML rainfall calculations 180 pairs of flow-rain gauge.*

## 4.7. Discussion

This study focuses on the strength of the relationship between microwave attenuation and quick flow and the application of flow calibration as a new concept to replace in hydrological models. Therefore, this study does not seek the best rainfall-runoff model. Instead, it proposes a replacement for the rainfall factor. With promising results, the novel approach for calibrating CML rainfall with flow data could be a new concept in various rainfall-runoff methods instead of using rain gauge data or conventional CML methods.

As a result of this study, not only extracting rainfall from attenuation is a better predictor of flow, but also optimising the coefficient of the correlation with flow, enhances the reliability on attenuation in simulating rainfall. Microwave links provide more precise spatiotemporal resolution for rainfall. Taking all the advantages of CML-estimated rainfall, the new suggested approach adds to the accuracy of runoff estimation and ensures to reflect more spatiotemporal variations in rainfall rate while the rainfall is calibrated with flow.

This is the advantage of introducing the concept of flow calibration and Equation 4-8. The new rainfall value of $R_{FC}$ serves as a detour between precipitation and flow in the stream. Moreover, it can be considered as an approximation of the actual amount of water falling on an area and a new reference for adjusting and calibrating the other rainfall measurement techniques and tools. As a result, hydrological models of catchments could be developed in more details and downscaled to more sub-catchments compared to the application of rain gauges.

As shown in Figure 4-4, Figure 4-5 and Figure 4-6, microwave attenuation can establish a stronger correlation with quick flow in a catchment compared to rain gauges. The relationship is even stronger when the CML rainfall is calibrated with flow. This is attributed to the ability to measure the effects of raindrops along a path rather than at a single point and provide more spatial resolution.

A path-averaged attenuation is a representation of water yield in a path, while a rain gauge is a representation of water yield in a point. Therefore, quick flow, which is a representation of water yield in an area, has a better relationship and correlation with path-averaged attenuation than with point measurements. This is the reason for the better results obtained by calibrating CML rainfall with flow, as they have a closer alliance with the total water balance in the catchment.

Figure 4-11 and Figure 4-12 show the variations of statistical parameters in simulation results. The reliability of the rainfall-runoff model varies widely by using a different rain gauge data as input for each flow station. Consequently, a single microwave link produces more uniform flow output which is even closer to the measured flow. The outcome of these results may suggest that the rainfall rate is more uniform in the area and twelve rain gauges give an unreal distribution of rainfall over the area.

As a result, linear interpolation based on distance alone may not provide an accurate estimation of rainfall rate at a specific location. Various interpolation methods are being used for evaluating rain gauge data or radar-gauge combinations, ranging from simplistic techniques to more sophisticated geostatistical methods (Foehn *et al.*, 2018). However, it is required to enhance interpolation and merging methods, conduct comprehensive evaluations of remote sensing techniques, improve the reanalysis of rainfall data, and explore the application of non-gauge-based rainfall data in greater depth (Hu *et al.*, 2019).

In addition, introducing a new tool and technology does not necessarily mean abandoning the previous methods. A great vast network of rain gauges which has been used for decades, has its advantages to be still continuously involved in calculation and modelling.

As the methodology of CML quick flow shows, there is still a need for calibration and classification of wet-dry periods for the data from microwave links. Although there are other methods of classification wet-dry periods, it is worth and other studies emphasise the importance of combining tools. For example, they highlight the limitations of using either rain gauges or weather radars alone and emphasise the benefits of combining these data sources (Goudenhoofdt and Delobbe, 2009; Sideris *et al.*, 2014; Jewell and Gaussiat, 2015; Foehn *et al.*, 2016). By combining multiple methods, the systematic errors inherent in each method can be partially or completely cancelled out, as they are likely to affect the measurements differently.

As the other outcome of this research, a lower rate for wet antenna factor enables the selection of more effective parameters while disregarding less effective factors. Therefore, the use of attenuation and flow calibration of CML rainfall instead of rain gauges leads to model simplification. The issue of over-parameterisation has been a topic of discussion in hydrological modelling studies (Jakeman and Hornberger, 1993) with evidence suggesting that increasing the number of parameters does not always result in improved predictions (Hornberger *et al.*, 1985; Loague and Freeze, 1985). Simpler models, such as empirical models, offer simplicity, ease of use, and cost-effectiveness however not necessarily inaccurate (Machado *et al.*, 2011).

The other application of CMLs is to provide a faster flood warning system in cities. In urban catchments, the small size of sub-catchments means that localised intense rainfall events can lead to localised overflows within the stormwater system. However, the limited number and distribution of rain gauges in urban areas often do not accurately represent the actual rainfall distribution. Microwave links, on the other hand, offer a greater coverage area for rainfall measurement compared to gauges. In addition, the results show a more uniform pattern of rainfall in the area while using CML rainfall for flow estimation. Therefore, CML rainfall could be more trustable in runoff estimation in small catchments, rather than rain gauges. The new flow calibration approach also provides a more accurate prediction of runoff.

The challenges in urban catchments extend beyond the lack of sufficient rain gauges. Factors such as gauge elevation, surrounding obstructions, and the dense concentration of buildings, trees, and other structures introduce uncertainties and variations in rainfall measurements (Ochoa-Rodriguez *et al.*, 2019). The higher percentage of impervious surfaces in urban catchments further reduces infiltration rates, making runoff more responsive to rainfall intensity.

### 4.7.1. Exceptions in results

A further analysis was conducted to investigate the exceptions in the results. The flow station Glen Waverley does not show any meaningful correlation between rainfall and quick flow, no matter

whether a rain gauge or CML is recruited. Although R-squared, NSE and KGE are higher while using attenuation and even better by flow calibration. Glen Waverley is a small catchment close to the microwave link. However, the quick flow range does not match with the rain gauge data, indicating that the flow is probably under control.

Two other flow stations also show a different pattern. Rowville and Blackburn. As can be seen in Figure 4-8, these are the only flow stations that using attenuation has no enhancement compared to rain gauges. Again, even in these two stations, flow calibration shows a slight improvement in correlation statistics.

The industrial area in Blackburn stands out with a larger ratio compared to other catchments. Moreover, Blackburn and Rowville catchments boast significantly larger areas of ponds and wetlands. Rowville catchment is also fortunate to have parklands and golf courses on either side, serving as protective buffers that mitigate the risk of frequent flooding (Monash City Council, 2020).

An analysis of the correlations between flow station data reveals that Rowville and Glen Waverley exhibit the weakest correlation and lowest R-squared values with the rest of the flow stations. The paler colours in the columns of these two stations in Figure 4-14 indicate that their discharge patterns diverge from the other catchments, while the remaining stations demonstrate a more consistent runoff pattern.

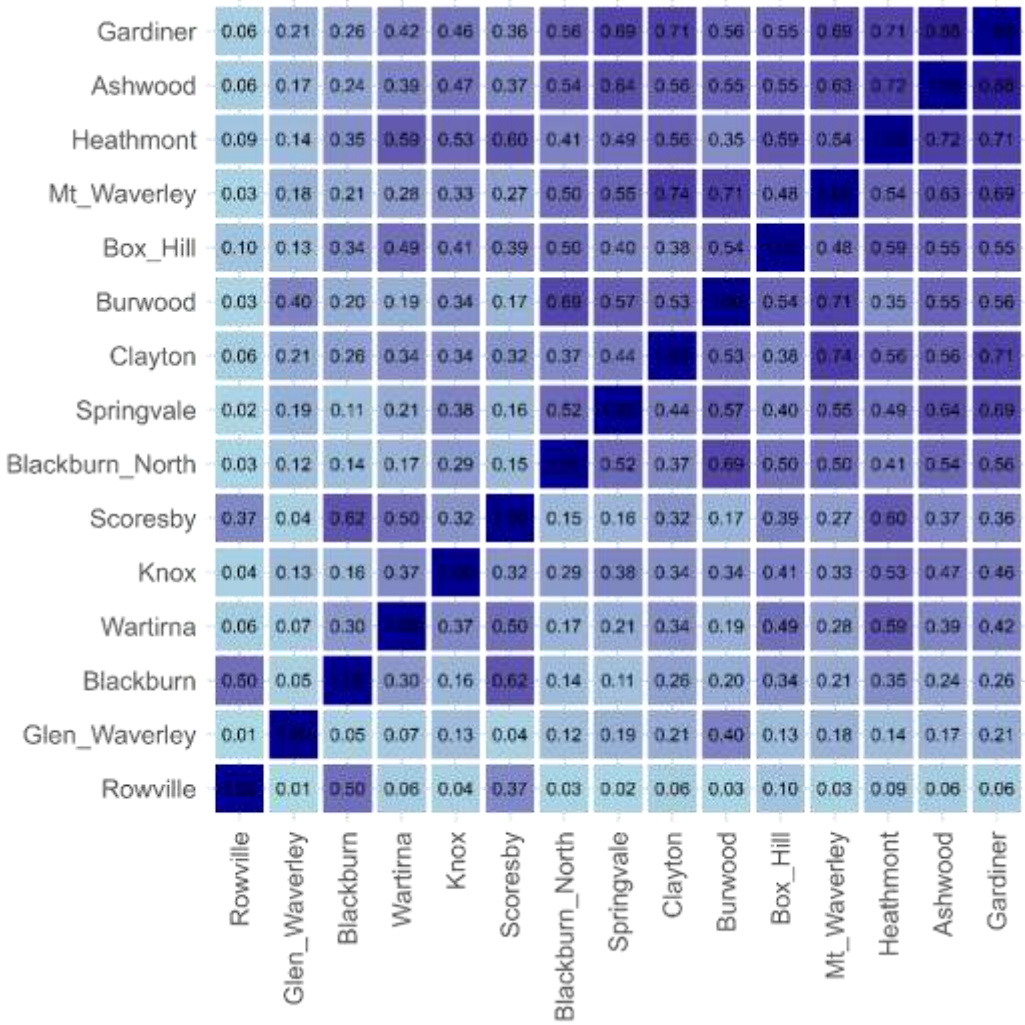


*Figure 4-14- The spectrum of R-squared of the correlation between the flow rates in any two flow stations*

Another investigation carried out to evaluate the similarity of rainfall records in rain gauges. Figure 4-15 illustrates the variation of r-squared values for the linear regression between the records of rainfall in any pair of two rain gauges. As the graph shows, there are some low r-squared values for Rowville gauge when it is paired to the other gauges like Blackburn North and Gardiner. These lower values for some stations can explain the variety in results.

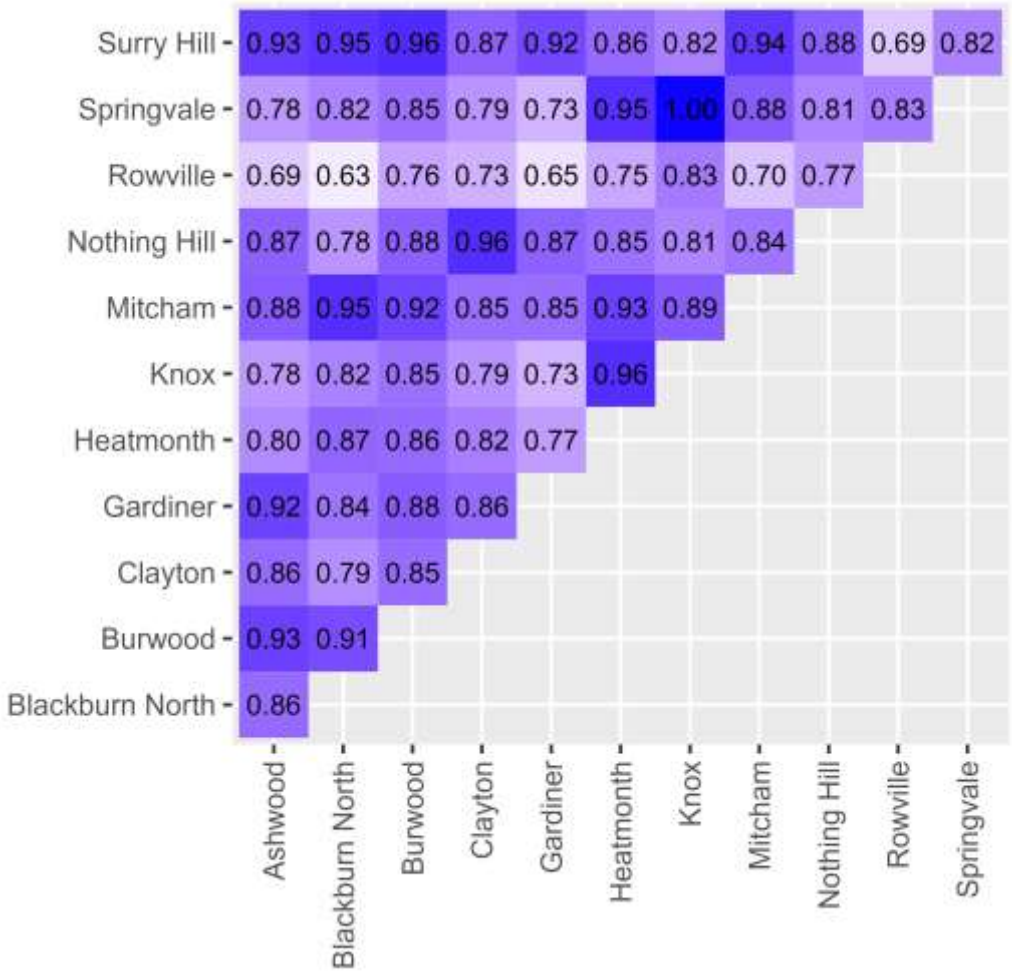


*Figure 4-15- The values of R-squared of the correlation between the rainfall rates in any two rain gauge.*

### 4.7.2. Coefficient of Variation (CV) for Rainfall Variability

In this study, rainfall data from 12 rain gauges were paired with a single microwave link to estimate rainfall across a wide region. The results demonstrated that the microwave link was capable of estimating rainfall over a broad area encompassing multiple catchments with variations in land use, elevation, slope, and other physical characteristics. Given this diversity, it is essential to evaluate the spatial variability of rainfall across the study area to assess how consistent or heterogeneous rainfall patterns are. Therefore, a study is required to evaluate the variation of rainfall over this area to determine whether the assumption of spatial uniformity in rainfall holds true and to what extent localized rainfall events might influence the accuracy of path-averaged measurements. This can be assessed using statistical tools such as the Coefficient of Variation (CV), which provides a normalized measure of rainfall variability across multiple locations.

The CV is a normalized measure of the dispersion of a probability distribution or frequency distribution. It is defined as the ratio of the standard deviation (σ) to the mean (μ):

$$CV = \frac{\sigma}{\mu}$$ Equation 4-10

Unlike the standard deviation, which is expressed in the same units as the data, the CV is a dimensionless number and is typically expressed as a percentage by multiplying the result by 100. This normalization makes the CV particularly useful for comparing variability between datasets with different units or widely different means.

In the context of rainfall analysis, CV is applied to examine the relative variability of daily rainfall across multiple rain gauges. For each day, the CV is calculated by computing the standard deviation and mean of rainfall values recorded across all stations. A low CV indicates high spatial consistency in rainfall measurements across the network of gauges, while a high CV reflects greater spatial variability, possibly due to localized convective storms or measurement inconsistencies.

The use of CV allows to identify patterns of spatial heterogeneity in rainfall and evaluate the representativeness of regional rainfall measurements. This metric is particularly helpful when assessing the performance of path-averaged measurements, such as those derived from commercial microwave links (CMLs), in comparison with point-based measurements from rain gauges.

In this study, CV is used both for:

- Overall spatial variability: Calculated from all gauges for each day to understand daily spatial consistency.
- Pairwise variability: Computed between each pair of rain gauges to examine how rainfall differences behave between specific locations.

This dual application provides insight into the temporal evolution of rainfall variability and the reliability of different rainfall measurement techniques across space.

- *Overall spatial variability*

For the overall CV, values are calculated across the 12 rain gauges for each day, representing the spatial variability of rainfall on a daily basis. To ensure meaningful interpretation of CV and to avoid inflated values during very low rainfall events (when even small differences result in high CVs), days with mean rainfall below 0.5 mm were excluded from the analysis. This helps eliminate artificially high CV values that often occur when some gauges record zero rainfall.

The remaining CV values were grouped into bins with 10% intervals (e.g., 0–0.1, 0.1–0.2, etc.), and the number of days falling into each bin was expressed as a percentage of the total number of valid days. Figure 4-16 illustrates the distribution of daily CV values, highlighting how often specific levels of spatial variability occur across the network of rain gauges. For example, in 23% of days during the period, CV is equal to 30%. All the days with CV less than 50% happen in 68% of the period which shows low variation between rain gauges. This analysis helps evaluate how homogeneous or heterogeneous rainfall tends to be over the study area.

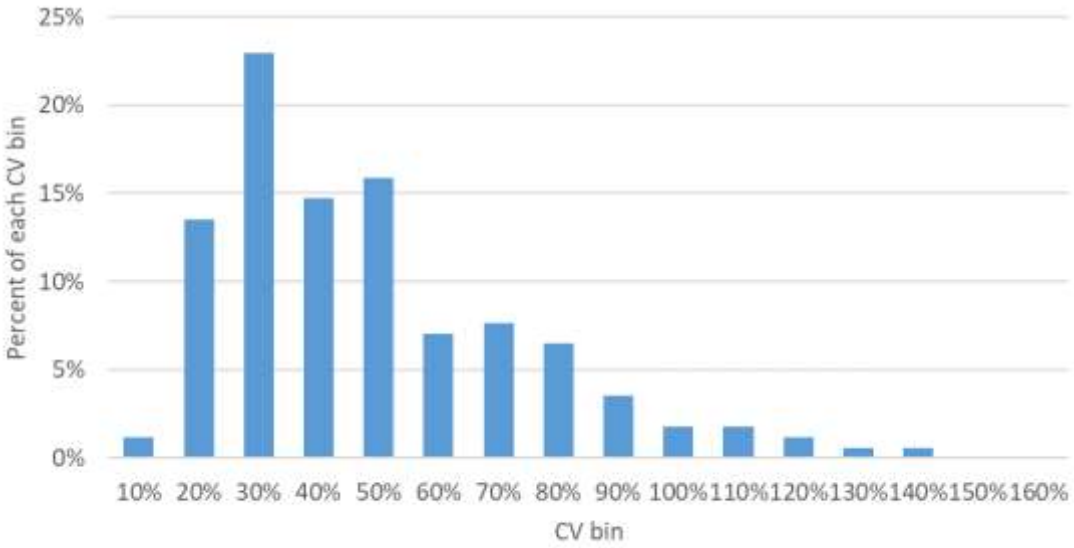


*Figure 4-16- Distribution of daily coefficient of variation (CV) values across 12 rain gauges, grouped into 10% intervals.*

- *Pairwise variability*

To further investigate the spatial variability of rainfall, a pairwise comparison was conducted between all combinations of the 12 available rain gauges. For each day, the rainfall values of each gauge pair were extracted and their mean, standard deviation (SD), and coefficient of variation (CV) were computed. This process was repeated for all 66 unique gauge pairs over the study period (300 days), resulting in a set of daily variability metrics for each pair.

Although calculating standard deviation for just two values (i.e., a single daily pairwise comparison) is mathematically valid, it comes with statistical limitations. When only two data points are involved, the standard deviation is simply half of the absolute difference between the values. This calculation is highly sensitive to small fluctuations and does not capture distributional characteristics. However, when performed consistently over many days, the daily SD values provide a useful measure of temporal variability in spatial rainfall patterns between locations. By summarizing these values over time, one can identify gauge pairs that consistently exhibit high or low variability.

Unlike the overall CV analysis, no rainfall threshold was applied here. illustrate the histograms of daily coefficient of variation (CV) values for each of the 66 rain gauge pairs, providing insight into the distribution of spatial variability over time across the study area. Figure 4-17, Figure 4-18, and Figure 4-19 illustrate the histograms of daily coefficient of variation (CV) values for each of the 66 possible rain gauge pairs, providing insight into the distribution of spatial variability over time across the study area. The y axis is the number of days and x axis shows CV values.

High number of days with CV greater than one is because of omitting the threshold in these graphs. Therefore, in some days when there is no rainfall recorded in some gauges and a low rainfall amount in other ones, the resulted CV is high and show a large variation. Ignoring this effect, the accumulation of numbers in the range of CV less than 0.5 (50%) shows a high similarity in records of rainfall gauges.

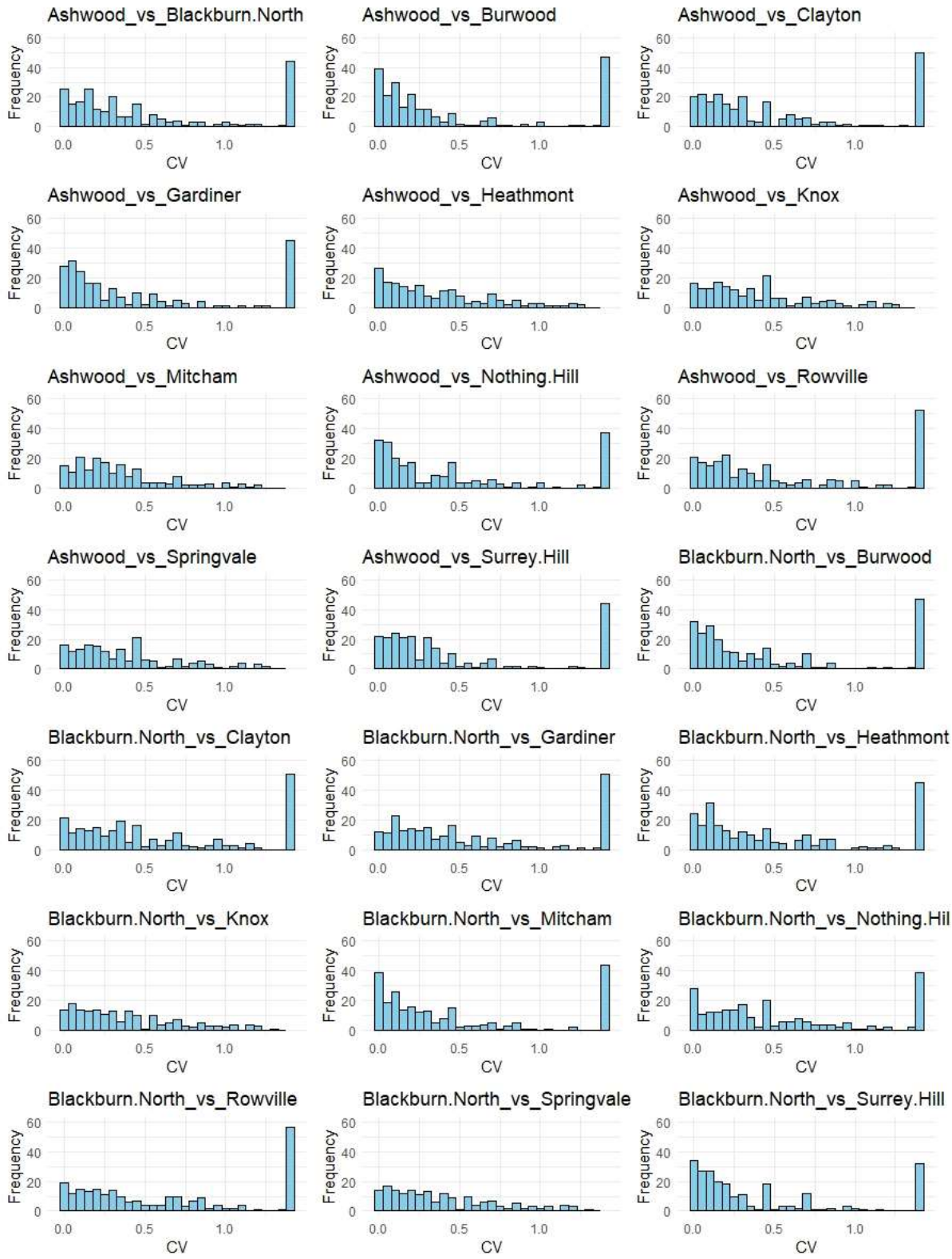


*Figure 4-17- Histograms of daily coefficient of variation (CV) values for the first 21 rain gauge pairs over the study period.*

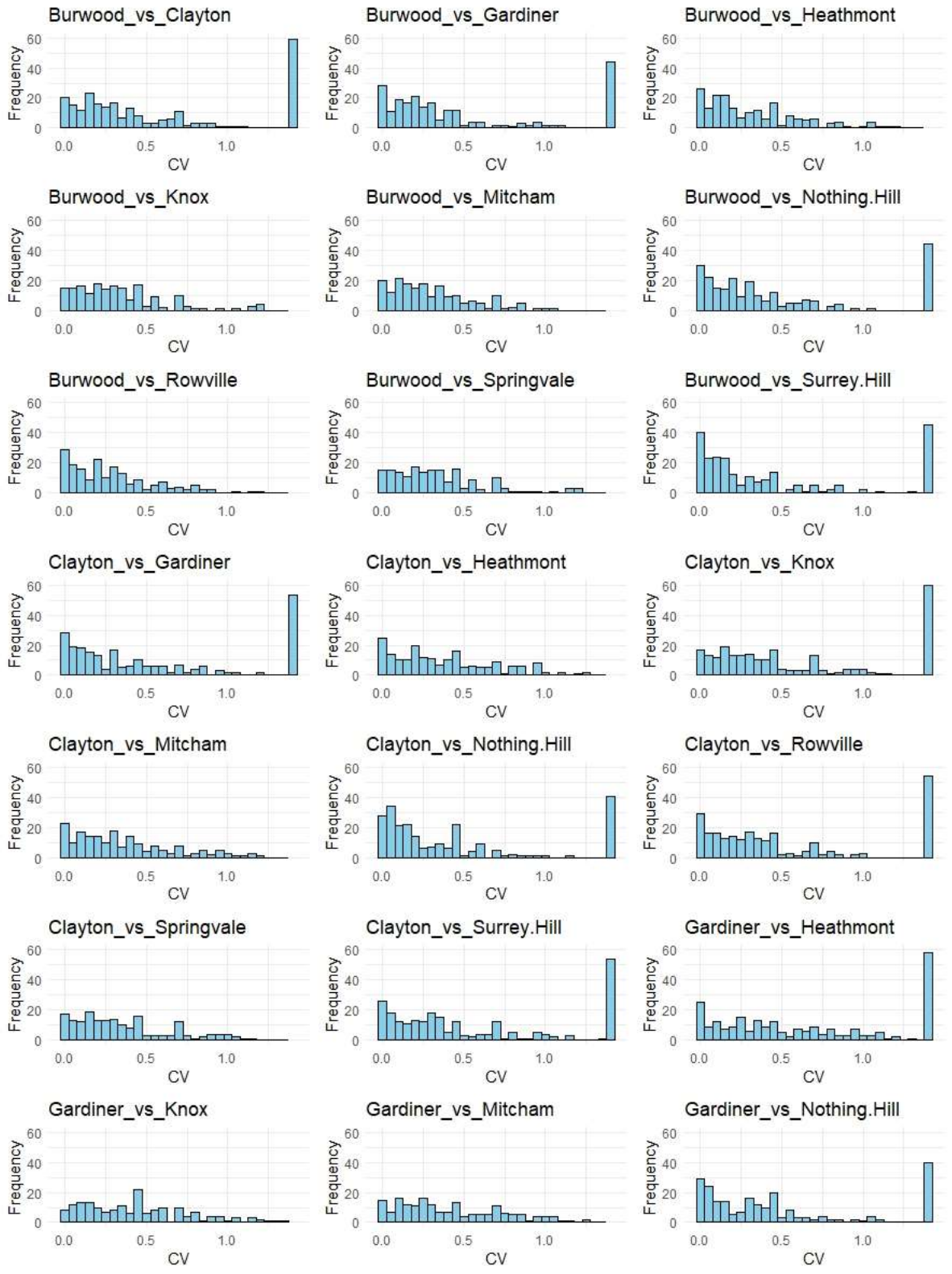


*Figure 4-18- Histograms of daily coefficient of variation (CV) values for the second 21 rain gauge pairs over the study period.*

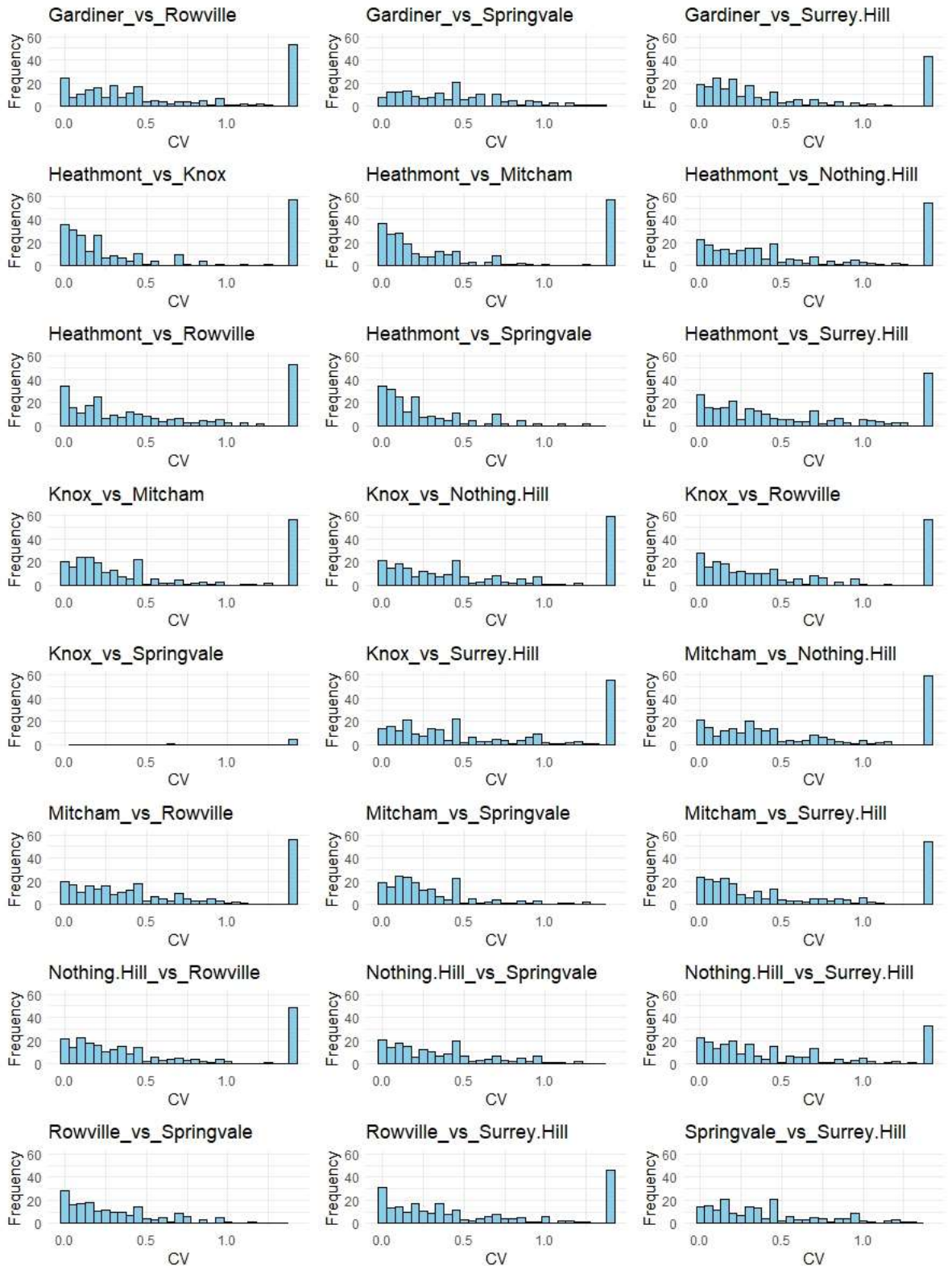


*Figure 4-19- Histograms of daily coefficient of variation (CV) values for the last 24 rain gauge pairs over the study period.*

# 5. Chapter five – Conclusion

## 5.1. Overall summary

The accomplishments of this PhD research are achieved in three defined sections, corresponding to the objectives of the study. In each of these segments, the outcomes highlight some advantages in improving the accuracy and adaptability of CML rainfall measurement methods.

Comprehensive discussions are provided at the end of each chapter. A summary of the achievements of this PhD study as a conclusion is provided here for each objective of the study.

- **Objective one (Chapter 2)**

The study explored the irregularities in cross-section of raindrops in frequencies 1 to 30 GHz. These irregularities found to affect the total attenuation while the rainfall intensity and consequently DSD varies. Therefore, varying coefficients are suggested for the power correlation between attenuation and rainfall.

This study found the values of scattering cross-sections and their variation in microwave frequencies lower than 10 GHz. The study calculated cross-sections of microwave frequencies passing through spherical drops. Mie-scattering theory and Maxwell equations are used to determine $C_{ext}$ in a range of frequencies between 1 and 30 GHz. Maxwell's equations were solved and simulated in COMSOL software (COMSOL Multiphysics Reference Manual, 1998) while scattering cross-sections were simply calculated in MiePlot (MiePlot) software.

The results show a difference between the variation of extinction cross-sections in higher and lower frequencies. The differences between changing rates and the appearance of the peaks affect the attenuation-rainfall correlation when enough raindrops appear in the range of peak cross-sections. The appearance of different sizes of drops is related to the rainfall intensity. Therefore, as the results show, in addition to the changes of coefficients for different frequencies, they are proposed to change with rainfall intensity variations. The results of calculating the coefficients of rainfall-attenuation correlation are provided in this study in for two DSD model compared to ITU recommendation.

The variation in coefficients is significantly different at frequencies higher and lower than 5 GHz. They are ascending with increasing rainfall intensity at frequencies higher than 5 GHz while descending at lower frequencies.

A comprehensive rainfall-attenuation formula (Equation 2-9) is suggested in this study to consider variable coefficients for frequency and rainfall intensity as well. The suggested equation needs to be proved with further field studies.

- **Objective two (Chapter 3)**

In summary, the selection of an appropriate denoising method is pivotal when dealing with microwave signals impacted by rainfall attenuation. While conventional methods have their place in noise reduction, their inherent limitations in detecting and addressing rainfall-induced distortions call for alternative strategies. The application of median-based techniques and our novel approach involving Butterworth and Chebyshev filters, along with moving average methods, has the potential to provide more accurate and reliable results and showed better performance in selected microwave links.

The moving average method consistently outperforms other methods across three microwave links. In link 26H, it achieves the lowest RMSE (0.47 mm/hr) and the highest NSE (0.83), outshining the conventional method in both metrics. Similarly, in links 38H and 38V, the moving average method demonstrates the lowest RMSE (0.48 mm/hr) and a high NSE (0.82). The conventional method lags behind in NSE and RMSE in links 38H and 38V, while in link 26H, it results in a higher RMSE (0.48

mm/hr) and lower NSE (0.82) compared to the moving average method. Notably, the suggested methods show substantially lower $A_a$ values compared to the conventional method, with the Chebyshev method consistently requiring a zero $A_a$ value across all links. Overall, moving average resulted in 2%, 16%, and 14% lower RMSE than the conventional method in microwave links 26H, 38H, and 38V, respectively. However, short-term validation reveals varying sensitivity, with shorter periods yielding low fitness and longer periods showing better NSE, R-squared, and lower RMSE.

In conclusion, the suggested methods showed that they could be applied in CML rainfall calculations if the filter parameters are investigated and determined correctly. Further studies are required to investigate other frequencies, locations, climate and rainfall patterns.

Common median methods are suitable for denoising microwave signals in the presence of rainfall attenuation. This is because median filtering is a non-linear operation that is able to remove impulsive noise components without blurring the signal. One defect in this method is the need for dry periods in power level. Therefore, this method is unable to produce reference level when the rainfall last for more than 21.5 hours.

In addition to median filtering, Butterworth and Chebyshev filters can also be used to denoise microwave signals in the presence of rainfall attenuation. These filters are able to attenuate noise components in a specific frequency band without significantly affecting the basic carrier signal level.

Another promising denoising method is moving average filtering. This method involves averaging a set of consecutive samples in the signal. This can be an effective way to remove noise components that are smaller in amplitude than the basic carrier signal level.

- **Objective three (Chapter 4)**

Based on the findings of this study and the promising results in the application of attenuation and flow-calibrated CML rainfall, we propose that the new calibration method of CML-derived rainfall with flow can be a potential alternative to rain gauge application in rainfall-runoff models. The introduction of the new replacement factor brings a simplification to hydrological models by enhancing the representation of rainfall amount while minimising the influence of unnecessary errors. This allows for a more focused and meaningful analysis of the hydrological processes.

The regression analysis shows that there is a stronger relationship between attenuation and quick flow in comparison with the relation between rain gauge data and quick flow. In this study, the attenuation is coupled with quick flow through a new concept of flow-calibrated CML rainfall ($R_{FC}$). The new rainfall estimation shows a weaker relationship with the rainfall depth by rain gauge compared to the conventional method of calibrating attenuation with rain gauge. However, the measured quick flow builds a stronger correlation with the simulated quick flow with the new method and achieved NSE and R-squared values up to 0.87 in regression. RMSE of the simulation also shows a significant enhancement. For example, the RMSE of quick flow dropped from an average of 1.0 to 0.65 mm/day in the Gardiner catchment and from 1.1 to 0.7 mm/day on average in the Ashwood and 1.8 to 1.4 mm/day in Glen Waverley catchments.

The results of the rainfall-runoff model are similar to regression and NSE, KGE, R-squared, and RMSE of models show enhancement by using CML rainfall and a greater achievement when CML attenuation is calibrated with flow. These factors are generally stronger with the new method, except in the Rowville catchment which is larger in area and different in land use and flow control structures. Blackburn catchment also shows improvement in the results of the model for some of the rain gauges and is weaker for the other rain gauges.

NSE and KGE values illustrate this enhancement, with the new suggested method achieving a maximum NSE of 0.78 and KGE of 0.86. Compared to rain gauges, the conventional CML model improves NSE by 197% on average, while the new model shows an additional 50% enhancement. KGE also sees an average 21% improvement with the conventional CML model and a further 4% with

the new method. RMSE optimisation shows a 15% improvement with the conventional CML model, with an additional 4% improvement on average using the new model.

One interesting achievement in this study was the lower value for wet antenna effect in the suggested methods. The effect is demonstrated by a decrease in wet antenna effect across all catchments, with a 49% reduction on average. The lower to zero wet antenna effect mitigate the effect of unknown parameters and the requirement of calibrating while the data availability is restricted.

The new flow calibration method also decreased the wet antenna effect by reaching lower values of ($A_{a_{FC}}$) compared to ($A_a$) for the conventional method. The factor shows a 49 per cent reduction on average.

However, it is important to carefully select the correlation between links and the flow at the catchment outlet. This consideration is not an additional effort in modelling, as different catchments exhibit varied hydrological patterns, including controlled flow and a mix of surface and groundwater resources. Therefore, conducting a thorough investigation of catchment hydrology is a common practice for establishing simulation models using traditional methods.

Furthermore, we recommend conducting an inspection of the optimal placement of flow meters, rain gauges, and links to determine the most suitable interpolation scheme and appropriate weighting of rainfall and attenuation records. This analysis will contribute to improving the accuracy and reliability of the simulation model.

## 5.2. Challenges

Several challenges and limitations constrained the scope of the study. Firstly, COVID-19 lockdowns during the initial phases hindered the setup of a microwave link and field study on real signals. Consequently, existing data from microwave links in the Netherlands and Australia were utilised.

Additionally, the study encountered limitations in computer performance, particularly with COMSOL simulations requiring high-performance computing due to mesh size variations based on frequency and droplet size. While supercomputers were considered, the iterative nature of simulations posed logistical challenges in queuing. Moreover, processing high-frequency CML data, containing billions of records ($2.5\times10^9$), required substantial RAM.

Data quality also checked before using them at the study. A lot of missing data and gaps in days, hours and seconds was a challenge as they were not clearly recognisable in the metadata files. Therefore, it necessitated extensive cleaning and preparation efforts before using them.

Furthermore, the absence of CML data in controlled catchments posed a significant challenge for examining attenuation-runoff models. Utilising CML data from Melbourne limited the ability to thoroughly explore various aspects of the study due to insufficient signal records and station availability.

## 5.3. Future research

Considering the limitations and barriers during this study there are some further studies and adjustments to be suggested for future. Suggestions are categorised in three parts as per the chapters of the thesis:

- **Drop scale (Chapter two)**

Considering the limitations of this study there are some further studies and adjustments to be suggested for future as listed below:

a) This research constituted an analytical examination of formulas and correlations. It is imperative to fortify and assess its findings through field studies. The field setup should

encompass multiple microwave links across different frequencies, incorporating rain gauges or disdrometers beneath the link paths. Correlations with measured rainfall must be established by utilising received signal power. Nevertheless, these correlations for each link need to be categorised by rainfall intensity and optimised to minimise errors in the rainfall-attenuation relationship.

b) The investigation should be replicated considering the actual shape of raindrops. The T-matrix method is the recommended approach for this endeavour.
c) A strategy for resolving the final correlation with varying constants should be developed. Given the interdependence of rainfall intensity, drop size distribution (DSD), and total attenuation, an iterative method is proposed for examination. Implementing such a method, especially with substantial data on signal power recorded at a high frequency, may necessitate suitable computer hardware for execution.
d) A comprehensive drop size distribution study is required in each location prior to microwave application. The results provide a better approximation of the constants and stablishing a better correlation utilising the suggested equation with varying coefficients.

- **Signal scale (Chapter three)**

Utilising the outcomes of this study and discerning the variations in accuracy among the proposed models across different time frames yields insights and recommendations for future investigations.

e) A more accurate model can be developed by study a changing (variable/nonstable) moving average window, for wet and dry periods. Without a wet/dry classification, this could be implemented by finding the periods with a deep or sharp drop in power. This also could be wet/dry classification method.
f) Parameters of lowpass filters also could be variable during the rainfall events and different times of the year or day/night.
g) Some methods have been developed for detecting the start and the end of the rainfall period. For example a method using dual frequency for interpolating dry period attenuation (Upton et al., 2005). However, this method is only for wet-dry classification and not for accurately predict the rainfall from start to end. It is possible to use this method or similar techniques to detect the start and the end of the rainfall event and use a different time step for moving average method, use a varying cut-off frequency, sampling frequency or even different constants for the power law of rainfall-attenuation relationship.
h) This study showed that calibrating and selecting the filter parameters is more important than selecting the method. Therefore, other filtering methods also need to be evaluated. The suggestion is finding a filtering method which needs the least number of parameters and the least sensitivity to calibration and variation of the parameters.
i) In violin graphs in Figure 3-25, Figure 3-26, and Figure 3-27, some outlier points show high values of NSE and R-squared and very low RMSE. These may show that some rainfall events could be predicted with high accuracy with any of these methods. Therefore, it is suggested to investigate the characteristics of those rainfall events and find the relationships that help to find a better technique for using CML methods in short-term rainfall durations and events.

- **Catchment scale (Chapter four)**

There are some suggestions for the future studies to enhance the suggested attenuation-runoff model and the traditional rainfall-runoff models. The application of CML derived rainfall in runoff prediction has shown promise in providing a finer spatiotemporal resolution for rainfall estimations. Nevertheless, to optimize its performance, the CML derived rainfall could be adjusted to achieve the best performance. Suggestions for the conventional rainfall-runoff models are including:

j) Trying different methods of interpolating rainfall or attenuation in mapping the rainfall depth over a catchment. Since the length and direction of microwave links are different, the weighting of each link on rainfall depth results may affect the runoff prediction significantly.
k) An investigation on the catchment parameters is suggested to evaluate how using CML rainfall may affect the hydrological parameters such as land use, shape factor, area, and slope.
l) Using a combination of different rainfall measurement techniques can improve the runoff prediction by finding a more precise estimation of rainfall.

For the proposed attenuation-runoff model, the primary recommendation involves conducting an in-depth investigation into a direct relationship between attenuation and rainfall. This study explored an indirect method for relating attenuation to runoff utilising a new concept of rainfall. A straightforward lumped rainfall-runoff model is employed to estimate runoff in this study and the flow calibrated CML rainfall replaces the conventional rain gauge calibration.

However, an opportunity exists to develop a mathematical model utilising only the attenuation data from microwave links directly correlated with runoff. This necessitates the establishment of new relationships and correlations between microwave parameters, catchment characteristics, and flow properties, involving the introduction of novel coefficients and constants. Results from this study indicate that flow-calibrated rainfall displays less similarity to rain gauge data compared to the conventional method. Consequently, it is advised not to rely on relating attenuation to rainfall, and instead, to establish new relationships directly from attenuation data.

# 6. References


Abdulrahman, A.Y. *et al.* (2012) 'Rain attenuation measurements over terrestrial microwave links operating at 15 GHz in Malaysia', *International Journal of Communication Systems*, 25(11), pp. 1479–1488. doi:10.1002/dac.1315.

Abrahart, R.J., See, L.M. and Solomatine, D.P. (2008) 'Practical hydroinformatics : computational intelligence and technological developments in water applications.', *Springer-Verlag, Berlin, Heidelberg, Germany*, p. 505.

Abulohom, M.S., Shah, S.M.S. and Ghumman, A.R. (2001) 'Development of a rainfall-runoff model, its calibration and validation', *Water Resources Management*, 15(3), pp. 149–163. doi:10.1023/A:1013069709740/METRICS.

Adriana Maria Erazo Chica (2017) 'HYDROLOGICAL TOOLS FOR FLOODING EARLY WARNING SYSTEMS', in *IWRA World Water Congress*. Cancun Mexico. Available at: https://iwra.org/member/index.php?page=286&abstract_id=4051.

Agnon, Y. *et al.* (2005) 'Fine scale inhomogeneity of wind-wave energy input, skewness, and asymmetry', *Geophysical Research Letters*, 32(12), pp. 1–4. doi:10.1029/2005GL022701.

*airGR: the INRAE GR Hydrological Models in a R Package* (2023). Available at: https://hydrogr.github.io/airGR/ (Accessed: 9 July 2023).

Al-Badrawi, M.H. (2017) *Statistical Properties and Applications of Empirical Mode Decomposition*. University of New Hampshire, Durham. Available at: https://scholars.unh.edu/dissertation/2280?utm_source=scholars.unh.edu%2Fdissertation%2F2280&utm_medium=PDF&utm_campaign=PDFCoverPages.

Alexander, L. V. *et al.* (2006) 'Global observed changes in daily climate extremes of temperature and precipitation', *Journal of Geophysical Research: Atmospheres*, 111(D5), p. 5109. doi:10.1029/2005JD006290.

Alpert, P., Messer, H. and David, N. (2016) 'Meteorology: Mobile networks aid weather monitoring', *Nature*. Nature Publishing Group, p. 617. doi:10.1038/537617e.

Amarjit and R P S Gangwar (2008) 'The finite element approach for evaluation of extinction cross-section of realistically distorted raindrops', *Indian Journal of Radio & Space Physics*, 37, pp. 114–120. Available at: http://nopr.niscair.res.in/handle/123456789/2484 (Accessed: 18 December 2019).

Andersen, J.N. (2015) *Wireless coverage in the public transportation system*. Aalborg University. Available at: https://projekter.aau.dk/projekter/files/213565162/master.pdf.

Andréassian, V. *et al.* (2009) 'Crash tests for a standardized evaluation of hydrological models', *Hydrology and Earth System Sciences*, 13(10), pp. 1757–1764. doi:10.5194/HESS-13-1757-2009.

Andrianov, I. V., Danishevskyy, V. and Awrejcewicz, J. (2021) 'Linear and Nonlinear Waves in Microstructured Solids : Homogenization and Asymptotic Approaches', *Linear and Nonlinear Waves in Microstructured Solids* [Preprint]. doi:10.1201/9781003146162.

Anmala, J. *et al.* (2000) 'Comparison of ANNs and Empirical Approaches for Predicting Watershed Runoff', *Journal of Water Resources Planning and Management*, 126(3), pp. 156–166. doi:10.1061/(ASCE)0733-9496(2000)126:3(156).

Aravindkumar, M. and Manjunathachari, K. (2017) 'Efficient Audio Noise Reduction System Using Butterworth Chebyshev and Elliptical filter', *International Journal of Multimedia and Ubiquitous Engineering*, 12(1), pp. 225–238. doi:10.14257/ijmue.2017.12.1.19.

Åsen, W. and Gibbins, C.J. (2002) 'A comparison of rain attenuation and drop size distributions measured in Chilbolton and Singapore', *Radio Science*, 37(3), pp. 6-1-6–15. doi:10.1029/2000RS002613.

Asif, S.Z. (2019) *5G Mobile Communications, Concepts and Technologies*. CRC Press, Taylor & Francis Group.

Atlas, D. and Thiele, O.W. (1981) 'Precipitation Measurements From Space: Workshop report. An element of the climate observing system study - NASA Technical Reports Server (NTRS)', in. Available at: https://ntrs.nasa.gov/citations/19830016998 (Accessed: 14 April 2023).

Atlas, D. and Ulbrich, C.W. (1977) 'Path- and Area-Integrated Rainfall Measurement by Microwave Attenuation in the 1–3 cm Band', in *Journal of Applied Meteorology*. Am Meteorol Soc, pp. 1322–1331. doi:10.1175/1520-0450(1977)016<1322:paairm>2.0.co;2.

Auckland Council (2022) *Code of Practice for Land Development and subdivision (Chapter4-Stormwater)*. Available at: https://content.aucklanddesignmanual.co.nz/regulations/codes-of-practice/Documents/SW-CoP-v3-January-2022.pdf (Accessed: 30 January 2023).

Axelsson, C. *et al.* (2021) 'Urban policy adaptation toward managing increasing pluvial flooding events under climate change', *Journal of Environmental Planning and Management*, 64(8), pp. 1408–1427. doi:10.1080/09640568.2020.1823346/SUPPL_FILE/CJEP_A_1823346_SM1293.DOCX.

Baltazar-Lopez, M.E. (2003) *Applications of tap-nde technique to non-contact ultrasonic inspection in tubulars*. Texas A&M University. Available at: https://www.researchgate.net/publication/26898388_Applications_of_TAP-NDE_technique_to_non-contact_ultrasonic_inspection_in_tubulars.

Bao, X. *et al.* (2017) 'Improving the extreme rainfall forecast of Typhoon Morakot (2009) by assimilating radar data from Taiwan Island and mainland China', *Journal of Meteorological Research*, 31(4), pp. 747–766. doi:10.1007/s13351-017-6007-8.

Barclay, L. (2003) *Propagation of Radiowaves*. 2nd edn. London, United Kingdom: The institution of Engineering and Technology.

Baxandall, P. (1968) 'In Transistor Circuits 1 . Mainly on fundamental noise concepts', *Wireless World* [Preprint].

Bayless, J. (2022) *Is the Kalman filter a low-pass filter? Sometimes!* Available at: https://jbconsulting.substack.com/p/is-the-kalman-filter-just-a-low-pass (Accessed: 24 August 2023).

Beard, K. V. (1976) 'Terminal Velocity and Shape of Cloud and Precipitation Drops Aloft', *Journal of the Atmospheric Sciences*, 33(5), pp. 851–864. doi:10.1175/1520-0469(1976)033<0851:TVASOC>2.0.CO;2.

Beard, K. V. (1977) 'Terminal Velocity Adjustment for Cloud and Precipitation Drops Aloft', *Journal of the Atmospheric Sciences*, 34(8), pp. 1293–1298. Available at: http://journals.ametsoc.org/doi/abs/10.1175/1520-0469%281977%29034%3C1293%3ATVAFCA%3E2.0.CO%3B2 (Accessed: 1 May 2019).

Beard, K. V., Bringi, V.N. and Thurai, M. (2010) 'A new understanding of raindrop shape', *Atmospheric Research*, 97(4), pp. 396–415. doi:10.1016/j.atmosres.2010.02.001.

Beard, K. V. and Chuang, C. (1987) 'A New Model for the Equilibrium Shape of Raindrops', *Journal of the Atmospheric Sciences*, 44(11), pp. 1509–1524. doi:10.1175/1520-0469(1987)044<1509:ANMFTE>2.0.CO;2.

van de Beek, C.Z. *et al.* (2012) 'Seasonal semi-variance of Dutch rainfall at hourly to daily scales',

*Advances in Water Resources*, 45, pp. 76–85. doi:10.1016/j.advwatres.2012.03.023.

Belarbi, H. *et al.* (2016) 'Sécheresse et modification de la relation pluie–débit: cas du bassin versant de l'Oued Sebdou (Algérie Occidentale)', *https://doi.org/10.1080/02626667.2015.1112394*, 62(1), pp. 1–13. doi:10.1080/02626667.2015.1112394.

Berger, U.S. (2003) *Microwave Communications*, *Encyclopedia of Physical Science and Technology*. Academic Press. doi:10.1016/B0-12-227410-5/00445-2.

Berne, A. and Uijlenhoet, R. (2007) 'Path-averaged rainfall estimation using microwave links: Uncertainty due to spatial rainfall variability', *Geophysical Research Letters*, 34(7), p. L07403. doi:10.1029/2007GL029409.

Beven, K.J. and Hornberger, G.M. (1982) 'ASSESSING THE EFFECT OF SPATIAL PATTERN OF PRECIPITATION IN MODELING STREAM FLOW HYDROGRAPHS1', *JAWRA Journal of the American Water Resources Association*, 18(5), pp. 823–829. doi:10.1111/J.1752-1688.1982.TB00078.X.

Bianchi, B., Rieckermann, J. and Berne, A. (2013) 'Quality control of rain gauge measurements using telecommunication microwave links', *Journal of Hydrology*, 492, pp. 15–23. doi:10.1016/j.jhydrol.2013.03.042.

Blanchet, F., Brunelle, D. and Guillon, A. (1992) '"Influence of the spatial heterogeneity of precipitation upon the hydrologic response of an urban catchment', in *2nd Int. Symp. Hydrological Applications of Weather Radar*. Hannover, p. 8.

Blettner, N. *et al.* (2022) 'Combining Commercial Microwave Link and Rain Gauge Observations to Estimate Countrywide Precipitation: A Stochastic Reconstruction and Pattern Analysis Approach', *Water Resources Research*, 58(10), p. e2022WR032563. doi:10.1029/2022WR032563.

Bohren, C.F. and Huffman, D.R. (1983) *Absorption and scattering of light by small particles*. John Wiley & Sons, Inc.

Bohren, C.F. and Huffman, D.R. (1998) *Absorption and Scattering of Light by Small Particles*, *Absorption and Scattering of Light by Small Particles*. Wiley. doi:10.1002/9783527618156.

Boudreau, C.A. and Stone, M.L. (1965) *26th REFERENCE BIBLIOGRAPHY Scattering and Attenuation by Precipitation Particles*.

Boughton, W.C. (1989) 'A review of the USDA SCS curve number method', *Soil Research*, 27(3), pp. 511–523. doi:10.1071/SR9890511.

Brauer, C.C. *et al.* (2016) 'The effect of differences between rainfall measurement techniques on groundwater and discharge simulations in a lowland catchment', *Hydrological Processes*, 30(21), pp. 3885–3900. doi:10.1002/hyp.10898.

Brocca, L. *et al.* (2014) 'Soil as a natural rain gauge: Estimating global rainfall from satellite soil moisture data', *Journal of Geophysical Research: Atmospheres*, 119(9), pp. 5128–5141. doi:10.1002/2014JD021489.

Bruni, G. *et al.* (2015) 'On the sensitivity of urban hydrodynamic modelling to rainfall spatial and temporal resolution', *Hydrology and Earth System Sciences*, 19(2), pp. 691–709. doi:10.5194/HESS-19-691-2015.

Butterworth, S. (1930) 'On the Theory of Filter Amplifiers', *Experimental Wireless and the Wireless Engineer*, 7, pp. 536–541.

C. Sidney Burrus, Gopinath, R. and Guo, H. (1997) *Introduction to Wavelets and Wavelet Transforms*. 1st edn. Pearson.

CADENCE PCB Solutions (2020) *What is Signal to Noise Ratio and How to calculate it?* Available at: https://resources.pcb.cadence.com/blog/2020-what-is-signal-to-noise-ratio-and-how-to-calculate-it.

Carvalho, J.M. de *et al.* (2018) *Digital Signal Processing*. Momentum Pres.

Cattoën, C., McMillan, H. and Moore, S. (2016) 'Coupling a high-resolution weather model with a hydrological model for flood forecasting in New Zealand on JSTOR', *Journal of Hydrology (New Zealand)*, 55(1), pp. 1–23. Available at: https://www.jstor.org/stable/43945083 (Accessed: 4 March 2024).

Charlton-Perez, C., Cloke, H.L. and Ghelli, A. (2015) 'Rainfall: high-resolution observation and prediction', *Meteorological Applications*, 22(1), pp. 1–2. doi:10.1002/MET.1496.

Chatterjee, S. *et al.* (2020) 'Review of noise removal techniques in ECG signals', *IET Signal Processing*, 14(9), pp. 569–590. doi:10.1049/IET-SPR.2020.0104.

Chen, J.L. *et al.* (1998) 'Seasonal global water mass budget and mean sea level variations', *Geophysical Research Letters*, 25(19), pp. 3555–3558. doi:10.1029/98GL02754.

Choi, J.H. *et al.* (2023) 'Improvement of Rainfall Measurements by Using a Dual Tipping Bucket Rain Gauge', *Asia-Pacific Journal of Atmospheric Sciences*, 59(2), pp. 271–280. doi:10.1007/S13143-022-00295-0/FIGURES/9.

Christchurch City Council (2022) *Christchurch City Council Infrastructure Design Standard, Part 5: Stormwater and Land Drainage*. Available at: https://ccc.govt.nz/assets/Documents/Consents-and-Licences/construction-requirements/IDS/Infrastructure-Design-Standard/Part-5-Stormwater-Land-Drainage.pdf.

Chvíla, B., Sevruk, B. and Ondrás, M. (2005) 'The wind-induced loss of thunderstorm precipitation measurements', *Atmospheric Research*, 77(1-4 SPEC. ISS.), pp. 29–38. doi:10.1016/j.atmosres.2004.11.032.

Chwala, C. *et al.* (2012) 'Precipitation observation using microwave backhaul links in the alpine and pre-alpine region of Southern Germany', *Hydrology and Earth System Sciences*, 16(8), pp. 2647–2661. doi:10.5194/hess-16-2647-2012.

Cicone, A., Liu, J. and Zhou, H. (2016) 'Adaptive local iterative filtering for signal decomposition and instantaneous frequency analysis', *Applied and Computational Harmonic Analysis*, 41(2), pp. 384–411. doi:10.1016/J.ACHA.2016.03.001.

Civera, M. and Surace, C. (2021) 'A Comparative Analysis of Signal Decomposition Techniques for Structural Health Monitoring on an Experimental Benchmark', *Sensors (Basel, Switzerland)*, 21(5), pp. 1–35. doi:10.3390/S21051825.

*ClimaCell – The world's leading weather intelligence engine* (no date). Available at: https://www.climacell.co/ (Accessed: 16 January 2020).

'COMSOL Multiphysics Reference Manual' (1998). Available at: www.comsol.com/blogs (Accessed: 9 July 2021).

Coron, L. *et al.* (2017) 'The suite of lumped GR hydrological models in an R package', *Environmental Modelling & Software*, 94, pp. 166–171. doi:10.1016/J.ENVSOFT.2017.05.002.

Corradini, C. and Singh, V.P. (1985) 'Effect of spatial variability of effective rainfall on direct runoff by a geomorphologic approach', *Journal of Hydrology*, 81(1–2), pp. 27–43. doi:10.1016/0022-1694(85)90165-9.

*CRAN - Package airGR* (no date). Available at: https://cran.r-

project.org/web/packages/airGR/index.html (Accessed: 9 July 2023).

*CRAN - Package FlowScreen* (2019). Available at: https://cran.r-project.org/web/packages/FlowScreen/ (Accessed: 28 April 2023).

Crane, R.K. (1975) 'Attenuation due to Rain—A Mini-Review', *IEEE Transactions on Antennas and Propagation*, 23(5), pp. 750–752. doi:10.1109/TAP.1975.1141130.

D'Amico, M., Manzoni, A. and Solazzi, G.L. (2016) 'Use of Operational Microwave Link Measurements for the Tomographic Reconstruction of 2-D Maps of Accumulated Rainfall', *IEEE Geoscience and Remote Sensing Letters*, 13(12), pp. 1827–1831. doi:10.1109/LGRS.2016.2614326.

Daher, A., Al Sakka, H. and Chaaban, A.K. (2023) 'Low complexity single-layer neural network for enhanced rainfall estimation using microwave links', *Journal of Hydroinformatics*, 25(1), pp. 101–112. doi:10.2166/HYDRO.2022.099/1151516/JH2022099.PDF.

Danso, S. *et al.* (2021) 'Denoising Terahertz Images Applying Wavelet Transform Filters', *PAIDEUMA JOURNAL*, XIV(4), pp. 17–27. Available at: https://www.researchgate.net/publication/351461565_Denoising_Terahertz_Images_Applying_Wavelet_Transform_Filters (Accessed: 3 November 2023).

David, N. *et al.* (2015) 'Cellular Network Infrastructure: The Future of Fog Monitoring?', *Bulletin of the American Meteorological Society*, 96(10), pp. 1687–1698. doi:10.1175/BAMS-D-13-00292.1.

David, N. *et al.* (2021) 'On the Power of Microwave Communication Data to Monitor Rain for Agricultural Needs in Africa', *Water 2021, Vol. 13, Page 730*, 13(5), p. 730. doi:10.3390/W13050730.

David, N., Alpert, P. and Messer, H. (2009) 'Technical Note: Novel method for water vapour monitoring using wireless communication networks measurements', *Atmospheric Chemistry and Physics*, 9(7), pp. 2413–2418. doi:10.5194/acp-9-2413-2009.

David, N., Alpert, P. and Messer, H. (2013) 'The potential of commercial microwave networks to monitor dense fog-feasibility study', 118(20). doi:10.1002/2013JD020346.

Davis, S. *et al.* (2022) 'A Flood Forecasting Framework Coupling a High Resolution WRF Ensemble With an Urban Hydrologic Model', *Frontiers in Earth Science*, 10, p. 883842. doi:10.3389/FEART.2022.883842/BIBTEX.

Dawdy, D.R. and Bergmann, J.M. (1969) 'Effect of rainfall variability on streamflow simulation', *Water Resources Research*, 5(5), pp. 958–966. doi:10.1029/WR005I005P00958.

Delrieu, G. *et al.* (1999) 'Attenuation in Rain for X- and C-Band Weather Radar Systems: Sensitivity with respect to the Drop Size Distribution', *Journal of Applied Meteorology*, 38(1), pp. 57–68. doi:10.1175/1520-0450(1999)038<0057:AIRFXA>2.0.CO;2.

Dezetter, A. *et al.* (2008) 'Simulation of runoff in West Africa: Is there a single data-model combination that produces the best simulation results?', *Journal of Hydrology*, 354(1–4), pp. 203–212. doi:10.1016/J.JHYDROL.2008.03.014.

Ditthakit, P. *et al.* (2021) 'Performance Evaluation of a Two-Parameters Monthly Rainfall-Runoff Model in the Southern Basin of Thailand', *Water 2021, Vol. 13, Page 1226*, 13(9), p. 1226. doi:10.3390/W13091226.

Donat, M.G. *et al.* (2016) 'More extreme precipitation in the world's dry and wet regions', *Nature Climate Change 2016 6:5*, 6(5), pp. 508–513. doi:10.1038/nclimate2941.

Donoho, D.L. (1995) 'De-Noising by Soft-Thresholding', *IEEE Transactions on Information Theory*, 41(3), pp. 613–627. doi:10.1109/18.382009.

Dragomiretskiy, K. and Zosso, D. (2014) 'Variational mode decomposition', *IEEE Transactions on Signal Processing*, 62(3), pp. 531–544. doi:10.1109/TSP.2013.2288675.

Duc, L. and Sawada, Y. (2023) 'A signal-processing-based interpretation of the Nash-Sutcliffe efficiency', *Hydrology and Earth System Sciences*, 27(9), pp. 1827–1839. doi:10.5194/HESS-27-1827-2023.

Durga Rao, K.H.V., Shravya, A. and Dadhwal, V.K. (2020) 'A novel method of satellite based river discharge estimation using river hydraulic geometry through genetic algorithm technique', *Journal of Hydrology*, 589, p. 125361. doi:10.1016/J.JHYDROL.2020.125361.

Eckhardt, K. (2005) 'How to construct recursive digital filters for baseflow separation', *Hydrological Processes*, 19(2), pp. 507–515. doi:10.1002/HYP.5675.

Edijatno (1991) *Mise au point d'un modèle élémentaire pluie-débit au pas de temps journalier*. Université Louis Pasteur.

Edijatno *et al.* (1999) 'GR3J: a daily watershed model with three free parameters', *Hydrological Sciences Journal*, 44(2), pp. 263–277. doi:10.1080/02626669909492221.

Edijatno and Michel, C. (1989) 'Un modèle pluie-débit journalier à trois paramètres', *La Houille Blanche*, 75(2), pp. 113–122. doi:10.1051/lhb/1989007.

Edwards, J. (2019) *Weather radar to be installed at Hindon*, *Otago Daily Times Online News*. Available at: https://www.odt.co.nz/news/dunedin/weather-radar-be-installed-hindon (Accessed: 13 January 2020).

Elshorbagy, A. *et al.* (2010) 'Experimental investigation of the predictive capabilities of data driven modeling techniques in hydrology - Part 1: Concepts and methodology', *Hydrology and Earth System Sciences*, 14(10), pp. 1931–1941. doi:10.5194/HESS-14-1931-2010.

Entekhabi, D. *et al.* (2010) 'The soil moisture active passive (SMAP) mission', *Proceedings of the IEEE*, 98(5), pp. 704–716. doi:10.1109/JPROC.2010.2043918.

Eshel, A. *et al.* (2017) 'On the Use of Measurements from a Commercial Microwave Link for Evaluation of Flash Floods in Arid Regions', *Atmospheric Chemistry and Physics Discussions*, (December), pp. 1–25. doi:10.5194/acp-2017-963.

*Fast Fourier Transformation FFT - Basics* (no date). Available at: https://www.nti-audio.com/en/support/know-how/fast-fourier-transform-fft (Accessed: 22 August 2023).

Feldman, M. (2006) 'Time-varying vibration decomposition and analysis based on the Hilbert transform', *Journal of Sound and Vibration*, 295(3–5), pp. 518–530. doi:10.1016/J.JSV.2005.12.058.

Fencl, Martin *et al.* (2015a) 'Commercial microwave links instead of rain gauges: fiction or reality?', *Water Science and Technology*, 71(1), pp. 31–37. doi:10.2166/wst.2014.466.

Fencl, Martin *et al.* (2015b) 'Commercial microwave links instead of rain gauges: Fiction or reality?', *Water Science and Technology*, 71(1), pp. 31–37. doi:10.2166/wst.2014.466.

Fencl, M *et al.* (2015) 'Dynamics of wet antenna attenuation', in *10th International Workshop on Precipitation in Urban Areas*. Pontresina, Switzerland. Available at: https://www.researchgate.net/publication/317345673_Dynamics_of_wet_antenna_attenuation?channel=doi&linkId=593530b945851553b6eed523&showFulltext=true (Accessed: 16 January 2020).

Fencl, M. *et al.* (2017) 'Gauge-adjusted rainfall estimates from commercial microwave links', *Hydrology and Earth System Sciences*, 21(1), pp. 617–634. doi:10.5194/hess-21-617-2017.

Fencl, M. *et al.* (2019) 'Quantifying Wet Antenna Attenuation in 38-GHz Commercial Microwave Links of Cellular Backhaul', *IEEE Geoscience and Remote Sensing Letters*, 16(4), pp. 514–518. doi:10.1109/LGRS.2018.2876696.

Fencl, M. *et al.* (2020) 'Atmospheric observations with E-band microwave links - Challenges and opportunities', *Atmospheric Measurement Techniques*, 13(12), pp. 6559–6578. doi:10.5194/AMT-13-6559-2020.

Feng, Z., Zhang, D. and Zuo, M.J. (2017) 'Adaptive Mode Decomposition Methods and Their Applications in Signal Analysis for Machinery Fault Diagnosis: A Review With Examples', *IEEE Access*, 5, pp. 24301–24331. doi:10.1109/ACCESS.2017.2766232.

Fenicia, F. *et al.* (2012) 'Microwave links for rainfall estimation in an urban environment: Insights from an experimental setup in Luxembourg-City', *Journal of Hydrology*, 464–465, pp. 69–78. doi:10.1016/j.jhydrol.2012.06.047.

Flores, N. *et al.* (2021) 'Comparison of Three Daily Rainfall-Runoff Hydrological Models Using Four Evapotranspiration Models in Four Small Forested Watersheds with Different Land Cover in South-Central Chile', *Water 2021, Vol. 13, Page 3191*, 13(22), p. 3191. doi:10.3390/W13223191.

Foehn, A. *et al.* (2016) 'Spatialization of precipitation data for flood forecasting applied to the Upper Rhone River basin', in.

Foehn, A. *et al.* (2018) 'Spatial interpolation of precipitation from multiple rain gauge networks and weather radar data for operational applications in Alpine catchments', *Journal of Hydrology*, 563, pp. 1092–1110. doi:10.1016/j.jhydrol.2018.05.027.

Frei, M.G. and Osorio, I. (2006) 'Intrinsic time-scale decomposition: timefrequencyenergy analysis and real-time filtering of non-stationary signals', *Proceedings of the Royal Society A: Mathematical, Physical and Engineering Sciences*, 463(2078), pp. 321–342. doi:10.1098/RSPA.2006.1761.

Frezghi, M. and Smithers, J. (2008) 'Merged rainfall fields for continuous simulation modelling (CSM)', *Water SA*, 34(5), pp. 523–528. Available at: http://www.scielo.org.za/scielo.php?script=sci_arttext&pid=S1816-79502008000500001.

Fu, Q. (2015) 'RADIATION TRANSFER IN THE ATMOSPHERE | Cloud-Radiative Processes', in *Encyclopedia of Atmospheric Sciences*. Elsevier, pp. 13–15. doi:10.1016/B978-0-12-382225-3.00338-8.

García-Etxarri, A. *et al.* (2011) 'Strong magnetic response of submicron Silicon particles in the infrared', *Optics Express*, 19(6), p. 4815. doi:10.1364/oe.19.004815.

Gazit, L. and Messer, H. (2018) 'Sufficient Conditions for Reconstructing 2-D Rainfall Maps', *IEEE Transactions on Geoscience and Remote Sensing*, 56(11), pp. 6334–6343. doi:10.1109/TGRS.2018.2836998.

Geetikaverma and Singh, V. (2018) 'Empirical Wavelet Transform & its Comparison with Empirical Mode Decomposition: A review', *International Journal of Engineering Research & Technology*, 4(15). doi:10.17577/IJERTCONV4IS15009.

Gilles, J. (2013) 'Empirical wavelet transform', *IEEE Transactions on Signal Processing*, 61(16), pp. 3999–4010. doi:10.1109/TSP.2013.2265222.

Gires, A. *et al.* (2014) 'Influence of small scale rainfall variability on standard comparison tools between radar and rain gauge data', *Atmospheric Research*, 138, pp. 125–138. doi:10.1016/J.ATMOSRES.2013.11.008.

Giuli, D. *et al.* (1991) 'Tomographic reconstruction of rainfall fields through microwave attenuation

measurements', *Journal of Applied Meteorology*, 30(9), pp. 1323–1340. doi:10.1175/1520-0450(1991)030<1323:TRORFT>2.0.CO;2.

Giuli, D., Facheris, L. and Tanelli, S. (1999) 'Microwave tomographic inversion technique based on stochastic approach for rainfall fields monitoring', *IEEE Transactions on Geoscience and Remote Sensing*, 37(5), pp. 2536–2555. doi:10.1109/36.789649.

Gleason, C.J. and Durand, M.T. (2020) 'Remote Sensing of River Discharge: A Review and a Framing for the Discipline', *Remote Sensing 2020, Vol. 12, Page 1107*, 12(7), p. 1107. doi:10.3390/RS12071107.

Goldshtein, O., Messer, H. and Zinevich, A. (2009) 'Rain Rate Estimation Using Measurements From Commercial Telecommunications Links', *IEEE Transactions on Signal Processing*, 57(4), pp. 1616–1625. doi:10.1109/TSP.2009.2012554.

Goodison, B.E. (1978) 'ACCURACY OF CANADIAN SNOW GAGE MEASUREMENTS.', *Journal of Applied Meteorology*, 17(10), pp. 1542–1548. doi:10.1175/1520-0450(1978)017<1542:AOCSGM>2.0.CO;2.

Gosset, M. *et al.* (2015) 'Improving Rainfall Measurement in Gauge Poor Regions Thanks to Mobile Telecommunication Networks', *Bulletin of the American Meteorological Society*, 97(3), pp. ES49–ES51. doi:10.1175/BAMS-D-15-00164.1.

Goudenhoofdt, E. and Delobbe, L. (2009) 'Evaluation of radar-gauge merging methods for quantitative precipitation estimates', *Hydrology and Earth System Sciences*, 13(2), pp. 195–203. doi:10.5194/HESS-13-195-2009.

*GPM, NASA Global Precipitation Measurement Mission* (2023). Available at: https://gpm.nasa.gov/data/sources/giovanni.

Graf, M. *et al.* (2020) 'Rainfall estimation from a German-wide commercial microwave link network: optimized processing and validation for 1 year of data', *Hydrology and Earth System Sciences*, 24(6), pp. 2931–2950. doi:10.5194/hess-24-2931-2020.

Green, M. (1970) 'Effects of exposure on the catch of rain gauges', *Journal of Hydrology (NZ)*, 9(2), pp. 55–71. Available at: http://www.hydrologynz.org.nz/journal_article.php?article_id=678.

Griffiths, G.W. and Schiesser, W.E. (2009) 'Linear and nonlinear waves', *Scholarpedia*, 4(7), p. 4308. doi:10.4249/SCHOLARPEDIA.4308.

Groisman, P.Y. and Legates, D.R. (1994) 'The accuracy of United States precipitation data', *Bulletin - American Meteorological Society*, 75(2), pp. 215–227. doi:10.1175/1520-0477(1994)075<0215:TAOUSP>2.0.CO;2.

*GSMA | WRC-23 – Keep up to date with mobile - Spectrum* (2023). Available at: https://www.gsma.com/spectrum/wrc-series/ (Accessed: 13 December 2023).

Gunn, R. and Kinzer, G.D. (1949) 'THE TERMINAL VELOCITY OF FALL FOR WATER DROPLETS IN STAGNANT AIR', *Journal of Meteorology*, 6(4), pp. 243–248. doi:10.1175/1520-0469(1949)006<0243:ttvoff>2.0.co;2.

Gupta, H. V. *et al.* (2009) 'Decomposition of the mean squared error and NSE performance criteria: Implications for improving hydrological modelling', *Journal of Hydrology*, 377(1–2), pp. 80–91. doi:10.1016/J.JHYDROL.2009.08.003.

Habi, H.V. and Messer, H. (2018) 'Wet-Dry Classification Using LSTM and Commercial Microwave Links', in *2018 IEEE 10th Sensor Array and Multichannel Signal Processing Workshop (SAM)*. IEEE, pp. 149–153. doi:10.1109/SAM.2018.8448679.

Hamel, P. *et al.* (2017) 'Predicting dry-season flows with a monthly rainfall–runoff model: Performance for gauged and ungauged catchments', *Hydrological Processes*, 31(22), pp. 3844–3858. doi:10.1002/HYP.11298.

Han, J., Kamber, M. and Pei, J. (2012) 'Data Preprocessing', in *Data Mining*. 3rd edn. Morgan Kaufmann, pp. 83–124. doi:10.1016/B978-0-12-381479-1.00003-4.

Hansen, M. (2011a) *A New Map of New Zealand's Wireless Networks*. Available at: https://www.markhansen.co.nz/nz-wireless-map/ (Accessed: 14 January 2020).

Hansen, M. (2011b) *NZ Wireless Map*. Available at: https://wirelessmap.markhansen.co.nz/ (Accessed: 14 January 2020).

Hazenberg, P., Leijnse, H. and Uijlenhoet, R. (2011) 'Radar rainfall estimation of stratiform winter precipitation in the Belgian Ardennes', *Water Resources Research*, 47(2). doi:10.1029/2010WR009068.

Hecht, E. (2002) *Optics*. 4th edn. Addison Wesley.

Henao Salgado, M.J. and Zambrano Nájera, J. (2022) 'Assessing Flood Early Warning Systems for Flash Floods', *Frontiers in Climate*, 4, p. 34. doi:10.3389/FCLIM.2022.787042/BIBTEX.

Ho, C.M. *et al.* (2004) *Estimation of Microwave Power Margin Losses Due to Earth's Atmosphere and Weather in the Frequency Range of 3–30 GHz, Report JPL D-27879. Prepared for the United States Air Force Spectrum Efficient Technologies for Test and Evaluation Advanced Range Telem*. Available at: https://descanso.jpl.nasa.gov/propagation/Ka_Band/JPL_D27879.pdf.

Holt, A.R. *et al.* (2000) 'Measurement of rainfall by dual-wavelength microwave attenuation', *Electronics Letters*, 36(25), pp. 2099–2101. doi:10.1049/el:20001468.

Hornberger, G.M. *et al.* (1985) 'Shenandoah Watershed Study: Calibration of a Topography-Based, Variable Contributing Area Hydrological Model to a Small Forested Catchment', *Water Resources Research*, 21(12), pp. 1841–1850. doi:10.1029/WR021i012p01841.

Hou, A.Y. *et al.* (2014) 'The Global Precipitation Measurement Mission', *Bulletin of the American Meteorological Society*, 95(5), pp. 701–722. doi:10.1175/BAMS-D-13-00164.1.

Hrachowitz, M. *et al.* (2013) 'A decade of Predictions in Ungauged Basins (PUB)—a review', *https://doi.org/10.1080/02626667.2013.803183*, 58(6), pp. 1198–1255. doi:10.1080/02626667.2013.803183.

Hsu, K. -l, Gupta, H.V. and Sorooshian, S. (1995) 'Artificial Neural Network Modeling of the Rainfall-Runoff Process', *Water Resources Research*, 31(10), pp. 2517–2530. doi:10.1029/95WR01955.

Hu, Q. *et al.* (2019) 'Rainfall Spatial Estimations: A Review from Spatial Interpolation to Multi-Source Data Merging', *Water 2019, Vol. 11, Page 579*, 11(3), p. 579. doi:10.3390/W11030579.

Huang, H. *et al.* (2023) 'Precipitation Monitoring Using Commercial Microwave Links: Current Status, Challenges and Prospectives', *Remote Sensing 2023, Vol. 15, Page 4821*, 15(19), p. 4821. doi:10.3390/RS15194821.

Huang, H. and Pan, J. (2006) 'Speech pitch determination based on Hilbert-Huang transform', *Signal Processing*, 86(4), pp. 792–803. doi:10.1016/J.SIGPRO.2005.06.011.

Huang, N.E. *et al.* (1998) 'The empirical mode decomposition and the Hilbert spectrum for nonlinear and non-stationary time series analysis', *Proceedings of the Royal Society of London. Series A: Mathematical, Physical and Engineering Sciences*, 454(1971), pp. 903–995. doi:10.1098/rspa.1998.0193.

Huang, N.E. *et al.* (2003) 'Applications of Hilbert-Huang transform to non-stationary financial time series analysis', *Applied Stochastic Models in Business and Industry*, 19, pp. 245–268. doi:10.1002/ASMB.506.

Huang, N.E. and Wu, Z. (2008) 'A review on Hilbert-Huang transform: Method and its applications to geophysical studies', *Reviews of Geophysics*, 46(2). doi:10.1029/2007RG000228.

Huffman, G. (2022) *IMERG precipitation algorithm and the Global Precipitation Measurement (GPM) Mission | Climate Data Guide*. Available at: https://climatedataguide.ucar.edu/climate-data/gpm-global-precipitation-measurement-mission (Accessed: 12 April 2023).

Iatsenko, D., McClintock, P.V.E. and Stefanovska, A. (2015) 'Nonlinear mode decomposition: A noise-robust, adaptive decomposition method', *Physical Review E - Statistical, Nonlinear, and Soft Matter Physics*, 92(3), p. 032916. doi:10.1103/PHYSREVE.92.032916/FIGURES/13/MEDIUM.

INOUE, S. *et al.* (2009) 'Comparison of Four Instruments for Measuring Solid Precipitation Below the Freezing Point Condition', *Journal of Agricultural Meteorology*, 65(1), pp. 77–82. doi:10.2480/agrmet.65.1.3.

Ippolito, L.J. (1989) *NASA Reference Publication 1082(04) Propagation Effects Handbook for Satellite Systems Design Satellite Links With Techniques for System Design Fourth Edition*.

Ishii, S. *et al.* (2016) 'Rain Attenuation in the Microwave-to-Terahertz Waveband', *Wireless Engineering and Technology*, 7(2), pp. 59–66. doi:10.4236/WET.2016.72006.

Ishimaru, A. *et al.* (1982) 'Multiple scattering calculations of rain effects', *Radio Science*, 17(6), pp. 1425–1433. doi:10.1029/RS017i006p01425.

Ishimaru, A. and Cheung, R.L.-T. (1980a) 'Multiple-scattering effect on radiometric determination of rain attenuation at millimeter wavelengths', *Radio Science*, 15(3), pp. 507–516. doi:10.1029/RS015i003p00507.

Ishimaru, A. and Cheung, R.L.-T. (1980b) 'Multiple scattering effects on wave propagation due to rain', *Annales Des Telecommunications*, 35(11–12), pp. 373–379. doi:10.1007/BF03003515.

ITU-R (2005) *Recommendation ITU-R P.838-3: Specific attenuation model for rain use in prediction methods*. Available at: https://www.itu.int/dms_pubrec/itu-r/rec/p/R-REC-P.838-3-200503-I!!PDF-E.pdf.

ITU-R (2012) 'P.837-6: Characteristics of precipitation for propagation modeling', *Radiowave Propagation*, 6. Available at: https://www.itu.int/dms_pubrec/itu-r/rec/p/R-REC-P.837-7-201706-I!!PDF-E.pdf.

ITU-R (2015) *V.431 : Nomenclature of the frequency and wavelength bands used in telecommunications*. Available at: https://www.itu.int/rec/R-REC-V.431-8-201508-I/en (Accessed: 28 December 2019).

ITU-R (2016) 'P.676-11: Attenuation by atmospheric gases', *P Series Radiowave propagation*, 11. Available at: http://www.itu.int/dms_pubrec/itu-r/rec/p/R-REC-P.676-11-201609-I!!PDF-E.pdf.

Jakeman, A.J. and Hornberger, G.M. (1993) 'How much complexity is warranted in a rainfall-runoff model?', *Water Resources Research*, 29(8), pp. 2637–2649. doi:10.1029/93WR00877.

Janco, R., Ostrometzky, J. and Messer, H. (2023) 'In-City Rain Mapping from Commercial Microwave Links—Challenges and Opportunities', *Sensors 2023, Vol. 23, Page 4653*, 23(10), p. 4653. doi:10.3390/S23104653.

Jewell, S.A. and Gaussiat, N. (2015) 'An assessment of kriging-based rain-gauge–radar merging

techniques', *Quarterly Journal of the Royal Meteorological Society*, 141(691), pp. 2300–2313. doi:10.1002/QJ.2522.

Jiang, H., Sano, M. and Sekine, M. (1997) 'Weibull raindrop-size distribution and its application to rain attenuation', *IEE Proceedings: Microwaves, Antennas and Propagation*, 144(3), pp. 197–200. doi:10.1049/ip-map:19971193.

John A. Richards (2008) *Radio wave propagation An Introduction for the Non-Specialist*, *Springer*.

John Price, T.G. (1993) *Telecommunications Engineer's Reference Book*, *Telecommunications Engineer's Reference Book*. Edited by F. Mazda. Elsevier. doi:10.1016/c2013-0-06529-2.

Jones, D.M.A. (1959) 'THE SHAPE OF RAINDROPS', *Journal of Meteorology*, 16(5), pp. 504–510. doi:10.1175/1520-0469(1959)016<0504:tsor>2.0.co;2.

Kantor, P. and Bito, J. (2015) 'Comparison of rain attenuation prediction models for terrestrial links and their impact on the performance of link transformation', in *2015 17th International Conference on Transparent Optical Networks (ICTON)*. IEEE, pp. 1–4. doi:10.1109/ICTON.2015.7193500.

Kathiravelu, G., Lucke, T. and Nichols, P. (2016) 'Rain Drop Measurement Techniques: A Review', *Water*, 8(1), p. 29. doi:10.3390/w8010029.

Kesavan, U. *et al.* (2014) 'Rain Attenuation Prediction for Higher Frequencies in Microwave Communication Using Frequency Scaling Technique', in *2014 International Conference on Computer and Communication Engineering*. IEEE, pp. 217–219. doi:10.1109/ICCCE.2014.69.

Kharadly, M.M.Z. and Ross, R. (2001) 'Effect of wet antenna attenuation on propagation data statistics', *IEEE Transactions on Antennas and Propagation*, 49(8), pp. 1183–1191. doi:10.1109/8.943313.

Kidd, C. (2001) 'Satellite rainfall climatology: a review', *International Journal of Climatology*, 21(9), pp. 1041–1066. doi:10.1002/JOC.635.

Kidd, C. *et al.* (2003) 'Satellite Rainfall Estimation Using Combined Passive Microwave and Infrared Algorithms in: Journal of Hydrometeorology Volume 4 Issue 6 (2003)', *Journal of Hydrometeorology*, 4(6), pp. 1088–1104. Available at: https://journals.ametsoc.org/view/journals/hydr/4/6/1525-7541_2003_004_1088_sreucp_2_0_co_2.xml (Accessed: 12 April 2023).

Kidd, C. *et al.* (2017) 'So, How Much of the Earth's Surface Is Covered by Rain Gauges?', *Bulletin of the American Meteorological Society*, 98(1), pp. 69–78. doi:10.1175/BAMS-D-14-00283.1.

Kidd, C. and Huffman, G. (2011a) 'Global precipitation measurement', *Meteorological Applications*, 18(3), pp. 334–353. doi:10.1002/met.284.

Kidd, C. and Huffman, G. (2011b) 'Global precipitation measurement', *Meteorological Applications*, 18(3), pp. 334–353. doi:10.1002/met.284.

Kim, M.-S. and Kwon, B. (2018) 'Rainfall Detection and Rainfall Rate Estimation Using Microwave Attenuation', *Atmosphere*, 9(8), p. 287. doi:10.3390/atmos9080287.

Knoben, W.J.M., Freer, J.E. and Woods, R.A. (2019) 'Technical note: Inherent benchmark or not? Comparing Nash-Sutcliffe and Kling-Gupta efficiency scores', *Hydrology and Earth System Sciences*, 23(10), pp. 4323–4331. doi:10.5194/HESS-23-4323-2019.

Koblinsky, C.J. *et al.* (1993) 'Measurement of river level variations with satellite altimetry', *Water Resources Research*, 29(6), pp. 1839–1848. doi:10.1029/93WR00542.

Koppenhoefer, K. (2013) *Mesh Refinement for Wave Problems | COMSOL Blog*. Available at:

https://www.comsol.com/blogs/mesh-refinement-for-wave-problems/ (Accessed: 26 January 2020).

Kotlarchyk, M. (1999) 'Scattering Theory', in *Encyclopedia of Spectroscopy and Spectrometry*. Elsevier, pp. 2074–2084. doi:10.1006/rwsp.2000.0274.

Kouraev, A. V. *et al.* (2004) 'Ob' river discharge from TOPEX/Poseidon satellite altimetry (1992–2002)', *Remote Sensing of Environment*, 93(1–2), pp. 238–245. doi:10.1016/J.RSE.2004.07.007.

Krajewski, W.F. *et al.* (1991) 'A Monte Carlo Study of rainfall sampling effect on a distributed catchment model', *Water Resources Research*, 27(1), pp. 119–128. doi:10.1029/90WR01977.

Krajewski, W.F. *et al.* (2006) 'A remote sensing observatory for hydrologic sciences: A genesis for scaling to continental hydrology', *Water Resources Research*, 42(7). doi:10.1029/2005WR004435.

Krajewski, W.F., Villarini, G. and Smith, J.A. (2010) 'Radar-rainfall uncertainties:Where are we after thirty years of effort', *Bulletin of the American Meteorological Society*, 91(1), pp. 87–94. doi:10.1175/2009BAMS2747.1.

Kucera, P.A. *et al.* (2013) 'Precipitation from Space: Advancing Earth System Science', *Bulletin of the American Meteorological Society*, 94(3), pp. 365–375. doi:10.1175/BAMS-D-11-00171.1.

Kumari, N. *et al.* (2021) 'Identification of Suitable Hydrological Models for Streamflow Assessment in the Kangsabati River Basin, India, by Using Different Model Selection Scores', *Natural Resources Research*, 30(6), pp. 4187–4205. doi:10.1007/S11053-021-09919-0/FIGURES/7.

Lanza, L.G. and Stagi, L. (2006) *ON THE QUALITY OF TIPPING-BUCKET RAIN INTENSITY MEASUREMENTS*.

Latron, J. and Gallart, F. (2008) 'Runoff generation processes in a small Mediterranean research catchment (Vallcebre, Eastern Pyrenees)', *Journal of Hydrology*, 358(3–4), pp. 206–220. doi:10.1016/j.jhydrol.2008.06.014.

Laurell, H. and Hillborg, J. (2018) *Towards a nanometer thick flat lens*.

Le-Wei Li *et al.* (1995) 'Microwave attenuation by realistically distorted raindrops: Part I. Theory', *IEEE Transactions on Antennas and Propagation*, 43(8), pp. 811–822. doi:10.1109/8.402200.

Lee, G.W. and Zawadzki, I. (2005) 'Variability of Drop Size Distributions: Noise and Noise Filtering in Disdrometric Data', *Journal of Applied Meteorology*, 44(5), pp. 634–652. doi:10.1175/JAM2222.1.

Leijnse, H. *et al.* (2010) 'Errors and Uncertainties in Microwave Link Rainfall Estimation Explored Using Drop Size Measurements and High-Resolution Radar Data', *Journal of Hydrometeorology*, 11(6), pp. 1330–1344. doi:10.1175/2010JHM1243.1.

Leijnse, H., Uijlenhoet, R. and Berne, A. (2010a) 'Errors and uncertainties in microwave link rainfall estimation explored using drop size measurements and high-resolution radar data', *Journal of Hydrometeorology*, 11(6), pp. 1330–1344. doi:10.1175/2010JHM1243.1.

Leijnse, H., Uijlenhoet, R. and Berne, A. (2010b) 'Errors and Uncertainties in Microwave Link Rainfall Estimation Explored Using Drop Size Measurements and High-Resolution Radar Data', *Journal of Hydrometeorology*, 11(6), pp. 1330–1344. doi:10.1175/2010JHM1243.1.

Leijnse, H., Uijlenhoet, R. and Stricker, J.N.M. (2007a) 'Hydrometeorological application of a microwave link: 2. Precipitation H.', *Water Resources Research*, 43(4). Available at: http://doi.wiley.com/10.1029/2006WR004988 (Accessed: 1 May 2019).

Leijnse, H., Uijlenhoet, R. and Stricker, J.N.M. (2007b) 'Rainfall measurement using radio links from cellular communication networks', *Water Resources Research*, 43(3). doi:10.1029/2006WR005631.

Leijnse, H., Uijlenhoet, R. and Stricker, J.N.M. (2008a) 'Microwave link rainfall estimation: Effects of link length and frequency, temporal sampling, power resolution, and wet antenna attenuation', *Advances in Water Resources*, 31(11), pp. 1481–1493. doi:10.1016/j.advwatres.2008.03.004.

Leijnse, H., Uijlenhoet, R. and Stricker, J.N.M. (2008b) 'Microwave link rainfall estimation: Effects of link length and frequency, temporal sampling, power resolution, and wet antenna attenuation', *Advances in Water Resources*, 31(11), pp. 1481–1493. doi:10.1016/j.advwatres.2008.03.004.

Leijnse, H., Uijlenhoet, R. and Stricker, J.N.M. (2008c) 'Microwave link rainfall estimation: Effects of link length and frequency, temporal sampling, power resolution, and wet antenna attenuation', *Advances in Water Resources*, 31(11), pp. 1481–1493. doi:10.1016/j.advwatres.2008.03.004.

León, O., Hernández-Serrano, J. and Soriano, M. (2011) 'SHORT COMMUNICATION Rain attenuation measurements over terrestrial microwave links operating at 15 GHz in Malaysia', *International Journal of Communication Systems*, 23(5), pp. 633–652. doi:10.1002/dac.

van Leth, T.C. *et al.* (2017) 'An urban microwave link rainfall measurement campaign', *Atmospheric Measurement Techniques Discussions*, (December), pp. 1–27. doi:10.5194/amt-2017-404.

van Leth, T.C. *et al.* (2018) 'A measurement campaign to assess sources of error in microwave link rainfall estimation', *Atmospheric Measurement Techniques*, 11(8), pp. 4645–4669. doi:10.5194/amt-11-4645-2018.

van Leth, T.C. *et al.* (2019) 'Estimating raindrop size distributions using microwave link measurements', *Atmospheric Measurement Techniques Discussions*, (April), pp. 1–27. doi:10.5194/amt-2019-51.

Leung, T. and Zhao, T. (2021) 'Financial time series analysis and forecasting with Hilbert–Huang transform feature generation and machine learning', *Applied Stochastic Models in Business and Industry*, 37(6), pp. 993–1016. doi:10.1002/ASMB.2625.

Levizzani, Vincenzo and Bauer, Peter and Turk, F.J. (2007) *Measuring precipitation from space: EURAINSAT and the future*. Springer Science \& Business Media.

Li, X. *et al.* (2019) 'A Novel Signal Separation and De-Noising Technique for Doppler Radar Vital Signal Detection', *Sensors (Basel, Switzerland)*, 19(21). doi:10.3390/S19214751.

Li, X. and Willems, P. (2020) 'A Hybrid Model for Fast and Probabilistic Urban Pluvial Flood Prediction', *Water Resources Research*, 56(6), p. e2019WR025128. doi:10.1029/2019WR025128.

Lian, B. *et al.* (2022) 'A Review on Rainfall Measurement Based on Commercial Microwave Links in Wireless Cellular Networks', *Sensors 2022, Vol. 22, Page 4395*, 22(12), p. 4395. doi:10.3390/S22124395.

Liang, H., Lin, Q.H. and Chen, J.D.Z. (2004) 'Application of the Empirical Mode Decomposition to the analysis of esophageal manometric data in gastroesophageal reflux disease', *Conference proceedings : ... Annual International Conference of the IEEE Engineering in Medicine and Biology Society. IEEE Engineering in Medicine and Biology Society. Annual Conference*, 2006, pp. 620–623. doi:10.1109/IEMBS.2004.1403234.

Liberman, Y. *et al.* (2014) 'New algorithm for integration between wireless microwave sensor network and radar for improved rainfall measurement and mapping', *Atmospheric Measurement Techniques*, 7(10), pp. 3549–3563. doi:10.5194/amt-7-3549-2014.

Ligges, U. *et al.* (2021) *CRAN - Package signal*. Available at: https://cran.r-project.org/web/packages/signal/ (Accessed: 11 November 2023).

Lin, D.P. and Chen, H.Y. (2001) 'Volume integral equation solution of extinction cross section by

raindrops in the range 0.6-100 GHz', *IEEE Transactions on Antennas and Propagation*, 49(3), pp. 494–499. doi:10.1109/8.918626.

Lin, J.C. and Ishimaru, A. (1971) *Propagation of Millimeter Waves in Rain*. Available at: https://apps.dtic.mil/docs/citations/AD0735291 (Accessed: 18 March 2020).

Lin, L., Wang, Y. and Zhou, H. (2011) 'ITERATIVE FILTERING AS AN ALTERNATIVE ALGORITHM FOR EMPIRICAL MODE DECOMPOSITION', *https://doi.org/10.1142/S179353690900028X*, 1(4), pp. 543–560. doi:10.1142/S179353690900028X.

Lin, S.H. (1973) 'Statistical Behavior of Rain Attenuation', *Bell System Technical Journal*, 52(4), pp. 557–581. doi:10.1002/j.1538-7305.1973.tb01977.x.

Liou, K.-N. (2002) *An introduction to atmospheric radiation*. Academic Press.

Liu, X. *et al.* (2023) 'Rainfall Monitoring Using a Microwave Links Network: A Long-Term Experiment in East China', *Advances in Atmospheric Sciences*, 40(9), pp. 1567–1583. doi:10.1007/S00376-023-2104-Z/METRICS.

Loague, K.M. and Freeze, R.A. (1985) 'A Comparison of Rainfall-Runoff Modeling Techniques on Small Upland Catchments', *Water Resources Research*, 21(2), pp. 229–248. doi:10.1029/WR021i002p00229.

Louis J. Ippolito, J. (1986) *RADIOWAVE PROPAGATION IN SATELLITE COMMUNICATIONS*. New York: Van Nostrand Reinhold Company Inc.

Luyckx, G. and Berlamont, J. (2001) 'Simplified method to correct rainfall measurements from tipping bucket rain gauges', in *Urban Drainage Modeling*, pp. 767–776. doi:10.1061/40583(275)72.

M. Hunger and P. Doll (2008) 'Value of river discharge data for global-scale hydrological modeling', *Hydrology and Earth System Sciences*, 12(3), pp. 841–861. Available at: https://hess.copernicus.org/articles/12/841/2008/hess-12-841-2008.html (Accessed: 14 April 2023).

Machado, F. *et al.* (2011) 'Monthly rainfall–runoff modelling using artificial neural networks', *https://doi.org/10.1080/02626667.2011.559949*, 56(3), pp. 349–361. doi:10.1080/02626667.2011.559949.

Manggau, F.X. *et al.* (2018) 'The Performance Of Wireless 802.11 B/G For Data Acquisition Utilization', in *The 3rd International Conference on Energy, Environmental and Information System (ICENIS 2018)*. E3S Web of Conferences. doi:doi.org/10.1051/e3sconf/20187313018.

Margrave, G.F. (1998) 'Theory of nonstationary linear filtering in the Fourier domain with application to time-variant filtering', *Geophysics*, 63(1), pp. 244–259. doi:10.1190/1.1444318.

Marshall, J.S. and Palmer, W.M.K. (1948) 'THE DISTRIBUTION OF RAINDROPS WITH SIZE', *Journal of Meteorology*, 5(4), pp. 165–166. doi:10.1175/1520-0469(1948)005<0165:TDORWS>2.0.CO;2.

Martínez-Sifuentes, A.R. *et al.* (2023) 'The Impact of Climate Change on Evapotranspiration and Flow in a Major Basin in Northern Mexico', *Sustainability 2023, Vol. 15, Page 847*, 15(1), p. 847. doi:10.3390/SU15010847.

MathWorks (2023a) *IIR Filter Design - MATLAB & Simulink - MathWorks Australia*. Available at: https://au.mathworks.com/help/signal/ug/iir-filter-design.html (Accessed: 22 August 2023).

MathWorks (2023b) *Practical Introduction to Frequency-Domain Analysis - MATLAB & Simulink Example - MathWorks Australia*. Available at: https://au.mathworks.com/help/signal/ug/practical-introduction-to-frequency-domain-analysis.html (Accessed: 22 August 2023).

McDonald, J.E. (1954) 'THE SHAPE AND AERODYNAMICS OF LARGE RAINDROPS', *http://dx.doi.org/10.1175/1520-0469(1954)011<0478:TSAAOL>2.0.CO;2* [Preprint]. doi:10.1175/1520-0469(1954)011<0478:TSAAOL>2.0.CO;2.

Medeiros Filho, F.C., Cole, R.S. and Sarma, A.D. (1986) 'MILLIMETRE-WAVE RAIN INDUCED ATTENUATION: THEORY AND EXPERIMENT.', *IEE Proceedings H: Microwaves, Antennas and Propagation*, 133(4), pp. 308–314. doi:10.1049/ip-h-2.1986.0054.

Melbourne Water (2021) *Hydrologic and hydraulic design*. Available at: https://www.melbournewater.com.au/building-and-works/developer-guides-and-resources/standards-and-specifications/hydrologic-and.

Melbourne Water (2022a) *Using our rainfall and river level app*. Available at: https://www.melbournewater.com.au/water-and-environment/water-management/rainfall-and-river-levels/understanding-our-rainfall-and (Accessed: 21 April 2023).

Melbourne Water (2022b) *Yarra River*. Available at: https://www.melbournewater.com.au/water-and-environment/water-management/rivers-and-creeks/yarra-river (Accessed: 19 April 2023).

Melbourne Water (2023) *Rainfall and river levels*. Available at: https://www.melbournewater.com.au/water-and-environment/water-management/rainfall-and-river-levels#/ (Accessed: 3 April 2023).

Meraki (2023) *Signal-to-Noise Ratio (SNR) and Wireless Signal Strength*, *Cisco*. Available at: https://documentation.meraki.com/MR/Wi-Fi_Basics_and_Best_Practices/Signal-to-Noise_Ratio_(SNR)_and_Wireless_Signal_Strength (Accessed: 17 October 2023).

Messer, H. (2006) 'Environmental Monitoring by Wireless Communication Networks', *Science*, 312(5774), pp. 713–713. doi:10.1126/science.1120034.

Messer, H. (2007) 'Rainfall monitoring using cellular networks', *IEEE Signal Processing Magazine*, 24(3). doi:10.1109/MSP.2007.361621.

Messer, H. and Sendik, O. (2015) 'A New Approach to Precipitation Monitoring: A critical survey of existing technologies and challenges', *IEEE Signal Processing Magazine*, 32(3), pp. 110–122. doi:10.1109/MSP.2014.2309705.

Messer, H., Zinevich, A. and Alpert, P. (2006) 'Environmental monitoring by wireless communication networks', *Science*, 312(5774), p. 713. doi:10.1126/science.1120034.

Messer, H., Zinevich, A. and Alpert, P. (2012) 'Environmental sensor networks using existing wireless communication systems for rainfall and wind velocity measurements', *IEEE Instrumentation & Measurement Magazine*, 15(2), pp. 32–38. doi:10.1109/MIM.2012.6174577.

Miao, C. *et al.* (2020) 'The Changing Relationship Between Rainfall and Surface Runoff on the Loess Plateau, China', *Journal of Geophysical Research: Atmospheres*, 125(8), p. e2019JD032053. doi:10.1029/2019JD032053.

Mie, G. (1908) 'Beiträge zur Optik trüber Medien, speziell kolloidaler Metallösungen', *Annalen der Physik*, 330(3), pp. 377–445. doi:10.1002/andp.19083300302.

*MiePlot* (no date). Available at: http://www.philiplaven.com/mieplot.htm (Accessed: 17 January 2020).

Mimikou, M., Rao, A.R. and Asce, M. (1983) 'Regional Monthly RainfallRunoff Model', *Journal of Water Resources Planning and Management*, 109(1), pp. 75–93. doi:10.1061/(ASCE)0733-9496(1983)109:1(75).

Min, S.K. *et al.* (2011) 'Human contribution to more-intense precipitation extremes', *Nature 2011 470:7334*, 470(7334), pp. 378–381. doi:10.1038/nature09763.

Minda, H. and Nakamura, K. (2005) 'High temporal resolution path-average rain gauge with 50-GHz band microwave', *Journal of Atmospheric and Oceanic Technology*, 22(2), pp. 165–179. doi:10.1175/JTECH-1683.1.

Mishchenko, M.I., Hovenier, J.W. and Travis, L.D. (2000) *Light scattering by nonspherical particles : theory, measurements, and applications*. Academic Press.

Mishchenko, M.I., Travis, L.D. and Mackowski, D.W. (1996) 'T-matrix computations of light scattering by nonspherical particles: A review', *Journal of Quantitative Spectroscopy and Radiative Transfer*, 55(5), pp. 535–575. doi:10.1016/0022-4073(96)00002-7.

Misra, A., B, K. and S, G. (2013) 'Noise Removal Techniques for Microwave Remote Sensing Radar Data and Its Evaluation', in *Computer Science & Information Technology ( CS & IT )*. Academy & Industry Research Collaboration Center (AIRCC), pp. 257–264. doi:10.5121/csit.2013.3629.

Molini, A., Lanza, L.G. and La Barbera, P. (2005) 'The impact of tipping-bucket raingauge measurement errors on design rainfall for urban-scale applications', *Hydrological Processes*, 19(5), pp. 1073–1088. doi:10.1002/hyp.5646.

Monash City Council (2020) *Monash Local Flood Guide*. Available at: https://www.ses.vic.gov.au/plan-and-stay-safe/flood-guides/monash-city-council.

Moriasi, D.N. *et al.* (2007) 'Model Evaluation Guidelines for Systematic Quantification of Accuracy in Watershed Simulations', *Transactions of the ASABE*, 50(3), pp. 885–900. doi:10.13031/2013.23153.

Mory, S. *et al.* (2024) 'Assessment of current and future trends in water resources in the Gambia River Basin in a context of climate change', *Environmental Sciences Europe 2024 36:1*, 36(1), pp. 1–21. doi:10.1186/S12302-024-00848-2.

Mouelhi, S. *et al.* (2006) 'Stepwise development of a two-parameter monthly water balance model', *Journal of Hydrology*, 318(1–4), pp. 200–214. doi:10.1016/J.JHYDROL.2005.06.014.

Murray, L. (2015) *Flying under the RADAR | MetService Blog*. Available at: https://blog.metservice.com/Radar (Accessed: 11 January 2020).

Nash, J.E. and Sutcliffe, J.V. (1970) 'River flow forecasting through conceptual models part I — A discussion of principles', *Journal of Hydrology*, 10(3), pp. 282–290. doi:10.1016/0022-1694(70)90255-6.

*National Institute of Water and Atmospheric (NIWA)- Welcome to the Climate Database* (no date). Available at: https://cliflo.niwa.co.nz/ (Accessed: 16 January 2020).

*National Water Account* (2015) *Australian Government, Bureau of Meteorology*. Available at: http://www.bom.gov.au/water/nwa/2015/melbourne/contextual/physicalinformation.shtml.

Nebuloni, R. *et al.* (2020) 'Rainfall estimate using Commercial Microwave Links (CML): first outcomes of the MOPRAM project', *EGU General Assembly* [Preprint]. doi:10.5194/EGUSPHERE-EGU2020-10407.

Nebuloni, R. *et al.* (2022) 'Comparison of CML Rainfall Data against Rain Gauges and Disdrometers in a Mountainous Environment', *Sensors 2022, Vol. 22, Page 3218*, 22(9), p. 3218. doi:10.3390/S22093218.

Neff, E.L. (1977) 'How much rain does a rain gage gage?', *Journal of Hydrology*, 35(3), pp. 213–220. doi:10.1016/0022-1694(77)90001-4.

Nespor, V. (2013) 'WIND INDUCED ERROR OF PRECIPITATION GAUGES', in *Operational Use of Radar Measurements in Precipitation for Switzerland*. Davos, Switzerland: World Meteorological Organization (WMO), COMMISSION FOR INSTRUMENTS AND METHODS OF OBSERVATION.

NIOSH (2019) *Advanced Tutorial on Wireless Communication and Electronic Tracking: Appendix B*, *The National Institute for Occupational Safety and Health (NIOSH)*. Available at: https://www.cdc.gov/niosh/mining/content/emergencymanagementandresponse/commtracking/advcommtrackingtutorialb.html (Accessed: 16 October 2023).

Norbiato, D. *et al.* (2009) 'Controls on event runoff coefficients in the eastern Italian Alps', *Journal of Hydrology*, 375(3–4), pp. 312–325. doi:10.1016/J.JHYDROL.2009.06.044.

Norbury, J.R. and White, W.J. (1971) 'A rapid-response rain gauge', *Journal of Physics E: Scientific Instruments*, 4(8), pp. 601–602. doi:10.1088/0022-3735/4/8/013.

Nounou, M.N. and Bakshi, B.R. (2000) 'Multiscale Methods for Denoising and Compression', in *Wavelets in Chemistry*. Elsevier, pp. 119–150. doi:10.1016/S0922-3487(00)80030-1.

Nupen., W. (1955) 'Annotated Bibliography on Radar as Applied to Cloud and Physics', *Meteorol Abstr Bibliogr*, 6, No 7, p. p 997-1050.

Obled, C., Wendling, J. and Beven, K. (1994) 'The sensitivity of hydrological models to spatial rainfall patterns: an evaluation using observed data', *Journal of Hydrology*, 159(1–4), pp. 305–333. doi:10.1016/0022-1694(94)90263-1.

Ochoa-Rodriguez, S. *et al.* (2015) 'Impact of spatial and temporal resolution of rainfall inputs on urban hydrodynamic modelling outputs: A multi-catchment investigation', *Journal of Hydrology*, 531, pp. 389–407. doi:10.1016/j.jhydrol.2015.05.035.

Ochoa-Rodriguez, S. *et al.* (2019) 'A Review of Radar-Rain Gauge Data Merging Methods and Their Potential for Urban Hydrological Applications', *Water Resources Research*, 55(8), pp. 6356–6391. doi:10.1029/2018WR023332.

Office of the Minister of Broadcasting, C. and D.M. (2019a) *Allocation of radio spectrum for 5G Mobile*.

Office of the Minister of Broadcasting, C. and D.M. (2019b) *Early Access to 5G radio spectrum*.

Ogden, F.L. and Julien, P.Y. (1994) 'Runoff model sensitivity to radar rainfall resolution', *Journal of Hydrology*, 158(1–2), pp. 1–18. doi:10.1016/0022-1694(94)90043-4.

Oguchi, T. (1960) 'Attenuation of electromagnetic wave due to rain with distorted raindrops. Part I', *J. Radio Res. Lab., Jap.*, 7(33), pp. 467–485.

Oguchi, T. (1981) 'Scattering from hydrometeors: A survey', *Radio Science*, 16(5), pp. 691–730. doi:10.1029/RS016i005p00691.

Ohm, J.-R. (2004) 'Signal Decomposition', in *Multimedia Communication Technology. Signals and Communication Technology.* Springer, Berlin, Heidelberg, pp. 417–442. doi:10.1007/978-3-642-18750-6_10.

Okamura, S. and Oguchi, T. (2010) 'Electromagnetic wave propagation in rain and polarization effects', *Proceedings of the Japan Academy Series B: Physical and Biological Sciences*, pp. 539–562. doi:10.2183/pjab.86.539.

Olsen, R.L., Rogers, D. V. and Hodge, D.B. (1978) 'The aRb Relation in the Calculation of Rain Attenuation', *IEEE Transactions on Antennas and Propagation*, 26(2), pp. 318–329. doi:10.1109/TAP.1978.1141845.

Ostrometzky, J. *et al.* (2017) 'Induced bias in attenuation measurements taken from commercial microwave links', in *2017 IEEE International Conference on Acoustics, Speech and Signal Processing (ICASSP)*. IEEE, pp. 3744–3748. doi:10.1109/ICASSP.2017.7952856.

Ostrometzky, J. and Messer, H. (2018) 'Dynamic Determination of the Baseline Level in Microwave Links for Rain Monitoring From Minimum Attenuation Values', *IEEE Journal of Selected Topics in Applied Earth Observations and Remote Sensing*, 11(1), pp. 24–33. doi:10.1109/JSTARS.2017.2752902.

Ouhamdouch, S. *et al.* (2020) 'Assessment the climate change impact on the future evapotranspiration and flows from a semi-arid environment', *Arabian Journal of Geosciences*, 13(2), pp. 1–14. doi:10.1007/S12517-020-5065-X/FIGURES/11.

Overeem, A. *et al.* (2013) 'Crowdsourcing urban air temperatures from smartphone battery temperatures', *Geophysical Research Letters*, 40(15), pp. 4081–4085. doi:10.1002/grl.50786.

Overeem, A. *et al.* (2021) 'Tropical rainfall monitoring with commercial microwave links in Sri Lanka', *Environmental Research Letters*, 16(7), p. 074058. doi:10.1088/1748-9326/AC0FA6.

Overeem, A., Buishand, A. and Holleman, I. (2008) 'Rainfall depth-duration-frequency curves and their uncertainties', *Journal of Hydrology*, 348(1–2), pp. 124–134. doi:10.1016/J.JHYDROL.2007.09.044.

Overeem, A., Holleman, I. and Buishand, A. (2009) 'Derivation of a 10-Year Radar-Based Climatology of Rainfall', *Journal of Applied Meteorology and Climatology*, 48(7), pp. 1448–1463. doi:10.1175/2009JAMC1954.1.

Overeem, A., Leijnse, H. and Uijlenhoet, R. (2011) 'Measuring urban rainfall using microwave links from commercial cellular communication networks', *Water Resources Research*, 47(12). doi:10.1029/2010WR010350.

Overeem, A., Leijnse, H. and Uijlenhoet, R. (2013) 'Country-wide rainfall maps from cellular communication networks', *Proceedings of the National Academy of Sciences of the United States of America*, 110(8), pp. 2741–2745. doi:10.1073/pnas.1217961110.

Overeem, A., Leijnse, H. and Uijlenhoet, R. (2016a) *RAINLINK: Retrieval algorithm for rainfall mapping from microwave links in a cellular communication network.* Available at: https://github.com/overeem11/RAINLINK/tree/master (Accessed: 6 November 2023).

Overeem, A., Leijnse, H. and Uijlenhoet, R. (2016b) 'Retrieval algorithm for rainfall mapping from microwave links in a cellular communication network', *Atmospheric Measurement Techniques*, 9(5), pp. 2425–2444. doi:10.5194/amt-9-2425-2016.

Overeem, A., Leijnse, H. and Uijlenhoet, R. (2016c) *The RAINLINK microwave link data set*. Available at: https://github.com/overeem11/RAINLINK/tree/master/data (Accessed: 6 November 2023).

Overeem, A., Leijnse, H. and Uijlenhoet, R. (2016d) 'Two and a half years of country-wide rainfall maps using radio links from commercial cellular telecommunication networks', *Water Resources Research*, 52(10), pp. 8039–8065. doi:10.1002/2016WR019412.

Owe, M. *et al.* (1999) 'Estimating soil moisture from satellite microwave observations: Past and ongoing projects, and relevance to GCIP', *Journal of Geophysical Research: Atmospheres*, 104(D16), pp. 19735–19742. doi:10.1029/1999JD900107.

Pablo Angueira, J.R. (2012) *Microwave Line of Sight Link Engineering | Wiley*, *Wiley*. Available at: https://www.wiley.com/en-nz/Microwave+Line+of+Sight+Link+Engineering-p-9781118072738 (Accessed: 13 July 2020).

Parker, M. (2017) *Digital Signal Processing 101: Everything You Need to Know to Get Started*. 2nd edn. Newnes.

PASHTOON, N.A. (1987) 'IIR Digital Filters', in *Handbook of Digital Signal Processing*. Elsevier, pp. 289–357. doi:10.1016/B978-0-08-050780-4.50009-6.

Pastorek, J. *et al.* (2022) 'Precipitation estimates from commercial microwave links: practical approaches to wet-antenna correction', *IEEE Transactions on Geoscience and Remote Sensing*, 60, p. 4104409 (9 pp.). doi:10.1109/TGRS.2021.3110004.

Peleg, N. *et al.* (2018) 'Spatial variability of extreme rainfall at radar subpixel scale', *Journal of Hydrology*, 556, pp. 922–933. doi:10.1016/J.JHYDROL.2016.05.033.

Pellarin, T. *et al.* (2008) 'Using spaceborne surface soil moisture to constrain satellite precipitation estimates over West Africa', *Geophysical Research Letters*, 35(2), p. L02813. doi:10.1029/2007GL032243.

Pellarin, T. *et al.* (2009) 'Soil moisture mapping over West Africa with a 30-min temporal resolution using AMSR-E observations and a satellite-based rainfall product', *Hydrology and Earth System Sciences*, 13(10), pp. 1887–1896. doi:10.5194/hess-13-1887-2009.

Peng, J. *et al.* (2021) 'A roadmap for high-resolution satellite soil moisture applications – confronting product characteristics with user requirements', *Remote Sensing of Environment*, 252, p. 112162. doi:10.1016/J.RSE.2020.112162.

Peng, L. *et al.* (2023) 'A Method of Noise Reduction for Radio Communication Signal Based on RaGAN', *Sensors (Basel, Switzerland)*, 23(1). doi:10.3390/S23010475.

Perera, D. *et al.* (2019) *Flood Early Warning Systems: A Review Of Benefits, Challenges And Prospects*. Hamilton, Canada. doi:10.53328/MJFQ3791.

Perrin, C., Michel, C. and Andréassian, V. (2003) 'Improvement of a parsimonious model for streamflow simulation', *Journal of Hydrology*, 279(1–4), pp. 275–289. doi:10.1016/S0022-1694(03)00225-7.

Philip B Bedient, Huber, W.C. and Vieux, B.E. (2013) *Hydrology and floodplain analysis*. 5th edn. Prentice Hall.

Pigorini, A. *et al.* (2011) 'Time-frequency spectral analysis of TMS-evoked EEG oscillations by means of Hilbert-Huang transform', *Journal of neuroscience methods*, 198(2), pp. 236–245. doi:10.1016/J.JNEUMETH.2011.04.013.

Pradhan, N. *et al.* (2016) *Community based flood early warning system – Resource manual*. Kathmandu: ICIMOD. Available at: https://www.preventionweb.net/files/51370_icimodcbfews016.pdf.

Prashant K. Srivastava, G.P.P. and Y.H.K. (2016) *Satellite Soil Moisture Retrieval. [Elektronisk resurs] Techniques and applications.* Elsevier. doi:https://doi.org/10.1016/C2014-0-03396-5.

Proakis, J.G. and Manolakis, D.G. (1996) *Digital Signal Processing: Principles Algorithms and Applications*. 3rd edn. Prentice-Hall International, INC.

Pruppacher, H.R. and Beard, K. V. (1970) 'A wind tunnel investigation of the internal circulation and shape of water drops falling at terminal velocity in air', *Quarterly Journal of the Royal Meteorological Society*, 96(408), pp. 247–256. doi:10.1002/qj.49709640807.

Pruppacher, H.R. and Pitter, R.L. (1971) 'A Semi-Empirical Determination of the Shape of Cloud and Rain Drops', *Journal of the Atmospheric Sciences*, 28(1), pp. 86–94. doi:10.1175/1520-

0469(1971)028<0086:asedot>2.0.co;2.

Pudashine, J. *et al.* (2020) 'Deep Learning for an Improved Prediction of Rainfall Retrievals From Commercial Microwave Links', *Water Resources Research*, 56(7). doi:10.1029/2019WR026255.

Pudashine, J. *et al.* (2021) 'Rainfall retrieval using commercial microwave links: Effect of sampling strategy on retrieval accuracy', *Journal of Hydrology*, 603, p. 126909. doi:10.1016/j.jhydrol.2021.126909.

*Radio Spectrum Management (RSM), The Register of Radio Frequencies* (no date). Available at: https://rrf.rsm.govt.nz/smart-web/smart/page/-smart/MedSecLogoffPage.wdk (Accessed: 16 January 2020).

Rahimi, A.R. *et al.* (2003) 'Use of dual-frequency microwave links for measuring path-averaged rainfall', *Journal of Geophysical Research*, 108(D15), p. 4467. doi:10.1029/2002JD003202.

Rajurkar, M.P., Kothyari, U.C. and Chaube, U.C. (2004) 'Modeling of the daily rainfall-runoff relationship with artificial neural network', *Journal of Hydrology*, 285(1–4), pp. 96–113. doi:10.1016/j.jhydrol.2003.08.011.

Rajurkar, M.P., Kothyari, U.C. and Chaube, U.C. (2009) 'Artificial neural networks for daily rainfall—runoff modelling', *https://doi.org/10.1080/02626660209492996*, 47(6), pp. 865–877. doi:10.1080/02626660209492996.

Ramos, B. *et al.* (2015) 'Measuring rain with microwave links: A pilot experiment in Ecuador', in *2015 IEEE-APS Topical Conference on Antennas and Propagation in Wireless Communications (APWC)*. IEEE, pp. 171–174. doi:10.1109/APWC.2015.7300149.

Ramos, B. *et al.* (2017) 'Rain rate estimation using a microwave link in Guayaquil City', in *2017 IEEE 2nd Ecuador Technical Chapters Meeting, ETCM 2017*. Institute of Electrical and Electronics Engineers Inc., pp. 1–6. doi:10.1109/ETCM.2017.8247522.

Rastogi, N. and Mehra, R. (2013) 'Analysis of Butterworth and Chebyshev Filters for ECG Denoising Using Wavelets', *IOSR Journal of Electronics and Communication Engineering*, 6(6), pp. 37–44. doi:10.9790/2834-0663744.

Rayleigh, Lord (1881) 'X. On the electromagnetic theory of light', *The London, Edinburgh, and Dublin Philosophical Magazine and Journal of Science*, 12(73), pp. 81–101. doi:10.1080/14786448108627074.

Rayleigh, Lord (1899) ' XXXIV. On the transmission of light through an atmosphere containing small particles in suspension, and on the origin of the blue of the sky ', *The London, Edinburgh, and Dublin Philosophical Magazine and Journal of Science*, 47(287), pp. 375–384. doi:10.1080/14786449908621276.

Recommendation ITU-R P.452-17 (2021) *Prediction procedure for the evaluation of interference between stations on the surface of the Earth at frequencies above about 0.1 GHz*.

Rincon, R.F. and Lang, R.H. (2002) 'Microwave link dual-wavelength measurements of path-average attenuation for the estimation of drop size distributions and rainfall', *IEEE Transactions on Geoscience and Remote Sensing*, 40(4), pp. 760–770. doi:10.1109/TGRS.2002.1006324.

Rios Gaona, M.F. *et al.* (2017) 'Evaluation of Rainfall Products Derived From Satellites and Microwave Links for The Netherlands', *IEEE Transactions on Geoscience and Remote Sensing*, 55(12), pp. 6849–6859. doi:10.1109/TGRS.2017.2735439.

Rios Gaona, M.F. *et al.* (2018) 'Rainfall retrieval with commercial microwave links in São Paulo, Brazil', *Atmospheric Measurement Techniques*, 11(7), pp. 4465–4476. doi:10.5194/amt-11-4465-

2018.

Rodda, J.C. (1967) 'A country-wide study of intense rainfall for the United Kingdom', *Journal of Hydrology*, 5, pp. 58–69. doi:10.1016/S0022-1694(67)80006-4.

Rodda, J.C. (1971) 'Report on precipitation', *International Association of Scientific Hydrology. Bulletin*, 16(4), pp. 37–47. doi:10.1080/02626667109493783.

Rossi, M. *et al.* (2017) 'Comparison of Satellite Rainfall Estimates and Rain Gauge Measurements in Italy, and Impact on Landslide Modeling', *Climate*, 5(4), p. 90. doi:10.3390/cli5040090.

Rossi, M.W., Whipple, K.X. and Vivoni, E.R. (2016) 'Precipitation and evapotranspiration controls on daily runoff variability in the contiguous United States and Puerto Rico', *Journal of Geophysical Research: Earth Surface*, 121(1), pp. 128–145. doi:10.1002/2015JF003446.

Rowlands, D.D. *et al.* (2005) 'Resolving mass flux at high spatial and temporal resolution using GRACE intersatellite measurements', *Geophysical Research Letters*, 32(4), pp. 1–4. doi:10.1029/2004GL021908.

Ruf, C.S. *et al.* (1996) '35-GHz dual-polarization propagation link for rain-rate estimation', *Journal of Atmospheric and Oceanic Technology*, 13(2), pp. 419–425. doi:10.1175/1520-0426(1996)013<0419:GDPPLF>2.0.CO;2.

Rwasoka, D.T. *et al.* (2014) 'Calibration, validation, parameter indentifiability and uncertainty analysis of a 2 – parameter parsimonious monthly rainfall-runoff model in two catchments in Zimbabwe', *Physics and Chemistry of the Earth, Parts A/B/C*, 67–69, pp. 36–46. doi:10.1016/J.PCE.2013.09.015.

Saakian, A.S. (2011) *Radio wave propagation fundamentals*. Artech House.

Saft, M. *et al.* (2015) 'The influence of multiyear drought on the annual rainfall-runoff relationship: An Australian perspective', *Water Resources Research*, 51(4), pp. 2444–2463. doi:10.1002/2014WR015348.

Saft, M. *et al.* (2016) 'Predicting shifts in rainfall-runoff partitioning during multiyear drought: Roles of dry period and catchment characteristics', *Water Resources Research*, 52(12), pp. 9290–9305. doi:10.1002/2016WR019525.

Savina, M. *et al.* (2011) 'Comparison of a tipping-bucket and electronic weighing precipitation gage for snowfall', *Atmospheric Research*, 103, pp. 45–51. doi:10.1016/j.atmosres.2011.06.010.

Schwemmle, R., Demand, D. and Weiler, M. (2021) 'Technical note: Diagnostic efficiency - Specific evaluation of model performance', *Hydrology and Earth System Sciences*, 25(4), pp. 2187–2198. doi:10.5194/HESS-25-2187-2021.

Seinfeld, J.H., Pandis, S.N. and Noone, K. (1998) 'Atmospheric Chemistry and Physics: From Air Pollution to Climate Change', *Physics Today*, 51(10), pp. 88–90. doi:10.1063/1.882420.

Sekine, M. and Lind, G. (1982) 'Rain Attenuation 0f Centimeter, Millimeter and Submillimeter Radio Waves', in *12th European Microwave Conference, 1982*. IEEE, pp. 584–589. doi:10.1109/EUMA.1982.333124.

Şen, Z. and Altunkaynak, A. (2004) 'Fuzzy awakening in rainfall-runoff modeling', *Hydrology Research*, 35(1), pp. 31–43. doi:10.2166/NH.2004.0003.

Serway, R.A. and John W. Jewett, J. (2005) *Principles of physics: a calculus-based text*. Thomson. doi:10.1017/CBO9781107415324.004.

Sevruk, B. (1973) 'Initial wetting losses incurred by ground level stereo gages', *Water Resources Research*, 9(3), pp. 759–763. doi:10.1029/WR009i003p00759.

Sevruk, B. (1982) *Methods of correction for systematic error in point precipitation measurement for operational use, WMO- No. 589; Operational hydrology report (OHR)- No. 21*. World Meteorological Organization (WMO).

Sevruk, B. (1996) 'Adjustment of tipping-bucket precipitation gauge measurements', *Atmospheric Research*, 42(1), pp. 237–246. doi:10.1016/0169-8095(95)00066-6.

Sevruk, B and Klemm, S. (1989) *Instruments and observing methods, Report No. 39*, *Catalogue of national standard presipitation gauges- WMO/TD-No.313*. Available at: http://scholar.google.ru/scholar?q=Sevruk,++Klemm+1989&btnG=&hl=ru&as_sdt=0,5#0%5Cnhttp://scholar.google.com/scholar?hl=en&btnG=Search&q=intitle:Types+of+standard+precipitation+gauges%230.

Sevruk, B. and Klemm, S. (1989) 'Types of standard precipitation gauges in precipitation measurement', in *WMO/IAHS/ETH International Workshop on Precipitation Measurement, 3– 7 December 1989*. St Moritz, Switzerland, pp. 227–232.

Seybold, J.S. (2005) *Introduction to RF Propagation*, *Introduction to RF Propagation*. Hoboken, NJ, USA. doi:10.1002/0471743690.

Sezen, C., Bezak, N. and Šraj, M. (2018) 'Hydrological modelling of the karst Ljubljanica river catchment using lumped conceptual model', *Acta Hydrotechnica*, 31(55), pp. 87–100. doi:10.15292/ACTA.HYDRO.2018.06.

Shah, A. *et al.* (2022) 'Comparative analysis of median filter and its variants for removal of impulse noise from gray scale images', *Journal of King Saud University - Computer and Information Sciences*, 34(3), pp. 505–519. doi:10.1016/J.JKSUCI.2020.03.007.

Shidore, P.M. *et al.* (2022) 'PERFORMANCE EVALUATION OF DIFFERENT FILTERING AND DENOISING TECHNIQUES ON NON-STATIONARY SIGNAL', *IJCRT - International Journal of Creative Research Thoughts (IJCRT)*, 10(12), pp. e612–e618. Available at: http://www.ijcrt.org/viewfull.php?p_id=IJCRT2212522 (Accessed: 26 June 2023).

Shrestha, S. and Choi, D.-Y. (2017) 'Rain attenuation over terrestrial microwave links in South Korea', *IET Microwaves, Antennas & Propagation*, 11(7), pp. 1031–1039. doi:10.1049/iet-map.2016.0553.

Sideris, I. V. *et al.* (2014) 'Real-time radar–rain-gauge merging using spatio-temporal co-kriging with external drift in the alpine terrain of Switzerland', *Quarterly Journal of the Royal Meteorological Society*, 140(680), pp. 1097–1111. doi:10.1002/QJ.2188.

Singh, A. and Lubecke, V. (2013) 'Adaptive noise cancellation for two frequency radar using frequency doubling passive RF tags', *IEEE Transactions on Microwave Theory and Techniques*, 61(8), pp. 2975–2981. doi:10.1109/TMTT.2013.2271609.

Sitterson, J. *et al.* (2018) 'An Overview of Rainfall-Runoff Model Types', *International Congress on Environmental Modelling and Software* [Preprint]. Available at: https://scholarsarchive.byu.edu/iemssconference/2018/Stream-C/41 (Accessed: 30 January 2023).

Sivapalan, M. *et al.* (2003) 'IAHS Decade on Predictions in Ungauged Basins (PUB), 2003–2012: Shaping an exciting future for the hydrological sciences', *Hydrological Sciences Journal*, 48(6), pp. 857–880. doi:10.1623/HYSJ.48.6.857.51421.

*SMAP, Soil Moisture Active Passive* (no date). Available at: https://smap.jpl.nasa.gov/ (Accessed: 12 April 2023).

Smith, J.S. (2005) 'The local mean decomposition and its application to EEG perception data', *Journal of The Royal Society Interface*, 2(5), pp. 443–454. doi:10.1098/RSIF.2005.0058.

Sneeuw, N. *et al.* (2014) 'Estimating Runoff Using Hydro-Geodetic Approaches', *Surveys in Geophysics*, 35(6), pp. 1333–1359. doi:10.1007/S10712-014-9300-4/FIGURES/10.

Song, K. *et al.* (2019a) 'Raindrop Size Distribution Retrieval Using Joint Dual-Frequency and Dual-Polarization Microwave Links', *Advances in Meteorology*, 2019. doi:10.1155/2019/7251870.

Song, K. *et al.* (2019b) 'Rainfall estimation using a microwave link based on an improved rain-induced attenuation model', *Remote Sensing Letters*, 10(11), pp. 1057–1066. doi:10.1080/2150704X.2019.1648902.

Stagnaro, M., Lanza, L.G. and Cauteruccio, A. (2018) 'Catching-type Rain Gauges: Standards and Performance Mattia', in *JMA/WMO Workshop on Quality Management of Surface Observations, RA II WIGOS Project, 19-23 March 2018*. Tokyo, Japan.

Stallone, A., Cicone, A. and Materassi, M. (2020) 'New insights and best practices for the successful use of Empirical Mode Decomposition, Iterative Filtering and derived algorithms', *Scientific Reports*, 10(1). doi:10.1038/S41598-020-72193-2.

Stamnes, K., Thomas, G.E. and Stamnes, J.J. (2017) *Radiative Transfer in the Atmosphere and Ocean*. 2nd Editio. Cambridge University Press. Available at: https://books.google.co.nz/books?hl=en&lr=&id=DxR2nEp0CUIC&oi=fnd&pg=PR21&ots=SfMvaIl8B5&sig=OeeKciENe2mQQ2sVFhWvvAZDjGE&redir_esc=y#v=onepage&q&f=false (Accessed: 21 May 2020).

Stoica, P. and Moses, R. (2005) *Spectral analysis of signals*. Upper Saddle River, New Jersey: Prentice Hall.

Strang, G. and Nguyen, T. (1996) *Wavelets and Filter Banks 2nd Edition*. 2nd edn. Wellesley-Cambridge Press.

Strangeways, I. (2004) 'Improving precipitation measurement', *International Journal of Climatology*, 24(11), pp. 1443–1460. doi:10.1002/joc.1075.

Strangeways, I. (2007) *Precipitation: Theory, Measurement and Distribution*, *Precipitation: Theory, Measurement and Distribution*. Cambridge: Cambridge University Press. doi:10.1017/CBO9780511535772.

Strangeways, I. (2010) 'A history of rain gauges', *Weather*, 65(5), pp. 133–138. doi:10.1002/wea.548.

Sun, A.Y., Wang, D. and Xu, X. (2014) 'Monthly streamflow forecasting using Gaussian Process Regression', *Journal of Hydrology*, 511, pp. 72–81. doi:10.1016/J.JHYDROL.2014.01.023.

Sygouni, V., Tsakiroglou, C.D. and Payatakes, A.C. (2006) 'Capillary pressure spectrometry: Toward a new method for the measurement of the fractional wettability of porous media', *Physics of Fluids*, 18(5), p. 53302. doi:10.1063/1.2203667/911124.

Szendro, P., Vincze, G. and Szasz, A. (2001) 'Pink-noise behaviour of biosystems', *European Biophysics Journal*, 30(3), pp. 227–231. doi:10.1007/S002490100143/METRICS.

Tait Communications (2016) *Radio Frequency Performance Parameters – Transmitter Output Power*. Available at: https://blog.taitcommunications.com/2016/01/07/radio-frequency-performance-parameters-transmitter-output-power/ (Accessed: 13 October 2023).

Tan, L. and Jiang, J. (2019) 'Subband and Wavelet-Based Coding', in *Digital Signal Processing*. 3rd edn. Academic Press, pp. 591–648. doi:10.1016/B978-0-12-815071-9.00012-9.

Tapley, B.D. *et al.* (2004) 'GRACE measurements of mass variability in the Earth system', *Science*, 305(5683), pp. 503–505. doi:10.1126/SCIENCE.1099192/SUPPL_FILE/TAPLEY.SOM.PDF.

Telecom Trainer (2023) *TSL Transmitted Signal level*. Available at: https://www.telecomtrainer.com/tsl-transmitted-signal-level/ (Accessed: 16 October 2023).

Tokar, A.S. and Johnson, P.A. (1999) 'Rainfall-Runoff Modeling Using Artificial Neural Networks', *Journal of Hydrologic Engineering*, 4(3), pp. 232–239. doi:10.1061/(ASCE)1084-0699(1999)4:3(232).

Trenberth, K.E. and Asrar, G.R. (2014) 'Challenges and Opportunities in Water Cycle Research: WCRP Contributions', *Surveys in Geophysics*, 35(3), pp. 515–532. doi:10.1007/S10712-012-9214-Y/FIGURES/3.

*TRMM: Tropical Rainfall Measuring Mission | Climate Data Guide* (no date). Available at: https://climatedataguide.ucar.edu/climate-data/trmm-tropical-rainfall-measuring-mission (Accessed: 12 April 2023).

*TRMM Comes to an End after 17 Years | NASA Global Precipitation Measurement Mission* (no date). Available at: https://gpm.nasa.gov/missions/trmm/mission-end (Accessed: 12 April 2023).

Trömel, S. *et al.* (2014) 'Using Microwave Backhaul Links to Optimize the Performance of Algorithms for Rainfall Estimation and Attenuation Correction', *Journal of Atmospheric and Oceanic Technology*, 31(8), pp. 1748–1760. doi:10.1175/JTECH-D-14-00016.1.

Tromp-Van Meerveld, H.J. and McDonnell, J.J. (2006) 'Threshold relations in subsurface stormflow: 1. A 147-storm analysis of the Panola hillslope', *Water Resources Research*, 42(2), p. 2410. doi:10.1029/2004WR003778.

Ulbrich, C.W. (1983) 'Natural Variations in the Analytical Form of the Raindrop Size Distribution', *Journal of Climate and Applied Meteorology*, 22(10), pp. 1764–1775. doi:10.1175/1520-0450(1983)022<1764:NVITAF>2.0.CO;2.

Ulbrich, C.W. and Atlas, D. (1984) 'Assessment of the contribution of differential polarization to improved rainfall measurements', *Radio Science*, 19(1), pp. 49–57. doi:10.1029/RS019i001p00049.

Upton, G.J.G. and Rahimi, A.R. (2003) 'On-line detection of errors in tipping-bucket raingauges', *Journal of Hydrology*, 278(1–4), pp. 197–212. doi:10.1016/S0022-1694(03)00142-2.

Upton, G.J.G.J.G. *et al.* (2005) 'Microwave links: The future for urban rainfall measurement?', *Atmospheric Research*, 77(1–4), pp. 300–312. doi:10.1016/J.ATMOSRES.2004.10.009.

Valtr, P., Fencl, M. and Bares, V. (2019) 'Excess Attenuation Caused by Antenna Wetting of Terrestrial Microwave Links at 32 GHz', *IEEE Antennas and Wireless Propagation Letters*, 18(8), pp. 1636–1640. doi:10.1109/LAWP.2019.2925455.

Vaseghi, S. V. (2000) *Advanced Digital Signal Processing and Noise Reduction*. Second. John Wiley & Sons, Ltd.

Vaze, J. *et al.* (2011) 'Guidelines for rainfall-runoff modelling: towards best practice model application'. eWater CRC.

De Vos, L. *et al.* (2017) 'The potential of urban rainfall monitoring with crowdsourced automatic weather stations in Amsterdam', *Hydrology and Earth System Sciences*, 21(2), pp. 765–777. doi:10.5194/hess-21-765-2017.

de Vos, L.W. *et al.* (2019) 'Rainfall estimation accuracy of a nationwide instantaneously sampling commercial microwave link network: Error dependency on known characteristics', *Journal of Atmospheric and Oceanic Technology*, 36(8), pp. 1267–1283. doi:10.1175/JTECH-D-18-0197.1.

Wang, B. and Cao, Z. (2019) 'A Review of Impedance Matching Techniques in Power Line Communications', *Electronics 2019, Vol. 8, Page 1022*, 8(9), p. 1022. doi:10.3390/ELECTRONICS8091022.

Wang, H. and Sengupta, K. (2016) 'Chapter 1 - Introduction', in Wang, H. and Sengupta, K. (eds) *RF and mm-Wave Power Generation in Silicon*. Oxford: Academic Press, pp. 1–13. doi:https://doi.org/10.1016/B978-0-12-408052-2.00001-3.

Wang, Z. *et al.* (2012) 'Using Markov switching models to infer dry and rainy periods from telecommunication microwave link signals', *Atmospheric Measurement Techniques*, 5(7), pp. 1847–1859. doi:10.5194/amt-5-1847-2012.

Wanhammar, L. (1999) 'Digital filters', in *DSP Integrated Circuits*. Academic Press, pp. 115–186. doi:10.1016/B978-012734530-7/50004-0.

Wania, A. *et al.* (2021) 'Increasing Timeliness of Satellite-Based Flood Mapping Using Early Warning Systems in the Copernicus Emergency Management Service', *Remote Sensing 2021, Vol. 13, Page 2114*, 13(11), p. 2114. doi:10.3390/RS13112114.

Wannachai, A. *et al.* (2022) 'HERO: Hybrid Effortless Resilient Operation Stations for Flash Flood Early Warning Systems', *Sensors (Basel, Switzerland)*, 22(11). doi:10.3390/S22114108.

Waterman, P.C. (1965) 'Matrix Formulation of Electromagnetic Scattering', *Proceedings of the IEEE*, 53(8), pp. 805–812. doi:10.1109/PROC.1965.4058.

*Weather Radar Fundamentals* (no date). Available at: http://kejian1.cmatc.cn/vod/comet/radar/basic_wxradar/navmenu.php_tab_1_page_3.2.0_type_text.htm (Accessed: 20 January 2020).

Weiler, M. and McDonnell, J.J. (2007) 'Conceptualizing lateral preferential flow and flow networks and simulating the effects on gauged and ungauged hillslopes', *Water Resources Research*, 43(3), p. 3403. doi:10.1029/2006WR004867.

Weissberger, A. (2019) *WRC 19 Wrap-up: Additional spectrum allocations agreed for IMT-2020 (5G mobile) – Technology Blog*. Available at: https://techblog.comsoc.org/2019/11/22/wrc-19-wrap-up-additional-spectrum-allocations-agreed-for-imt-2020-5g-mobile/ (Accessed: 6 January 2020).

Westra, S., Alexander, L. V. and Zwiers, F.W. (2013) 'Global Increasing Trends in Annual Maximum Daily Precipitation', *Journal of Climate*, 26(11), pp. 3904–3918. doi:10.1175/JCLI-D-12-00502.1.

Whitaker, J.C. (2005) *The electronics handbook*. CRC Press, Taylor & Francis Group.

Whiton, R.C. *et al.* (1998) *History of Operational Use of Weather Radar by U.S. Weather Services. Part I: The Pre-NEXRAD Era*, *Weather and Forecasting*. American Meteorological Society. doi:10.1175/1520-0434(1998)013<0219:HOOUOW>2.0.CO;2.

Wolff, W. *et al.* (2022) 'Rainfall retrieval algorithm for commercial microwave links: stochastic calibration', *Atmospheric Measurement Techniques*, 15(2), pp. 485–502. doi:10.5194/amt-15-485-2022.

*World Meteorological Organization; Observing stations and WMO catalogue of radiosondes. WMO Publ. 9, Vol. A* (2011). Available at: https://www.wmo.int/pages/prog/www/ois/volume-a/vola-home.htm (Accessed: 15 January 2020).

Wu, Z. and Huang, N.E. (2011) 'ENSEMBLE EMPIRICAL MODE DECOMPOSITION: A NOISE-ASSISTED DATA ANALYSIS METHOD', *https://doi.org/10.1142/S1793536909000047*, 1(1), pp. 1–41. doi:10.1142/S1793536909000047.

Xiao, Z. *et al.* (2018) 'The Spatiotemporal Variations of Runoff in the Yangtze River Basin under Climate Change', *Advances in Meteorology*, 2018. doi:10.1155/2018/5903451.

Xu, C.Y. and Vandewiele, G.L. (1995) 'Parsimonious monthly rainfall-runoff models for humid basins with different input requirements', *Advances in Water Resources*, 18(1), pp. 39–48. doi:10.1016/0309-1708(94)00017-Y.

Yahiaoui, S. *et al.* (2022) 'Rainfall-runoff modeling using airGR and airGRteaching: application to a catchment in Northeast Algeria', *Modeling Earth Systems and Environment*, 8(4), pp. 4985–4996. doi:10.1007/S40808-022-01444-0/TABLES/7.

Younis, J., Anquetin, S. and Thielen, J. (2008) 'The benefit of high-resolution operational weather forecasts for flash flood warning', *Hydrology and Earth System Sciences*, 12(4), pp. 1039–1051. doi:10.5194/HESS-12-1039-2008.

Zehe, E. *et al.* (2010) 'Plot and field scale soil moisture dynamics and subsurface wetness control on runoff generation in a headwater in the Ore Mountains', *Hydrology and Earth System Sciences*, 14(6), pp. 873–889. doi:10.5194/HESS-14-873-2010.

Zenteno, E., Isaksson, M. and Handel, P. (2015) 'Output impedance mismatch effects on the linearity performance of digitally predistorted power amplifiers', *IEEE Transactions on Microwave Theory and Techniques*, 63(2), pp. 754–765. doi:10.1109/TMTT.2014.2387060.

Zhang, H., Arslan, T. and Flynn, B. (2013) 'Wavelet de-noising based microwave imaging for brain cancer detection', *2013 Loughborough Antennas and Propagation Conference, LAPC 2013*, pp. 482–485. doi:10.1109/LAPC.2013.6711946.

Zhang, H.L. *et al.* (2020) 'EEG Self-Adjusting Data Analysis Based on Optimized Sampling for Robot Control', *Electronics 2020, Vol. 9, Page 925*, 9(6), p. 925. doi:10.3390/ELECTRONICS9060925.

Zhang, J. *et al.* (2021) 'Serial-EMD: Fast empirical mode decomposition method for multi-dimensional signals based on serialization', *Information Sciences*, 581, pp. 215–232. doi:10.1016/J.INS.2021.09.033.

Zhang, X., Lai, K.K. and Wang, S.Y. (2008) 'A new approach for crude oil price analysis based on Empirical Mode Decomposition', *Energy Economics*, 30(3), pp. 905–918. doi:10.1016/J.ENECO.2007.02.012.

Zhang, Y. *et al.* (2018) 'Characterizing drought in terms of changes in the precipitation-runoff relationship: A case study of the Loess Plateau, China', *Hydrology and Earth System Sciences*, 22(3), pp. 1749–1766. doi:10.5194/HESS-22-1749-2018.

Zhao, D., Su, B. and Zhao, M. (2006) 'Soil moisture retrieval from satellite images and its application to heavy rainfall simulation in eastern China', *Advances in Atmospheric Sciences*, 23(2), pp. 299–316. doi:10.1007/s00376-006-0299-4.

Zhao, N. *et al.* (2014) 'Soil Moisture Dynamics and Effects on Runoff Generation at Small Hillslope Scale', *Journal of Hydrologic Engineering*, 20(7), p. 05014024. doi:10.1061/(ASCE)HE.1943-5584.0001062.

Zheng, J., Cheng, J. and Yang, Y. (2013) 'A rolling bearing fault diagnosis approach based on LCD and fuzzy entropy', *Mechanism and Machine Theory*, 70, pp. 441–453. doi:10.1016/J.MECHMACHTHEORY.2013.08.014.

Zheng, X. *et al.* (2022) 'On the potential of commercial microwave link networks for high spatial resolution rainfall monitoring in urban areas', *AtmRe*, 277, p. 106289. doi:10.1016/J.ATMOSRES.2022.106289.

Zinevich, A., Alpert, P. and Messer, H. (2008) ‘Estimation of rainfall fields using commercial microwave communication networks of variable density’, *Advances in Water Resources*, 31(11), pp. 1470–1480. Available at: https://www.sciencedirect.com/science/article/pii/S030917080800050X?via%3Dihub (Accessed: 1 November 2019).

Zinevich, A., Messer, H. and Alpert, P. (2009) ‘Frontal Rainfall Observation by a Commercial Microwave Communication Network’, *Journal of Applied Meteorology and Climatology*, 48(7), pp. 1317–1334. doi:10.1175/2008JAMC2014.1.

Zinevich, A., Messer, H. and Alpert, P. (2010a) ‘Prediction of rainfall intensity measurement errors using commercial microwave communication links’, *Atmospheric Measurement Techniques*, 3(5), pp. 1385–1402. doi:10.5194/amt-3-1385-2010.

Zinevich, A., Messer, H. and Alpert, P. (2010b) ‘Prediction of rainfall intensity measurement errors using commercial microwave communication links’, *Atmospheric Measurement Techniques*, 3(5), pp. 1385–1402. doi:10.5194/amt-3-1385-2010.

Zumbahlen, H. (2008) ‘Analog Filters’, in *Linear Circuit Design Handbook*. Newnes, pp. 581–679. doi:10.1016/B978-0-7506-8703-4.00008-0.

Zverev, A.I. (1967) *Handbook of Filter Synthesis*. Available at: https://www.wiley.com/en-us/Handbook+of+Filter+Synthesis-p-9780471749424 (Accessed: 21 August 2023).

# 7. Appendix A – Theoretical background and technical definition

Given the multidisciplinary nature of this study, key concepts and terms used in this PhD thesis are defined in the following for clarity and ease of understanding.

### 7.1.1. Rainfall characteristics

- *Rainfall intensity*

The instant intensity of rainfall, which is equal to the volume of water, falls on an area at a specific time. Usually, defined as millimetres per hour (mm/hr).

- *Shape of raindrops*

The shape of raindrops changes when their diameter extends. Small drops are more spherical while the large drops have a flattened base (Barclay, 2003). Some more accepted shape models of raindrops are suggested to show the real shape of the drop (Pruppacher and Beard, 1970; Pruppacher and Pitter, 1971; Beard and Chuang, 1987) Four models of raindrops are shown in Figure *7-1* and Figure 7-2 explains the Beard and Chuang model of raindrops for different diameter sizes (Beard and Chuang, 1987; Beard, Bringi and Thurai, 2010).

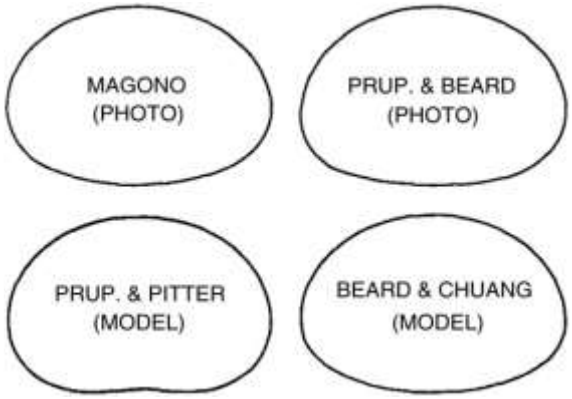


*Figure 7-1- Comparison of drop shape in different models for a 5 mm diameter drop, source: (Beard and Chuang, 1987; Beard, Bringi and Thurai, 2010)*

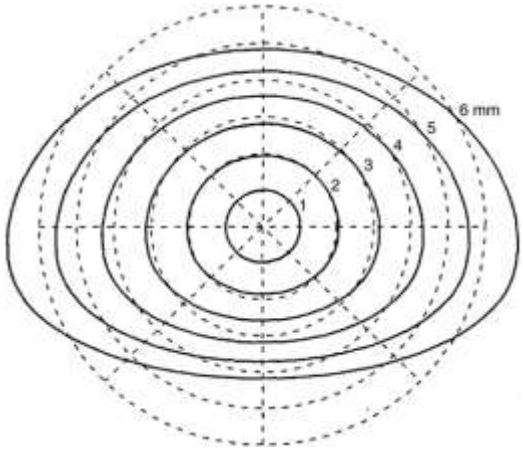


*Figure 7-2- Computed shapes for drops in comparison with equivalent spherical drops with diameters equal to D=1, 2, 3, 4, 5, and 6 mm based om Beard and Chuang model, source: (Beard and Chuang, 1987; Beard, Bringi and Thurai, 2010)*

- *Maximum drop size and the maximum velocity of raindrops*

Bigger drops are unstable and are split when they extend. Raindrops larger than 6 mm in diameter divide into smaller drops due to drag force at the bottom (Marshall and Palmer, 1948; Gunn and Kinzer, 1949; Pruppacher and Beard, 1970; Beard, 1976, 1977). The same studies showed that drag force, drop size, and gravity result in a maximum speed of 9 m/s for drops larger than 5 mm in diameter.

- *Drop size distribution (DSD)*

The statistical distribution of the size of raindrops. Among a few DSD models, which are proven generally and are being used in studies, Marshall and Palmer's (1948) model has been widely applied in studies.

$$N_D = N_0 e^{-\Lambda D} \quad \text{Equation 7-1}$$

where $D$ in diameter, $N_D \delta D$ is the number of drops of diameter between $D$ and $D + \delta D$ in a unit volume of space, and $N_0$ is the value of $N_D$ for $D = 0$, which is equal to:

$$N_0 = 0.08\ cm^{-4} \quad \text{Equation 7-2}$$

For any intensity of rainfall, and:

$$\Lambda = 41\ R^{-0.21} cm^{-1} \quad \text{Equation 7-3}$$

where $R$ is the rate of rainfall in $mm\ hr^{-1}$.

There are also other DSD estimations. Ulbrich (1983) showed that a three-parameter gamma distribution can describe the raindrops' variation. The general form of gamma distribution of DSD is:

$$N(D) = N_0 D^{\mu} exp(-\Lambda D), \qquad 0 \le D \le D_{max} \quad \text{Equation 7-4}$$

where the $\mu$ can have any positive or negative value and $N_0$ now has the unit $m^{-3} cm^{-1-\mu}$.

A Weibull distribution (Sekine and Lind, 1982) is also suggested with different values for parameters:

$$N(D) = N_0 \frac{c}{b} \left(\frac{D}{b}\right)^{c-1} exp\left(-\left(\frac{D}{b}\right)^{c}\right) \quad \text{Equation 7-5}$$

$$N_0 = 1000\ m^{-3} \quad \text{Equation 7-6}$$

$$b = 0.26\ R^{0.44}\ mm \quad \text{Equation 7-7}$$

$$c = 0.95\ R^{0.14} \quad \text{Equation 7-8}$$

### 7.1.2. Rainfall measurement and rain gauges

The principles of rain gauges, which involved collecting the volume of rainfall in various-sized containers, remained unchanged until the seventeenth century. During that period, the tipping bucket, a device invented to measure rainfall, was introduced (Strangeways, 2010). The most widely used gauges in operation today are not significantly different. Over the past decades, rain gauges have been enhanced with mechanical and electronic devices for automatic data logging. Consequently, gauges can be categorized based on how data is recorded (Strangeways, 2007):

- **Manual rain gauges:** A survey indicates the existence of over 50 types of manual gauges employed in various countries (B. Sevruk and Klemm, 1989; Strangeways, 2007). It is estimated that the most prevalent rain gauges globally include 30,080 German Hellmann gauges, 19,676 Chinese gauges, and 17,856 of two types (English Mark two and Snowdon third) (Strangeways, 2007).
- **Mechanical rain gauges:** Typically used to record rain data with a moving pen on a paper chart, mechanical rain gauges come in two types. One type operates with a floating system

to move the pen, while the others are weight-operated (Strangeways, 2010). These gauges require a siphon to empty the container for continuous recording, and their sensitivity varies with the water volume in the containers (Strangeways, 2010).

- **Electronic rain gauges:** Tipping bucket rain gauges are the most common automatic rainfall measurement devices, but various other types of electronic gauges have been developed (Strangeways, 2007, 2010).

Different kinds of electronic rain gauges include:

- **Tipping bucket rain gauges:**

Widely employed for automatic rainfall monitoring due to easy signal digitization (Kim and Kwon, 2018). They record and log automatically, eliminating the need for periodic emptying. Moreover, they not only measure rainfall amounts but also determine rain rates. Some mechanical tipping buckets have been developed.

- **Electronic weighing rain gauges:**

Utilize strain gauge load cells to weigh collected water in their container, offering precision up to 0.01 mm, providing finer details on rain intensity compared to tipping buckets (Strangeways, 2007).

- **Capacitance rain gauges:**

Employ the dielectric properties of water in the gauge, measuring water amount between two electrodes (Strangeways, 2007). They require emptying after filling, typically done by a siphon.

- **Drop counting gauges:**

Rapid-response gauges collect rain, drip it in fixed-sized drops, and count them (Norbury and White, 1971). Capable of measuring up to 200 mm/hr rainfall intensity, but accuracy is affected by changes in drop size in different conditions (Strangeways, 2007).

All the mentioned rain gauges collect rainwater to measure the volume. With the development of electronic devices, non-catching rain gauges have been adopted to measure rainfall without gathering rain in any amount (Stagnaro, 2018):

- **Disdrometer**

A laser instrument measuring the size and number of falling hydrometeors, is categorised into various types(Kathiravelu, Lucke and Nichols, 2016):

  - Impact disdrometers
  - Acoustic disdrometers
  - Displacement disdrometers
  - Optical disdrometers
  - Optical imaging
  - Optical scattering
- Doppler radar sensor

Simple Doppler radars, akin to speed cameras looking upward, measure the fall speed of raindrops. They convert drop speed to drop size and rainfall intensity (Strangeways, 2007). Doppler radars are relatively cost-effective compared to other electronic devices, though scientific resources on them are limited.

### 7.1.3. Microwave characteristics

- **Electromagnetic wave**

Electromagnetic wave (EM wave) is the result of the oscillating of electric and magnetic fields. EM wave travels perpendicular to the electric and magnetic field vectors (John A. Richards, 2008). Figure 7-3 shows the direction of oscillating H as Magnetic field and E as Electric field and the direction of propagation of the wave, S.

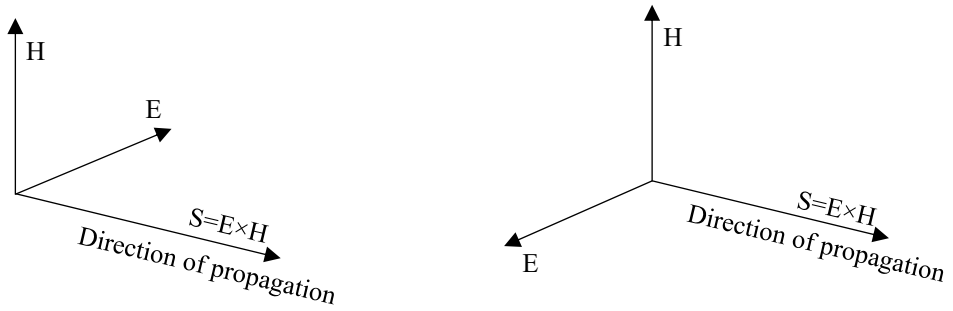


*Figure 7-3- Transverse electric and magnetic field components and the direction of wave propagation, source:* (John A. Richards, 2008)

- **Polarization**

When the direction of the electric field is referred to the earth's surface, horizontal and vertical polarization is defined (John A. Richards, 2008). Transmitters and receivers send and receive the waves in different polarizations, depending on the design and their application.

- **Wavelength**

Wavelength is the distance between two successive crests of the wave (Serway and John W. Jewett, 2005). It is also the distance between two consecutive points of the wave in the same phase.

- **Frequency**

While the speed of a wave is $v$, any point on the wave moves as long as a wavelength in time as long as one-period $T$. The frequency $f$ is the inverse of the period $1/T$. The frequency of one wavelength travels in one second is one hertz ($Hz$).

- **Microwave**

Although the radio spectrum includes frequencies between 3 kHz and 3 THz, the significant use lies between 10 kHz and 275 GHz (Barclay, 2003). The International Telecommunication Union (ITU) recommended names for radio frequency bands (ITU-R, 2015). Microwave frequencies range between 300 MHz to 300 GHz which is defined in Table 7-1 (Saakian, 2011).

*Table 7-1- Radio frequency band and microwave range (Saakian, 2011)*

| Band Number, N | | Frequency Band Name by ITU-R | Acronym | Frequency Range, (Hz) | Wave-length (m) | Descriptive Name | Acronym |
|---|---|---|---|---|---|---|---|
| - | | Extremely Low Frequency | ELF | $< 3x10^3$ | $> 10^5$ | - | - |
| 4 | | Very Low Frequency | VLF | (3 to 30) $x10^3$ | $10^4$ to $10^5$ | Miriameter Waves | - |
| 5 | | Low Frequency | LF | (30 to 300) $x10^3$ | $10^3$ to $10^4$ | Kilometer Waves | - |
| 6 | | Medium Frequency | MF | (0.3 to 3) $x10^6$ | $10^2$ to $10^3$ | Hectometer Waves | - |
| 7 | | High Frequency | HF | (3 to 30) x $10^6$ | 10 to $10^2$ | Decameter Waves | - |
| 8 | | Very High Frequency | VHF | (30 to 300)$x10^6$ | 1 to 10 | Meter Waves | MW |
| 9 | Microwaves | Ultra High Frequency | UHF | (0.3 to 3)$x10^9$ | $10^{-1}$ to 1 | Decimeter Waves* | DMW |
| 10 | | Super High Frequency | SHF | (3 to 30)$x10^9$ | $10^{-2}$ to $10^{-1}$ | Centimeter Waves* | CMW |
| 11 | | Extremely High Frequency | EHF | (30 to 300)$x10^9$ | $10^{-3}$ to $10^{-2}$ | Millimeter Waves * | MMW |
| 12 | | - | - | (0.3 to 3)$x10^{12}$ | $10^{-4}$ to $10^{-3}$ | Sub-Millimeter Waves * | SMMW |

- **Wave propagation**

James Clerk Maxwell gathered and defined four relationships known as Maxwell's equations to explain the theoretical basis of all electrical and magnetic fields. The equations predict that oscillating electric and magnetic fields results in electromagnetic wave (Serway and John W. Jewett, 2005) and defined as:

$$\oint \vec{E} \cdot d\vec{A} = \frac{q}{\epsilon_0} \qquad \text{Equation 7-9}$$

$$\oint \vec{B} \cdot d\vec{A} = 0 \qquad \text{Equation 7-10}$$

$$\oint \vec{E} \cdot d\vec{s} = -\frac{d\Phi_B}{dt} \qquad \text{Equation 7-11}$$

$$\oint \vec{B} \cdot d\vec{s} = \mu_0 I + \epsilon_0 \mu_0 \frac{\Phi_E}{dt} \qquad \text{Equation 7-12}$$

Where $E$ is electric filed, $B$ is Magnetic field, $I$ is conduction current, $\Phi_E$ is the flux of the electric field, $\Phi_B$ is the flux of the Magnetic field, $A$ is the area of the capacitor plates, $q$ is the charge on the plates at any instant, $\vec{s}$ is a Poynting vector, and $\mu_0$ and $\epsilon_0$ are constants.

- **Attenuation**

The reduction in signal amplitude is called attenuation (Louis J. Ippolito, 1986). Many different factors cause attenuation including gaseous constituents of the Earth's atmosphere, hydrometeors (rain, clouds, fog, snow, Ice), depolarization, and radio noise (Louis J. Ippolito, 1986).

$$P_r = P_t e^{-kL} \qquad \text{Equation 7-13}$$

Where $k$ is the attenuation coefficient and $L$ is distance. The attenuation of the wave, usually described as a positive value, in decibel (dB) unit, is the logarithmic proportion of transmitted power to the received power (Louis J. Ippolito, 1986):

$$A(dB) = 10\, log_{10} \frac{P_t}{P_r} \qquad \text{Equation 7-14}$$

Using e base for logarithm and the combination of Equation 7-13 and Equation 7-14 results:

$$A(dB) = 4.343kL \qquad \text{Equation 7-15}$$

The attenuation coefficient $k$ could be expressed as:

$$k = \rho C_{ext} \qquad \text{Equation 7-16}$$

Where $\rho$ is particle (raindrop) density and $C_{ext}$ is attenuation cross-section or extinction cross-section.

In hydrological studies, where the attenuation depends on rain rate, simple relationships between specific attenuation and Rainfall rate (Equation 1-1 and Equation 1-2) assist in measurement.

- **Free path loss**

Because of the characteristics of wave propagation, there is a loss of power at the receiver antenna in comparison with the output power at the transmitter. The minimum loss between two isotropic receiver and transmitter antennae without any obstruction is free space path loss (Whitaker, 2005). It is usually described as the ratio of the transmitted power $P_t$ to the received power $P_r$:

$$\frac{P_r}{P_t} = \left(\frac{\lambda}{4\pi D}\right)^2 \qquad \text{Equation 7-17}$$

where $\lambda$ is wavelength and $D$ is the distance between transmitter and receiver antennae. Equation 7-14 could be reshaped in terms of frequency as:

$$L_{fs} = 32.5 + 20\,log\,D + 20\,log\,f \qquad \text{Equation 7-18}$$

Where $L_{fs}$ is free space path loss, $D$ is the distance in ($km$), and $f$ is the frequency in ($MHz$).

- **Scattering theories**

The scattering theories are developed to solve Maxwell's equation for waves passing a media containing particles. Fundamental studies have given rise to the introduction of Mie and Rayleigh scattering (approximations) for the propagation of electromagnetic waves through particles in a given space (Rayleigh, 1881, 1899; Mie, 1908). The Mie theory serves as a mathematical representation of the absorption and elastic scattering of waves by particles (Seinfeld, Pandis and Noone, 1998). Figure 7-4 illustrates the interaction of a wave beam with a particle.

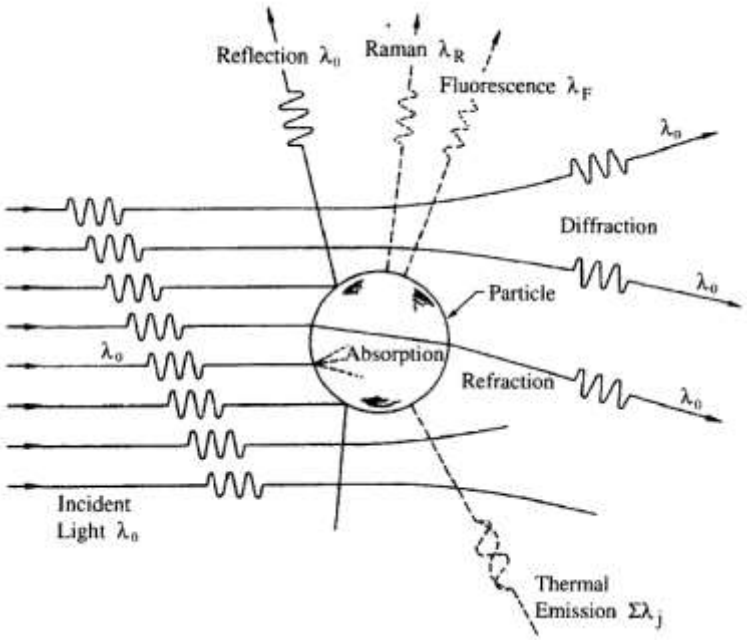


*Figure 7-4- Different mechanisms of wave interacts with a particle, source: (Seinfeld, Pandis and Noone, 1998)*

These studies not only provided explanations for phenomena like the blue colour of the sky but also found applications in the calculation of radio waves travelling through air containing various elements such as air molecules, dust, rain, and snow.

The distinction between the two theories lies in the relative size of particles and wavelength. Rayleigh scattering is relevant when the particle, characterized by its radius $a$ and refractive index $n$ is electrically small $(2\pi a/\lambda \ll 1)$ (Barclay, 2003). On the other hand, Mie scattering applies to particles with a sufficiently large size (Hecht, 2002), independent of wavelength, having a diameter equal to or larger than the wavelength.

- **Scattering cross-sections**

A scattering cross-section, $\sigma$ or $C$, is the amount that relates to the rate of interaction between target and radiation (Kotlarchyk, 1999). It is more dependent on the relative size of the particle to wavelength and the angle of radiation. The cross-section is related to the volume of the target (Bohren and Huffman, 1983):

$$C_{abs} = (\pi D^2/4)Q_{abs} \qquad \text{Equation 7-19}$$

Where, $C_{abs}$ is scattering cross-section, $Q_{abs}$ is scattering efficiency and $D$ is the Diameter of the particle. The absorption efficiency, $(abs)$, is extinction efficiency, $(ext)$, minus scattering efficiency, $(sca)$:

$$Q_{abs} = Q_{ext} - Q_{sca} \qquad \text{Equation 7-20}$$

And efficiencies are:

$$Q_{ext} = 4x\,Im\left\{\frac{m^2-1}{m^2+2}\left[1+\frac{x^2}{15}\left(\frac{m^2-1}{m^2+2}\right)\frac{m^4+27m^2+38}{2m^2+3}\right]\right\}+\frac{8}{3}x^4\,Re\left\{\left(\frac{m^2-1}{m^2+2}\right)^2\right\} \qquad \text{Equation 7-21}$$

$$Q_{sca} = \frac{8}{3}x^4\left|\frac{m^2-1}{m^2+2}\right|^2 \qquad \text{Equation 7-22}$$

$$Q_{abs} = 4x\,Im\left\{\frac{m^2-1}{m^2+2}\right\}\left[1+\frac{4x^3}{3}Im\left\{\frac{m^2-1}{m^2+2}\right\}\right] \qquad \text{Equation 7-23}$$

Where $m$ is the relative refractive index of particle and the surrounding medium, $x$ is the size parameter, $Im$ is the Imaginary part, and $Re$ is the real part. The energy scattered or absorbed by a particle is proportional to the incident energy (Seinfeld, Pandis and Noone, 1998):

$$\tilde{F}_{sca} = C_{sca}F_0 \qquad \text{Equation 7-24}$$

$$\tilde{F}_{abs} = C_{abs}F_0 \qquad \text{Equation 7-25}$$

Therefore, the size of the particle and its proportion to the wavelength are the main ruling criteria in scattering theories.

### 7.1.4. Telecommunication and cell phones

- **Cellular network**

A cellular network, or mobile network, employs wireless connections in the final segment of communication between users. In a mobile network, cell phones establish connections with the network through microwaves.

- **Cell phone antenna**

Cell phones communicate with each other using their individual antennas and intermediary antennae. Each link between two cell phones is facilitated through a ground antenna positioned atop a tower, known as a Base Transceiver Station (BTS). The number of BTSs varies based on the distance between the communicating cell phones, and additional intermediary stations, connected via either wire or fibre-optic connections, contribute to establishing connectivity.

- **Microwave links**

Any connection between a transmitter and a receiver via electromagnetic waves in the range of microwaves is a microwave link.

- **Commercial microwave links**

A Commercial Microwave Link (CML) refers to a microwave connection established by telecommunication companies between two Base Transceiver Stations (BTS) or tower antennas. Telecommunication companies strategically deploy a sufficient number of BTSs to ensure optimal coverage in both urban and rural areas, catering to the needs of their customers.

- **Generations of cellular networks**

The first generation (1G) of cellular networks emerged in the 1980s, followed by subsequent generations up to the present (Asif, 2019). Currently, the fifth generation (5G) is in its initial stages of development and is poised for global implementation. Each successive generation offers increased speed, higher data rates, and reduced latency (Asif, 2019). Notably, 5G technology presents the capability to connect a greater number of devices simultaneously.

- **The radiofrequency range of cellular network**

The older generation of cellular networks typically utilizes lower frequencies ranging from about 800 MHz to 2.6 GHz, whereas the upcoming 5G networks are slated to be allocated higher frequency bands. The Office of the Minister of Broadcasting, Communications, and Digital Media recommends the 3.5 GHz frequency with a bandwidth of 390 MHz for 5G deployment (Office of the Minister of Broadcasting, 2019a, 2019b). The frequency range of 3.3-4.2 GHz is widely accepted as the standard commercial 5G frequency, striking a balance between coverage and capacity (Weissberger, 2019). Discussions regarding the allocation of additional spectrum in this range, as well as below 1 GHz, planned to take place during the World Radiocommunication Conference 2023 (WRC-23), aiming to enhance 5G applications in both urban and rural areas, particularly in the context of the Internet of Things (IoT) (Weissberger, 2019). The discussions centred around advancing sub-1 GHz spectrum to

improve rural and in-building connectivity, aiming to aid 5G in bridging the digital divide (*GSMA | WRC-23 – Keep up to date with mobile - Spectrum*, 2023).

# 8. Appendix B – Signals and denoising methods

## 8.1. Wave characteristics

Key factors to consider in wave propagation include dispersion, dissipation, and nonlinearity. These effects arise from processes such as polarization, reflections, and refraction at micro-scale irregularities, along with geometric, physical, and structural nonlinearities (Pérez-Rendón and Robles, 2004).

### 8.1.1. Stationary and non-stationary signals

The changes in signal properties play a significant role in signal power analysis and selecting the data analysis methods. A stationary signal has relatively constant properties over time or space while non-stationary signals experience various frequencis at different time and locations (Pérez-Rendón and Robles, 2004).

### 8.1.2. Linear and non-linear waves

Linear waves are governed by linear equations, meaning that in these equations, the dependent variable and its derivatives are raised to no more than the first degree (Griffiths and Schiesser, 2009). As a result, linear systems adhere to the superposition principle, allowing the combination of simple solutions to create more intricate ones. This provides analysts with access to various tools for linear system analysis, with Fourier analysis being particularly valuable. It enables the expression of general solutions by using sums or integrals of well-established fundamental solutions (Griffiths and Schiesser, 2009).

Nonlinear waves are governed by nonlinear equations, which typically do not adhere to the superposition principle. Consequently, analysing nonlinear wave equations presents greater mathematical complexity, and there isn't a universal analytical method available for their solutions. Regrettably, this implies that each specific wave equation must be approached on a case-by-case basis (Griffiths and Schiesser, 2009).

When elastic strain waves move through composite materials, they undergo numerous instances of reflection and refraction at the internal structural irregularities. This phenomenon results in the dispersion of the wave field and the scattering of mechanical energy (Andrianov, Danishevskyy and Awrejcewicz, 2021).

The influence of nonlinearity, on the contrary, leads to the concentration of energy and to the generation of higher harmonics. In the case of a balance between the effects of dispersion and nonlinearity, the formation of stationary non-linear waves (periodic or solitary) is possible, which propagate without changing the shape and speed (Andrianov, Danishevskyy and Awrejcewicz, 2021).

### 8.1.3. Skewness and asymmetric

Skewness shows the waves' departure from symmetry around the horizontal axis and characterizes their nonlinearity, while asymmetry indicates whether the waves lean forward or backward (Agnon *et al.*, 2005).

## 8.2. Signal power

In this section, definitions and terms are described first, to introduce the aspects of signal power fluctuations and the effective factors across different time scales.

The structure of a microwave link should be elucidated first to understand how it works and what are the different electrical and environmental components, their role, and their intricate interplay.

### 8.2.1. power amplifier

The power amplifier (PA) plays a vital role in wireless transceiver systems. It is a bridge between the signal generation in radio frequency (RF) systems and the signal radiation through the antenna. The PA boosts the high-frequency signal for wireless transmission, ensuring it meets the proper power level and spectrum requirements (Wang and Sengupta, 2016).

The transmitter typically consists of three amplification stages: the Pre-Driver, the Driver, and the Final with different active devices. Figure 8-1 shows a simplified diagram of the Tait Mobile Radio transmitter block. In this diagram, the Tx Drive signal which comes from the Synthesizer amplifies by the pre-driver from +5dBm to around +20dBm (100mW). The Driver stage takes the output, magnifying it to a level of around +33dBm (2W). This signal enters the Final and is amplified up to a level of approximately +45dBm (32W). Before the antenna, the Tx / Rx Switch, and a Harmonic Filter, decline the RF signal level by almost 1dB. As a result, the final transmitted signal level is +44dBm or 25W (Tait Communications, 2016).

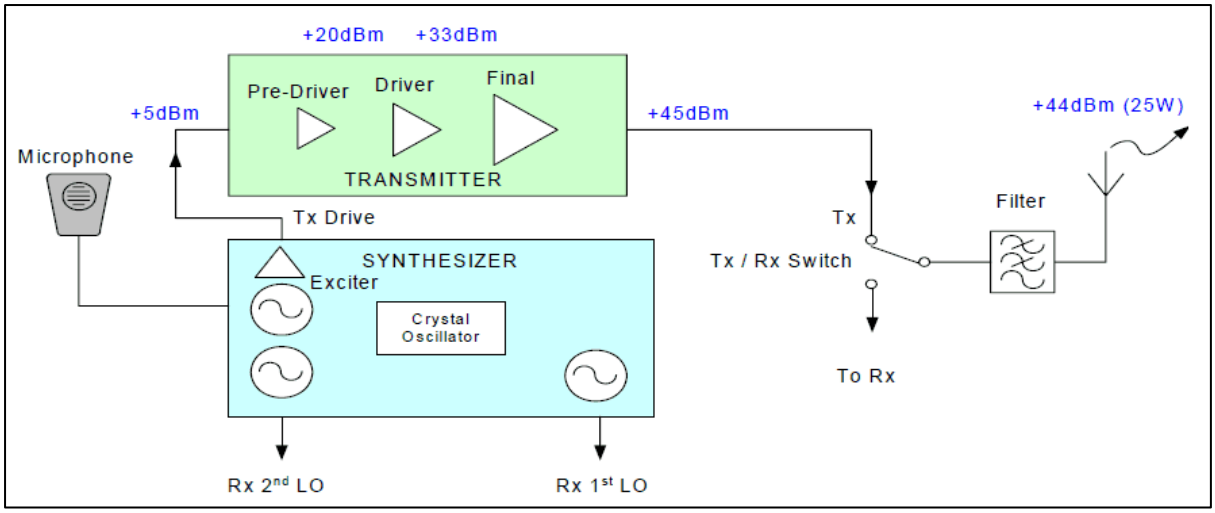


*Figure 8-1- The simplified diagram of the Tait Mobile Radio transmitter block (source:* (Tait Communications, 2016)*)*

### 8.2.2. Transmitter Signal Level ($TSL$)

The Transmitter Signal Level signifies the power or intensity of a signal when it is sent from a sender or transmitter within a communication system. This is a vital parameter that has a direct impact on the excellence and reach of wireless communication (Telecom Trainer, 2023).

Transmitted Signal Level holds significant importance for several reasons. $TSL$ significantly influences the effective communication range of wireless signals, where higher $TSL$ values enable extended transmission distances before signal weakening. Additionally, a robust $TSL$ ensures a high signal-to-noise ratio, essential for dependable communication by mitigating background noise, interference, and environmental signal degradation. Moreover, an optimal $TSL$ reduces the risk of signal interference with neighbouring signals and minimizes collisions in multi-device communication scenarios. Careful $TSL$ selection is vital to align with the receiver's sensitivity range, preventing communication failures resulting from an excessively low $TSL$ (Telecom Trainer, 2023).

In some references, the power of the propagating signal is identified as the effective isotropic radiated power.

### 8.2.3. Effective Isotropic Radiated Power ($EIRP$)

$EIRP$ refers to the power that an antenna emits into the surrounding environment. This measurement is taken at the antenna's output and can be calculated in the following manner (NIOSH, 2019):

$$EIRP = P_T - LL_T + G_T$$ Equation 8-1

where $EIRP$ is the effective isotropic radiated power ($dBm$), $P_T$ is transmitter power ($dBm$), $LL_T$ is the line loss ($dB$), and $G_T$ is transmitter antenna gain ($dBi$). Therefore, $EIRP$ is the tower of the signal which is leaving the transmitter antenna.

### 8.2.4. Receiver Signal Level ($RSL$)

The receiver Signal Level is the level of the signal power at the receiver (Manggau *et al.*, 2018).

Using the term $EIRP$, the receiver signal level can be explained as:

$$RSL = EIRP - L_{propagation} + G_R - L_R$$ Equation 8-2

where, $RSL$ is the Receiver Signal Level ($dBm$), $L_{propagation}$ is the losses during propagation ($dB$), $G_R$ is receiver antenna gain ($dBi$), and $L_R$ is receiver channel losses ($dB$).

Therefore, $RSL$ is the remained power level of the propagating signal collected at the receiver system.

### 8.2.5. Interference in signal propagation

Interference in the transmission of radio frequency electromagnetic waves can significantly impact the quality of signal reception. Interference refers to disturbances affecting the desired signal. In electromagnetic theory, it describes the combination of electromagnetic waves, including those from different sources or the same propagation origin, but receiving from different directions (Saakian, 2011).

Interference appears in two terms. The first is the random fluctuations in the parameters of the desired signal. The other is known as additive interference or noise, superimposing on the desired signal. This noise spans a broad spectrum and can affect the amplitude and phase of the signal as it passes through the propagation path, causing random fluctuations (Saakian, 2011).

Figure 8-2 classifies the types of interferences in radio frequency links. Fast and slow fading are two types of random fluctuations, that are produced in the propagation medium. Seasonal variations are also another type of multiplicative noise (Saakian, 2011).

Two main sources of interference are internal and external. The receiver noise or internal noise originates from electronic components and devices like antennas, amplifiers, and filters. External noise can include man-made noise, atmospheric noise from sources like lightning discharges and air molecule collisions, and cosmic noise from space radiation (Saakian, 2011).

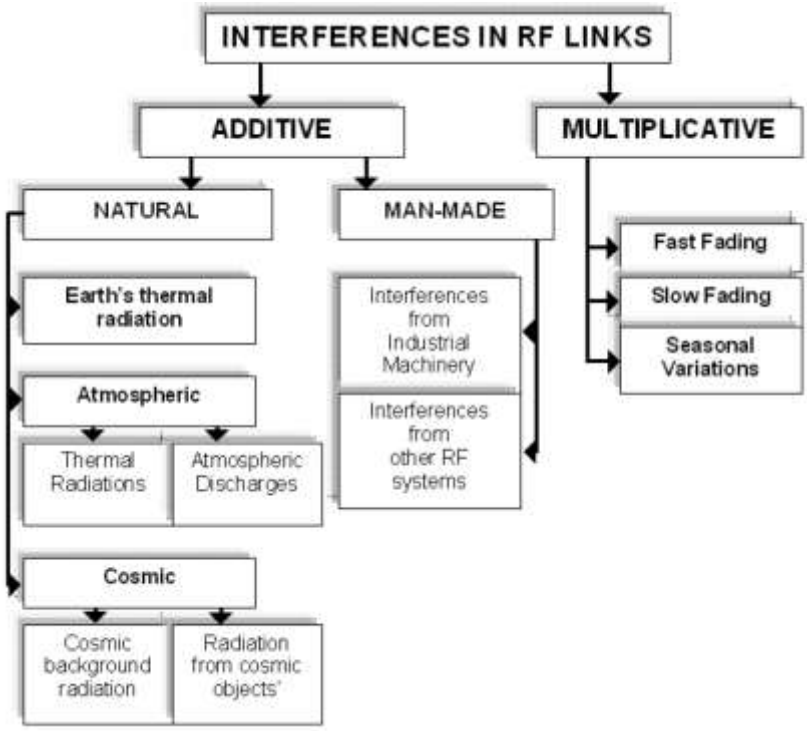


*Figure 8-2- Different types of interferences in radio frequency links (source:* (Saakian, 2011)*)*

### 8.2.6. Rim coverage probability

Given the fluctuations in transmitter signal levels and the random nature of the interferences in signal propagation, the received signal level is not stable. Therefore, there is a chance to receive a signal level less than the desired level if the power is not strong enough or the attenuation is too high. Therefore, a probability factor is defined to provide a concept that helps in design and calculations.

The rim coverage probability quantifies the likelihood that the power level exceeds a set threshold at a specific distance from the antenna (Andersen, 2015). The calculation for the fade margin, expressed in $dB$, depends on the statistical properties of the fading environment and is determined as (NIOSH, 2019):

$$P(RSL > RSL_{Th}) = P(x > x_0) = 1 - \frac{1}{\sigma\sqrt{2\pi}} \int_{-\infty}^{x_0} e^{-1/2\left(\frac{x-\mu}{\sigma}\right)^2} dx \qquad \text{Equation 8-3}$$

Where $P$ is the rim coverage probability, $x$ is the receiver signal level ($RSL$), $x_0$ is the receiver signal threshold ($RSL_{Th}$), $\mu$ is the average value received signal level, and $\sigma$ is the standard deviation.

The area coverage probability extends this concept, representing the probability that within a designated area, the power level remains above the threshold (Andersen, 2015).

### 8.2.7. Signal-to-Noise Ratio ($SNR$)

SNR is a measure used to quantify the strength of a desired signal in relation to the background noise present in a system. It indicates how much the signal stands out from the noise, providing insight into the quality and reliability of the signal. This ratio could be calculated as (John Price, 1993):

$$SNR = 10\log_{10}\left(\frac{Signal\ Power}{Noise\ Power}\right) \qquad \text{Equation 8-4}$$

where, $Signal\ Power$ and $Noise\ Power$ are in $watts$ or $milliwatts$ and $SNR$ is in $dB$. In this formula, the signal power represents the power of the desired signal, and the noise power represents the power of the unwanted background noise. According to the principles of logarithmic equations, the signal-to-noise ratio can then be calculated from dBm levels (Seybold, 2005):

$$SNR = RSL_{dBm} - Noise_{dBm} \qquad \text{Equation 8-5}$$

Where, $RSL_{dBm}$ is the received signal level in $dBm$, and $Noise_{dBm}$ is the noise level in $dBm$.

SNR values are typically measured in decibels (dB), and the interpretation of what constitutes a good or bad SNR can vary based on the application and the specific context. However, a general guideline for understanding SNR levels in different scenarios is (CADENCE PCB Solutions, 2020):

- Excellent SNR (> 40 dB): This is considered a very strong SNR and indicates an excellent signal quality with minimal noise interference. Communication or analysis should be highly reliable.
- Good SNR (25 - 40 dB): This range indicates a strong signal with relatively low noise. Communication or analysis should be reliable and robust.
- Fair SNR (15 - 25 dB): The signal is still distinguishable from noise, but there might be some susceptibility to interference. Communication or analysis might experience occasional disruptions.
- Poor SNR (5 - 15 dB): In this range, the signal is getting closer to the noise level. Communication or analysis could be significantly affected, leading to errors or data loss.
- Very Poor SNR (< 5 dB): The signal is severely affected by noise, making communication or analysis highly unreliable or practically unusable.

It's important to note that the specific acceptable SNR level can vary based on the technology, application, and industry standards. For example, in telecommunications, a mobile phone might work well with an SNR of around 10 dB, while high-quality audio systems might require an SNR of 90 dB or more (Meraki, 2023).

Ultimately, what constitutes a good or bad SNR depends on the specific requirements of the system or application. Higher SNR values generally indicate better signal quality and more reliable performance.

### 8.2.8. Microwave signal base level

In CML rainfall retrieval methods, rainfall is derived from the attenuation of the microwave signal. The drop in power is reflected in the received signal level ($RSL$). However, because of all the interferences in signal level, $TSL$ oscillates, not only during the rainy periods but also in dry weather conditions. Therefore, the rainfall attenuation is not the difference between $TSL$ and $RSL$. The difference between these two signal levels is the full attenuation of the signal due to all the natural, manmade, additive, and multiplicative noises in the transmitter, receiver, and the link path.

Figure 8-3 shows a reference level for the power of a microwave link compared to three levels of signal power, minimum, maximum and average records. The reference power is estimated using a conventional method of median of dry periods. The difference between the green line (reference power) and the dropped attenuated power level is used for calculating rainfall. Various methods of reference power suggest different methods of calculation and using different levels of power of the signal during the recording periods.

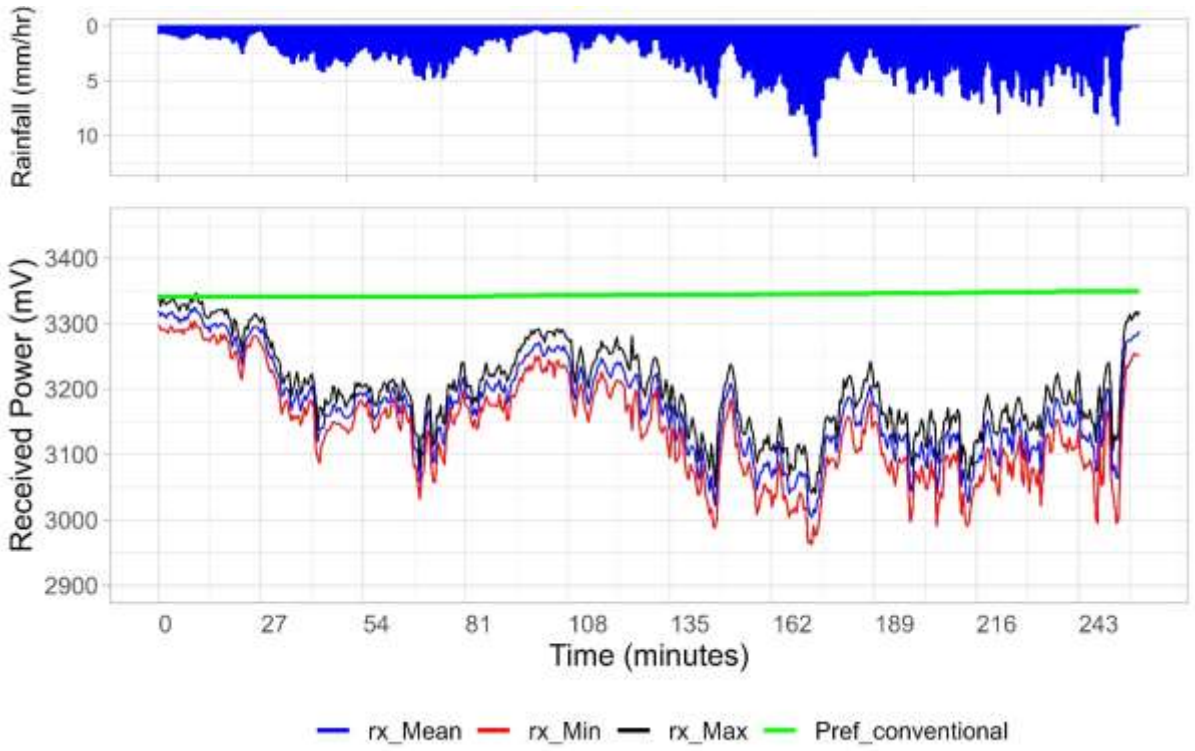


*Figure 8-3- Minimum, maximum, and average received signal power for a microwave link and the reference (base) power for the signal (calculated with median dry method)*

The entire period in Figure 8-3 is characterized by rainfall, consisting of a variation in the distance between the reference level and the average signal power. Consequently, the precision of our rainfall estimates is contingent on the accuracy of the power law or any attenuation-based rainfall retrieval methods. However, the difference between the base signal level and the current received signal power is not always produced according to rainfall attenuation. There will be occasions during which the signal indicates attenuation despite the absence of rainfall. Conversely, there will be periods when rainfall is absent, yet power fluctuations occur below the baseline, indicating some degree of attenuation. Figure 8-4 shows a sample period of rainfall and dry weather where the attenuation of signal power does not correspond to the rainfall periods.

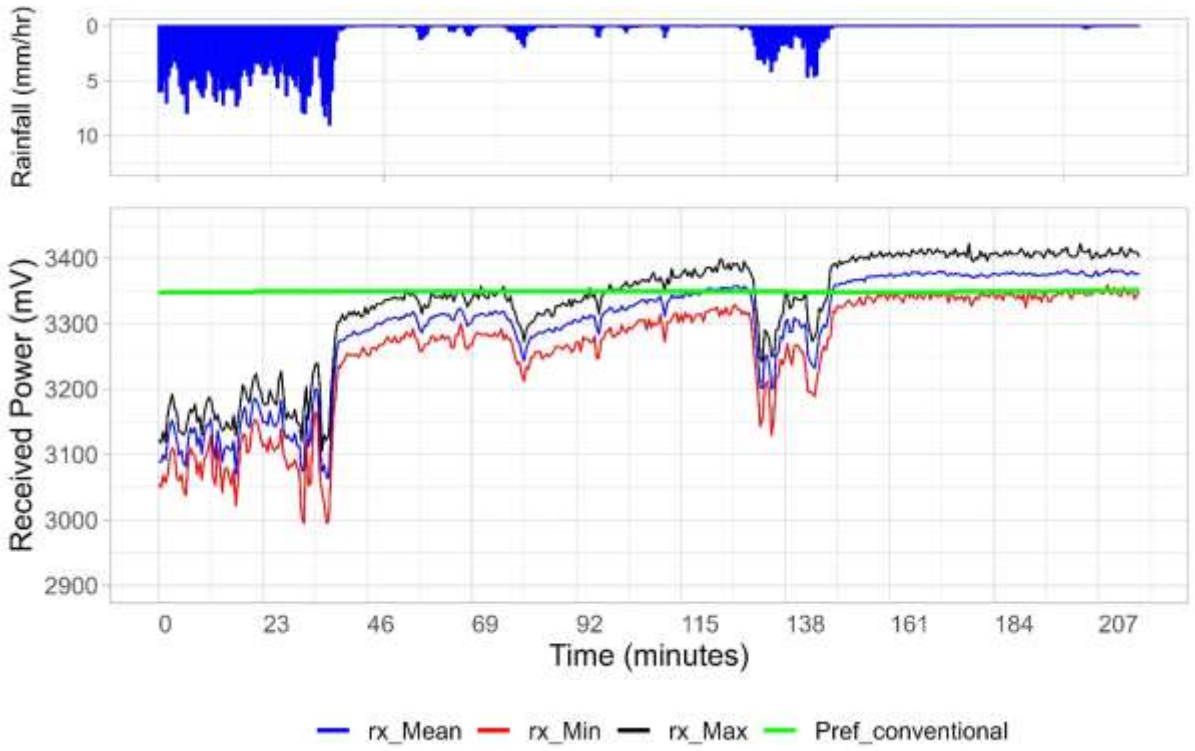


*Figure 8-4- Fluctuations of signal power level under base level while the attenuation is not aligned with rainfall periods.*

The other challenge is that the attenuation is not proportional to rainfall intensity. Figure 8-5 illustrate this difference which appears in different periods. As Figure 8-5 shows, using Equation 1-2 ($R = aA^b$) with a constant reference power level results in a wrong estimation of rainfall. The order of rainfall intensities in this graph is 1-3-2, while a constant reference level results in the order of 1-2-3 for attenuation. A varying reference level like the blue dashed line (a hypothetical line) in Figure 8-5 can fix this problem and result in the right order of 1-3-2 for attenuation according to the rainfall intensity order.

Therefore, a varying reference level is needed to establish a correct ratio between rainfall and attenuation.

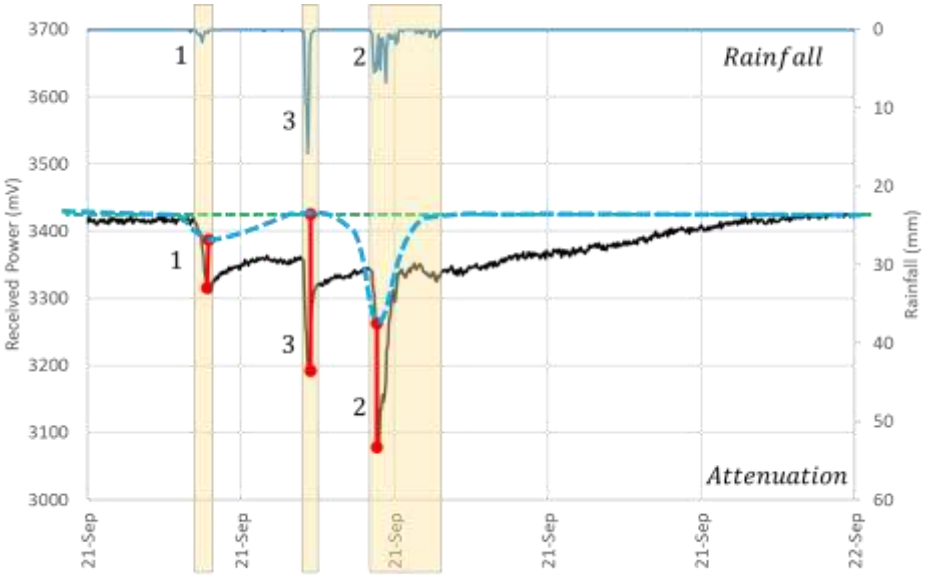


*Figure 8-5- A sample period of rainfall and received signal power with a hypothetical constant and varying reference levels.*

Establishing a baseline signal power helps filter out factors contributing to attenuation and exclude those unrelated to rainfall. This baseline serves as the foundation for addressing rainfall-induced attenuation. Due to the similarity of rainfall and other hydrometeors, the base power of a microwave signal refers to the underlying power level of the signal in the absence of any specific atmospheric or environmental conditions, such as rainfall, snowfall, fog, and mist.

The signal reference or base level must be established according to the received signal level in rain-free periods (Overeem, Leijnse and Uijlenhoet, 2011). Various methods and techniques are used to detect and estimate the base power of microwave signals.

## 8.3. Noise

Noise is an undesired signal that interferes the transmission or measurement of another signal (Vaseghi, 2000). Noise itself represents a signal carrying information about its source. In processing microwave signals, noise carries the information from different sources such as temperature fluctuations, electronic devices, and other signal-related factors. If this noise can be identified and quantified, it becomes feasible to distinguish and extract it from the primary carrier wave. Consequently, establishing a noise-free signal level and detecting alterations during rainfall becomes straightforward. However, this is a challenging task due to the multitude of noise sources with often unknown characteristics. Hence, the significance of denoising techniques in signal processing becomes evident.

Noises are categorized based on their frequency, time characteristics, or spectrum. These categories include (Vaseghi, 2000):

a) **White noise:** This strictly random noise exhibits an impulse autocorrelation function and a flat power spectrum. It encompasses all frequencies with equal power.
b) **Band-limited white noise:** refers to a type of noise that maintains a uniform power spectrum within a restricted frequency range, typically aligned with the bandwidth of the device or signal being analysed.
c) **Coloured noise:** Different from white noise, this term refers to any broadband noise with a non-flat spectrum shape. Examples of this include pink noise, brown noise, and autoregressive noise.

d) **Narrowband noise:** This type of noise is characterized by a narrow bandwidth, often resembling frequencies like 50/60 Hz from the electricity supply.
e) **Transient noise pulses:** These are noise pulses with relatively lengthy durations, such as burst noise and clicks.
f) **Impulsive noise:** Comprising short-duration pulses with random amplitude, duration, and time of occurrence, this type of noise is highly variable.

The term coloured noise, for instance pink and red noise, is often used especially in electroacoustic area (Baxandall, 1968) and explains the ratio of higher and lower frequencies for power and amplitude. The colour of noise which refers to noise spectrum gives information about the noise power spectrum and clarify the power distribution into frequency constituents of the signal (Stoica and Moses, 2005). The power spectrum and frequency are proportional in reverse (Szendro, Vincze and Szasz, 2001):

$$S(f) \propto \frac{1}{f^{\alpha}} \qquad \text{Equation 8-6}$$

where $S(f)$ is the spectral density function and $f$ is frequency and $\alpha$ is a constant between 0 and 2. When $\alpha = 1$, the signal is called a pink noise and for $\alpha = 2$ the signal is a brown noise (Szendro, Vincze and Szasz, 2001).

## 8.4. The concept of noise and denoising in rainfall attenuation derivation

Noises could be categorized into impulsive and transient noises. Impulsive noise is characterized by short-duration noise pulses that rapidly alternate between on and off states (Vaseghi, 2000). Impulsive noise filters are employed to improve the quality and clarity of noisy signals and to enhance the resilience of pattern recognition and adaptive control systems.

On the other hand, there are transient noise pulses which exhibit longer durations and a relatively higher proportion of low-frequency energy content, and they tend to occur less frequently than impulsive noise (Vaseghi, 2000). Typically, transient noise pulses consist of a short, sharp initial pulse followed by diminishing low-frequency oscillations. The initial pulse often results from external or internal impulsive interference, while the oscillations typically stem from the resonance of the communication channel triggered by the initial pulse (Vaseghi, 2000).

Excluding the impact of rainfall attenuation, the power of a CML signal primarily equals the carrier signal power. During rainfall events, attenuation is introduced to the signal, resulting in a reduction in power. A comparison between the carrier signal and the attenuated signal reveals that the patterns of power decline resemble electromagnetic wave noise. However, the period of rainfall attenuation affecting the CML signal fluctuates in accordance with the duration of the rainfall event.

In shorter periods, the power reduction resembles impulsive noise. Recognizing the resemblance between rainfall attenuation and noise from other sources, the concept of developing the application of impulsive noise filters in rainfall measurement emerges.

By denoising techniques, it is possible to mitigate the effects of rainfall and isolate the CML signal's base level. Consequently, rainfall attenuation can be understood as the outcome of subtracting the received power from the base level.

## 8.5. Base level detecting methods in CML rainfall retrieval methods

To delete noise, including rainfall attenuation, in signals and extract the main fluctuating wave, various signal processing techniques could be employed. The techniques and methods to determine the signal base level depend on the application and the background of studies in each field. Hence, the methods are different in electrical engineering, medical science, and hydrology.

In rainfall measurement techniques, the signal base level is generally determined by applying the characteristics of the signal level during the adjacent dry periods and applying those properties to the rainy periods. Below are the commonly used methods in rainfall measurement studies.

### 8.5.1. Moving average

In this method, the baseline attenuation estimate is derived by averaging attenuation measurements taken just before and after a rainstorm (Zinevich, Messer and Alpert, 2010a). To precisely identify the rainstorm's duration in the area, the timing is determined using nearby rain gauges, allowing for a 10-minute buffer to account for variations in the physical distance between the measurement point and the rain gauge. Subsequently, measurements spanning a duration of 2 to 27 hours, depending on data availability, are utilized for the calculations outlined below (Zinevich, Messer and Alpert, 2010b). For practical applications, they employed the established techniques for detecting rainy and non-rainy conditions as well.

### 8.5.2. Rolling Median dry period

Determining the base signal level by using the median of the power in a dry period is one of the most common methods in rainfall estimations (Huang *et al.*, 2023). This baseline algorithm employs a rolling median across all data categorized as "dry" within the central 24-hour period to establish the baseline signal for every time step (van Leth *et al.*, 2017, 2018).

The method involves an ongoing calibration system where the average baseline attenuation level for each frequency is continuously adjusted when there is no rain (Rahimi *et al.*, 2003). They utilise the latest baseline levels from dry weather to calculate the attenuations in the following rainy period. To enhance accuracy, we can later modify the estimates of attenuations during rainy periods by comparing them to the baseline from the subsequent dry period.

The median method is a simple denoising technique that can also be used for certain types of filtering, including for noise reduction. The median method is a non-linear filter that replaces each sample in the signal with the median value of neighbouring samples. It is effective in removing impulsive noise or outliers, as the median is less sensitive to extreme values compared to the mean. The median method is less suitable for preserving the fine details of the signal, as it can smooth out sharp changes.

### 8.5.3. Interpolating dry period attenuation

The baseline variates even in the wet period. Therefore, a method is developed to address this variation by interpolating the baseline at the start and the end of the rainfall event to establish a base level (Upton *et al.*, 2005).

In this method, noticeable minute-to-minute increases in attenuation are monitored as a rainstorm approaches the signal path. As a result, the beginning of a wet period during dry weather can be detected. However, decreases in attenuation over minutes do not necessarily mean the storm has ended; it might just be a temporary reduction in intensity.

This method has been developed for a dual-frequency microwave link. Two values, $R_L$ and $R_H$, represent path-averaged rain rates calculated for low and high frequencies, respectively, using the power law of attenuation-rainfall with different constants. Typically, these values overestimate the true path-averaged rain rate due to the chosen frequencies. As the lower frequency has a higher power value, it's common for $R_L$ to be greater than $R_H$. During dry weather, signal fluctuations are relatively small, and the condition $R_L > R_H$ is used to pinpoint the starting minute of a rainy period. The baseline at the event's beginning is determined as the average received signal strength in the 10 minutes before the start (Upton *et al.*, 2005).

For detecting the end of the e rainfall event, the ratio $\rho$ is calculated for each minute as:

$$\rho = \frac{R_H}{R_L}$$ Equation 8-7

During rainy periods, $\rho$ is typically less than 1, while in dry weather, a wide range of values is observed. Two indicator functions $I_t$ and $J_t$ are defined as below to indicate the time of the event (Upton *et al.*, 2005):

$$\begin{aligned} &\text{If } R_H < 0 \text{ or } R_H < 0 \text{ (or both)} && I_t = I_{t-1} + 1 \\ &\text{Otherwise} && I_t = \max(0, I_{t-1} - 1) \end{aligned}$$ Equation 8-8

where, $R_L$ and $R_H$ are defined for each minute and $I_t$ is the minute indicator.

$$\begin{aligned} &\text{If } \rho < 0.35 \text{ or } \rho > 1.5 && J_t = J_{t-1} + 1 \\ &\text{Otherwise} && J_t = \max(0, J_{t-1} - 1) \end{aligned}$$ Equation 8-9

where $J_t$ is the minute indicator.

When $I_t$ or $J_t$ reaches 10, the baseline after the event is established by taking the mean received signal strength over the preceding 10 minutes. The baseline during the event is then calculated by interpolation between the values before and after, generally differing for each minute of the event (Upton *et al.*, 2005).

### 8.5.4. First order low-pass filter

In this single parameter model a dynamic baseline ($B_2$) is defined as (Fenicia *et al.*, 2012):

$$B_1(t_i) = min\big(B_1(t_{i-1}), P(t_i)\big)$$ Equation 8-10

$$B_2(t_i) = min\big((1-m)B_1(t_{i-1}) + mP(t_i), P(t_i)\big)$$ Equation 8-11

where $B\ (dBm)$ is the baseline, $P\ (dBm)$ is the negation of the received power, taking negative values, $m$ is the filter parameter and $t$ signifies the time at the step $i$. The total attenuation is the difference between the baseline ($B$) and the power ($P$) (Fenicia *et al.*, 2012):

$$A_m(t) = P(t) - B(t)$$ Equation 8-12

Figure 8-6 illustrate the baseline extracted by a first order low-pass filter compared to a constant baseline (Fenicia *et al.*, 2012).

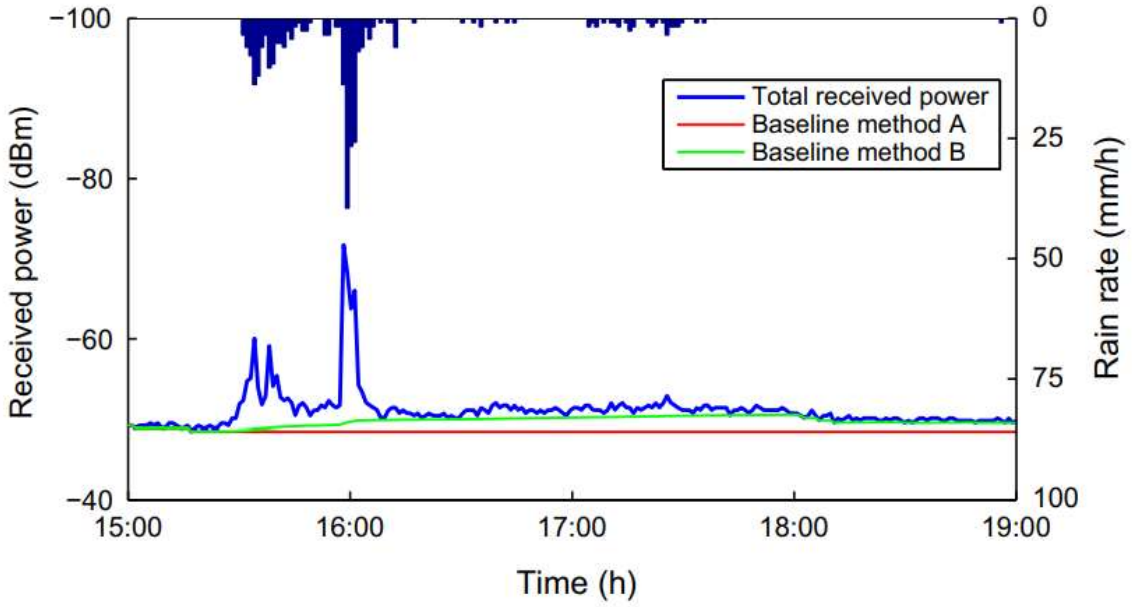


*Figure 8-6- Comparing constant baseline (method A) and first order low-pass filter (method B) (source: (Fenicia et al., 2012))*

## 8.6. Base level detecting methods in other applications

Detecting the baseline and accurately identifying the primary sources of signal power or amplitude fluctuations are fundamental processes in signal processing. This practice is pivotal across various domains where signals, including electromagnetic waves, play a crucial role, spanning applications in medicine to telecommunications. One of the key aspects of signal processing is the capacity to detect subtle oscillations within a waveform and effectively distinguish them from the main signal. This process commonly falls under two categories of denoising methods and decomposition methods.

Both signal decomposition and signal denoising involve manipulating signals but they serve different purposes. Signal decomposition aims to understand the structure of a signal by breaking down a complex signal into its constituent components (Civera and Surace, 2021). However, signal denoising aims to enhance the signal by reducing unwanted components, such as random noise, that may degrade its quality.

Signal decomposition aims to extract and segregate individual signal elements from complex signals, ideally with relevance to meaningful entities (Ohm, 2004). Therefore, they cover a vast area of applications. This includes identifying specific objects within images or videos, distinguishing between various video segments, extracting melodic sequences in music, isolating spoken words or sentences within speech signals, and microwave imaging enhancement (Jens-Rainer Ohm 2004). On the other hand, vibration-based Structural Health Monitoring (SHM) is an important application of signal decomposition to detect damages and distortions which are similar to noise in vibrational response of the target structure (Civera and Surace, 2021).

Complex signals typically consist of multiple components, often displaying nonstationary and nonlinear characteristics (Feng, Zhang and Zuo, 2017). This means that each constituent element exhibits variations over time in terms of amplitude, phase, and/or frequency. Each of these elements can be thought of as an oscillatory mode with both amplitude modulation and frequency modulation (AM-FM). Consequently, any intricate multi-component signal can be described as a combination of various AM-FM components (Feng, Zhang and Zuo, 2017).

The process of decomposition becomes vital for extracting the meaningful physical components within these signals. In real world measurements, signals are often characterised by their multi-component, non-linear, and non-stationary attributes. Separating or breaking down these multi-

component signals into their fundamental scales Is crucial for unveiling the underlying physical characteristics inherent in these measurements (Al-Badrawi, 2017).

Widely used signal decomposition methods include the Empirical Mode Decomposition (EMD), the Local Mean Decomposition (LMD), the Local Characteristic scale Decomposition (LCD), the Hilbert Vibration Decomposition (HVD), the Empirical Wavelet Transform (EWT), and the Variational Mode Decomposition (VMD) (Civera and Surace, 2021).

On the other hand, signal denoising is a well-established field that involves the precise separation of unwanted noise or minor fluctuations from the desired signal. (Donoho, 1995). The purpose of de-noising is to extract valuable information from noisy measurements while keeping its characteristics intact. Noise is an unavoidable part of real data, which can range from highly correlated to uncorrelated with the corrupted signal (Al-Badrawi, 2017).

Various techniques are employed for denoising, such as spectral analysis and filtering (Donoho, 1995). These methods enable researchers and engineers to characterize the frequencies associated with fluctuations in signal amplitude and to filter out or suppress those that are undesirable. Several statistical techniques primarily focus on optimizing the mean-squared error. This necessitates a balance between bias and variance, ensuring that both terms are approximately of the same magnitude (Donoho, 1995). The ultimate goal is to enhance the signal-to-noise ratio (SNR) and preserve the integrity of the original signal.

This practice is integral in diverse applications, from removing background noise in audio recordings to extracting weak signals from noisy environments in telecommunications. It underpins the reliability and quality of signal processing across numerous disciplines.

Over the past thirty years, techniques for eliminating noise in data have predominantly circled around a combination of adaptive and nonadaptive methods and both spatial and frequency domain approaches have been applied to enhance data quality to different extents (Misra, B and S, 2013).

Radar signals possess a remarkable ability to penetrate deeply, making them highly valuable for extended physiological monitoring during unique situations. This significance is particularly prominent in the realms of health monitoring and sleep analysis, where radar technology fulfils a vital role (Li *et al.*, 2019).

While the analogue circuit within these radar systems can mitigate some noise, it remains susceptible to interference from external objects and the inherent motion of the human body at a comparable range. Furthermore, the presence of respiratory harmonics can obscure heartbeat signals, posing challenges in their extraction. Conventional techniques for processing doppler radar vital signals predominantly rely on filtration to eliminate noise and distinguish respiratory and cardiac signals, enabling the extraction of pristine respiratory and heartbeat signals (Li *et al.*, 2019).

### 8.6.1. Empirical mode decomposition (EMD)

Empirical mode decomposition (EMD) is a signal decomposition algorithm designed for non-linear and non-stationary signals, developed by Huang and colleagues in 1998 (Huang *et al.*, 1998). EMD, or Empirical Mode Decomposition, serves to break down the desired signal into a limited set of intrinsic oscillatory modes known as IMFs (Intrinsic Mode Functions) (Huang *et al.*, 1998). These IMFs are oscillations embedded within the original signal and exhibit varying amplitudes and frequencies as time progresses. The high frequency constituents of the wave, e.g. noise, can be separated in dynamic filters of EMD approximations (Al-Badrawi, 2017).

This EMD algorithm employs a recursive process to identify local minimum and maximum points within a signal. It then fits the data between these extrema with interpolation, creating lower and upper envelopes at a local time scale. The algorithm removes the instantaneous mean from these envelopes, effectively creating a "low-pass" centreline. This process isolates the high-frequency components as intrinsic mode functions (IMFs), each of which is mono-component in nature. The

algorithm then repeats recursively on the remaining "low-pass" centreline (Feng, Zhang and Zuo, 2017). This iterative sifting results in breaking down any signal into a series of IMFs that fulfil two main conditions (Feng, Zhang and Zuo, 2017):

- Over the entire time span, the number of extrema and zero crossings must be equal or differ by at most one. This condition is akin to the traditional narrow band requirements for a stationary Gaussian process.
- At any given time, the instantaneous mean of the upper and lower envelopes must be zero. This requirement shifts from a global requirement to a local one, ensuring that the instantaneous frequency avoids unwanted fluctuations caused by asymmetric waveforms.

Figure 8-7 presents an EMD analysis on a sample wave including seven IMFs and the residue, the main signal, and the Hilbert power spectrum (Feng, Zhang and Zuo, 2017). The local energy and instantaneous frequency obtained from the IMFs using the Hilbert transform provide a comprehensive energy-frequency-time distribution of the data. This representation is referred to as the Hilbert spectrum and is particularly suitable for analysing nonlinear and non-stationary data (Huang *et al.*, 1998). In fact, the Hilbert spectrum is a weighted non-normalized joint amplitude-frequency-{time distribution (Huang *et al.*, 1998).

In Figure 8-7 the two main components are distinctly separated and recognized. The initial two components correspond to the sinusoidal frequency modulation (FM) and amplitude modulation (AM) aspects, respectively. The remaining components are not genuine constituents of the signals. They may arise due to approximations when using cubic spline fitting and end effects, but their amplitudes are minimal and can be disregarded. The instantaneous frequency for each IMF is determined using the Hilbert transform-based analytic signal approach (Feng, Zhang and Zuo, 2017).

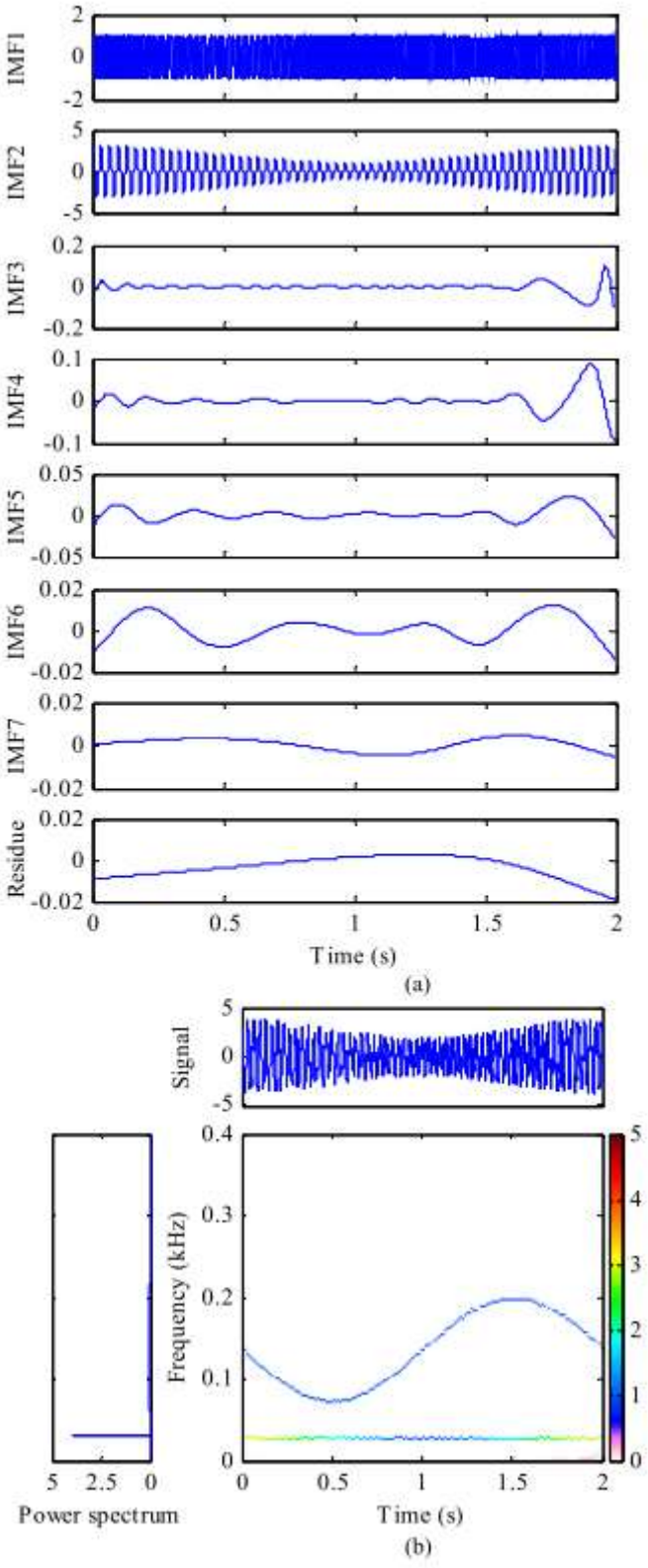


*Figure 8-7- Results of EMD analysis for a sample wave. (a) IMFs and the residue, (b) Hilbert energy spectrum (source:* (Feng, Zhang and Zuo, 2017)*).*

Ensemble EMD (EEMD) and complete ensemble EMD with adaptive noise (CEEMDAN) are noise-assisted variants of EMD method (Zhang *et al.*, 2021). In addition, EMD has been effectively expanded to address the decomposition of multi-variable, multi-dimensional signals since new challenges have been encountered in physics and engineering, associated with complexity, uncertainty, non-linearity, and multi-channel dynamics. Some of developed models include, multivariate EMD (MVEMD), bidimensional EMD (BEMD), Green's function in tension BEMD (GiT-BEMD) which designed for BEMD, Pseudo-bidimensional EMD (pseudo BEMD), image EMD (IEMD) and a novel signal-serialization method (serial-EMD) (Zhang *et al.*, 2021).

EMD has been used in many different fields and applications including biomedical engineering, functional neuroimaging, image enhancement, and or fault diagnosis of mechanical systems (Zhang *et al.*, 2021). EMD also was used for oesophageal manometric time series data analysis in gastroesophageal reflux disease (Liang, Lin and Chen, 2004). Figure 8-8 shows the application of serial versions of EMD and the standard GiT-BEMD in analysing noisy images and the IMFs extracted from the images. Figure 8-8 illustrates the application of serial versions of EMD and the standard GiT-BEMD in analysing noisy images and the IMFs extracted from the images.

EMD method is widely used in mechanical systems for rotating machinery fault diagnosis, gearbox fault diagnosis, analysing gear vibration signals and detecting gear root cracks, diagnosing faults in rolling bearings, gears, and rotors, rolling bearing anomaly detection, and planet bearing fault diagnosis (Feng, Zhang and Zuo, 2017).

The method has been also applied in neuroscience (Pigorini *et al.*, 2011), crude oil price analysis (Zhang, Lai and Wang, 2008), financial analysis (Huang *et al.*, 2003; Leung and Zhao, 2021), and speech recognition (Huang and Pan, 2006).

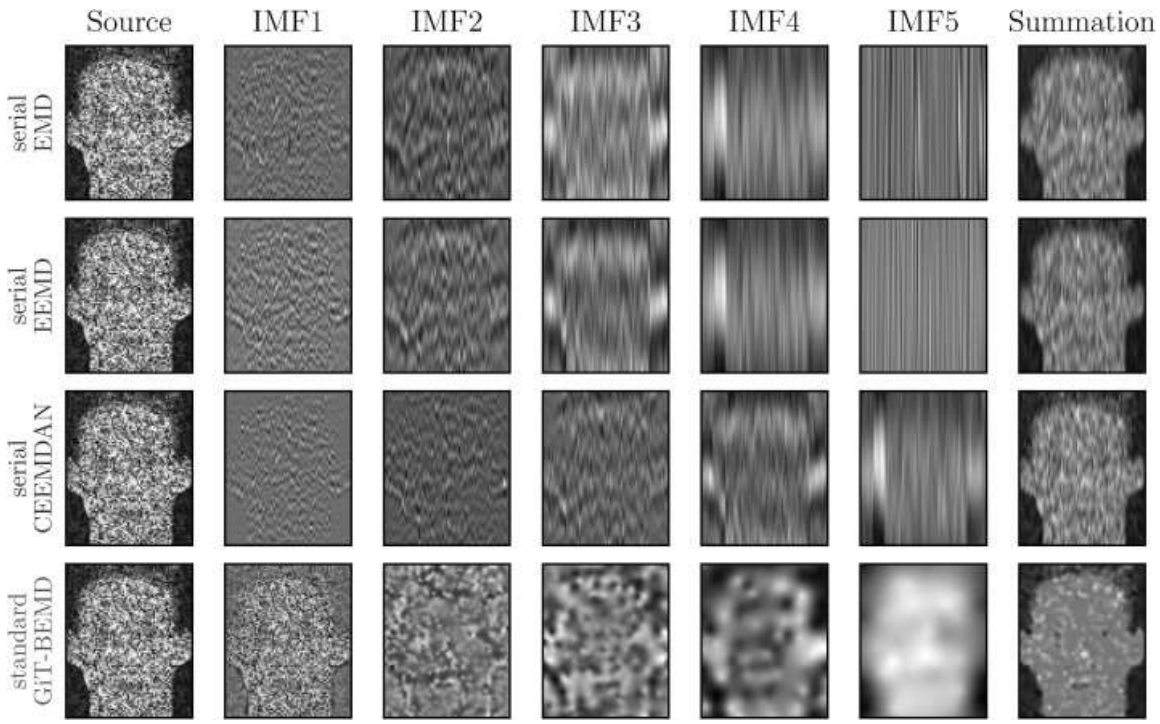


*Figure 8-8- The application of serial versions of EMD and the standard GiT-BEMD in analysing noisy images and the IMFs extracted from the images (IMF6 to IMF12 are not presented) (source: (Zhang et al., 2021))*

### 8.6.2. Ensemble Empirical Mode Decomposition (EEMD)

While the EMD is a popular and extensively utilized method, it has a significant limitation known as "mode mixing." This phenomenon occurs when distinct scales are present within a single Intrinsic Mode Function (IMF) or when a coherent component of similar scale exists in multiple IMFs (Feng, Zhang and Zuo, 2017). Mode mixing often results from irregularities in the signals. To address this issue, a modified version of EMD, called Ensemble Empirical Mode Decomposition (EEMD), was introduced (Feng, Zhang and Zuo, 2017; Stallone, Cicone and Materassi, 2020).

EEMD method involves adding finite amplitude white noise to a signal and sifting it multiple times. The ensemble's mean is treated as the final result, and this process is designed to force the signal into IMFs with different scales, guided by dyadic filter banks (Wu and Huang, 2011). By conducting numerous trials, the added white noise is averaged out, leaving the true component of the original data. The added noise creates a consistent reference frame in time-frequency space, facilitating the collation of portions of the signal with similar scales into one IMF. Unlike the original EMD algorithm, EEMD doesn't require subjective criteria for intermittence testing, making it a more statistically robust and improved noise-assisted data analysis (NADA) method (Wu and Huang, 2011).

Some of the EEMD method applications are including (Feng, Zhang and Zuo, 2017):

- Detecting rotor-stator rubbing.
- Bearing fault diagnosis.
- Wind turbine planetary gearbox fault diagnosis.
- Rotating machinery fault diagnosis, covering rolling bearings, gears, and rotors.

### 8.6.3. Local Mean Decomposition (LMD)

The local mean decomposition (LMD) was introduced as a technique for estimating the instantaneous frequency and amplitude of signals (Feng, Zhang and Zuo, 2017). LMD dissects a signal into a mono-component structure, representing it as a combination of amplitude modulation and frequency modulation. It then goes on to separate the frequency modulation from the amplitude modulation through an iterative process (Feng, Zhang and Zuo, 2017).

The separation process involves smoothing the initial signal, subtracting the smoothed version from the original, and subsequently demodulating the amplitude using an estimated envelope (Smith, 2005). The envelope estimate and the smoothed version of the original signal are derived using a moving average technique weighted by the time intervals between consecutive extrema in the original signal. If the resulting signal doesn't exhibit a flat envelope, the process is reiterated until a frequency-modulated signal with a flat envelope is obtained. The instantaneous frequency is then computed from this frequency-modulated signal. The envelope estimates are multiplied to create a final envelope, which is subsequently multiplied by the frequency-modulated signal, forming a product function. This product function is then subtracted from the original signal. The entire process is repeated on the resulting signal, generating a second product function along with an associated envelope and instantaneous frequency. This decomposition continues until the remaining signal no longer contains oscillations. The resulting instantaneous frequency and envelope values can be visually represented as a demodulated signal time-frequency representation (tfr) (Smith, 2005).

Unlike EMD, which uses cubic spline fitting for decomposition, LMD employs data smoothing methods to obtain mono-components. One notable distinction is that while the IMFs derived from EMD lack oscillations without zero-crossings between extrema, the Product Functions (PFs) produced by LMD may contain oscillations that don't necessarily cross zero. As a result, LMD has the potential to preserve more of the signal's frequency and amplitude variations compared to EMD (Feng, Zhang and Zuo, 2017).

Likewise EMD method, LMD also has a wide application in diagnosing rotor fault, bearing and gearbox and gear faults, analysing wind turbine gearbox vibration signals, and locomotive rolling

bearing faults (Feng, Zhang and Zuo, 2017). LMD is also suitable for analysing diverse natural signals, including electrocardiograms, earthquake data, and functional magnetic resonance imaging data (Smith, 2005).

### 8.6.4. Intrinsic Time-Scale Decomposition (ITD)

Intrinsic time–scale decomposition (ITD) proposed for time–frequency–energy (TFE) efficiently and precisely (Frei and Osorio, 2006). Extrema in signal waveforms imply oscillations. The mono-component in ITD is called proper rotation component (PRC) and is suitable for calculating instantaneous frequency and amplitude. A PRC is a riding wave with highest frequency on a baseline. The baseline is constructed based on extrema to preserve the monotonicity of the residual signal. In each decomposition, a PRC can be obtained by subtracting the baseline from the input signal (Feng, Zhang and Zuo, 2017).

### 8.6.5. Local Characteristic Scale Decomposition (LCD)

A recent approach called Local Characteristic Scale Decomposition (LCD) was inspired by the idea that for mono-component waveforms, the upper and lower lines connecting local maxima and minima are symmetric about the waveform's instantaneous mean (Feng, Zhang and Zuo, 2017). This algorithm is designed to decompose complex signals into different Intrinsic Scale Components (ISCs), with each ISC being independent (Zheng, Cheng and Yang, 2013). In the context of fault diagnosis in mechanical systems, changes in intrinsic oscillations' complexity are crucial (Feng, Zhang and Zuo, 2017). Measuring this complexity, Fuzzy Entropy (FuzzyEn), which quantifies the self-similarity and complexity of time series, is used. Since these changes occur across different scales, the non-stationary signal analysis method, LCD, is applied to adaptively decompose vibration signals into a series of ISCs at varying scales. This decomposition approach, combined with FuzzyEn, forms a novel method for diagnosing rolling bearing faults (Zheng, Cheng and Yang, 2013).

### 8.6.6. Hilbert Vibration Decomposition (HVD)

This is a decomposition with time-varying vibration based on the Hilbert transform (Feldman, 2006). In this method non-stationary frequency of the largest component is estimated as an average function of the instantaneous frequency of the composition, and the corresponding envelope is estimated according to synchronous demodulation (Feldman, 2006).

HVD employs the Hilbert transform and synchronous detection demodulation to calculate the instantaneous frequency and instantaneous amplitude of signals. It dissects intricate multi-component signals into mono-components, prioritizing those with greater instantaneous amplitude before proceeding to smaller ones (Feng, Zhang and Zuo, 2017).

### 8.6.7. Filtering method

Filtering helps to extract the main frequency content and suppress unwanted high-frequency noise. Filtering is a widely used technique in signal processing to remove unwanted noise components and extract the desired signal characteristics. It involves manipulating the frequency content of a signal to attenuate or eliminate specific frequency components. There are various types of filters available, each with its own characteristics and applications. Figure 8-9 shows sample graphs of filters which ideally stop or pass the magnitude response or gain by some particular frequencies. The filters are lowpass, highpass, bandpass, and bandstop filters.

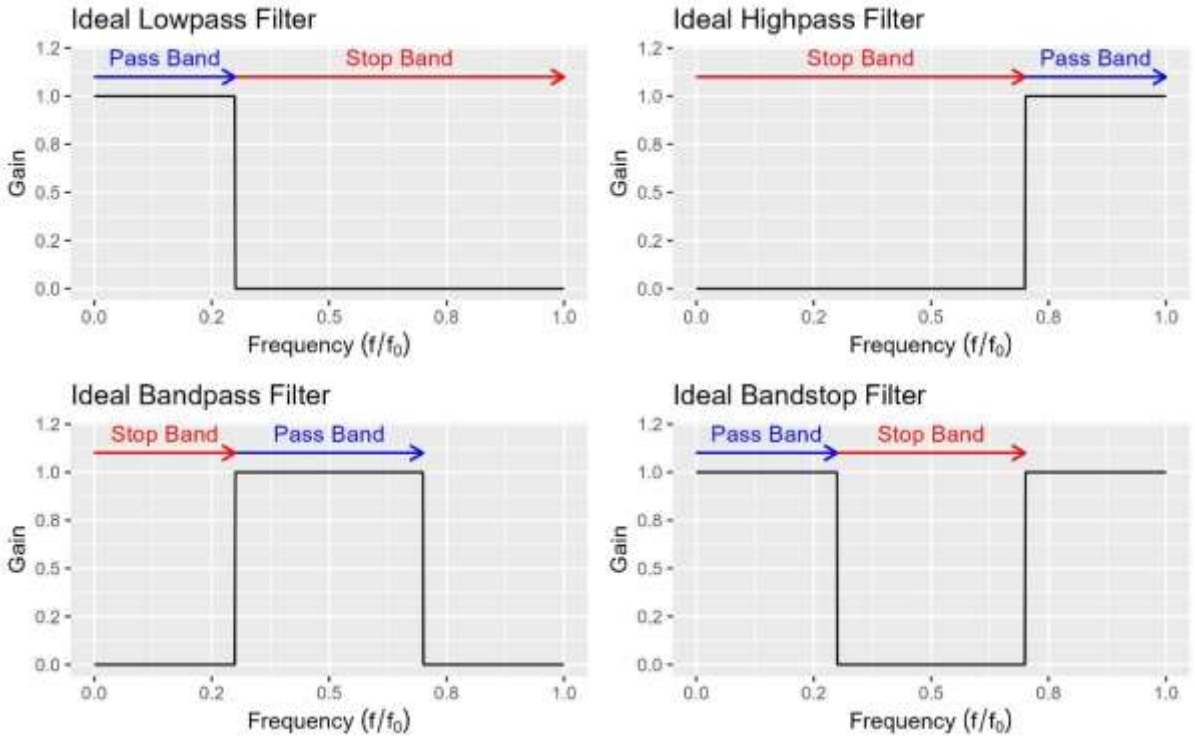


*Figure 8-9- Illustration of sample ideal lowpass, highpass, bandpass, and bandstop filters and their magnitude response (generated from sample signals)*

- Lowpass Filter: A lowpass filter allows frequencies below a certain cutoff frequency to pass through while attenuating higher frequencies. It is commonly used to remove high-frequency noise and extract the low-frequency components of a signal. This type of filter is particularly useful when the main sinusoidal wave of interest has a lower frequency compared to the noise.
  Figure 8-10 (Proakis and Manolakis, 1996) illustrates a frequency response curve for a low-pass filter. Transition band, passband and stopband zones and their ripple and edge ripple are depicted in the picture. The ideal lowpass filter provides a narrowest transition band. The adjustment of the parameters of a filter can help to design a more ideal transition band. Passband ripple refers to the amplitude variation within the specified passband of a filter, typically measured in decibels (dB) (Wanhammar, 1999). This variation indicates fluctuations in the frequency magnitude response curve, occurring in both the passband and stop band. The passband ripple denotes the degree of gain fluctuation within the passband. For instance, a passband ripple of 2 dB signifies a 2 dB gain variation within the passband (PASHTOON, 1987). Managing and comprehending passband ripple is essential in filter design to fulfil precise performance criteria and mitigate undesired fluctuations in signal characteristics.

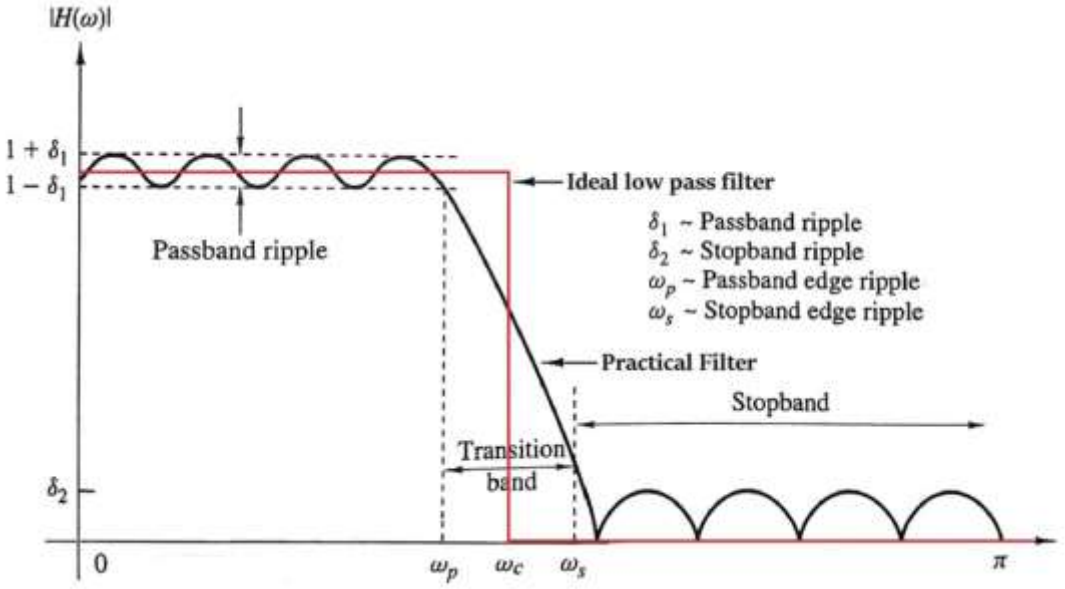


*Figure 8-10- A sample frequency response for a low-pass filter and the ripple and edge ripple zones (source: (Proakis and Manolakis, 1996))*

- Bandpass/bandstop Filter: A bandpass/bandstop filter allows a specific range of frequencies, defined by an upper and lower cutoff frequency, to pass through while attenuating frequencies outside that range. It is effective in isolating a specific frequency band, including the main sinusoidal wave, while rejecting frequencies below and above it. Band-pass filters are useful when the desired signal is concentrated within a specific frequency range, and noise exists outside that range.
- Highpass Filter: A highpass filter can also be designed to pass the high frequency noise shape part of the signal and stop the low frequency part of the signal. This is less practical as it allows the noises to pass and stop the main fluctuations of the transmitting signal.

Filters could be designed with different methods and techniques. Regarding the duration of the impulse response, digital filters can be categorized as either having an infinite-duration impulse response (IIR) or a finite-duration impulse response (FIR) (PASHTOON, 1987). Finite Impulse Response (FIR) and Infinite Impulse Response (IIR) are two types of digital filtering methods used to process signals and remove unwanted noise or alter frequency characteristics. They differ in their filter structure and behaviour.

### 8.6.8. Finite Impulse Response (FIR) Filter Design Techniques:

FIR filters have a finite impulse response, meaning that their output is determined solely by the input and a set of filter coefficients. The impulse response of the FIR filter has a finite duration, gradually reaching zero within a finite time span (Shidore *et al.*, 2022). FIR filters can be designed using various mathematical methods such as:

- Windowing Method: This involves multiplying a window function with the ideal frequency response to create the filter coefficients. Popular windows include Hamming, Hanning, and Blackman windows.
- Frequency Sampling Method: This technique sets desired frequency response samples and uses the inverse discrete Fourier transform to obtain the filter coefficients.
- Optimal Least Squares Method: This method aims to minimize the least squares error between the desired and actual frequency responses using optimization techniques.

FIR filters have a finite impulse response, meaning that the filter's output is a weighted sum of a finite number of past input values (impulses). The filter coefficients are often called the "taps" or

"weights," and they determine how the input samples are combined to create the output. FIR filters are always stable and have linear phase characteristics, which means that all frequency components of the input signal experience the same delay. FIR filters can achieve sharp roll-offs in the frequency domain, making them useful for applications where precise control over frequency response is needed. The design of FIR filters often involves techniques like windowing, frequency sampling, or optimal least squares fitting.

### 8.6.9. Infinite Impulse Response (IIR) Filter Design Techniques:

IIR digital filters are implemented recursively by incorporating a weighted sum of previous output values, adding them to a weighted sum of present and past input values. In essence, these filters possess infinite memory (PASHTOON, 1987). The primary advantage of IIR digital filters, as opposed to FIR digital filters, lies in their ability to design highly selective recursive filters for a given order N. In simpler terms, the recursive implementations of IIR digital filters are computationally efficient. However, a drawback of the recursive approach is that the designer needs to carefully consider factors such as stability, parasitic phenomena, and, if relevant to the design, phase nonlinearity (PASHTOON, 1987).

Some of the IIR filters are including Butterworth, Chebyshev, Elliptic, and Bessel filters.

### 8.6.10. Butterworth filter

Butterworth filter is a signal processing tool with a frequency response (Butterworth, 1930). This filter is widely used in electrocardiogram signal analysis (Rastogi and Mehra, 2013) and audio noise reduction.

The Butterworth filter is a type of infinite impulse response (IIR) filter that represents the optimal balance between attenuation and phase response. It lacks any oscillation in both the passband and stopband and provides a maximally flat frequency response in the passband (Zumbahlen, 2008). Therefore, this filter is designed to have a maximally flat magnitude response in the passband. It's often used for applications where preserving the signal shape is important.

Butterworth filter attenuates frequencies outside the passband according to a specific roll-off rate. The magnitude-squared expression for the Butterworth function with a degree of n is as follows (PASHTOON, 1987):

$$|H_a(j\omega)|^2 = \frac{1}{1 + (\omega/\omega_c)^{2n}} \qquad \text{Equation 8-13}$$

Where $H$ is the transfer function, $\omega_c$ is the cutoff frequency that makes $|H_a(j\omega)|^2 = 1/2$.

Figure 8-11 shows normalised Butterworth filters of orders ranging from 1 to 5 and their magnitude-squared responses.

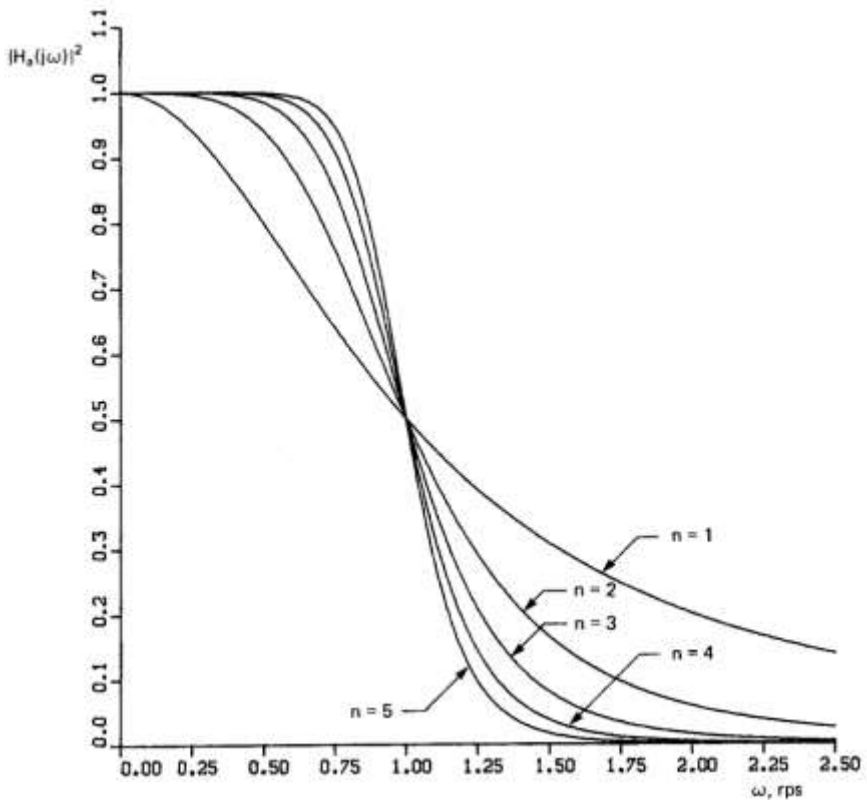


*Figure 8-11- Normalised Butterworth lowpass filter and its magnitude-squared characteristics(source: (PASHTOON, 1987)).*

### 8.6.11. Chebyshev filter (Type I)

Chebyshev filter (or Chevyshev, Tschebychev, Tschebyscheff or Tchevysheff, by different Russian translations (Zumbahlen, 2008)) exhibits a narrower transition region compared to an equivalently ordered Butterworth filter, achieved by introducing ripples within its passband. This type of filter is referred to as the Chebyshev filter due to its focus on reducing the magnitude of the highest ripple, a principle known as the Chebyshev criterion (Zumbahlen, 2008).

The magnitude response specification of a filter can be estimated within a frequency range known as the passband, achieved by minimizing the maximum discrepancy of the approximating function within this range (PASHTOON, 1987).

The Chebyshev filter is a type of IIR filter that provides a steeper roll-off rate compared to the Butterworth filter. It allows for a trade-off between passband ripple and stopband attenuation, providing flexibility in filter design. The Chebyshev filter is commonly used when a sharper roll-off is required, even at the expense of some passband ripple.

The transfer function of the Chebyshev filter for a normalised lowpass ( $\omega_p$=1) is defined as (PASHTOON, 1987):

$$|H_a(j\omega)|^2 = \frac{1}{1+\epsilon^2 C_n^2(\omega)} \qquad \text{Equation 8-14}$$

Where $\epsilon$ is the ripple factor and $C_n(\omega)$ is the Chebyshev polynomial of $n$th-order:

$$\begin{aligned} C_n(\omega) &= \cos(n\cos^{-1}\omega), \quad 0 \le \omega \le 1 \\ &= \cosh(n\cosh^{-1}\omega), \quad \omega > 1 \end{aligned} \qquad \text{Equation 8-15}$$

Figure 8-12 shows a normalised Chebyshev filter with the magnitude-squared response of the filter and the ripple in passband frequencies for two filters of orders five and six.

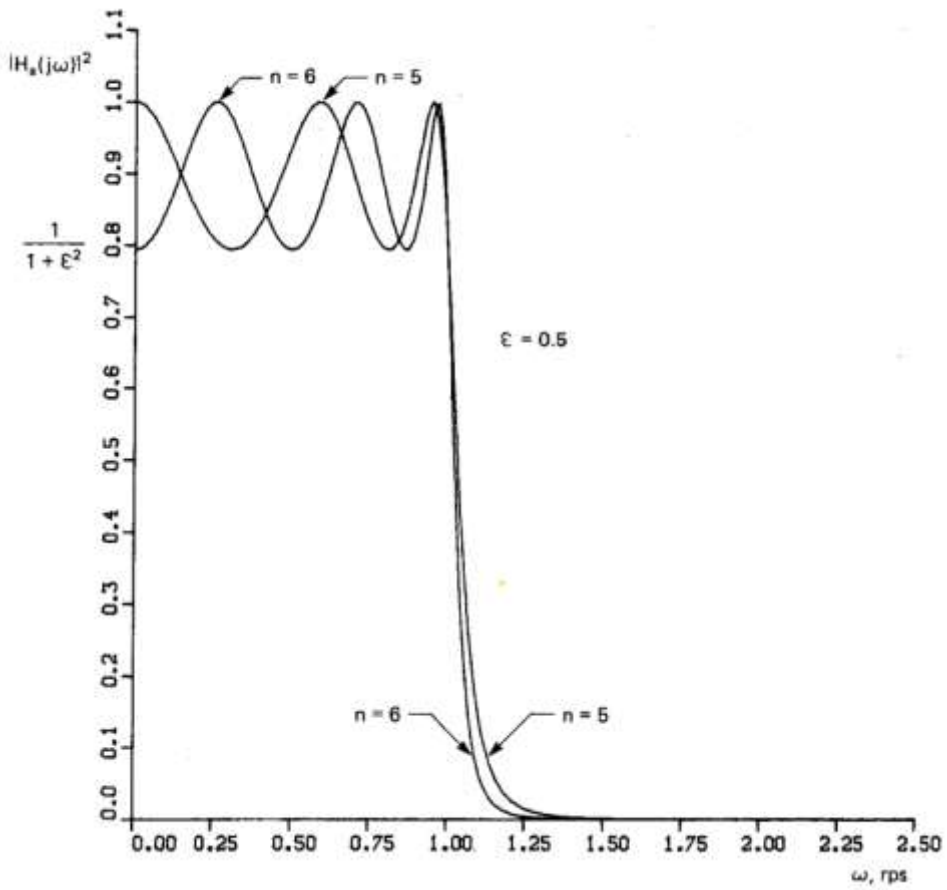


*Figure 8-12- Normalised Chebyshev filters with orders of 5 and 6 and their magnitude-squared response (source: (PASHTOON, 1987))*

### 8.6.12. Chebyshev filter, type II (Inverse)

The Chebyshev characteristic exhibits fluctuations within the passband and a consistent decline in the stopband. Conversely, the inverse Chebyshev characteristic can be described as having a flat consistent magnitude within passband and ripple and fluctuations in the stopband (PASHTOON, 1987). The inverse Chebyshev response performs better in the passband than the Butterworth response, and it outperforms the Chebyshev response except for the immediate proximity to the cutoff frequency. Notably, the inverse Chebyshev response features the sharpest rolloff in the transition band (Zumbahlen, 2008).

### 8.6.13. Elliptic (Cauer) filter

Also known as the "equal-ripple" filter, it provides a more flexible way to control both the passband and stopband ripple. By distributing the approximation error across both the passband and stopband, it is possible to fulfil the specified magnitude response requirements.

This filter exhibits a transition region that is briefer compared to the Chebyshev filter, achieved by permitting ripples in both the stopband and passband (Zumbahlen, 2008).

Filters with this kind of response are referred to as elliptic or Cauer filters with a response function as (PASHTOON, 1987):

$$|H_a(j\omega)|^2 = \frac{1}{1+\epsilon^2 R_n^2(\omega)} \qquad \text{Equation 8-16}$$

Where $R_n(\omega)$ is the Chebyshev rational function and $\epsilon$ is the ripple factor.

The elliptic filter provides a steep roll-off rate and offers the most efficient use of filter order for a given set of specifications. Figure 8-13 illustrates a normalised elliptic filter and the magnitude response of the filter and the ripples in passband and stopband frequencies.

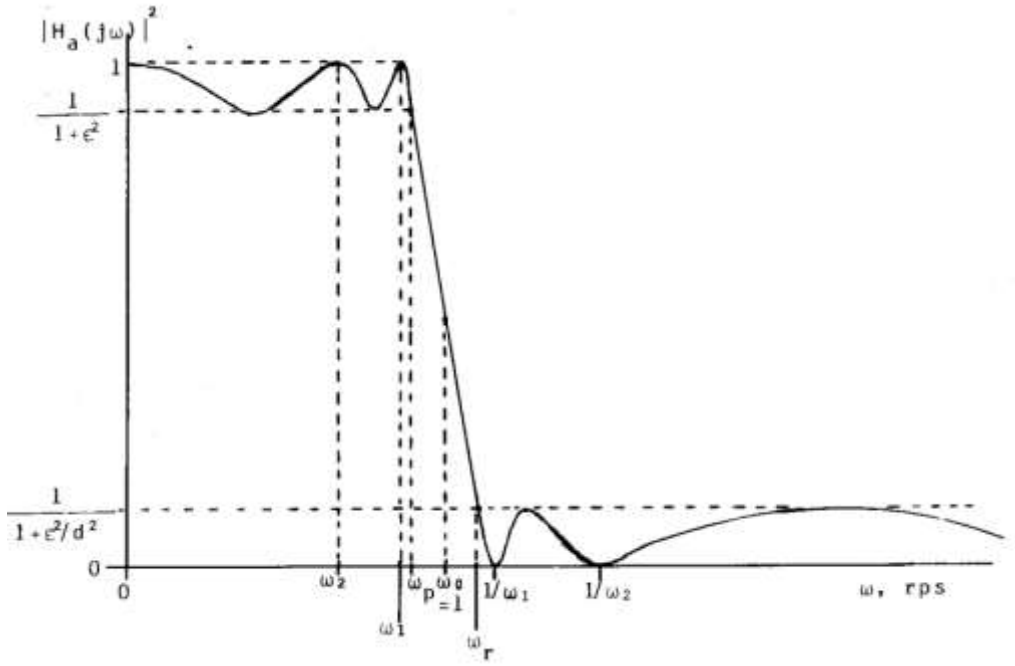


*Figure 8-13- Normalised lowpass elliptic filter and its magnitude-squared response (source: (PASHTOON, 1987))*

### 8.6.14. Bessel filter

This filter has a maximally flat group delay and is designed to enhance its transient response by maintaining a linear phase within the passband, resulting in consistent delay. However, this design choice leads to a comparatively reduced frequency response (lower amplitude discrimination) (Zumbahlen, 2008). The level of nonlinearity becomes more evident when transitioning from Butterworth filters to elliptic filters, particularly near the frequency at the edge of the passband (PASHTOON, 1987).

Particular approximation leads to improved responses in the time domain and progressively approaches the ideal Gaussian curve as the degree of approximation is elevated (Zverev, 1967)

The form of the transfer function for the elliptic filter is (PASHTOON, 1987):

$$H_a(S) = \frac{B_0^n}{\sum_{i=0}^{n} B_i s^i} \qquad \text{Equation 8-17}$$

where for the order of $n$:

$$B_i = \frac{(2n-1)!}{2^{n-i} i!\,(n-1)!} \qquad \text{Equation 8-18}$$

The response of Bessel filter is similar to Butterworth while Butterworth provides a sharper cutoff. Figure 8-14 shows four filters, comparing the sharpness of the cutoff frequency and the transition band for each filter. As the graph shows Bessel filter has a wider transition band and Butterworth and Bessel have a flat passband gain.

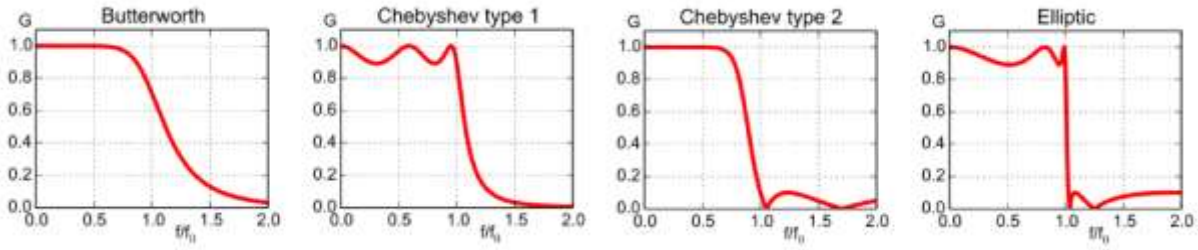


*Figure 8-14- Discrete-time gain a signal with different methods of filtering (source: (Zhang et al., 2020))*

### 8.6.15. Fixed filters vs tunable filters

Fixed filters are characterized by their unchanging passband and stopband frequencies. In contrast, tunable filters offer adjustable passband and stopband frequencies, catering to specific application demands. These frequencies are adaptable, ensuring flexibility as required by various applications. Tunable digital filters find extensive utilization in diverse fields, including medical electronics, digital audio tools, telecommunications, and control systems (Aravindkumar and Manjunathachari, 2017). These filters play a pivotal role, particularly in eliminating noise from audio signals, which is a fundamental necessity.

### 8.6.16. Wavelet Transform

The wavelet transform is a mathematical tool that can be used to decompose a signal into constituent wavelets, which are small, oscillating waves of different frequencies and time durations. Wavelet transforms are useful for a variety of applications, including signal compression, denoising, and feature extraction (Strang and Nguyen, 1996).

By varying the scale factor, $a$, and shift parameter, $b$, the wavelet transform can be used to analyse a signal at different frequencies and time resolutions.

A signal, $f(t)$, can be examined, characterized, or manipulated when represented as a linear decomposition as (C. Sidney Burrus, Gopinath and Guo, 1997):

$$f(t) = \sum_{l} a_l \, \psi_l(t) \qquad \text{Equation 8-19}$$

where $l$ is the sum index (finite or infinite), $a_l$ are the coefficients of the real-valued expansion, and $\psi_l(t)$ is the expansion set.

The coarser resolution coefficients can be computed from the finer resolution coefficients using an organized method known as a "filter bank" (C. Sidney Burrus, Gopinath and Guo, 1997). This approach enables a highly efficient calculation of the expansion coefficients, also referred to as the discrete wavelet transform. It establishes a connection between wavelet transforms and a pre-existing domain in digital signal processing.

The fundamental operations of translation and scaling significantly contribute to the efficiency of wavelets as expansion functions (C. Sidney Burrus, Gopinath and Guo, 1997). When the wavelet's position shifts along the horizontal axis, it enables the transform to explicitly depict the timing or location of events in time or space. On the other hand, variation of the wavelet's scale offers a representation of detail or resolution (C. Sidney Burrus, Gopinath and Guo, 1997).

Notably, as the scale becomes finer, the time steps become smaller which the narrower wavelet and the smaller steps together allow for the representation of finer details or higher resolution (C. Sidney Burrus, Gopinath and Guo, 1997).

Wavelet transform is a powerful tool for signal processing. It offers time-frequency analysis through the use of wavelets or basic functions that can be shifted and dilated in time. The transform can

provide either good time resolution or good frequency resolution. There are two types of wavelet transforms: continuous wavelet transform (CWT) and discrete wavelet transform (DWT). The DWT is particularly useful for signal coding (Tan and Jiang, 2019).

Regarding the applications of wavelet transform, the term denoising with wavelet transform, refers to various techniques that reject noise by damping or thresholding in the wavelet domain (Donoho, 1995). Wavelet analysis is utilised in signal analysis widely and most frequently (Gilles, 2013).

The Wavelet Transform is particularly effective in analysing signals with time-varying frequency content. By using wavelet decomposition, specific frequency bands could be isolated, and the main sinusoidal wave could be extracted while eliminating noise at different scales (Donoho, 1995).

Some of the applications of wavelet denoising include microwave imaging for detecting brain cancer. Wavelet transform is also a common method in noise removal from electrocardiogram (ECG) signals (Chatterjee *et al.*, 2020).

### 8.6.17. Empirical Wavelet Transform (EWT)

The wavelet transform uses a fixed set of wavelets, while the empirical wavelet transform adapts its wavelets to the signal. This adaptability can make EWT more suitable for certain types of non-stationary or complex signals.

Conventional techniques such as Fourier or wavelet transforms rely on predetermined bases or frames that are created independently of the specific signal being analysed. In contrast, adaptive methods seek to formulate these bases directly by considering the information inherent in the signal itself (Gilles, 2013). Empirical Wavelet Transform proposes a method to build a family of wavelets adapted to the processed signal (Geetikaverma and Singh, 2018).

While the adaptability of EMD appears beneficial for numerous applications, its primary drawback is the absence of a solid theoretical foundation. The core concept of EWT involves isolating various signal modes through the development of a well-suited wavelet filter bank (Gilles, 2013). EWT build a family of wavelets for the processed signal, specifying a bank of wavelet filters, based on a proper Fourier support (Geetikaverma and Singh, 2018).

This method constructs adaptive wavelets designed to extract the AM-FM components of a signal. The underlying concept is based on the notion that these constituent AM-FM components exhibit Fourier spectra with compact support. The process of isolating different modes is akin to segmenting the Fourier spectrum and applying specific filters corresponding to each identified Fourier support (Feng, Zhang and Zuo, 2017). Unlike adhering to a predefined scheme for dilation factors, as seen in dyadic discretization, EWT empirically determines these factors based on the characteristics of the signal's Fourier spectrum, thus earning the name empirical wavelet transform (Feng, Zhang and Zuo, 2017).

### 8.6.18. Variational Mode Decomposition (VMD)

A fully non-iterative variational mode decomposition model introduced which simultaneously extracts multiple modes and identifies their individual centre frequencies (Dragomiretskiy and Zosso, 2014). The objective is to ensure that these modes, when combined, faithfully replicate the input signal. Moreover, each mode exhibits smoothness after being transformed into a baseband signal (Dragomiretskiy and Zosso, 2014).

This algorithm effectively dissects intricate multi-component signals into their constituent AM-FM elements in a non-recursive manner, and it exhibits resilience against noise. VMD is a wholly non-recursive decomposition approach that simultaneously and adaptively extracts the constituent AM-FM components of complex multi-component signals. It characterizes IMFs as explicit AM-FM models and establishes a connection between the parameters of AM-FM models and the bandwidth of IMFs. By capitalizing on the narrow-band trait of IMFs, it derives AM-FM parameters by minimizing the

bandwidth, resulting in the generation of IMFs. This method outperforms other existing mode decomposition techniques, offering advantages such as a solid theoretical basis and robustness against noise and sampling issues (Feng, Zhang and Zuo, 2017)

### 8.6.19. Nonlinear Mode Decomposition Principle

Nonlinear mode decomposition (NMD) is a method for decomposing signals into meaningful oscillations while effectively eliminating noise (Iatsenko, McClintock and Stefanovska, 2015). It leverages a potent combination of time-frequency analysis methods and adaptive parameter selection, ensuring robustness to noise (Iatsenko, McClintock and Stefanovska, 2015).

This method is developed through a fusion of time-frequency analysis, surrogate data tests, and harmonic identification, making it highly resistant to noise. It excels in detecting interconnected oscillations and distinguishing deterministic patterns from random ones (Feng, Zhang and Zuo, 2017). It's important to note that the "nonlinear" aspect in NMD doesn't refer to classical nonlinear analysis but rather indicates that the resulting modes exhibit intricate waveforms, often attributed to nonlinear characteristics within the originating system or measurement process (Feng, Zhang and Zuo, 2017).

### 8.6.20. Adaptive Filtering

Adaptive filtering techniques, such as the Least Mean Squares (LMS) algorithm, can be employed to adaptively estimate the main sinusoidal wave and suppress noise (Singh and Lubecke, 2013). These algorithms iteratively adjust filter coefficients based on the input signal, reducing the influence of noise and enhancing the desired signal components.

### 8.6.21. Adaptive Local Iterative Filtering

The Adaptive Local Iterative Filtering (ALIF) method is a novel approach was introduced to combines the iterative filtering strategy (decomposing to IMFs) with a filter length selection which is adaptive and data-driven to accomplish the decomposition (Cicone, Liu and Zhou, 2016).

The instantaneous mean in EMD is defined as the mean function of upper and lower envelopes, but it is unstable under perturbations. An iterative filtering algorithm was proposed (Lin, Wang and Zhou, 2011) to address this issue, which derives the instantaneous mean by low pass filtering the signal. However, to effectively analyse non-linear and non-stationary signals, filters with compact support and flexible length along time are desired. An adaptive local iterative filtering (ALIF) algorithm (Cicone, Liu and Zhou, 2016) proposed to meet this need. It effectively analyse non-linear and non-stationary signals, filters with compact support and flexible length along time (Feng, Zhang and Zuo, 2017).

### 8.6.22. Instantaneous Frequency Estimation Approaches

Instantaneous frequency estimation methods aim to directly and accurately estimate the instantaneous frequency of signal components. On the other hand, decomposition methods like EMD, EEMD, LMD, and ITD are mainly designed for signal decomposition into simpler components or modes, and they may indirectly provide information about frequency content but with a different focus (Feng, Zhang and Zuo, 2017).

Instantaneous frequency is a crucial aspect for unveiling the frequency characteristics and their temporal changes within nonstationary signals (Feng, Zhang and Zuo, 2017). This allows for a comprehensive understanding of the precise mechanisms responsible for signal generation and the genuine physical properties conveyed by these signals. Several methods have been developed to accurately estimate the instantaneous frequency of a single component. These methods encompass techniques such as Hilbert Transform Based Analytic Signal (HT), Direct Quadrature (DQ), Normalized Hilbert Transform (NHT), Generalized Zero-Crossing (GZC), Energy Separation (ES) (Feng, Zhang and Zuo, 2017).

### 8.6.23. Moving Average

A simple moving average can help smooth out variations and attenuate high-frequency noise. Moving average filter performs as a lowpass filter (Shidore *et al.*, 2022). By calculating the average value of the signal over a window of time, the main sinusoidal wave is preserved while noise fluctuations are suppressed. Moving average filter is defined as:

$$Y(i) = \left(\frac{1}{M}\right) \times \sum_{j=0}^{M-1} x(i+j) \qquad \text{Equation 8-20}$$

where $Y$ is the output signal, which is denoised, $M$ is the size of the window and $x$ is the noisy signal.

The sole adjustable parameter in a moving average filter is the window size ($M$), representing the number of preceding signal entries that can be averaged. Noise may be pronounced if the window is excessively small, while a too large window might result in the omission of crucial signal information. The optimal window size is typically determined through a trial-and-error process (Shidore *et al.*, 2022).

### 8.6.24. Fast Fourier Transform

Fast Fourier Transform (FFT) transforms a signal into separate spectral components, offering frequency details of the signal in the process and analysing the frequency spectrum of the signal. By converting the signal from the time domain to the frequency domain, the dominant frequency components could be identified and separated from noise (MathWorks, 2023b). Applying a threshold or frequency cutoff can help retain the main sinusoidal wave while discarding noise components.

Figure 8-15 shows a signal in time domain and the three main components of it in frequency domain. By recognising the frequency of the signal components, the Fourier transform can decompose the signal.

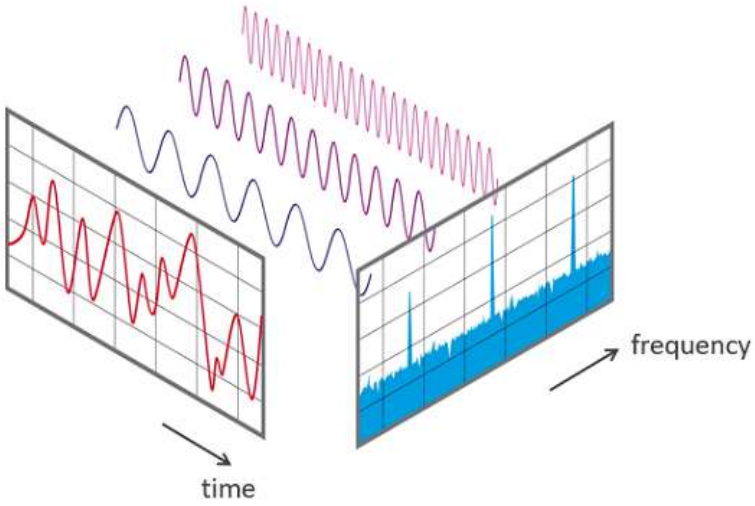


*Figure 8-15- A signal in time domain and frequency domain with separated components of different frequencies (source: (Fast Fourier Transformation FFT - Basics, no date)).*

## 8.7. Comparing Methods

Selecting a method for denoising or other purposes depends on the specific requirements of the application, including noise characteristics, desired signal quality, and frequency response.

A summary of various filter types can be classified as:

- Passive or Active: Filters can be passive (composed of only passive components) or active (incorporating active components like transistors or op-amps).
- Analog or Digital: Filters can operate in the analogue domain (continuous-time signals) or digital domain (discrete-time signals).
- High-Pass, Low-Pass, Band-Pass, Band-Stop, All-Pass: Filters can be classified by their frequency response characteristics, including high-pass, low-pass, band-pass, band-stop (notch), and all-pass filters.
- Discrete-Time or Continuous-Time: Filters can operate in discrete-time (sampled) or continuous-time (analogue) domains.
- Linear or Non-Linear: Filters can be linear, preserving the linearity of the input-output relationship, or non-linear, introducing non-linearities.
- Infinite Impulse Response (IIR) or Finite Impulse Response (FIR): Filters can be categorized based on their impulse response characteristics. IIR filters have feedback, while FIR filters do not.

A suitable starting point for the comparison is the evaluation of conventional methods, such as the median of dry periods. While FIR and IIR filters offer more control over filtering characteristics, the median method is effective for specific noise types and might be preferred when preserving sharp changes in the signal is crucial. Median filtering is better suited for removing impulsive noise or outliers but might not be as effective in preserving signal details (Shah *et al.*, 2022). Therefore, it might be the reason for selecting the median method for defining the base level of the signal to recognise the sharp changes in times of rain.

FIR filters are inherently stable due to their finite impulse responses and can have a linear phase for distortion-free transmission. They often require higher orders than IIR filters to achieve the same specifications, leading to increased complexity, cost, and processing time. High-order FIR filters with sharp cutoffs require considerable computational resources, making IIR designs more favourable in such cases (Carvalho *et al.*, 2018).

The main benefit of IIR filters compared to FIR filters is their tendency to fulfil specified requirements using a significantly smaller filter order than an equivalent FIR filter (MathWorks, 2023a). While IIR filters do exhibit non-linear phase characteristics, data processing in software such as MATLAB® often takes place "offline," meaning the complete data sequence is accessible before filtering. This permits a noncausal, zero-phase filtering strategy (achieved through the filtfilt function in MATLAB), effectively removing the non-linear phase distortion associated with an IIR filter (MathWorks, 2023a).

IIR filters have an infinite impulse response, which means that their output depends on both current and past input values as well as past output values. They use feedback in their structure, which can lead to complex frequency response shapes and phase characteristics (Parker, 2017). IIR filters can achieve similar filtering characteristics as FIR filters with fewer coefficients, but their design can be more complex due to the feedback nature(Parker, 2017). They also can be unstable if not properly designed, leading to unpredictable and undesirable behaviour. They might introduce phase distortions, especially in the stopband of the frequency response (Parker, 2017).

In summary, the choice between FIR and IIR filters depends on the application requirements and trade-offs. FIR filters are often preferred when linear phase response and precise control over frequency response are important. IIR filters can be more computationally efficient and require fewer coefficients for similar frequency responses, but their stability and phase characteristics need careful

consideration during design. Therefore, IIR filters possess the advantage of achieving a sharp transition zone with a reduced number of coefficients in comparison to FIR filters. Hence, IIR filters are the preferred choice for notch filter design.

The choice of filter design depends on the specific requirements of the application, such as the desired frequency response, passband ripple, stopband attenuation, and transition bandwidth. Each filter type has its advantages and trade-offs, and the selection should be based on the specific needs of the signal processing task at hand.

The classical IIR filters, Butterworth, Chebyshev, elliptic, and Bessel, each provide distinct approximations to the ideal "brick wall" filter (MathWorks, 2023a). Each filter types has specific advantages and trade-offs in terms of rolloff steepness, group-delay linearity, and passband characteristics (PASHTOON, 1987).

Bessel filters exhibit monotonically decreasing magnitude responses in the stopband and emphasise maximally flat group-delay characteristics (PASHTOON, 1987). The Bessel filter is tailored to achieve superior transient response by maintaining a linear phase (constant delay) within the passband. Consequently, this leads to a relatively diminished frequency response (lower amplitude differentiation) (Zumbahlen, 2008).

Butterworth filters prioritise maximally flat magnitude responses (PASHTOON, 1987). This filter exhibit satisfactory amplitude and transient characteristics (Zumbahlen, 2008).

Chebyshev filters enhance the amplitude response while compromising transient behaviour (Zumbahlen, 2008). Chebyshev filters showcase equiripple magnitude response characteristics in the passband. Inverse Chebyshev filters combine maximally flat passband magnitude responses with equiripple stopband characteristics (PASHTOON, 1987). Elliptic filters present equiripple magnitude responses in both passband and stopband, with the steepest rolloffs for a given order n (PASHTOON, 1987).

Butterworth and Chebyshev filters are more versatile in handling various noise types and can provide control over passband ripple and stopband attenuation. The choice between these methods depends on the nature of the noise, desired signal fidelity, and the specific filtering goals.

Figure 8-16 shows the difference between Butterworth, Chebyshev and Bessel filters for a sample signal, while Chebyshev is using a 0.5 dB ripple and the responses have been normalized for a cutoff of 1 Hz (Zumbahlen, 2008). In this graph, the compromises inherent in different response types could be observed. The transition from Bessel to Butterworth and then to Chebyshev reveals an enhancement in amplitude discrimination (Zumbahlen, 2008).

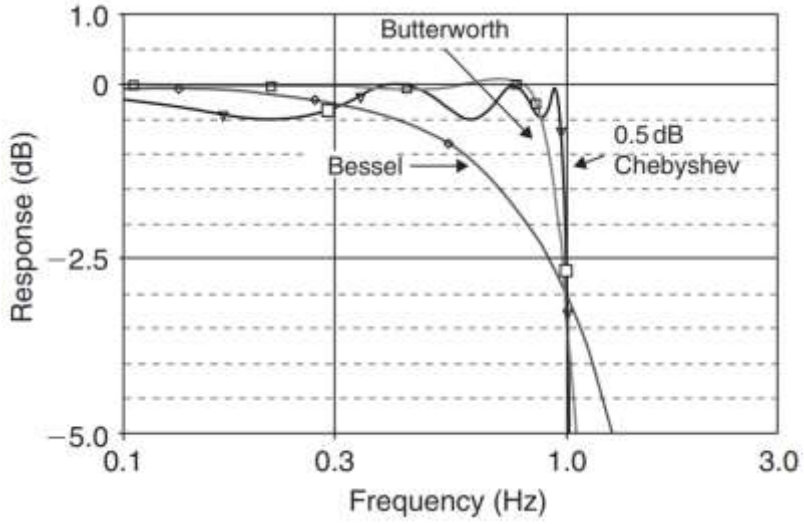


*Figure 8-16- Comparison of IIR filters and their amplitude response (source: (Zumbahlen, 2008))*

In summary, while the median method is effective for specific noise types, Butterworth and Chebyshev filters offer more flexibility in terms of frequency response control and noise reduction, making them suitable for a wider range of applications.

In contrast, methods, like Fourier transform, wavelet-based denoising, might not be the best choices for this specific scenario, as they could potentially alter the sinusoidal variations or require more complex considerations.

The choice of filtering method depends on the specifics of the signal, the noise characteristics, and the desired outcome. It is always a good idea to experiment with different filters and evaluate their effects on your signal to find the most suitable approach.

In the Fourier Transform (FT), signals are represented as a combination of harmonics, specifically sine and cosine waves, which come in an infinite variety of frequencies. In contrast, the Wavelet transform expresses a signal through wavelets at various scales and positions. In this case, the fundamental component of the wavelet transform is the wavelet itself, which exhibits different scales and positions (Danso *et al.*, 2021).

Fourier transform is not able to determine the timing of specific events (Baltazar-Lopez, 2003). This limitation is insignificant when dealing with stationary signals. However, many of signals exhibit various nonstationary or transient features such as drift, trends, sudden shifts, and the initiation and conclusion of events. These features often constitute the most crucial aspect of the signal which cannot be identified using Fourier analysis (Baltazar-Lopez, 2003). However, wavelets seems to provide a better analysis of these characteristics (Sygouni, Tsakiroglou and Payatakes, 2006).

When a Fourier series is selected, the sinusoidal basis functions are fixed and cannot be changed. However, this is not the case for wavelets. In the realm of wavelets, there exists an infinite variety of distinct wavelets, all of which meet the properties described above (C. Sidney Burrus, Gopinath and Guo, 1997).

The Fourier Transform is a powerful method for analysing frequency domains. The short-time Fourier Transform is a variation that operates in both the time and frequency domains. Nevertheless, it faces a challenge in providing high resolution in both domains simultaneously. To address this limitation, wavelets offer an alternative approach to balance resolution across time and frequency domains through multi-resolution analysis (Zhang, Arslan and Flynn, 2013).

Wavelet expansion coefficients drop off quickly with increasing scales and positions. This property, known as being an unconditional basis, makes wavelets highly effective for tasks like signal and image compression, denoising, and detection. Donoho demonstrated that wavelets are nearly optimal for these purposes across a broad spectrum of signals (C. Sidney Burrus, Gopinath and Guo, 1997).

Wavelet expansion allows for precise local description and separation of signal characteristics. In contrast to Fourier coefficients, which represent components lasting for extended durations, wavelet coefficients are more localized and easier to interpret. This feature facilitates the separation of signal components that overlap in both time and frequency (C. Sidney Burrus, Gopinath and Guo, 1997).

Wavelets are also adjustable and adaptable because they come in various forms, allowing for customization to suit specific applications. This adaptability is ideal for systems that need to adjust to different types of signals (C. Sidney Burrus, Gopinath and Guo, 1997).

The generation of wavelets and the calculation of discrete wavelet transforms align well with digital computers. Wavelets' defining equation involves basic operations like multiplication and addition, without requiring calculus, derivatives, or integrals. This makes wavelets computationally efficient for digital systems (C. Sidney Burrus, Gopinath and Guo, 1997).

Regarding the efficacy, one of the limitations in a wavelet transform is preselecting a wavelet basis function (Li *et al.*, 2019). The wavelet transform denoising is intricately tied to factors like the depth of decomposition, the choice of wavelet basis function, and the selection of the threshold (Peng *et al.*, 2023). An insufficient number of decomposition layers can compromise denoising, while an excessive number can distort the signal (Peng *et al.*, 2023). Moreover, selecting the appropriate wavelet basis function and optimal threshold is typically based experience (Peng *et al.*, 2023). On the other hand, while noise reduction using Empirical Mode Decomposition (EMD) excels at handling nonlinear and nonstationary signals, it struggles with issues like mode aliasing and end effects (Peng *et al.*, 2023).

The Discrete Wavelet Transform (DWT) shares a connection with the Discrete Fourier Transform (DFT), which is a signal processing method involving trigonometric functions. However, generally speaking, the DWT outperforms DFT in terms of lossy compression. In other words, if an equal number of coefficients are selected for both a DWT and a DFT applied to a given data vector, the DWT will offer a more precise representation of the original data. Consequently, to achieve a comparable level of approximation, the DWT demands less storage space than the DFT. One key distinction is that wavelets, unlike the DFT, are highly localized in space, leading to the preservation of local details (Han, Kamber and Pei, 2012).

The underlying idea in using frequency- and time-frequency-based decomposition methods is that many real-world signals exhibit compact, limited-frequency spectra (Civera and Surace, 2021). These methods assume that the independent components of the signal have narrow-frequency characteristics with distinct spectral features (Civera and Surace, 2021). What sets these reviewed approaches apart from the traditional Fourier transform (FT) is their ability to analyse signals that change over time, known as nonstationary signals. These techniques are defined either analytically or empirically, operating based on algorithms rather than strict mathematical definitions (Civera and Surace, 2021).

The other methods of filtering are using the signal decomposition methods. They break down the target signal into its constituent parts. This breakdown can occur directly in the time domain, similar to the EMD and related techniques, or in the frequency domain, as seen in methods like the VMD. Another option is performing this breakdown in the time-frequency or time-scale domain (Civera and Surace, 2021).

Table 8-1 presents a comparison among adaptive mode decomposition methods and instantaneous frequency estimation methods and their cons and pros. The methods include EMD, LMD, ITD, LCD, HVD which have been introduced in this chapter and some other less common methods especially in mechanics and machines' noise and defect control (Feng, Zhang and Zuo, 2017).

*Table 8-1- Comparison of different adaptive mode decomposition methods (reference: (Feng, Zhang and Zuo, 2017)).*

| Category | Method | Pros | Cons |
|---|---|---|---|
| Adaptive mode decomposition | EMD | Effective for most signals | Lack of rigorous mathematical formulation, subject to mode mixing, end effects, over/under shooting of cubic spline fitting, and higher sampling frequency demand |
| | LMD | Free from distortions by AM effects, positive instantaneous frequency | High computational complexity, prone to mode mixing |
| | ITD | Better suppresses end effect and mode mixing, avoids spikes in instantaneous frequency and negative frequency, low computational complexity | Low time resolution |
| | LCD | Higher computational efficiency, better mitigates mode mixing | Subject to end effects |
| | HVD | Mathematically rational, simple algorithm, low computational complexity, suited for quasi and almost periodic signals | Unsuited for impulsive and aperiodic signals |
| | EWT | Rigorous mathematical formulation, suited for constant frequency and almost periodic signals | Possible mode splitting, unsuited for highly nonstationary signals |
| | VMD | Rigorous mathematical formulation, suited for constant frequency and almost periodic signals | Possible mode splitting, unsuited for highly nonstationary signals, high computational complexity |
| | ALIF | Rigorous mathematical formulation, suited for constant frequency and almost periodic signals | Possible mode splitting, unsuited for highly nonstationary signals |
| | NMD | Rigorous mathematical formulation, best mono-component decomposition and time-frequency readability, suited for arbitrary complicated waveforms | High computational complexity |
| Instantaneous frequency estimation | HT | Suited for most signals | Subject to Nuttall and Bedrosian theorems, possible spikes in instantaneous frequency and negative frequency |
| | GZC | Meaningful mean local frequency, simple algorithm | Low time resolution |
| | ES | Simple algorithm, highly adaptive to transient changes | Subject to Nuttall and Bedrosian theorems, possible spikes in instantaneous frequency and negative frequency |
| | NHT | Free from Nuttall and Bedrosian theorems constraint, stable | Based on empirical AM-FM decomposition |
| | DQ | Free from Nuttall and Bedrosian theorems constraint, accurate | Based on empirical AM-FM decomposition |

The EMD method dissects the target signal into a limited set IMFs (Intrinsic Mode Functions) (Huang *et al.*, 1998). IMFs are oscillations within the original signal, and their amplitude and frequency dynamically change over time, in contrast to the fixed harmonics generated by the Fourier transform. In essence, IMFs maintain the real-time frequency data (Civera and Surace, 2021).

The EMD is intuitive, direct, and adaptive with a basis derived from the data and operates in temporal space, not frequency space (Huang and Wu, 2008). The decomposition assumes that the data has multiple simple oscillatory modes with different frequencies superimposed at any given time (Huang and Wu, 2008).

Comparing ITD and EMD, ITD is computationally efficient, operates in real-time and is well-suited for non-stationary signals, minimises edge effects, preventing signal distortion, doesn't use splines, avoiding associated difficulties, ensures proper rotation components and preserves temporal information without smearing or smoothing, eliminates the need for a sifting procedure, offers improved accuracy in trend extraction and minimizes edge effects, and detects small signal changes more effectively during seizures or small variations (Frei and Osorio, 2006).

In recent years, conventional techniques for processing radar vital signals have primarily relied on filtration for eliminating noise and distinguishing between respiratory and heartbeat signals (Li *et al.*, 2019). However, these methods face limitations. They can only remove noise that falls outside the essential signal frequency range due to passband constraints. Noise and respiratory harmonics within this range remain, resulting in a less precise vital signal due to stopband attenuation (Li *et al.*, 2019). Addressing this challenge, some researchers have suggested using an adaptive noise cancellation algorithm to extract periodic vital signals from noisy data (Singh and Lubecke, 2013). Nonetheless, this approach has its own limitations, as it requires two radar systems for reference signal inputs. This introduces complexities and reduces experimental accuracy.

Some of the methods to overcome these issues, include using a peak detection algorithm for denoising and an adaptive linear enhancement method which utilises the delayed signal from the original data as a reference input (Li *et al.*, 2019).

## 8.8. Selecting Method

The processing of microwave signals is a critical task in various applications such as weather radar systems, communication systems, and remote sensing. A common challenge in these applications is the presence of noise and interference, particularly the impact of rainfall attenuation. Rainfall attenuation is a phenomenon where electromagnetic signals are absorbed and scattered by raindrops, leading to signal degradation. Thus, extracting the underlying carrier signal free from the effects of rainfall attenuation is essential for reliable data analysis.

In this chapter, different denoising methods are introduced. These methods are widely used for noise reduction in various signal processing applications, and they have demonstrated their effectiveness in many contexts. However, when it comes to handling rainfall attenuation, some of them fall short as they primarily focus on noise smoothing and do not specifically target rainfall-induced distortions.

Selecting a filtering method for analysis of the microwave signals requires to know about the characteristics of the signal, it's behaviour in time domain and frequency domain, and its changes during days and seasons.

The frequency spectrum and noise characteristics offer valuable insights into noise behaviour. Then, a more precise and proper method could be applied to achieve the desired output from the denoising method and decomposing the carrier signal. A few samples of noisy signals are generated and illustrated in Figure 8-17 to compare the effects of the power of frequency ($\alpha$) in Equation 8-6. The value of alpha varies from 0.00001 (to avoid 0) to 2.0 producing white to brown noise. Figure 8-18 is presented as a comparison to give some idea about the microwave signal characteristics in time domain.

Comparing the received signal level in a microwave link in Figure 8-18 with the noisy signals in Figure 8-17, shows that the microwave signal shares more similarities with brown noise in the time domain. This is somehow the same in frequency domain.

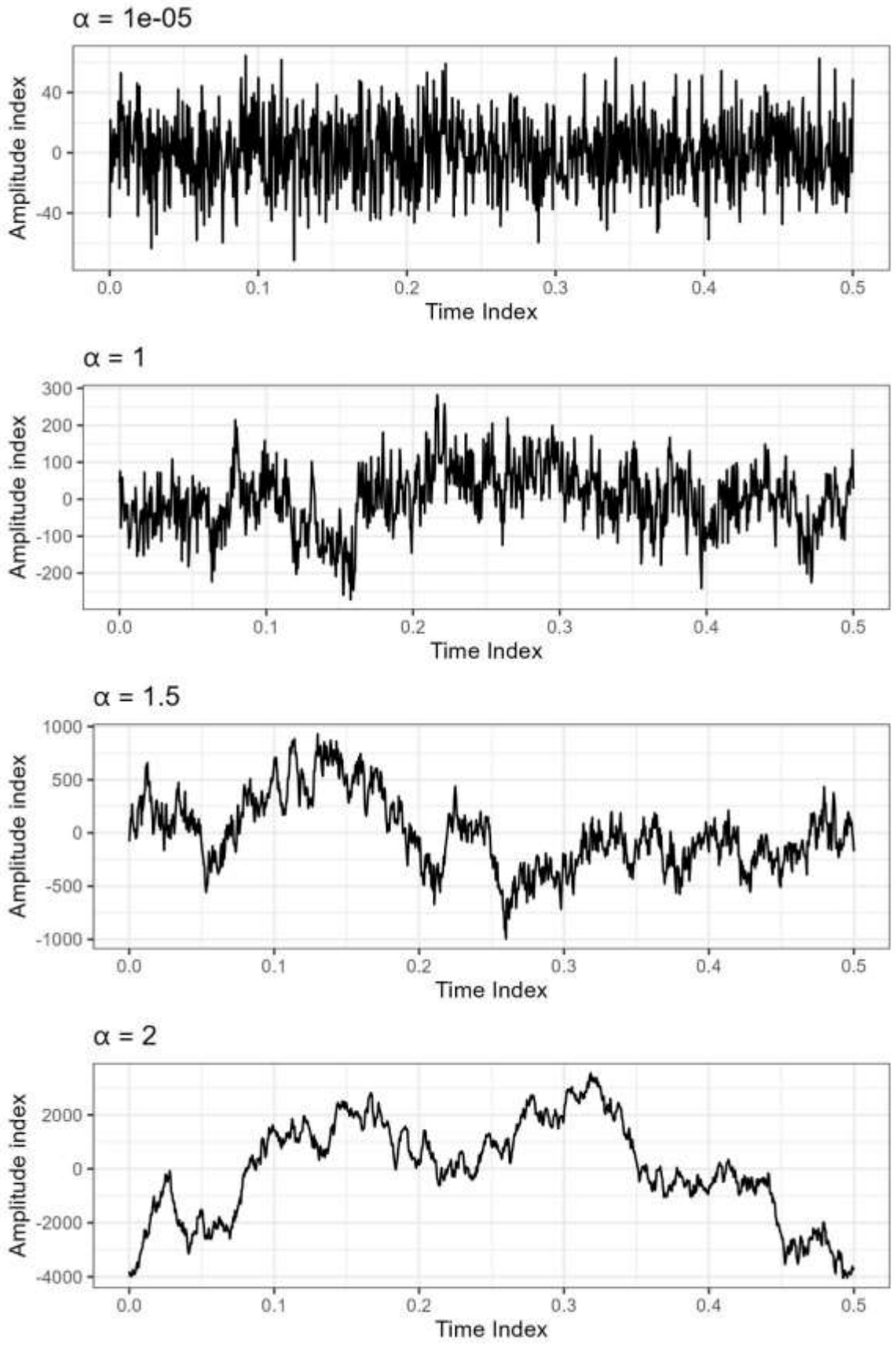


*Figure 8-17- Different noisy signals (sample generated) with different α values (α=1e-5 white noise, α=1 pink noise, α=2 brown noise).*

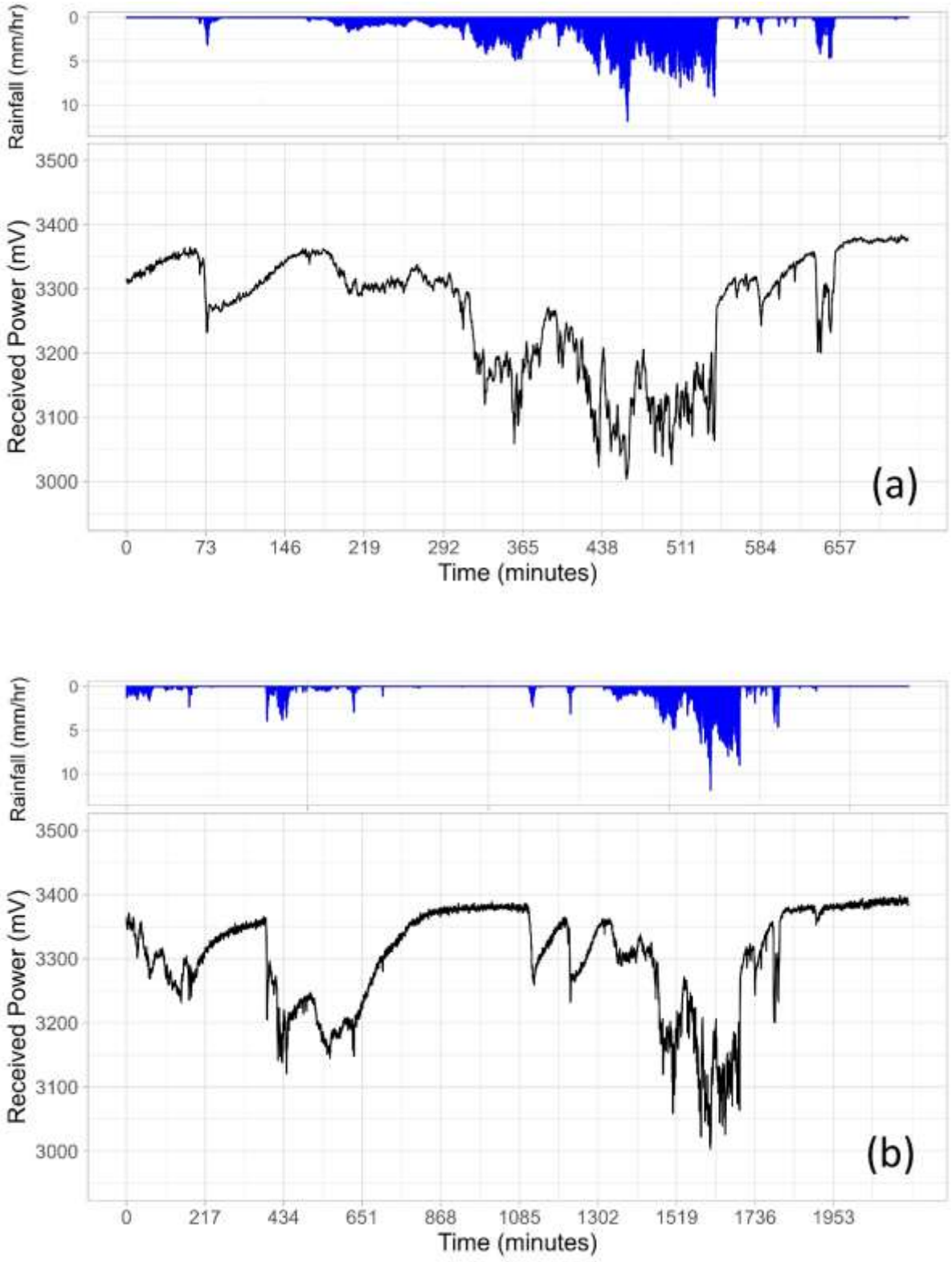


*Figure 8-18- Two sample time series of rainfall and the average received signal level for a 38GHz microwave link, vertically polarised.*

The time frames depicted in Figure 8-18 are half a day in graph (a) and one and a half days in graph (b). During these periods, the signal fluctuations shown in Figure 8-18 are predominantly influenced by rainfall events. Consequently, it is challenging to discern any extended, consistent trends in the reference signal level during this time. Therefore, employing a more extended timeframe could potentially unveil long-term signal level patterns Figure 8-19 presents signal levels and rainfall events over an extended period. This graph reveals sinusoidal oscillations, particularly between days 7 and 15, characterized by seven distinctive peaks occurring across seven days. Notably, this time frame corresponds to a period of minimal to negligible rainfall. Consequently, it can be inferred that during this period, the microwave reference signal exhibits sinusoidal fluctuations, with peaks during the night and troughs during the day. An examination of the available microwave link data for other days and seasons indicates that this same day-night signal level trend is consistently observed.

The third graph in Figure 8-19 displays the signal's frequency spectrum. It illustrates the variations in power for both small and large waves, found at low and high frequencies of occurrence. The higher power levels in the spectrum are associated with signal fluctuations that have occurred relatively infrequently. This is primarily linked to rainfall event attenuation, which varies with each rainfall occurrence and exhibits minimal resemblance to the attenuation of other events. Consequently, the frequency of such events is relatively low compared to the minor power fluctuations. Those minor changes caused by low-intensity noises that persist throughout wave propagation and persist due to various additive and multiplicative interferences. The daily fluctuations in the signal's power levels fall somewhere between these high and low-frequency components.

Figure 8-20 illustrates the frequency domains of the signals depicted in Figure 8-17 offering a detailed analysis of the power values and their respective frequencies. As shown in Figure 8-20, in a brown noise signal with $\alpha = 2$, the lower-frequency amplitudes exhibit higher power levels in contrast to white and pink noise. This phenomenon accounts for the presence of larger-scale waves. Similar to Figure 8-19, the diminished power in higher frequencies in Figure 8-20 is a consequence of the finer fluctuations present within the noisy signal. These fine-scale fluctuations occur more frequently and are observable over shorter time intervals.

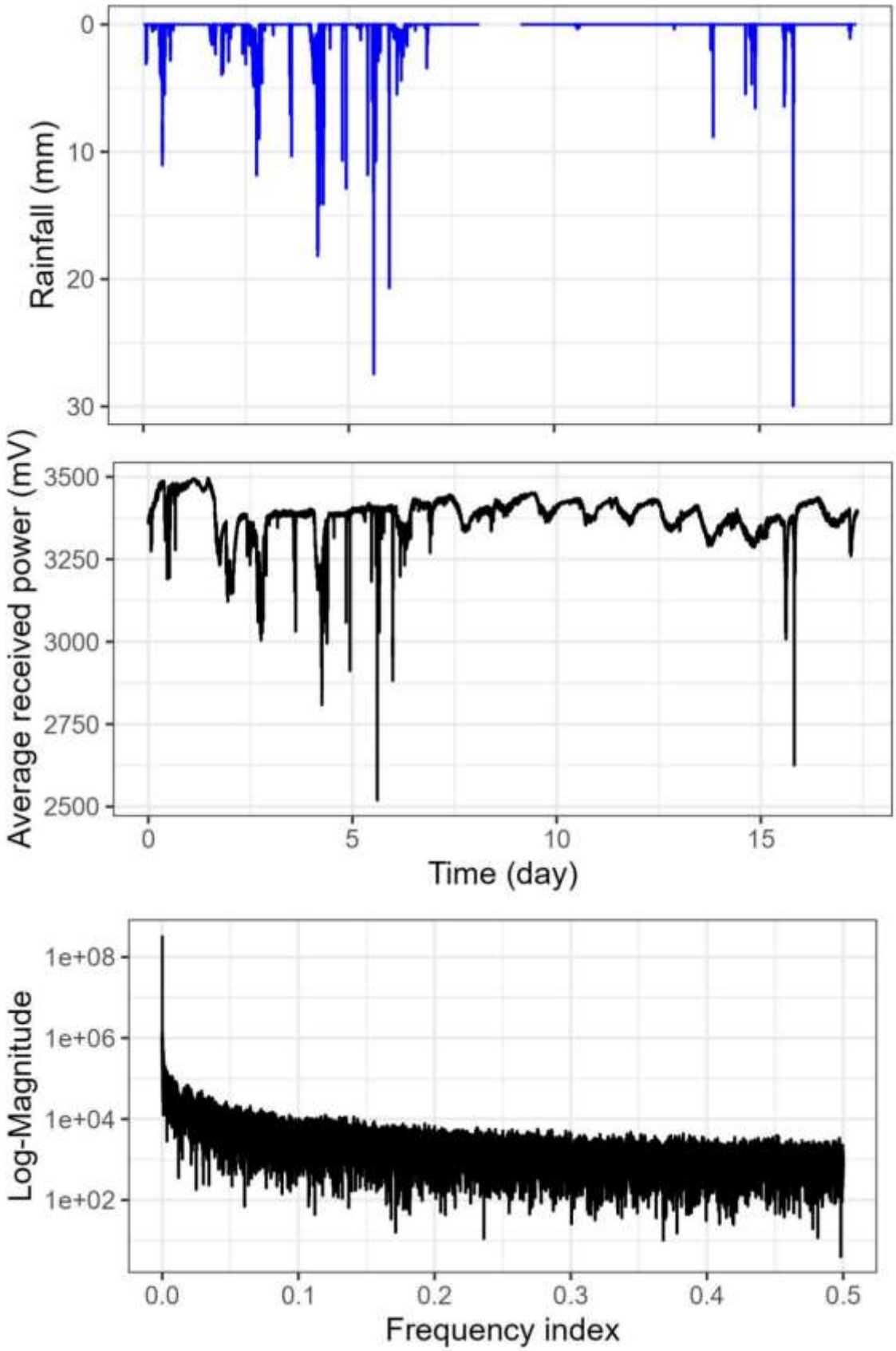


*Figure 8-19- Rainfall and microwave signal level for 17 days and the frequency spectrum for this signal*

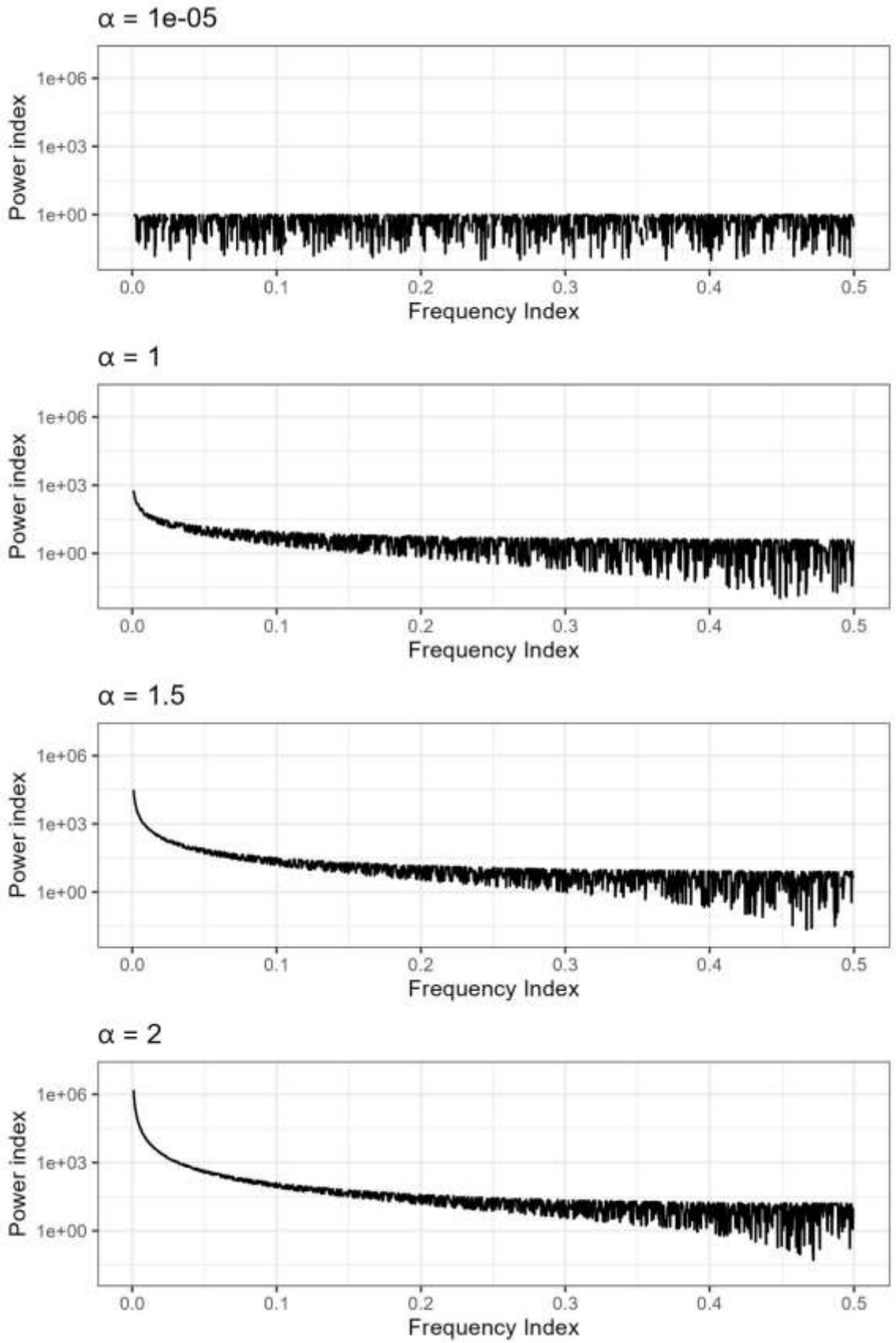


*Figure 8-20- Frequency domain of coloured noise signals (sample generated) with different α values (α=1e-5 white noise, α=1 pink noise, α=2 brown noise).*

The frequency domain of a microwave signal might not encompass all the essential information needed for signal analysis. Additional analyses are essential for obtaining a more comprehensive understanding of the short-term and long-term variations in received signal strength. In addition, it is necessary to obtain a vision on the main frequencies in received signal power when selecting discretion methods such as Fourier series and wavelength.

A dynamic reference level which varies with daily, monthly fluctuations in signal, temperature, humidity, and water vapour in atmosphere, can reveal and differentiate the main consistent signal from abrupt changes, for example rainfall effects, in power level. Consequently, it becomes feasible to extract rainfall attenuation from a noise free signal. Therefore, any tools which can analyse the time and frequency domains of the received power can assist with discretisation of the signal to base, rainfall peaks, and other noisy fluctuations.

Another significant consideration is the evolution of the signal's frequency domain over an extended duration. It is imperative to thoroughly analyse and scrutinise the fluctuations in each signal component—such as the base, rainfall, and noise—over time. Any alterations in the frequency characteristics of these signals can potentially impact the outcomes of discretisation and signal decomposition. Consequently, if the attributes of the signal components undergo changes after certain periods, the initial parameters for decomposition and denoising may become ineffective.

A useful assistance in time series analysis is ACF. The autocorrelation function (ACF) is a tool which help to find how different records in data are correlated (Nounou and Bakshi, 2000). It represents a correlation between the signal and a copy of itself that has been delayed. provides insights into how the relationship between any pair of signal values evolves as their temporal separation varies. It characterizes the memory of a stochastic process in the time domain but does not offer any insights into the process's frequency characteristics (Nounou and Bakshi, 2000).

ACF is a useful indicator of white noise. A white noise process remains time-independent, and its autocorrelation function shows zero values at all lags except for a value of one at lag zero, indicating complete lack of correlation. Conversely, a correlated process like ARMA or ARIMA exhibits non-zero values at lags other than zero, signifying correlations between different lagged observations. However, the wavelet coefficients associated with a correlated process display a degree of decorrelation at various scales (Nounou and Bakshi, 2000). This benefit of multiscale representation will enhance the denoising quality.

Figure 8-21 presents an analysis of the autocorrelation function (ACF) applied to the received signal power from a 38GHz microwave link (vertically polarised). The analysis compares the signal power of the initial 10 days with signals of the same duration over the subsequent 2, 4, 6, 8, 10, and 12 months. The corresponding rainfall periods are presented in red in the rainfall graph.

The figures reveal that the signal in the first days of the initial period shares some similarities with the power of the signal in the subsequent days. Specifically, the power of certain frequencies repeats in the first and second days (24 and 48 hours) and seven and eight days (168 and 192 hours). However, these power levels do not repeat on other days. The power pattern may reoccur in three or four days after the initial comparison, around 6 to 8 months later. Nevertheless, this pattern lacks consistency, and the power frequency remains in the white noise area for the rest of the days.

In a purely white noise scenario, 95% of spikes should fall within $\pm 2/\sqrt{T}$ where $T$ is the length of the time series. However, more than 5% of spikes in this data series fall outside this range, indicating a departure from complete white noise, although there isn't a robust correlation with other frequencies. The correlation remains under 20% in the ACF after 24 hours.

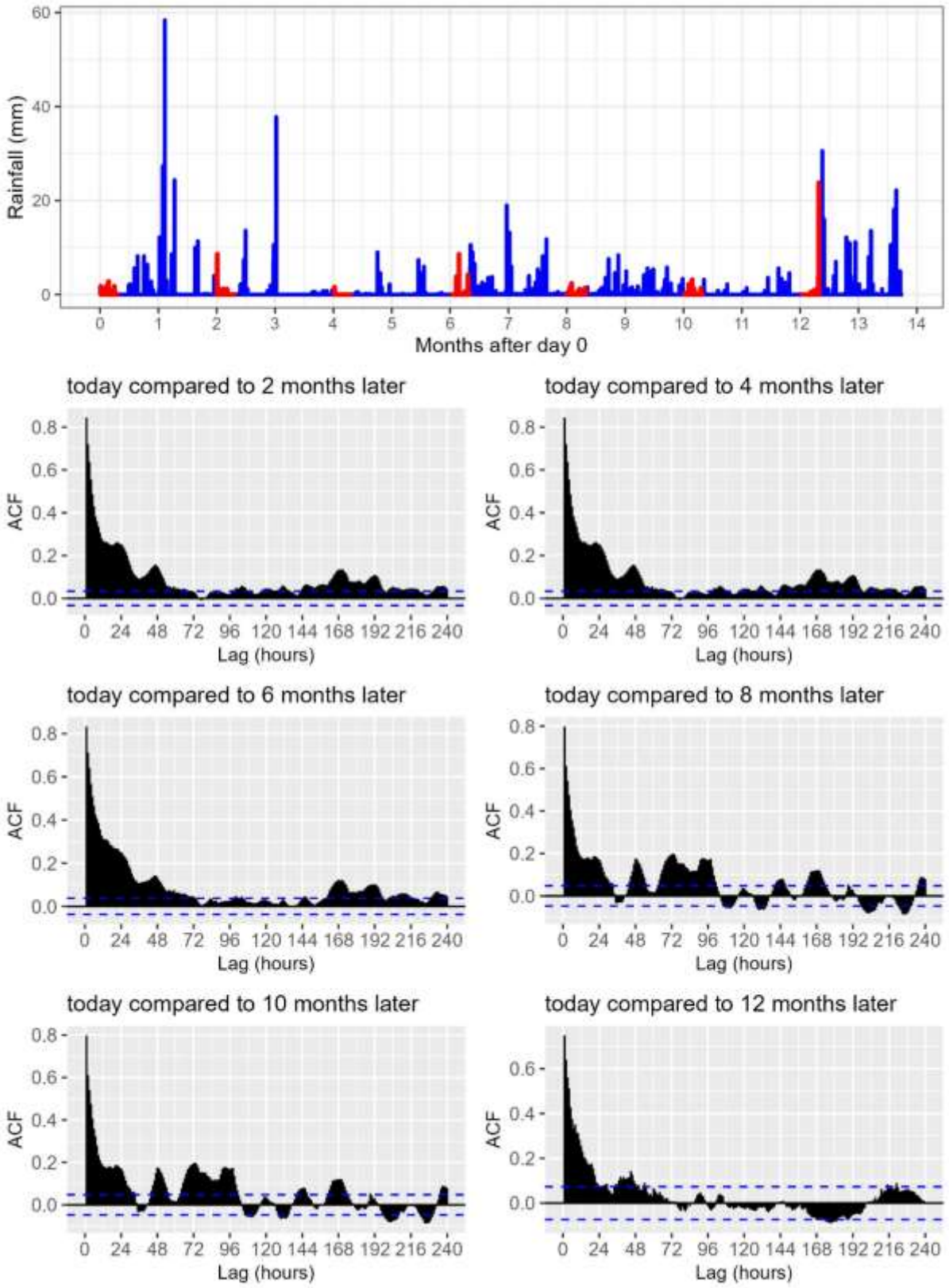


*Figure 8-21- The autocorrelation function (ACF) of the microwave received power in a 38GHz link (vertically polarised) comparing 10 days power fluctuations with 2 to 12 months lag.*

Given that Figure 8-21 and the observed peaks and troughs do not indicate a strong repeating pattern in the signal power, it suggests that frequency discretisation techniques may be ineffective in excluding the main patterns of the signal, making it challenging to extract the base power of the received signal.

Analysing the characteristics of the microwave signal and its temporal variations across various scales, ranging from minutes to days and from days to seasons, provides insights into the appropriateness of employing a low-pass filter. This choice proves beneficial in retaining long-term daily fluctuations while effectively eliminating or smoothing out minute-scale noise. Meanwhile, the decrease in power caused by rainfall attenuation will be filtered out, revealing the disparity in attenuation.

Figure 8-22 shows the application of a lowpass and a highpass filter and how they affect the signal fluctuations. The lowpass filter results in the long-term oscillations remaining close to the main signal, creating a smoother overall signal, while filtering out short-term noises.

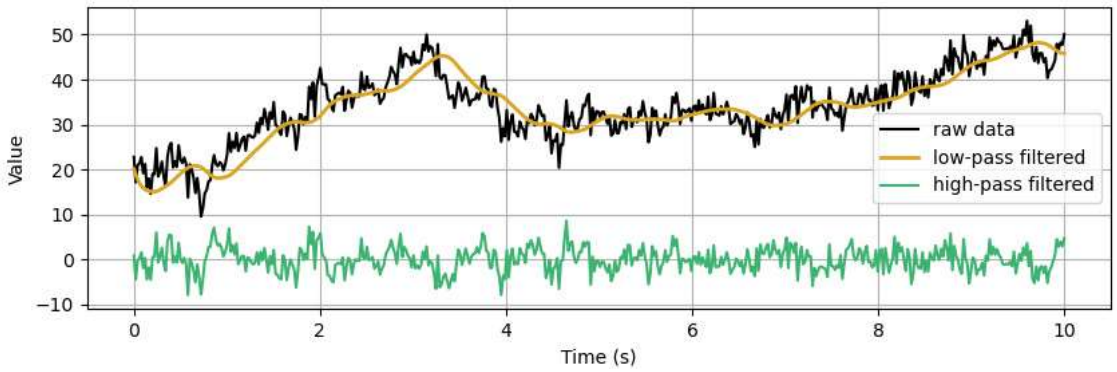


*Figure 8-22- A sample noisy signal and the results of applying a low-pass and a high-pass filter (reference:* (Bayless, 2022)*)*

Conventional techniques like wavelet analysis and standard Fourier transform are not the best approaches and considered as inefficient for processing non-linear and non-stationary signals (Margrave, 1998). They are effective for either non-linear or non-stationary signals, but not both (Al-Badrawi, 2017).

Fourier Spectral analysis is widely used in data interpretation due to its simplicity. However, it has limitations such as linearity and stationarity. Fourier approaches lack adaptability and suffer from energy leakage (Al-Badrawi, 2017).

Wavelet approaches are an advanced version of Fourier Spectral methods with a predefined window. Each window can be adjusted for a specific application. Wavelet methods are non-adaptive, and the decomposition basis is selected a priori (Al-Badrawi, 2017). EMD is an adaptive data driven tool with basis defined a posteriori. It can effectively analyse non-linear and non-stationary signals. EMD has the advantage of decomposing signals locally and is significant when the signal varies with time. However, EMD is empirical and requires formulating a mathematical frame (Al-Badrawi, 2017).

The decomposition method is examined by its ability to effectively decompose non-linear and non-stationary signals, adaptively derive the decomposition basis from the signal itself, extract signal features in the presence of noise, and represent signal frequencies locally (Al-Badrawi, 2017).

Filtering through EMD is a natural approach, where the relevant signal components are separated during the sifting operation (Al-Badrawi, 2017). But selecting the appropriate IMFs is challenging, especially with high noise power. Unfortunately, there are no analytical expressions for the signal IMFs, so most of the important findings on EMD are based on empirical results from numerical experiments (Al-Badrawi, 2017).

In contrast to traditional signal processing methods, EMD excels in several aspects. It overcomes the constraints of the Fourier transform, eliminating the need to preselect a wavelet basis function as required by wavelet transforms. EMD offers excellent time resolution and adapts to signals effectively, enabling precise signal reconstruction (Li et al., 2019).

The Local Characteristic scale Decomposition (LCD) method shares the EMD framework but differs in instantaneous mean extraction. Nonetheless, this step employs an EMD-like approach, utilizing cubic spline interpolation and encountering familiar technical challenges (Civera and Surace, 2021). Likewise, the Local Mean Decomposition (LMD) method encounters the same limitations as EMD and is notably influenced by the choice of smoothing and step size parameters (Civera and Surace, 2021).

On the other hand, CML power signal is not a linear wave as it is affected by some parameters in the propagation media, such as humidity, temperature, and the density of gasses in the atmosphere. The effective factors vary not only during a day and day to night, but also by changing the seasons.

The power of the CML (the received signal power) also shows skewness and non-asymmetric patterns. Therefore, the efficiency of the EMD methods and FFT and wavelet transform to decompose the carrier signal and establishing a reliable reference level are in doubt. The skewness is greater when the rainfall begins which is related to the wet antenna effect. This can be observed in Figure 8-18 (b) when the rainfall stops.

For a signal with sinusoidal variations during the day (periodic behaviour) along with noise, a Butterworth filter could be a better choice for smoothing or denoising. A summary of the literature provides some reasons for selecting Butterworth as a filtering method in this study:

- Frequency Characteristics: Butterworth filters are designed to have a smooth frequency response with a flat passband and gradual roll-off. Since your signal exhibits sinusoidal variations, a Butterworth filter's gradual roll-off can help preserve the periodic behaviour of the signal while attenuating the noise outside the frequency range of interest.
- Trade-off Between Smoothing and Preservation: The gradual roll-off of a Butterworth filter strikes a balance between noise reduction and preserving the underlying periodic variations. This is crucial because you want to retain the peaks and valleys that correspond to specific times of day.
- Simple Design: Butterworth filters have a simple design process and require specifying the cutoff frequency. This makes them suitable for cases where you want to remove high-frequency noise while keeping the periodic low-frequency components intact.
- Avoiding Distortion: Other filters like Chebyshev or elliptic filters with steeper roll-offs might cause distortion in the sinusoidal variations due to their ripple characteristics. The sharp transitions in these filters could potentially introduce unwanted artefacts in the signal.
- Adaptability: The adaptability of Butterworth filters allows you to choose the order of the filter to control the trade-off between smoothness and noise attenuation. Higher-order Butterworth filters offer steeper roll-offs, which can be useful for attenuating higher-frequency noise.